ABSTRACT

YOUSEFPOOR, NIMA. Control of Advanced Power Converter Topologies for Transmission Grid Management. (Under the direction of Dr. Subhashish Bhattacharya).

Currently, there is common agreement that the power grid needs to be upgraded and modernized. The transmission grid assets are getting aged, especially in the US, and growing number of variable renewable energy sources has made the situation even worse. This requires a huge upfront investment to renew the current transmission infrastructure and further increase its capacity. The most valuable assets in the transmission grid are high power transformers. Transformers have the single highest cost value of the equipment installed in high voltage substations; therefore, utilities and system operators are most interested to extend the utilization time of this expensive component of the transmission grid. This dissertation seeks to integrate flexible active solutions to existing transmission assets to control power flow and increase power transmission capacity.

First, the concept of Convertible Static Transmission Controller (CSTC) using Modular Transformer Converter (MTC) as the building block is investigated. The MTC is a bidirectional back-to-back AC/AC power conversion unit and the CSTC is a versatile transmission controller asset in case of transmission system contingencies and normal conditions for dynamic power flow control and contingency management of the transmission grid. The proposed CSTC with new functions has several advantages compared to existing FACTS controllers. System modularity for manufacturers and utilities/system operators using standard high power electronic systems is one of the advantages of this structure. In this thesis, algebraic models of the CSTC are derived in three main operation modes (series-

shunt, series-series, and shunt-shunt connecting configurations). The proposed algebraic models are used to define the reference values for active and reactive power flow of the CSTC converters based on the desired operating points for the meshed power system, the power transformers in particular. The dynamic performance of the CSTC with the proposed control structures and algebraic models will be investigated based on the PSCAD simulation.

The vulnerability of electric power grid to man-made and natural disasters, such as hurricanes, tsunami, earthquake, geomagnetic storms etc. has become crucially important. In this dissertation, the concept of transmission-level Active Mobile Substations (AMS) is introduced for disaster management. The AMS is a mobile substation enabled by integrated power electronics. In this thesis, a detailed comparative analysis of different power converter topologies for AMS is presented. Also, a modular topology with high frequency isolation is proposed for AMS application. In this configuration, several single-phase AC/DC power conversion building blocks are connected in series. The isolation in each building block is provided through a high frequency transformer within a DC/DC converter. In the high frequency isolated modular converter configuration, several floating DC capacitors in all three phases are connected in series, and voltage balancing control of these floating dc capacitors is required. In this dissertation, an appropriate control structure with the capacitor voltage balancing controller is proposed.

Also, the concept of embedded multi-terminal dc grid in meshed ac power system is explored. The proposed technology can provide back-up in case of transmission line failure, and it can enhance power transmission capacity and flexibility in existing ac grids. In this thesis, the algebraic model of multi-terminal DC grid is derived and validated in a meshed ac

power system. Algebraic model will present the behavior of ac grid with respect to various operating points of dc grid. The control structure of dc grid based on master/slave and droop control scheme is explored. Also, a droop control structure with dead-band controller is proposed for multi-terminal DC grid control. To verify the model and the control structure, dynamic performance of the integrated multi-terminal DC grid in a reduced order three-bus AC equivalent NYPA power system is investigated through PSCAD and real time digital simulation.

Furthermore, the dynamic performance of the proposed solutions under fault operating conditions is explored. The AMS must be designed to operate satisfactorily under fault operating conditions. In this dissertation, component design considerations in development of the AMS under AC fault operating condition will be provided, and a new control strategy is proposed to control AMS under AC fault when component design is not sufficient to prevent overcurrent and trips. The appropriate control algorithm of AMS and multi-terminal DC grid for DC fault operation and recovery after DC fault is also proposed. The dynamic performance of multi-terminal DC grid with master/slave control scheme and droop control with dead-band controller is also explored and compared under loss of terminal station.

Finally, to prove the MTC and high frequency isolated modular converter based AMS as transmission assets and to verify the control structure and algorithm, ultra-high fidelity Controller Hardware-in-the-Loop (CHIL) testing has been conducted and comparative results will be presented. Lab-scale experimental results for both configurations are also reported to verify the proposed control schemes.

Control of Advanced Power Converter Topologies for Transmission Grid Management

by
Nima Yousefpoor

A dissertation submitted to the Graduate Faculty of
North Carolina State University
in partial fulfillment of the
requirements for the degree of
Doctor of Philosophy

Electrical Engineering

Raleigh, North Carolina

2014

APPROVED BY:

_____   _____
Dr. Subhashish Bhattacharya   Dr. Iqbal Husain
Committee Chair

_____   _____
Dr. Srdjan Lukić   Dr. Xiangwu Zhang

DEDICATION

To my beloved wife

Golbarg

BIOGRAPHY

The author, Nima Yousefpoor was born in Tehran, Iran, in 1986. He received the B.Sc. and M.Sc. degrees in electrical engineering from Amirkabir University of Technology (formerly Tehran Polytechnic), Tehran, in 2008 and 2010, respectively. He is currently working toward the Ph.D. degree at North Carolina State University, Raleigh. His research interests include HVDC transmission systems, multilevel converters, flexible ac transmission system devices, and renewable energy systems.

ACKNOWLEDGMENTS

TABLE OF CONTENTS

LIST OF FIGURES

LIST OF TABLES

Chapter 1. INTRODUCTION

Currently, there is common consensus that the power grid needs to be upgraded and modernized to accommodate more renewable sources of generation. One hurdle that impedes the investment in grid infrastructure and transmission capacity especially in the US is intermittency nature of these sources. There are reports that show high penetration of renewables can cause overloading conditions in the power grid that necessitates either network upgrade or curtailment in the generation while there is unutilized capacity in the transmission network, i.e. >138kV [1]-[2]. Therefore, power flow control or as recently termed power router solutions have been gaining more attractions. From the conventional Unified Power Flow Controller (UPFC) for AC systems to advanced multi-terminal High Voltage Direct Current (HVDC) systems using Modular Multilevel Converter (MMC) technologies, researchers have proposed several power electronic solutions in this field to improve and increase reliability, efficiency, cost-benefit factors, functions and many more.

Among those, mainly for distribution network, hybrid transformer [3] or controllable network transformer [4]-[6] can be considered retrofitting approaches in which a fractionally-rated power electronic system is integrated to conventional 50/60 Hz transformer and therefore it makes a controllable node. Unlike hybrid solutions for distribution system, recently completely solid-state approaches, with advances in semiconductor switches such as 15kV IGBTs and magnetic materials have been practiced at the research level [7]-[11]. This solution is often called Solid-State Transformer (SST) [12]-[19].

In case of transmission-level solutions due to the lack of sufficiently high-voltage semiconductor switches (i.e. 138 KV), different combinations of components have been mainly proposed for conventional forms of power router such as different MMC topologies [20]-[26]. Perhaps, the transformerless UPFC proposed by [27] is among the few examples of innovation at the transmission-level solutions where system configuration is also different from conventional UPFC.

On the other hand, the transmission grid and its assets are getting aged especially in US. A very familiar example of such assets is the power transformer, a very robust component of every power system and the main node in the power transmission. It has been reported that the average age of the transformers in the US is about 40 years although most transformers are built for 30 years of operation [28]. Looking into available equipment failure data provided by US EIA, we can observe an increasing outage trend from 2008 to 2009 just due to transformer operational mechanism [29]. Specific attention to 300-399 kV class of transmission transformers reveals that 345 kV transformers need immediate attention and revised management [30]. To the best knowledge of authors, there is no practice or report of locally controlled device addressing this issue except more software-based asset management tools.

Our society's security and economic health depends critically on the availability and reliability of electric power. Anyone living in North America was certainly aware of, if not affected by, the 14 August 2003 blackout. The investigation into the blackout shows that the cause was an unfortunate chain of events that disrupted power flow to key areas of load and resulted in confusion over the status of the power delivery network. Electric power demand

continued, and without an effective way to move power into major metropolitan areas, the system became unstable [31]. The vulnerability of electric power grid to man-made and natural disasters, such as hurricanes, tsunami, earthquake, geomagnetic storms etc. has become crucially important. In this regard, geomagnetic storms due to unusual solar activity are unlike any other natural terrestrial threat to the power grid. These storms not only can develop rapidly but also have continental footprints that can result in widespread, simultaneous impact to many nodes in the bulk power system. A recent study carried out by NERC, and DOE has determined that a severe geomagnetic disturbance (GMD) has the potential to cause crippling and long-lasting damage to the North American electric power grid [32]. Perhaps the most well-known GMD event in North America is the March 13-14, 1989 geomagnetic storm that caused the Hydro Québec Blackout. On March 13, 1989, an exceptionally intense geomagnetic storm caused the shutdown of seven static var compensators (SVCs), essential for control of Hydro Québec grid, and its loss caused voltage to drop, frequency to increase, and the resulting instability caused the tripping of La Grande transmission lines [33]. The chain of power system disturbances led to collapse of the Hydro Québec system within seconds of loss of about 9,500 MW of generation from La Grande network.

At the heart of the power delivery network, where power flows from transmission lines to the distribution network, are large power transformers that step the transmission voltage down to that needed for distribution for final use. Large power transformers have the single highest cost value of the equipment installed in high voltage substations and are scarce and hard to replace. However, these valuable assets are getting aged and are more vulnerable to

disturbances caused by abrupt operation changes in the power network. These operation changes are due to several reasons including overloading, harmonics other than 60Hz, weather conditions, and GMD. Figure 1-1 shows simulation results of geomagnetically-induced current (GIC) flow in US power grid due to a severe GMD, almost 10 times bigger than the one in 89 [34]. The regions prone to unprecedented power system collapse are outlined. Figure 1-2 shows the areas of at-risk large power transformers in the US with high percentage regions experiencing severe black-outs due to GIC flow [35]. These disturbances constantly upsurge the risk and vulnerability of power grid operation because; for instance, severe-impact GMD events are not fully addressed in conventional bulk power system planning, design, and operating processes.
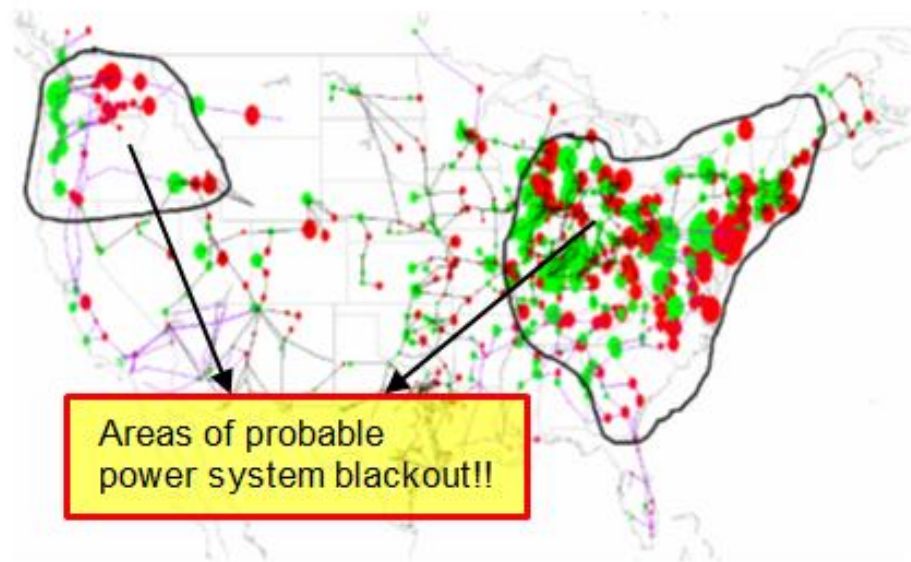
Figure 1-1. Simulation results showing probable blackout in US grid due to severe geomagnetic storm.
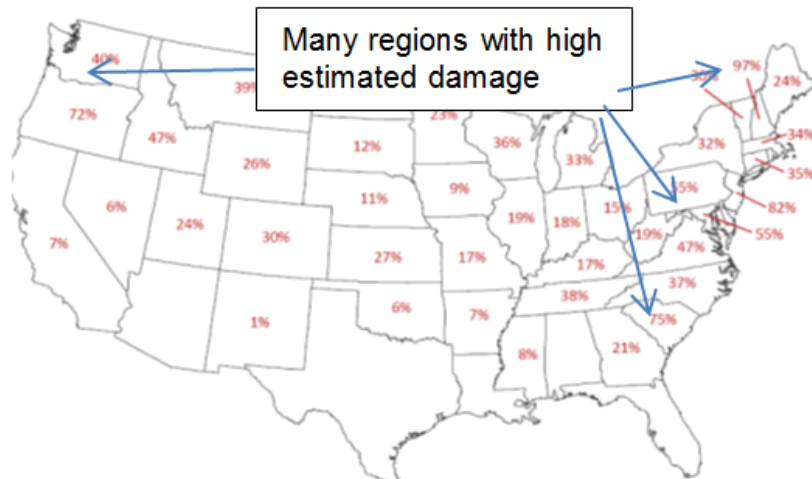
Figure 1-2. Areas of at-risk large power transformers due to GMD and GIC flow.

One of the main motivations of our research is ultimately to increase the security of electricity transmission and distribution. The approach is through the development of a modular, mobile and controllable utility asset which is referred to as Active Mobile Substation (AMS). The AMS provides the preventive measures as well as the corrective measures to ensure the security of the electricity delivery as shown in Figure 1-3. The AMS provides the flexibility of full or partial utilization for the transmission lines and power transformers. This flexibility effectively increases the system spare capacity and operating margins, and also provides back-up in case of power transformer failure (or forced reduced transformer rating operation) scenarios by providing real-time continuous power flow control and thereby, increased transfer capacity of existing transmission systems. These features allow the AMS to be deployed dispersedly or aggregated in case of natural and manmade disasters and emergencies to meet power, voltage, VAR and configuration requirements.
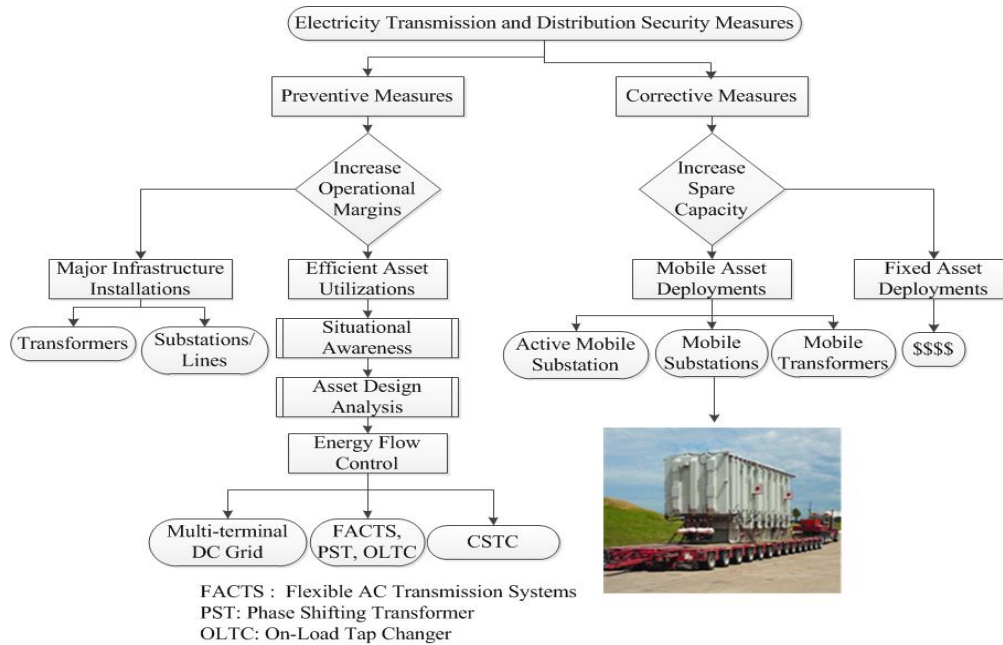
Figure 1-3. Electricity Delivery security measures flowchart.

The proposed technology used in the AMS is called Convertible Static Transmission Controller (CSTC) which is desired to be transportable and connected across the substation power transformer and can be reconfigured to the required modes of operation. The representative scheme is presented in Figure 1-4. The proposed solution advances the current FACTS technology solution for instance; deployed in New York Power Authority (NYPA) network which is a 200 MVA Convertible Static Compensator (CSC). The CSC is a versatile FACTS controller with eleven modes of operation including STATCOM, SSSC, UPFC and IPFC [36]-[38]. In addition to these modes, the CSTC technology provides (partial) back-up in case of substation failure or forced reduced power operation scenarios. The offered solution with added values for mesh systems provides the following functions and benefits:

- Transmission or distribution transformer life extender.

- Recovery transformer for disaster management.

- Seasonal renewable transmission controller.
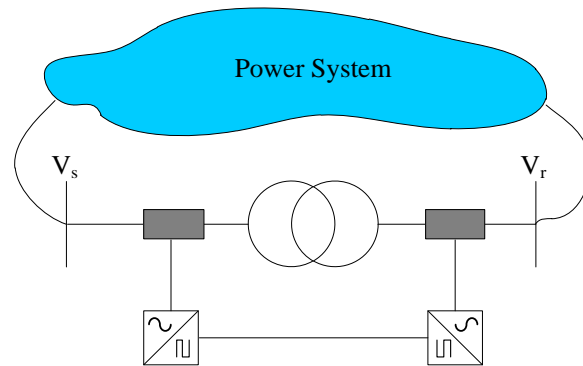
Figure 1-4. Schematic of the proposed transmission controller at the substation.

1.1 State of the Art

Unified Power Flow Controller (UPFC) is the most comprehensive FACTS Controller invented and developed in the US at Westinghouse R&D center (now Siemens). UPFC not only regulates the active and reactive power through the transmission line but also provides VAR support for the connecting bus. A very successful albeit costly project is the Convertible Static Compensator (CSC) which is the most versatile FACTS Controller in the world, installed by New York Power Authority, NYPA at Marcy substation. For NYPA CSC eleven modes of operation including the UPFC, has been operating since 2003. The custom designed CSC helps NYPA to mitigate congestion issues so that not only it has recovered its

investment cost but also provides revenue as spinning VAR reserve and as a power flow controller for contingency management for NY-ISO [39].

Controllable transformer or hybrid transformer has been proposed recently and under investigation to add dynamic control to regular or existing power transformers and possibly reduce the overall costs by using a fractionally rated converter integrated to the main transformer [40]-[41]. Although, several functions such as active and reactive power control can be obtained, direct connection of power converters with high dv/dt and harmonics is typically not possible. One potential issue is associated with the secondary B-H loops and increased losses due to the high frequency switching. Consequently, an overrated or even a special power transformer, and/or a more complex power converter must be used. All of these factors affect the reliability, efficiency and cost of the overall system and not only of the power converter itself. It can be concluded that the application map of the proposed approaches, if successful, is limited to distribution grids with custom designed *new* 60 Hz transformer which may be replaced with advent of Solid State Transformers [42].

Polytransformer is a practical approach that adds values and flexibility to conventional power transformers [43]. It is a compact (autotransformer structure), multi-voltage power transformer that helps utilities to secure operation of the transmission grid. It has multiple voltage ratings for high, low and tertiary voltages. The voltage rating is selected by changing connections internally prior to moving the transformer to a new location. The flexibility in voltage range, connections and compact design allows the TOs to provide the spare transformer for their interested region (system) and even lease their spare transformers when they do not need it.

1.2   Outline of the Research

Chapter 2 explores the modular transformer converter (MTC) based convertible static transmission controller (CSTC). For power flow control with specific attention to renewable energy resources based transmission in a meshed network, less complex coordinated control can be obtained with the proposed Convertible Static Transmission Controller (CSTC) concept which is connected across the substation power transformer and can be reconfigured to the required modes of operation. Convertible Static Transmission Controller (CSTC) is a versatile transmission controller which can perform several functions including power flow control for renewable resources transmission and transformer back-up for disaster management or life extension purposes. Different connecting configuration options (shunt-shunt, series-shunt, and series-series) can be obtained in the proposed transmission controller. In this chapter, the algebraic model of CSTC in different modes of operation is derived. Algebraic model of CSTC is used for steady state and transient stability analysis. Algebraic model will present the behavior of transformer power flow with respect to various operating points of CSTC converters. The control structure of CSTC in different modes of operation is also presented in this chapter, and dynamic performance of the CSTC based on the proposed control structures is further investigated in three different connecting configurations in PSCAD/EMTDC environment.

Chapter 3 introduces the active mobile substation (AMS) which can be used in normal conditions as a power router and contingencies as a recovery transformer. The AMS is a mobile substation with integrated power electronics and it can be connected across different transformers of the grid. This chapter proposes transmission-level active mobile substations

that provide back-up in case of power transformer failure or forced reduced operation scenarios in addition to power flow control for seasonal renewable energy transmission. In this chapter, design considerations in development of the AMS will be provided in terms of power electronics building blocks, converter system control and its effects, and required supervisory control. The high frequency isolated modular converter is introduced as the power electronics building block of AMS, and an appropriate control strategy with the phase and module voltage balancing controller is proposed to achieve voltage balancing control of multiple floating dc capacitors in the high frequency isolated modular converter based AMS.

Chapter 4 presents the algebraic model and control of embedded multi-terminal dc network in meshed ac power system. Algebraic model will present the behavior of ac grid with respect to various operating points of dc grid. The control structure of multi-terminal dc grid based on droop control structure with dead-band controller is proposed. The dynamic performance of the embedded multi-terminal dc grid in meshed ac power system is also investigated. PSCAD and RTDS results will be presented to verify the proposed algebraic model and controller.

In chapter 5, the dynamic performance of AMS is explored under fault operating conditions, and a new control strategy is proposed to control AMS under AC fault operating conditions when component design is not sufficient to prevent overcurrent and trips. In this chapter, the dynamic performance of high frequency isolated modular converter based AMS is evaluated under DC fault operating condition, and an appropriate control algorithm for DC fault operation and recovery after DC fault is also proposed. Using the proposed control algorithm for DC fault operation, the high frequency isolated modular converter based AMS

can be protected against dc fault without using expensive DC circuit breakers. The dynamic behavior of multi-terminal DC grid under DC fault operating condition and loss of converter station is also explored in this section.

Chapter 6 describes the hardware prototype of CSTC and AMS. Experimental results are presented to verify the control structures of CSTC and AMS under normal and AC fault operating conditions. Controller Hardware-in-the-loop (CHIL) test of CSTC and AMS is also performed by Typhoon HIL400, and CHIL results are presented to verify the validity of the proposed control architecture for CSTC operation during normal and unbalanced power system conditions for different connecting configurations. Controller Hardware-in-the-loop (CHIL) test of high frequency isolated modular converter based AMS is also performed by Real Time Digital Simulator (RTDS). Lab-scale experimental results are also presented to verify the proposed controller performance of high frequency isolated modular converter based AMS.

Chapter 7 draws the conclusions of the present work and offers future work and research paths that can be taken from the opportunities that this dissertation has identified.

Chapter 2.   MODULAR TRANSFORNER CONVERTER (MTC) BASED CONVERTIBLE STATIC TRANSMISSION CONTROLLER (CSTC)

2.1 Introduction

The transmission grid and its assets are getting aged especially in the US. A very familiar example of such assets is the power transformer, a very robust component of every power system. It has been reported that the average age of the transformers in the US is 40 years although most transformers are built for 30 years of operation. Figure 2-1, according to NERC, presents the outage duration of transmission level transformers due to the device malfunction in the recent years that reflects the need for immediate care [44]. Looking into available equipment failure data, we can observe an increasing outage trend from 2008 to 2009, just due to transformer operational mechanism. Specific attention to 300-399 kV class of transmission transformers reveals that 345 kV transformers need immediate attention and revised management [45]. One of the motivations of this work is to propose a unique power electronics (active) based solution that provides back-up in case of substation transformer failure or forced reduced transformer operation scenarios. It is worth noting that the required control can be embedded in the CSTC simplifying the power system operation, if the necessary commands are received from the main transformer [46]. This mode of operation is called distributed control vs. centralized control that may be requested in contingencies. In addition, the CSTC may be desired to be transportable and compatible with different voltage

levels and therefore operates as a recovery transformer in case of natural and manmade hazards and disasters. In normal mode of operation, CSTCs are functioning to extend the life time of existing transformers by partially bypassing and conditioning the substation throughput power. In case of transformer failure, CSTCs can be deployed dispersedly or in an aggregated form to meet power, voltage, VAR and configuration requirements [47]. To achieve these goals, the solution must be modular not only from the core power converter topology but also from the utility and transmission operator's perspectives. Therefore, the building block to realize the CSTC is an AC/AC conversion unit that can be stacked together to provide required power and voltage requirements. The considered building block is termed as Modular Transformer Converter (MTC) which in this paper is standard or future standard 2-10 MVA drive converters.
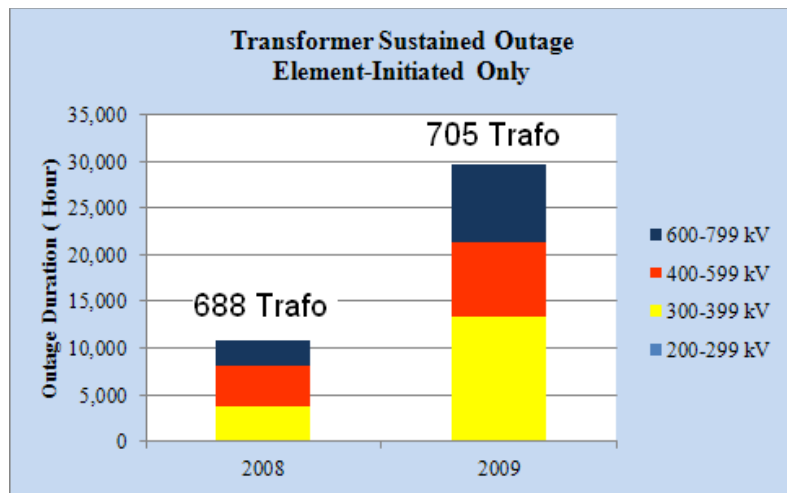
Figure 2-1. Transmission transformer outage durations in the US.

2.2 Modular Transformer Converter (MTC) System

MTC is a transportable bidirectional AC/AC conversion unit. If several MTC building blocks are combined they can be considered as transmission or distribution level equipment or assets. MTC is potentially cost effective since it utilizes the standard power electronics converter systems, for instance, standard medium voltage drive converters. Currently, standard medium voltage drive systems are commercially available up to 10 MVA with IGCT based three-level NPC converters and up to 2 MVA with IGBTs which are more than 97% energy efficient. With advent of new high voltage SiC based semiconductor switches such as 15kV SiC IGBT and 10kV SiC JBS diode technologies higher power and higher efficiencies can be foreseen for MTC building blocks.

The key component of MTC converters is semiconductor switch and better performance can be obtained through hybrid semiconductor configuration (like Si switch and SiC diode), circuit topology and control considerations. In addition to common benefits, high efficiency is one of the key factors that enables the transportability of the MTC system. From the control point of view, three different control structures have been considered denoted as angle control, vector control, and hybrid control methods. A simplified advanced angle control structure is shown in Figure 2-3. In the angle control structure, the output voltage magnitude is determined naturally by the operation of the converter; i.e., constant ratio between AC input and DC output is considered [48]. Consequently, the control objectives are determined by regulating only the output voltage angle. In addition, angle control structure in multi-pulse converters ensures superior harmonic spectrum which is essential for transmission level equipment. It should be mentioned that this method is well adopted for

commercial STATCOMs and [11] showed the possibility of extending this method for active and reactive power control. The other control methos is the so-called vector control which is typically applied to PWM converters, Figure 2-4. This control structure presents higher controllability compared to the angle control structure. However, this controllability is obtained through higher switching frequencies and higher converter losses compared to angle-controlled converters being operated at line frequency. Another approach is to combine two control structures to create a hybrid control structure. In this scheme, one converter or a group of converters operates with angle control and the others operate with vector control.
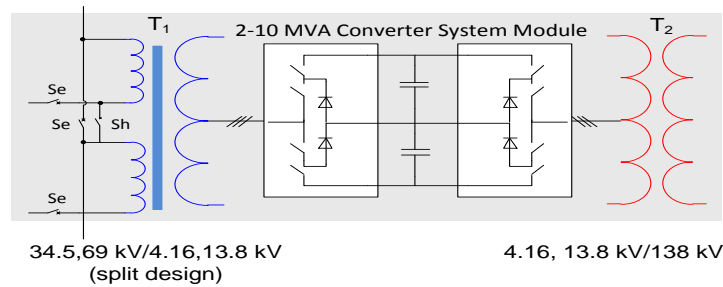
Figure 2-2.   An example of MTC based on three-level NPC MV drive converters.
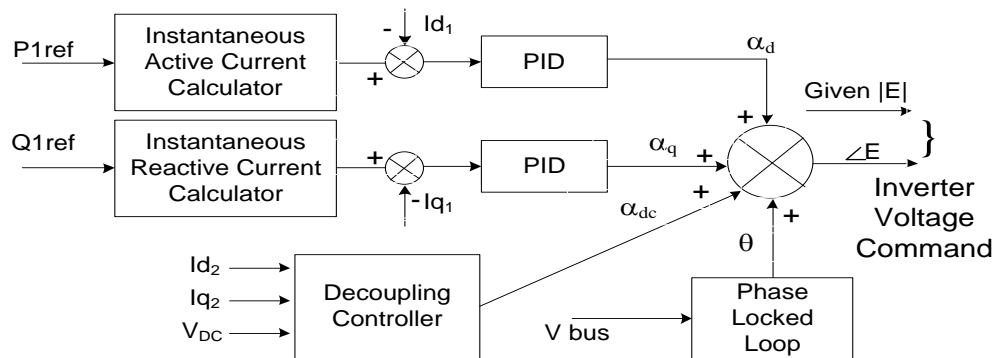
Figure 2-3.   Advanced angle control structure for voltage-sourced converters.
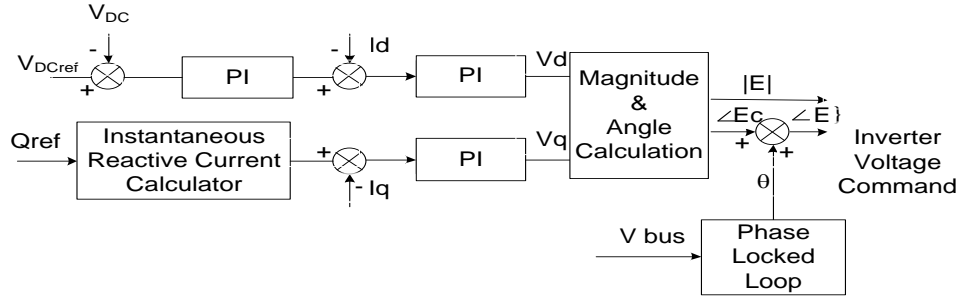
Figure 2-4.   Vector control structure for voltage-sourced converters.

2.3   Convertible Static Transmission Controller (CSTC) System

Convertible or reconfigurable FACTS controllers with increased functions have several advantages for system operators. A very successful albeit costly project is the Convertible Static Compensator (CSC) which is the most versatile FACTS controller in the world, installed by New York Power Authority (NYPA) at Marcy substation. For the CSC eleven modes of operation, including the UPFC and IPFC, has been operating since 2003. The custom designed CSC helps NY-ISO to mitigate congestion issues as explained in [49].

Conventionally, FACTS controllers like the CSC have been developed and inspired mainly for improving power transfer capability. However, due to the aging transmission transformers and effects of high penetration of renewables on flow-gates, more controls may be needed on transformers right at substations. Consequently, we propose a Convertible Static Transmission Controller (CSTC) which is installed across the transmission transformer to increase the system spare capacity and operating steady state and dynamic margins. The proposed CSTC with MTC building block is presented in Figure 2-5 which different modes are realized through breakers operation.

16
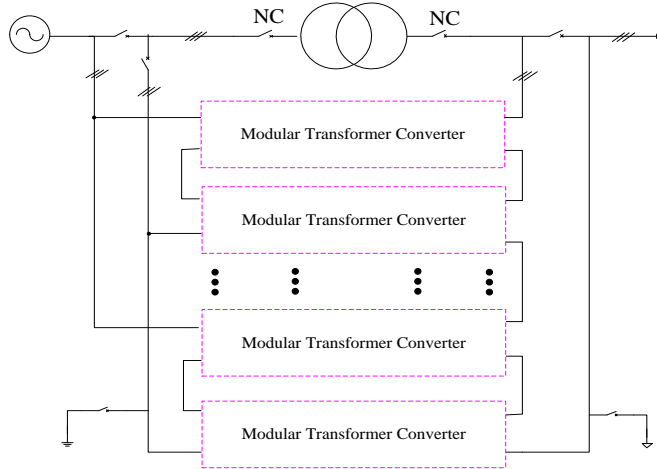
Figure 2-5. Representative schematic of MTC based CSTC.

The proposed CSTC and its different integration options are presented in Figure 2-6. With MTC structures, three major integration options with multiple operation modes can be realized. These integration options are shunt-shunt, series-shunt, and series-series.
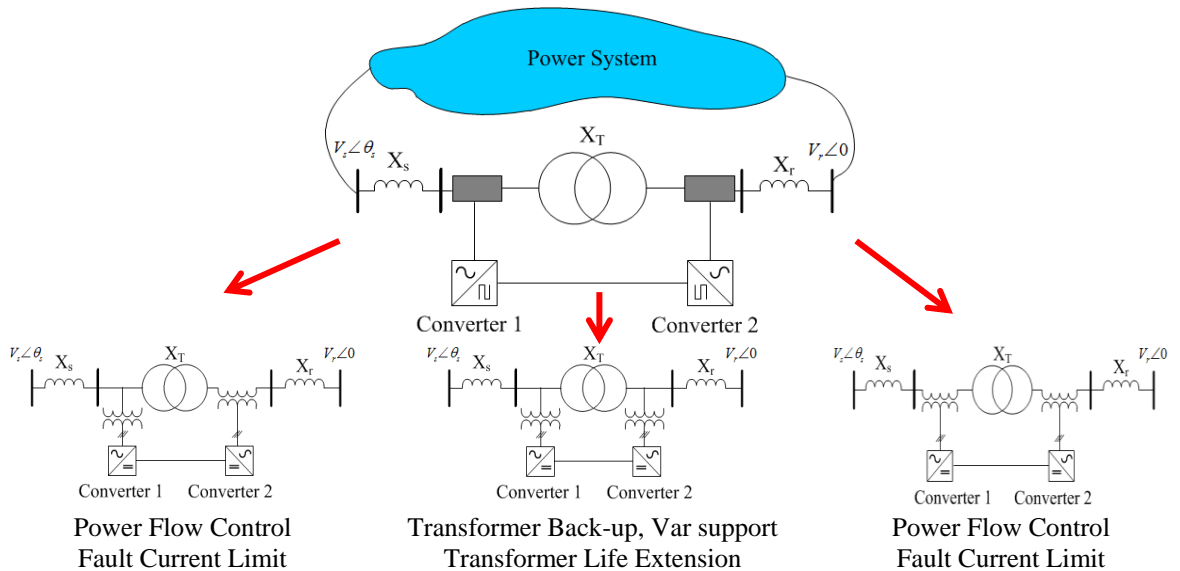
Figure 2-6. Different connecting configurations of the CSTC at the substation.

MTC building blocks can be connected in series or parallel to achieve higher power. The interleaved modulation can be used to increase the effective switching frequency. An example of interleaved carrier waveforms for 4 MTC building blocks connected in series is shown in Figure 2-7. The output voltage waveform is illustrated in Figure 2-8. The switching frequency for each converter is $f_{sw}=1500\ Hz$ whereas the effective switching frequency is $f_{sw}\ (effective)=4{\times}1500=6000\ Hz$. As a result, higher effective switching frequencies and lower converter losses can be obtained by the interleaved switching method.
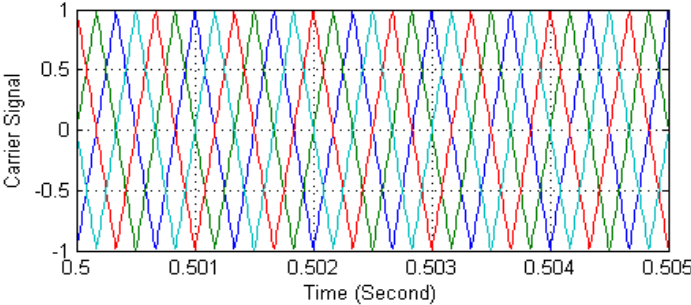
Figure 2-7.   Interleaved carrier waveform.
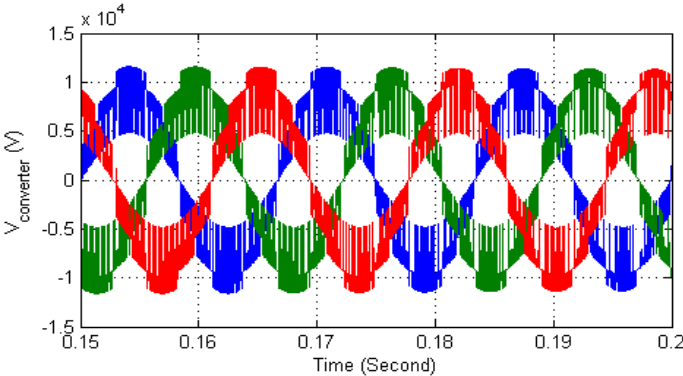
Figure 2-8.   Converter PWM output voltage waveform.

18

2.4 Algebraic Model of CSTC in Three Different Connecting Configurations

In this section, the algebraic model of CSTC in different modes of operation is derived. Algebraic model of CSTC is used for steady state and transient stability analysis [50]. Algebraic model will present the behavior of transformer power flow with respect to various operating points of CSTC converters. The objective of algebraic model development is to set the reference values of active and reactive power flow of CSTC converters based on the desired operating points for transformer active and reactive power flow. The P-Q transformer operating range can also be obtained based on the proposed algebraic model.

2.4.1 Shunt-Shunt Connecting Configuration

The shunt-shunt configuration shown in Figure 2-9 can be utilized as an active back-up for the main transformer up to its rating. The algebraic model of CSTC in shunt-shunt mode of operation is shown in Figure 2-10. This model can be used for load flow and transient stability analysis. According to Figure 2-10, Eq. (2.1) ~ Eq. (2.5) can be used to obtain three phase AC currents (I_s, I_T, I_1, I_2, I_r). With the three phase AC currents, active and reactive power flow of transformer and CSTC converters can be easily computed.

Based on the operating points of CSTC converters, Eq. (2.6) ~ Eq. (2.9) are solved to calculate the magnitude and the angle of voltage sources $(V_{c1}<\theta_{c1})$, $(V_{c2}<\theta_{c2})$ at each iteration step. As a result, active and reactive power flow of transformer can be obtained by Eq. (2.10), and Eq. (2.11) respectively for each CSTC operating point.
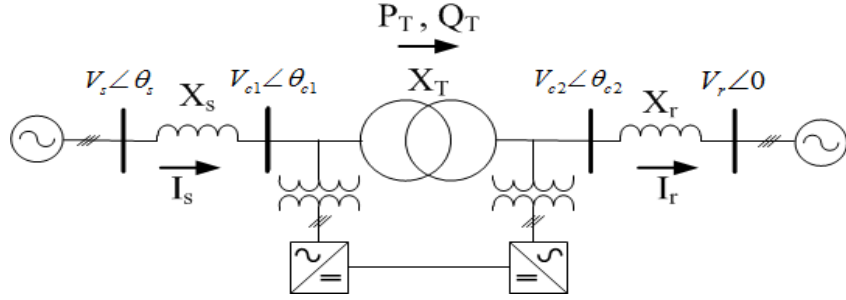
Figure 2-9. Test system to analyze the CSTC in shunt-shunt connecting configuration.
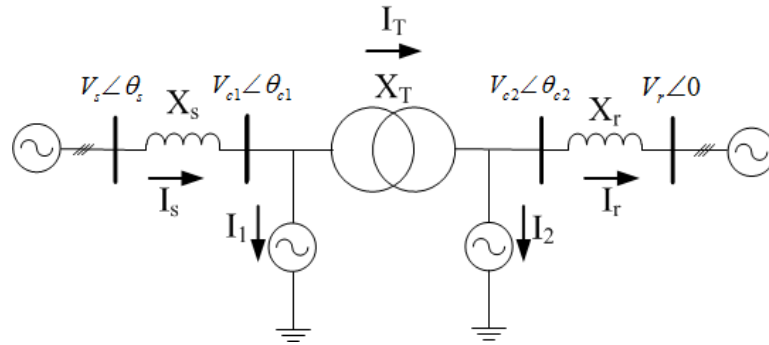
Figure 2-10. Algebraic model of CSTC in shunt-shunt connecting configuration.

$$\vec{I_s} = \frac{V_s \measuredangle \theta_s - V_{c1} \measuredangle \theta_{c1}}{jX_s} \qquad (2.1)$$

$$\vec{I_T} = \frac{V_{c1} \measuredangle \theta_{c1} - V_{c2} \measuredangle \theta_{c2}}{jX_T} \qquad (2.2)$$

$$\vec{I_r} = \frac{V_{c2} \measuredangle \theta_{c2} - V_r \measuredangle 0}{jX_r} \qquad (2.3)$$

$$\vec{I_1} = \vec{I_s} - \vec{I_T} = \frac{V_s \measuredangle \theta_s - V_{c1} \measuredangle \theta_{c1}}{jX_s} - \frac{V_{c1} \measuredangle \theta_{c1} - V_{c2} \measuredangle \theta_{c2}}{jX_T} \qquad (2.4)$$

$$\vec{I_2} = \vec{I_T} - \vec{I_r} = \frac{V_{c1} \measuredangle \theta_{c1} - V_{c2} \measuredangle \theta_{c2}}{jX_T} - \frac{V_{c2} \measuredangle \theta_{c2} - V_r \measuredangle 0}{jX_r} \qquad (2.5)$$

20

$$P_1 = \frac{V_{c1}V_s}{X_s}\sin(\theta_s - \theta_{c1}) - \frac{V_{c1}V_{c2}}{X_T}\sin(\theta_{c1} - \theta_{c2}) = P_{converter} \tag{2.6}$$

$$Q_1 = \left[\frac{V_{c1}V_s}{X_s}\cos(\theta_{c1} - \theta_s) - \frac{V_{c1}^2}{X_s}\right] - \left[\frac{V_{c1}^2}{X_T} - \frac{V_{c1}V_{c2}}{X_T}\cos(\theta_{c1} - \theta_{c2})\right] \tag{2.7}$$

$$P_2 = \frac{V_{c1}V_{c2}}{X_T}\sin(\theta_{c1} - \theta_{c2}) - \frac{V_{c2}V_r}{X_r}\sin(\theta_{c2}) = -P_{converter} \tag{2.8}$$

$$Q_2 = -\left[\frac{V_{c1}V_{c2}}{X_T}\cos(\theta_{c2} - \theta_{c1}) - \frac{V_{c2}^2}{X_T}\right] + \left[\frac{V_{c2}^2}{X_r} - \frac{V_{c2}V_r}{X_r}\cos(\theta_{c2})\right] \tag{2.9}$$

$$P_T = \frac{V_{c1}V_{c2}}{X_T}\sin(\theta_{c1} - \theta_{c2}) \tag{2.10}$$

$$Q_T = \frac{V_{c1}^2}{X_T} - \frac{V_{c1}V_{c2}}{X_T}\cos(\theta_{c1} - \theta_{c2}) \tag{2.11}$$

Figure 2-11 shows transformer active power flow with respect to CSTC active power flow when X_T=0.1 pu, X_s=0.1 pu, and θ_s=5.74° based on the algebraic model of CSTC in shunt-shunt mode of operation. As can be seen, when the reference value of CSTC active power flow increases from 0pu to 1pu, CSTC transformer active power flow is varied according to the receiving end impedance. For instance, transformer active power flow is decreased form 0.46pu to -0.09pu (0.46pu-(-0.09pu) = 0.55pu) when $X_r = 0.02pu$, but this variation is 0.75pu (0.25pu-(-0.5pu)=0.75pu) when $X_r = 0.2pu$. As can be observed, transformer active power flow variations with respect to CSTC active power flow increase as X_r increases. Figure 2-12 gives transformer reactive power flow as a function of converter1 reactive power flow. As can be seen, transformer reactive power flow is reduced form 0pu to -0.45pu (0pu-(-0.45pu) = 0.45pu) when $X_r = 0.02pu$, and this variation is 0.24pu (0pu-(-0.24pu) = 0.24pu) when X_r =0.2pu. As a result, transformer reactive power flow variations with respect to converter 1

reactive power flow decrease as X_r increases. Figure 2-13 also shows transformer reactive power flow versus converter 2 reactive power flow. As can be observed, transformer reactive power flow is varied from 0 to -0.09pu (0pu-(-0.09pu) = 0.09pu) when $X_r =0.02pu$, and this variation is 0.47pu (0pu-(-0.47pu) = 0.47pu) when $X_r =0.2pu$. Therefore, the higher value of X_r results in wider range of change in the transformer reactive power flow with respect to converter 2 reactive power.

In order to validate the proposed algebraic model, the simulation study has been extended for different CSTC operating points. Figure 2-14-Figure 2-16 shows transformer active and reactive power flow versus CSTC power flow based on steady state values of simulation results. Comparison of Figure 2-14 and Figure 2-11 shows that the algebraic model is accurate enough to represent the behavior of transformer active power flow with respect to the CSTC active power flow. Figure 2-15, and Figure 2-16 show transformer reactive power flow with respect to converter 1, and 2 reactive power flow respectively for different operating points of CSTC converters based on the obtained simulation results. Comparison of simulation results (Figure 2-15, and Figure 2-16) and algebraic model results (Figure 2-12, and Figure 2-13) show that the behavior of transformer reactive power flow with respect to CSTC operating points can be appropriately represented by the algebraic model. Simulation results also show that the dynamic operation is satisfactory with appropriate response time.

The P-Q transformer operating range is shown in Figure 2-17-Figure 2-19 for different values of X_r when the active and reactive power references for each converter is varied between -1pu to 1pu in steps of 0.05pu. As can be seen, transformer power flow variation is almost 0.55pu when $X_r =0.02pu$, and it is around 0.8pu when $X_r =0.2pu$. Therefore, it can be

concluded that the transformer operating region is dependent on power system parameters, and it increases as X_r increases.
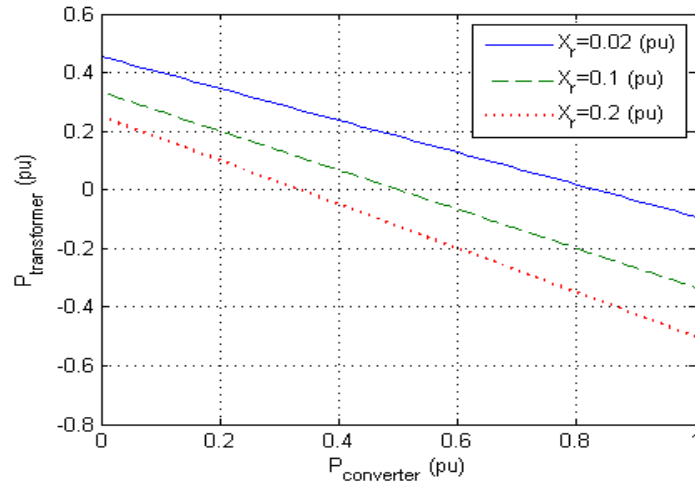
Figure 2-11. Transformer active power flow with respect to converter active power ($Q_1 = 0$(pu), $Q_2 = 0$ (pu))- Algebraic model.
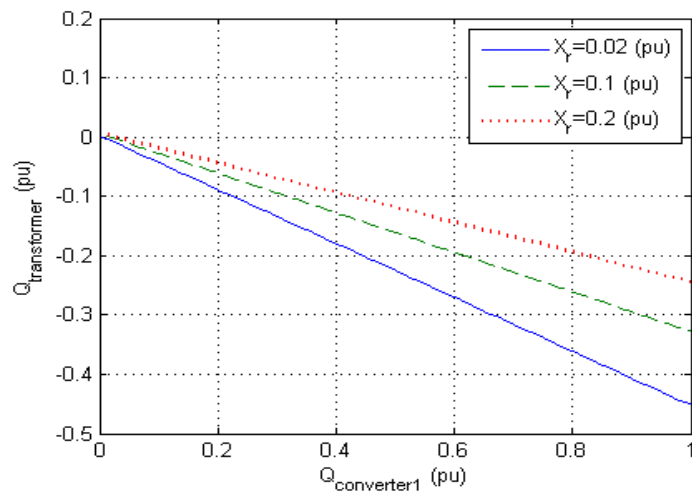
Figure 2-12. Transformer reactive power flow with respect to converter 1 reactive power ($P_{ref} = 0$(pu), $Q_2 = 0$ (pu))- Algebraic model.
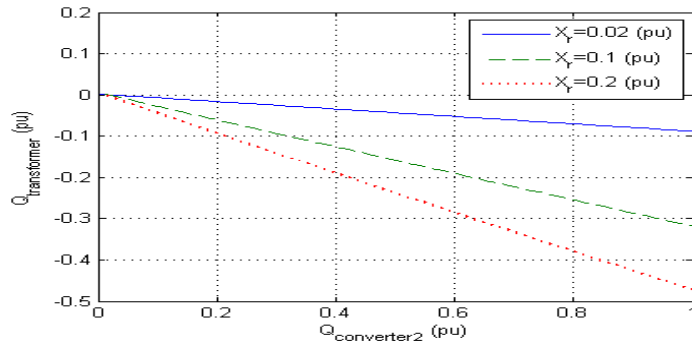
Figure 2-13. Transformer reactive power flow with respect to converter 2 reactive power (P_{ref} =0(pu), Q_1 =0 (pu))- Algebraic model.
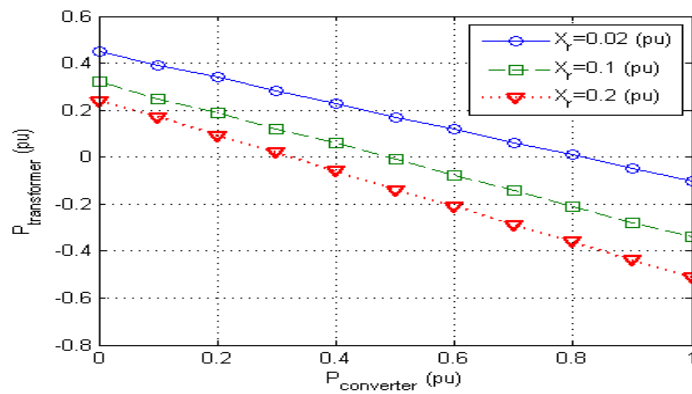
Figure 2-14. Transformer active power flow with respect to converter active power (Q_1 =0(pu), Q_2 =0 (pu))- PSCAD results.
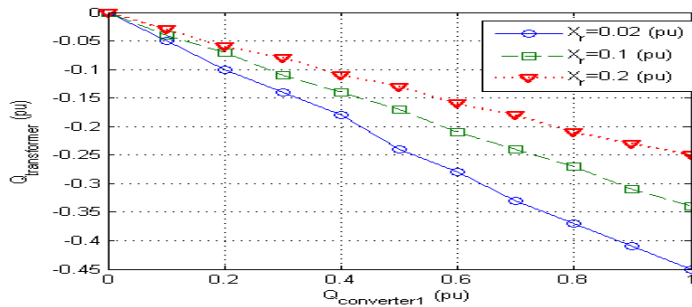
Figure 2-15. Transformer reactive power flow with respect to converter 1 reactive power (P_{ref} =0(pu), Q_2 =0 (pu))- PSCAD results.
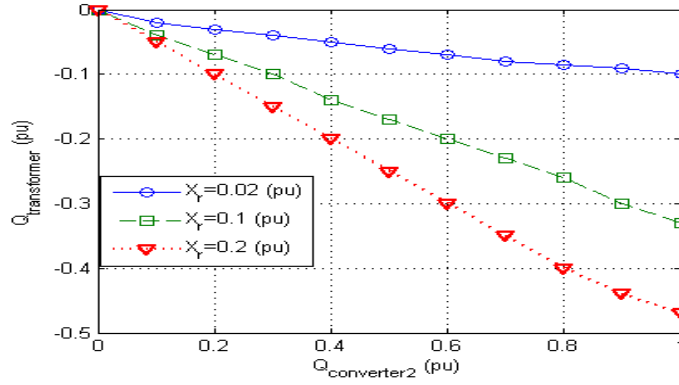
Figure 2-16. Transformer reactive power flow with respect to converter 2 reactive power (P_{ref} =0(pu), Q_1 =0 (pu))- PSCAD results.
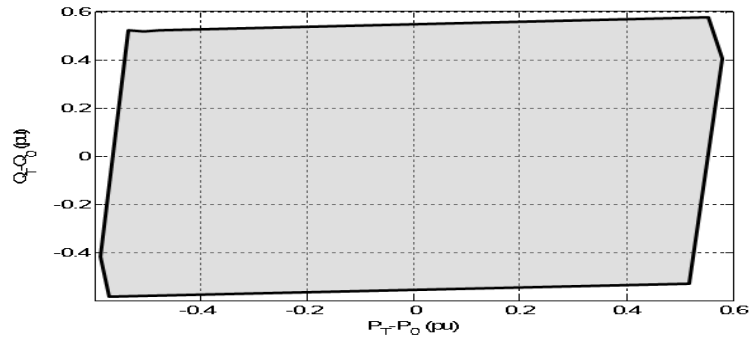
Figure 2-17. P-Q transformer operating range in shunt-shunt mode of operation (X_r=0.02 (pu)).
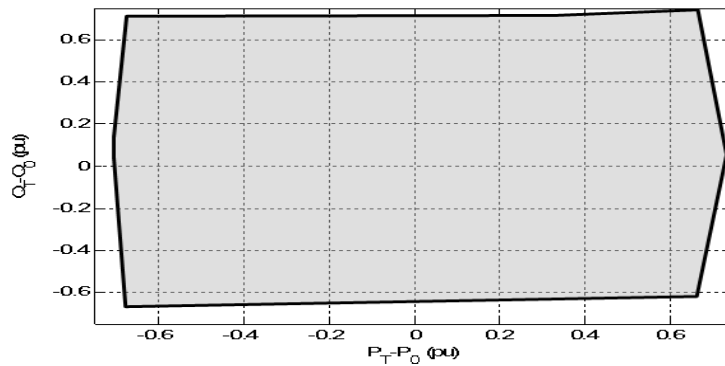
Figure 2-18. P-Q transformer operating range in shunt-shunt mode of operation (X_r=0.1 (pu)).
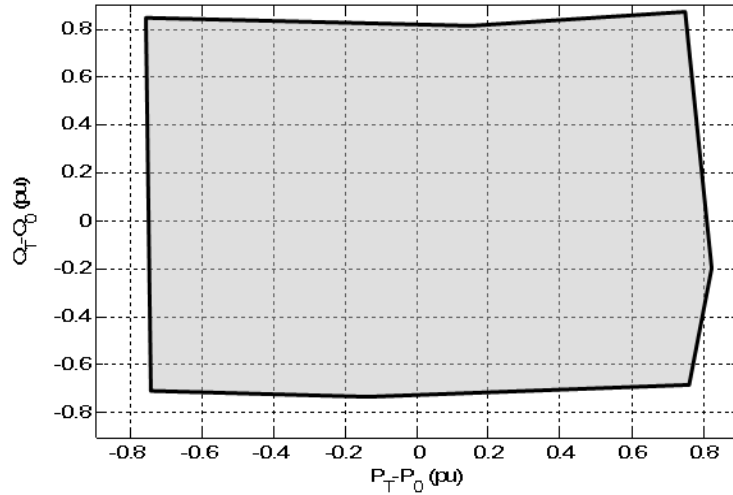
Figure 2-19. P-Q transformer operating range in shunt-shunt mode of operation ($X_r=0.2\ (pu)$).

2.4.2 Series-Shunt Connecting Configuration

Although the shunt-shunt option may be necessary for back-up operation, there are unsolved issues and constraints regarding the power flow control during the normal operation of the transformer. Series voltage injection is conventionally used for the power flow control [51]-[52]. When this compensator is equipped with an active power source, it can control the active and reactive power independently. An algebraic model of CSTC in series-shunt configuration is shown in Figure 2-20. The shunt converter by providing the reactive power to the receiving end bus maintains the voltage magnitude. Meanwhile, it can transfer the active power to the series converter to provide a different voltage and angle. Hence, this configuration can control the active and reactive power flow through the transformer while maintaining the bus voltage magnitude. The algebraic model of CSTC in series-shunt mode of operation is similar to that of UPFC.
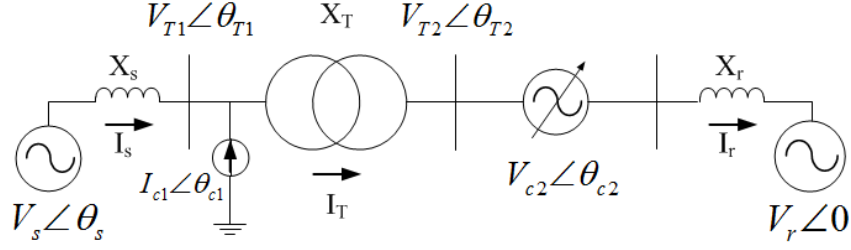
Figure 2-20. Algebraic model of CSTC in series-shunt connecting configuration.

According to Figure 2-20, Eq. (2.12) can be used to obtain the sending-end ac current (I_s). With input ac current, the transformer ac current can be expressed by Eq. (2.13) ($I_T = I_r$). The voltages across transformer can be easily obtained by Eq. (2.14)~(2.15). As a result, active and reactive power of transformer can be obtained by Eq. (2.16), and Eq. (2.17) respectively. In this mode of operation, the reference values of active and reactive power flow of CSTC converters (converter 2) is exactly equal to the reference values of transformer active and reactive power flow. So, supervisory control is not required to determine the reference values of transformer power flow.

$$\overrightarrow{I_s} = \frac{V_s \measuredangle \theta_s + V_{c2} \measuredangle \theta_{c2} - V_r \measuredangle 0}{j(X_s + X_T + X_r)} - \frac{X_T + X_r}{X_s + X_T + X_r} I_{c1} \measuredangle \theta_{c1} \tag{2.12}$$

$$\overrightarrow{I_T} = \overrightarrow{I_r} = \overrightarrow{I_s} + \overrightarrow{I_{c1}} = \frac{V_s \measuredangle \theta_s + V_{c2} \measuredangle \theta_{c2} - V_r \measuredangle 0}{j(X_s + X_T + X_r)} + \frac{X_s}{X_s + X_T + X_r} I_{c1} \measuredangle \theta_{c1} \tag{2.13}$$

$$V_{T1} \measuredangle \theta_{T1} = V_s \measuredangle \theta_s - jX_s \overrightarrow{I_s} \tag{2.14}$$

$$V_{T2} \measuredangle \theta_{T2} = -V_{c2} \measuredangle \theta_{c2} + jX_r \overrightarrow{I_r} + V_r \measuredangle 0 \tag{2.15}$$

$$P_T = \frac{V_{T1}V_{T2}}{X_T}\sin(\theta_{T1} - \theta_{T2}) \tag{2.16}$$

$$Q_T = \frac{V_{T1}{}^2}{X_T} - \frac{V_{T1}V_{T2}}{X_T}\cos(\theta_{T1} - \theta_{T2}) \tag{2.17}$$

The P-Q transformer operating range is shown in Figure 2-21-Figure 2-23 for different values of X_r when the magnitude of injected voltage (V_{c2}) is varied between 0 pu to 0.1 pu (X_T=0.1 pu, X_s=0.1 pu, θ_s=5.74°). As can be seen, transformer power flow variation is almost 0.45pu when X_r =0.02pu, and it is around 0.25pu when X_r =0.2pu. So, from the obtained results it can be concluded that the operating region of the transformer in the series-shunt mode of operation decreases as X_r increases whereas in shunt-shunt mode of operation, the transformer operating range increases as X_r increases.
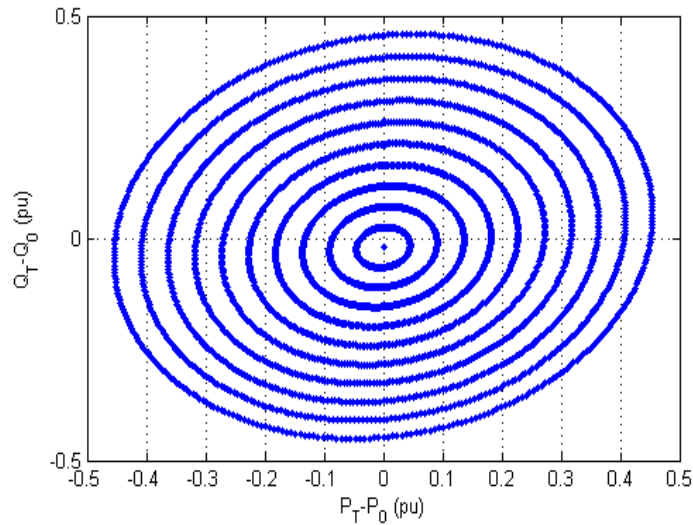
Figure 2-21. P-Q transformer operating range in series-shunt mode of operation (X_r=0.02 (pu)).
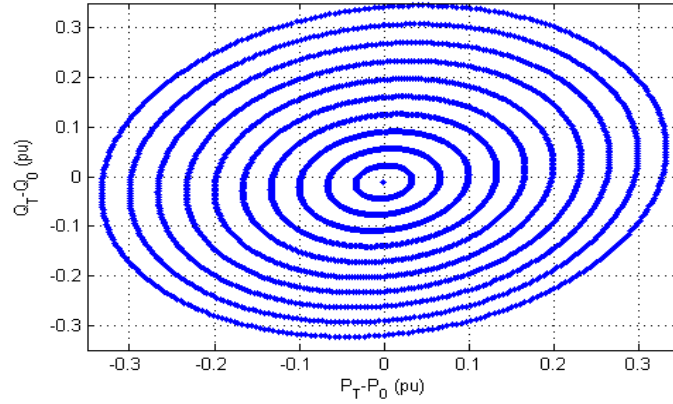
Figure 2-22. P-Q transformer operating range in series-shunt mode of operation ($X_r=0.1 \ (pu)$).
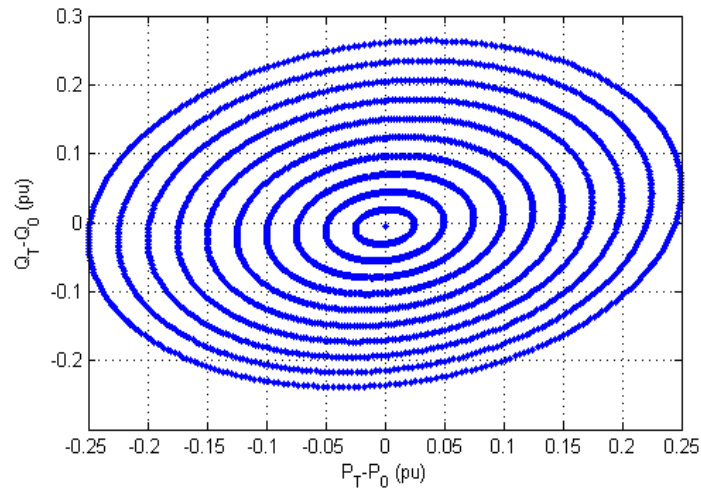
Figure 2-23. P-Q transformer operating range in series-shunt mode of operation ($X_r=0.2 \ (pu)$).

2.4.3 **Series-Series Connecting Configuration**

The presence of the transformer makes it possible to connect two series converters across the transformer which is quite unique in the FACTS controllers. It is important to distinguish this approach from IPFC (Interline Power Flow Controller). This mode of

operation is called Dual Series Static Controller (DSSC). In order to maintain power balance in the DC side, the constraint shown in (2.18) must be considered.

$$\text{Re}\left\{\overrightarrow{V_{c1}} \times \overrightarrow{I_T}^*\right\} = -\text{Re}\left\{\overrightarrow{V_{c2}} \times \overrightarrow{I_T}^*\right\} \tag{2.18}$$
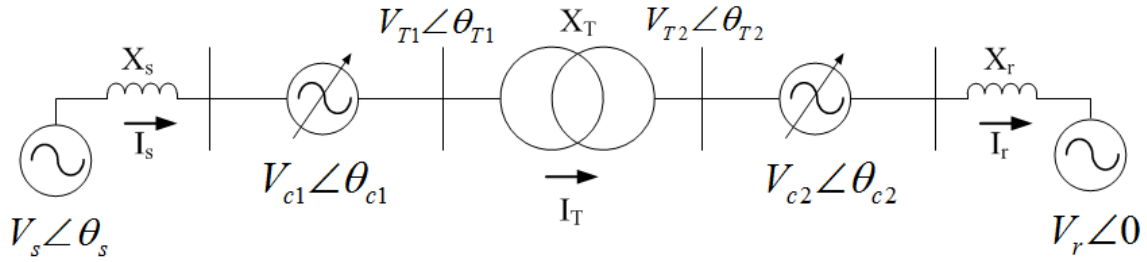
Figure 2-24. Algebraic model of CSTC in series-series connecting configuration.

According to Figure 2-24, Eq. (2.19) can be used to obtain the transformer current ($I_T = I_r = I_s$). The voltages across transformer can be easily obtained by Eq. (2.20)~(2.21). As a result, active and reactive power of transformer can be obtained by Eq. (2.22), and Eq. (2.23) respectively.

$$\overrightarrow{I_s} = \overrightarrow{I_T} = \overrightarrow{I_r} = \frac{V_s \angle \theta_s + V_{c1} \angle \theta_{c1} - V_{c2} \angle \theta_{c2} - V_r \angle 0}{j(X_s + X_T + X_r)} \tag{2.19}$$

$$V_{T1} \angle \theta_{T1} = V_s \angle \theta_s + V_{c1} \angle \theta_{c1} - jX_s \overrightarrow{I_s} \tag{2.20}$$

$$V_{T2} \angle \theta_{T2} = V_{c2} \angle \theta_{c2} + jX_r \overrightarrow{I_r} + V_r \angle 0 \tag{2.21}$$

$$P_T = \frac{V_{T1}V_{T2}}{X_T}\sin(\theta_{T1} - \theta_{T2}) \tag{2.22}$$

$$Q_T = \frac{V_{T1}^2}{X_T} - \frac{V_{T1}V_{T2}}{X_T}\cos(\theta_{T1} - \theta_{T2}) \tag{2.23}$$

The P-Q transformer operating range is shown in Figure 2-25~Figure 2-27 for different values of X_r when the magnitude of injected voltage (V_{c1}, V_{c2}) is varied between 0 pu to 0.1 pu $(X_T=0.1$ pu, $X_s=0.1$ pu, $\theta_s=5.74°)$. As can be seen, transformer power flow variation is almost 0.9pu when $X_r = 0.02pu$, and it is around 0.5pu when $X_r = 0.2pu$. So, from the obtained results it can be concluded that the active power operating region of the transformer in the series-series mode of operation is twice the transformer active power operating range in series-shunt mode of operation whereas the operating range of transformer reactive power flow is so limited.
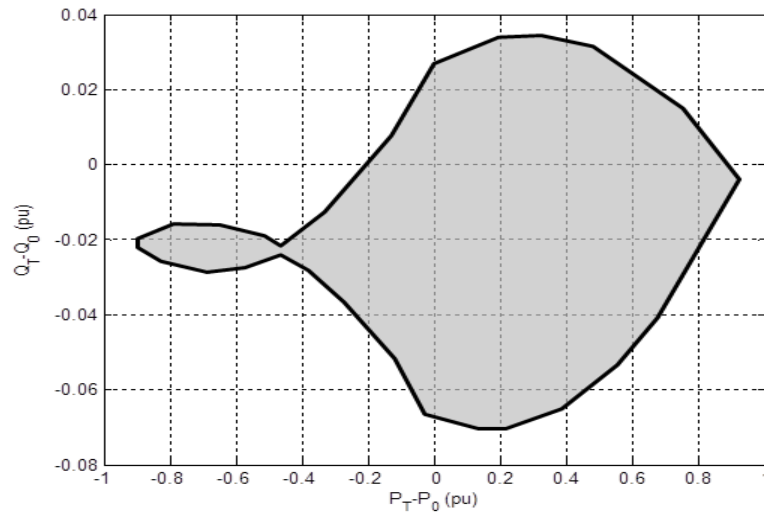
Figure 2-25. P-Q transformer operating range in series-series mode of operation $(X_r=0.02 (pu))$.
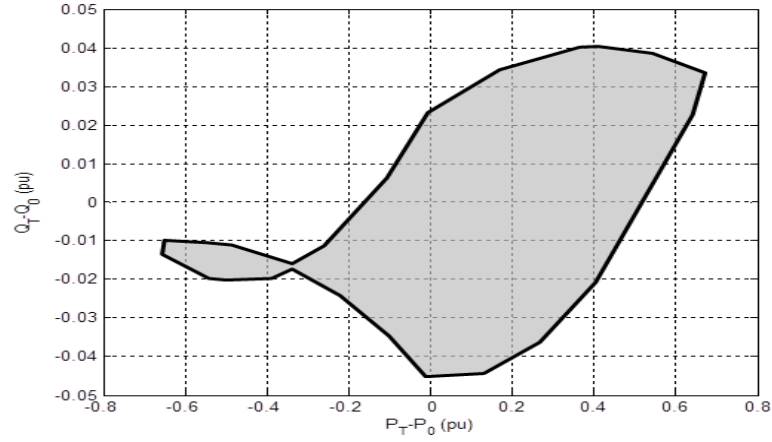
Figure 2-26. P-Q transformer operating range in series-series mode of operation ($X_r=0.1$ (pu)).
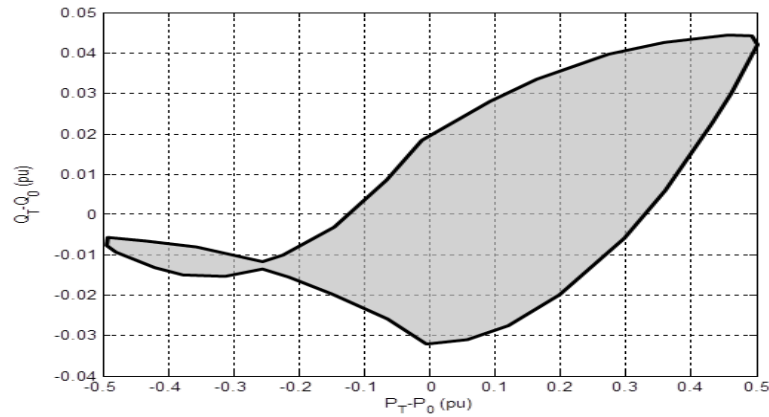
Figure 2-27. P-Q transformer operating range in series-series mode of operation ($X_r=0.2$ (pu)).

2.5 Control Structure of CSTC in Three Different Connecting Configurations

2.5.1 Shunt-Shunt Connecting Configuration

Figure 2-28 shows the control scheme of the CSTC in the shunt-shunt mode of operation.

The DC voltage controller is based on the energy concept of the DC link capacitor and the interface inductor, and the state for DC link voltage is defined as $V_{DC}{}^2$. To improve the dynamic performance while maintaining the low switching frequency, the power reference can be used as a feed-forward signal in the DC voltage control scheme. The current references are limited by the rated current of the switching devices. In this control structure, the algebraic model is used to find the operating points of CSTC converters based on the appropriate reference values of transformer power flow. The second converter will control active and reactive power flow at the desired transformer operating points based on the CSTC operating points computed by the algebraic model. Figure 2-29 also shows the AC current controller in detail. Grid angle detection structure based on voltage PLL is shown in Figure 2-29a [53], and current control block is illustrated in Figure 2-29b.
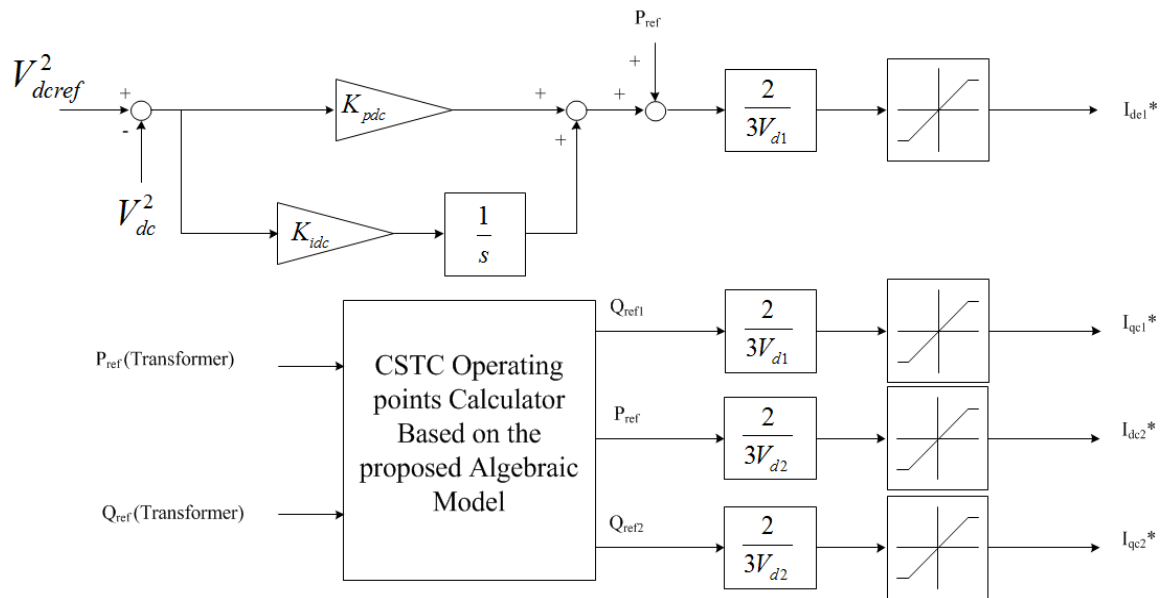
Figure 2-28. Control structure of the CSTC in the shunt-shunt mode of operation.
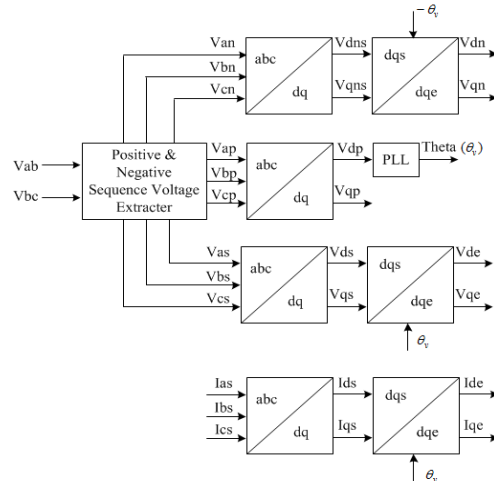
(a) Grid angle detection and feed-forward voltage.
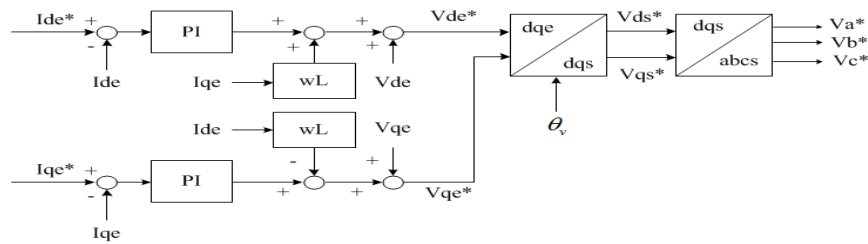
(b) Current control block.

Figure 2-29. AC Current Controller in shunt-shunt mode of operation.

2.5.2 Series-Shunt Connecting Configuration

The control structure of CSTC in series-shunt mode of operation is illustrated in Figure 2-30. In this mode of operation, one converter regulates dc bus voltage (rectifier side), and the other converter regulates power flow of transformer. The series converter is used to control active and reactive power flow through the transformer, and the shunt converter maintains the bus voltage magnitude to the desired value by injecting or absorbing reactive power. The control structure in this mode is similar to the one used in conventional UPFCs.

(a) DC voltage controller.

(b) Power flow controller.
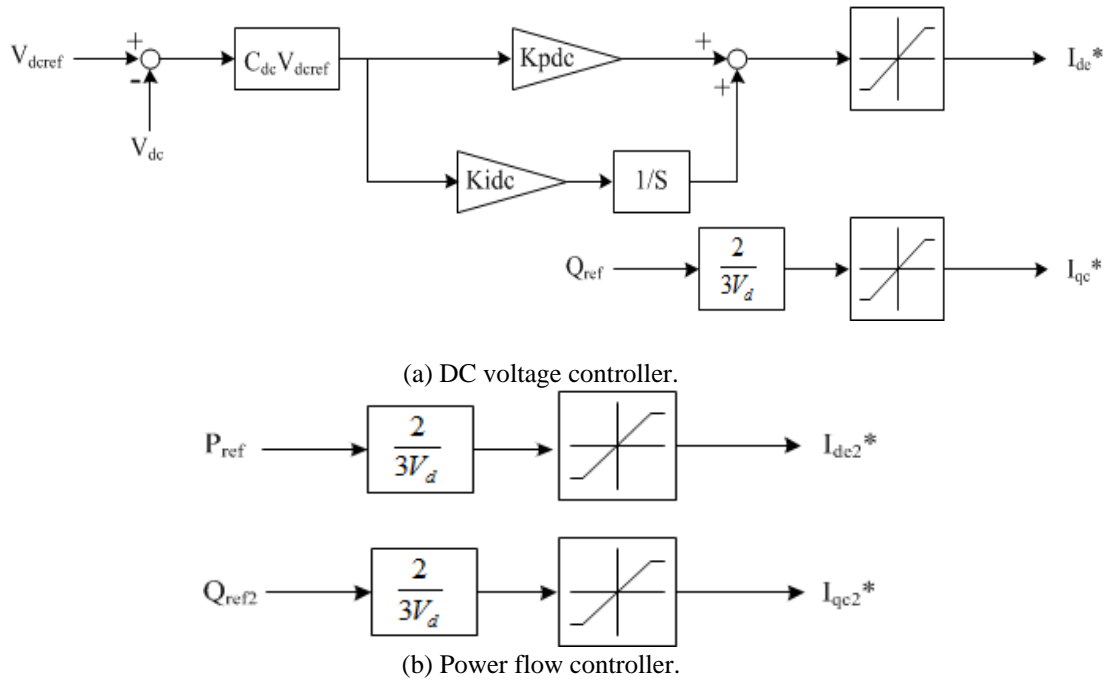
Figure 2-30. Control structure of CSTC in series-shunt mode of operation.

2.5.3 **Series-Series Connecting Configuration**

The proposed control structure for series-series mode of operation is presented in Figure 2-31. A measurement of the absolute phase angle of line current is needed. Zero phase sequence components should be removed from these signals, and line currents should be filtered before the control system can utilize them. The first step is to convert the ac signals into constant quantities. A DQ transformation process on line currents is performed in stationary reference frame. Then, current angle is calculated as it can be observed from Figure 2-32. Voltage control block is also shown in Figure 2-33.

(a) DC voltage controller (Rectifier Side)

(b) Power flow controller (Inverter Side)
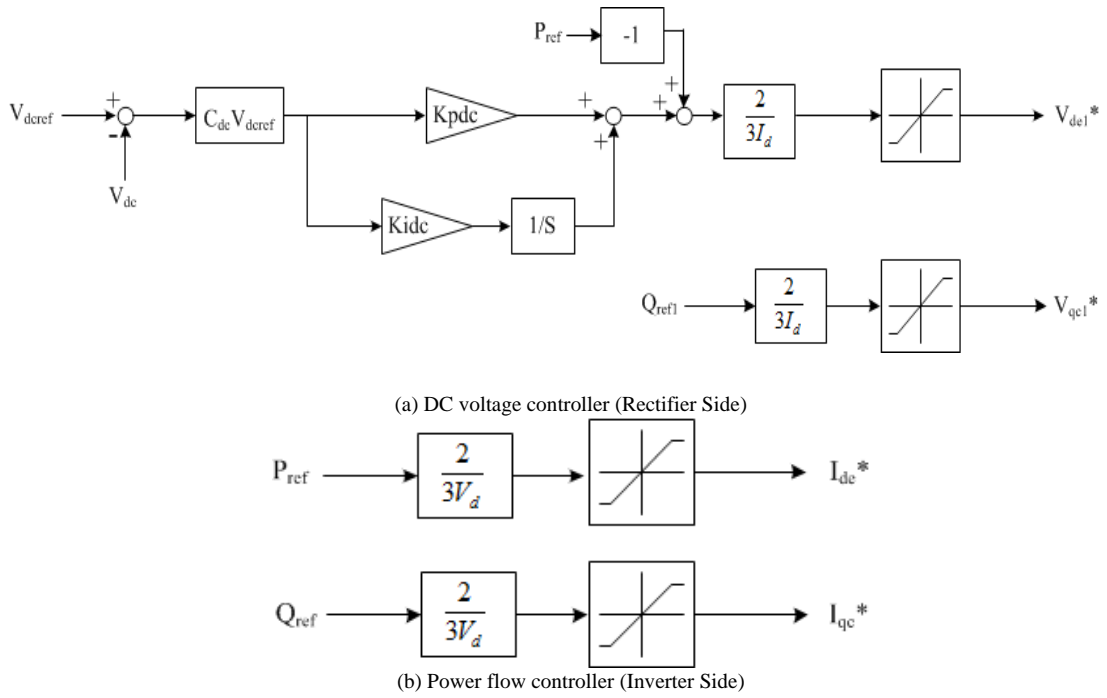
Figure 2-31. Control structure of CSTC in series-series mode of operation.
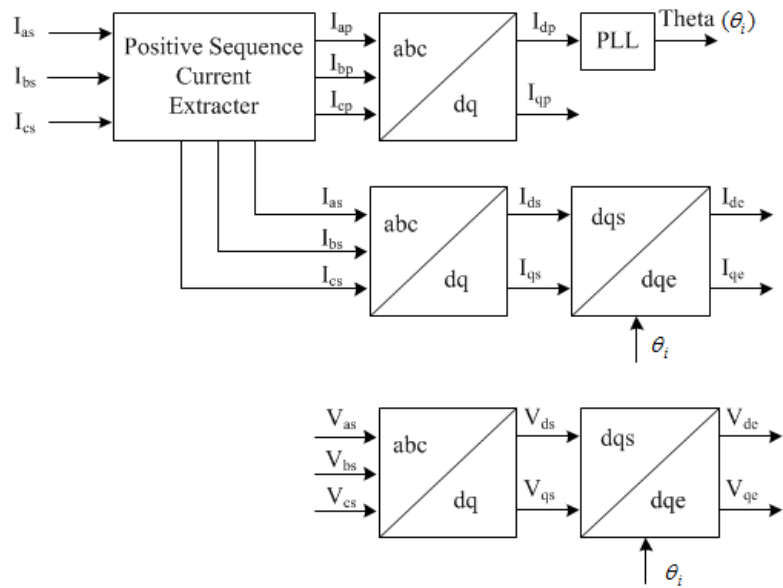
Figure 2-32. Current angle extraction.
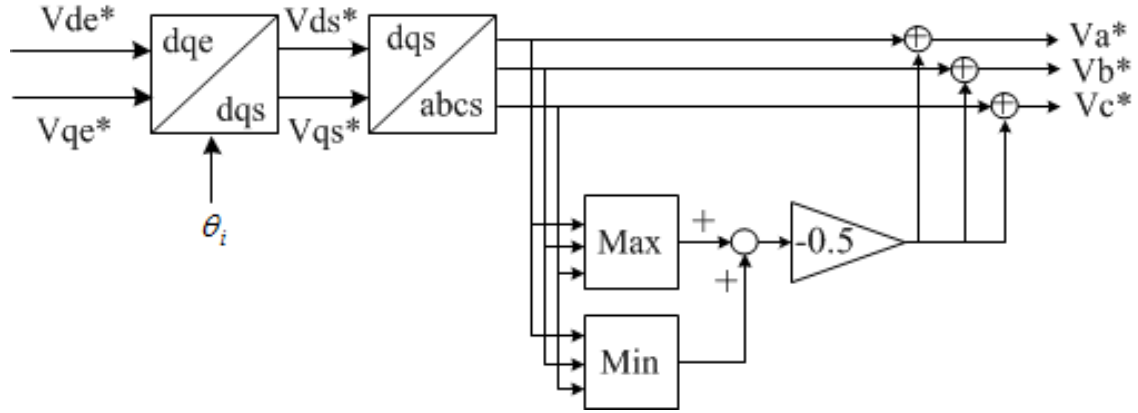
Figure 2-33. Voltage Control Block for series-series mode of operation.

2.6 Design procedure of controller gains

2.6.1 PI Current Controller

The converter can be modeled as simple R–L load, with constant disturbance voltage. The disturbance can be rejected by feed-forward compensation as shown in Figure 2-34. In addition to this rejection of the disturbance voltage, by canceling the pole of the system, which comes from R, L with a zero of PI regulator, the transfer function of the closed-loop system can be set as that of the first-order low-pass filter. This kind of gain tuning method is referred to as the technical optimum [54]. Under this gain tuning method, the proportional and integral gain can be set as (2.24), and then the closed-loop transfer function of the current regulator is deduced like (2.25).

$$K_P = L\omega_c ; K_i = R\omega_c \tag{2.24}$$

$$\frac{i_{dq}(s)}{i^*_{dq}(s)} = \frac{\omega_c}{s+\omega_c} = \frac{1}{T_c s+1}; T_c = \frac{1}{\omega_c} \qquad (2.25)$$
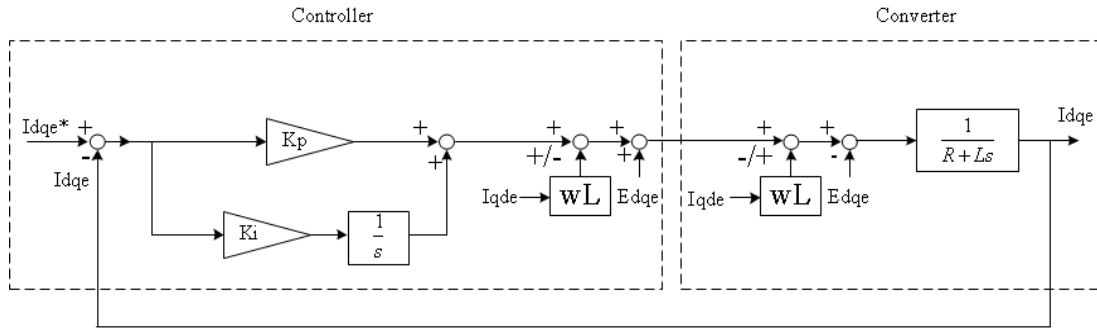
Figure 2-34. PI current regulator.

2.6.2 **Anti-Wind-up**

All physical variables in the control system are bounded by physical limitations. If the converter voltage is saturated by the physical limitation, and if the output of the current controller is not bounded at that physical limitation, then the control system is out of control of the closed loop, where the regulator output has nothing to do with the input to the physical system under control. In this case the response to the command of the control system is oscillatory and is uncontrollable by the regulator. To prevent this situation, the output of the regulator can be simply bounded by a limiter. However, if the integrator terms are included in the output of the regulator, then the output of the integrator is not bounded by the limiter and it would be wound up above the limited value of the regulator though the output of the regulator is limited. This phenomenon is called "wind-up." If the wind-up of the integrator of

the regulator occurs, then the input to the integrator, which is the regulation error, should have a sign opposite to that of the output of the integrator for a while to clear the wind-up. In this reason, the response would have a large overshoot or undershoot because of the integrator wind-up. In the worst case the control system may be unstable. The limitation of the integrator output, which is called an "anti-wind-up," can be done as shown in Figure 2-35.

In Figure 2-35, K_a is usually set as $1/K_p$. However, in general, such a setting gives a reasonable performance, but the anti-wind-up gain, K_a, can be tuned to get better performance in the range of 1/3~3 of K_p. Other methods such as turning-on or turning-off the integrator of the PI regulator according to the operating condition can be used [55]. Because the main reason to use the integrator in the regulator is to null the steady-state error, the integrator may be turned off whenever the error is large. If the error is small and the output of the regulator is within the physical bound, then the integrator may be turned on to reduce the steady-state error.
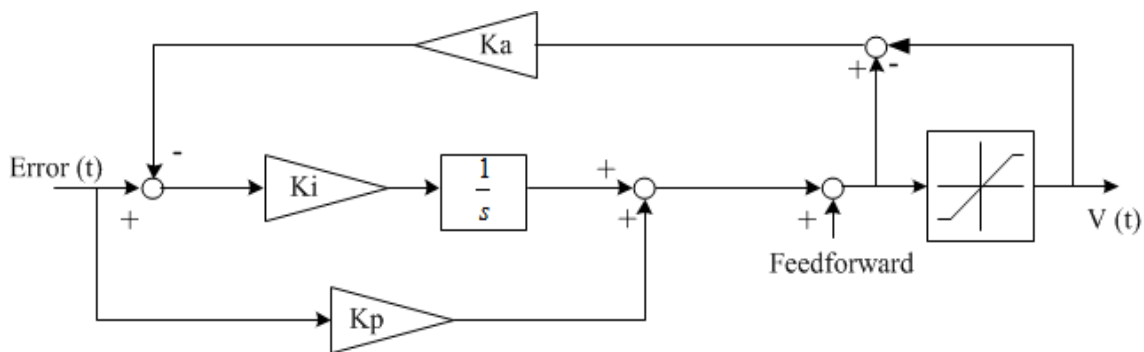
Figure 2-35. Anti-wind-up controller.

2.6.3 **DC Link Voltage Controller**

As seen from Figure 2-36, DC link voltage increases when the active power from the AC source is larger than the power consumed by the load and vice versa. Hence, DC link voltage can be regulated by adjusting active power to a DC link from an AC source. Hence, the d-axis current reference can be composed of the sum of a feed-forward term, which corresponds to the estimated load power, and a term to regulate DC link voltage as (2.26). As a feedback controller to regulate DC link voltage, a PI controller can be used to prevent overshoot of DC link voltage even with the step change of DC link voltage reference.
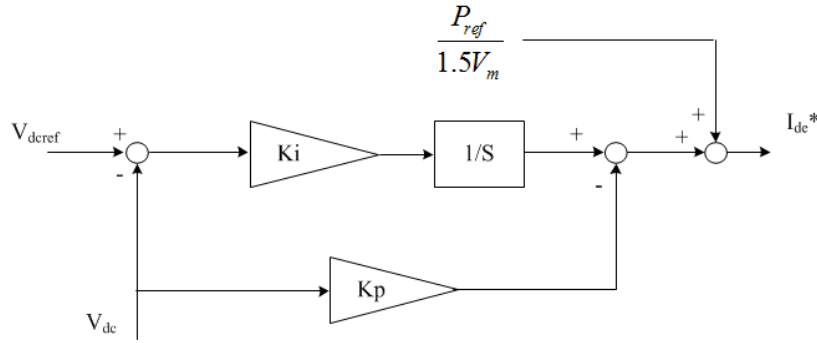
Figure 2-36. DC link voltage controller.

$$i_{de}^* = -K_p V_{dc} + K_i \int (V_{dcref} - V_{dc}) dt + \frac{P_{ref}}{1.5 V_m} \tag{2.26}$$

The differential equation to represent the DC link voltage can be represented as (2.27).

$$\frac{1}{2} C_{dc} \frac{d}{dt} (V_{dc}^2) = P_{in} - P_{out} \tag{2.27}$$

If the feed-forward compensation for load power is perfect, then DC link voltage can be described by (2.28).

$$\frac{1}{2}C_{dc}\frac{d}{dt}(V_{dc}^2)=1.5V_m(-K_pV_{dc}+K_i\int(V_{dcref}-V_{dc})dt) \qquad (2.28)$$

(2.28) is a nonlinear differential equation, and it can be linearized at an operating point using small signal analysis. A linearized differential equation at an operating point can be derived as (2.29).

$$C_{dc}V_{dc0}\frac{d}{dt}(V_{dc})=1.5V_m(-K_pV_{dc}+K_i\int(V_{dcref}-V_{dc})dt) \qquad (2.29)$$

From (2.29), a transfer function between reference DC link voltage and actual DC link voltage can be written as (2.30).

$$\frac{V_{dc}(s)}{V_{dcref}(s)}=\frac{\dfrac{1.5V_mK_i}{C_{dc}V_{dc0}}}{s^2+\dfrac{1.5V_mK_p}{C_{dc}V_{dc0}}s+\dfrac{1.5V_mK_i}{C_{dc}V_{dc0}}}=\frac{\omega_n^2}{s^2+2\zeta\omega_ns+\omega_n^2} \qquad (2.30)$$

Where ω_n stands for the natural undamped frequency and ς stands for a damping coefficient. The gains of a PI controller can be represented as (2.31).

$$K_P=2\zeta\omega_n\frac{C_{dc}V_{dc0}}{1.5V_m};$$
$$K_i=\frac{\omega_n^2C_{dc}V_{dc0}}{1.5V_m} \qquad (2.31)$$

2.7 Dynamic Performance Evaluation of MTC Based CSTC

2.7.1 Shunt-Shunt Connecting Configuration

In this section, the dynamic performance of the CSTC in shunt-shunt mode of operation is presented. PSCAD/EMTDC based simulation has been carried out to verify the control structure performance. CSTC as a recovery transformer can operate similarly to BTB HVDC converters. The CSTC in shunt-shunt mode of operation is used for power flow control. One converter operates in PQ mode and the other one is responsible to compensate for the losses and ensures a stable operation of the DC bus voltage while it supports its reactive power demands. The CSTC system parameters are tabulated in Table 2-1.

Table 2-1.   CSTC System Parameters for PSCAD simulation

Base Power	S	9 MVA
Line-to-line peak voltage	E	4.5 kV
Line frequency (grid)	f	60 Hz
Input voltage phase	θ_s	5.74°
sending-end Leakage inductance	L_s	0.1 pu=0.298 (mH)
Transformer inductance	L_T	0.1 pu=0.298 (mH)
receiving-end Leakage inductance	L_r	0.1 pu=0.298 (mH)
DC link voltage	V_{DC}	9 kV
DC link capacitance	C_{DC}	10 (mF)
Switching frequency	f_{sw}	6 (kHz)

DC bus voltage is shown in Figure 2-37. As can be seen, the capacitor voltage is zero initially. For initial charging, the bypass-resistor is inserted between the AC grid and the CSTC converter. This resistor was decided to reduce the initial charging current under the rated current of the CSTC converter. For start-up, all gating signals are initially off for 0s to

0.1s. From 0.1s, all controllers are starting to work and all gating signals are enabled to regulate dc bus voltage at 9 kV.

The dynamic performance of bidirectional active power flow is also displayed in Figure 2-38. The reference value of active power is increased from zero to the rated power at 0.4s, and it is varied from 0 to -9 (MW) at 1.4s to show bidirectional active power flow through CSTC converter. As it can be observed from Figure 2-38, transformer and input active power flow also changes depending on the operating points of CSTC converters. Transformer active power flow can be regulated at the desired value by determining the appropriate operating points for CSTC converters. Algebraic model is used to compute the active and reactive power references of CSTC converters based on the desired transformer active and reactive power flow. Three phase ac current is shown in Figure 2-39. A zoomed portion of three phase ac current is also depicted in Figure 2-40.
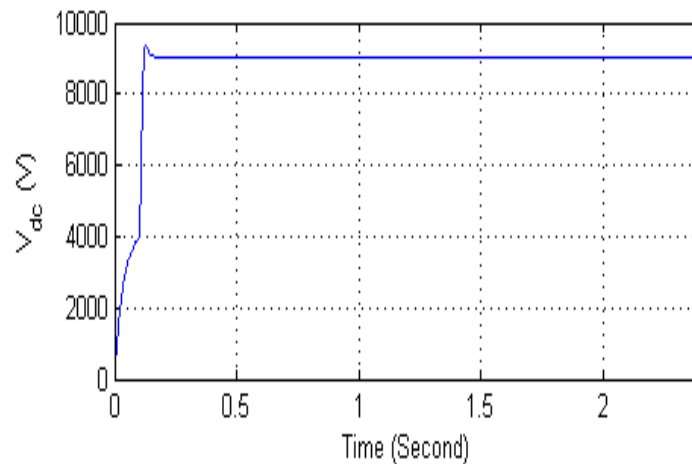
Figure 2-37. DC bus voltage in shunt-shunt mode of operation.
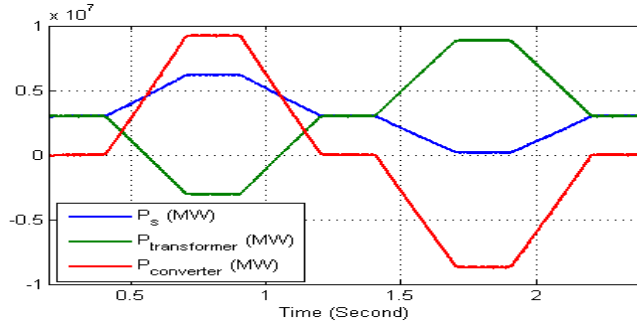
Figure 2-38. Dynamics of bidirectional active power flow in shunt-shunt mode of operation.
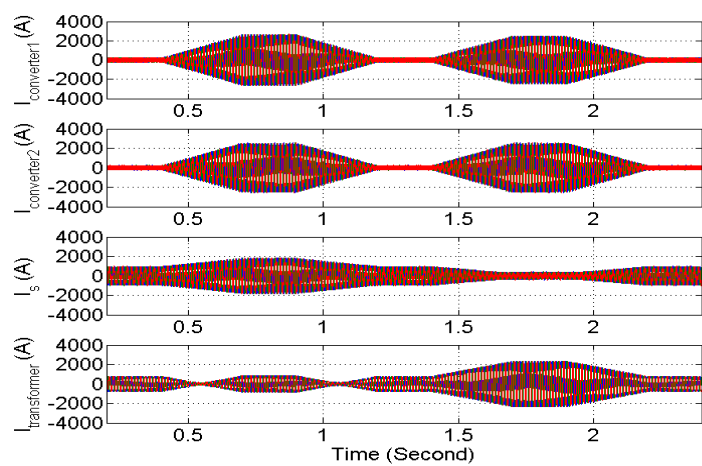
Figure 2-39. Three phase ac current for bidirectional active power flow in shunt-shunt mode of operation.
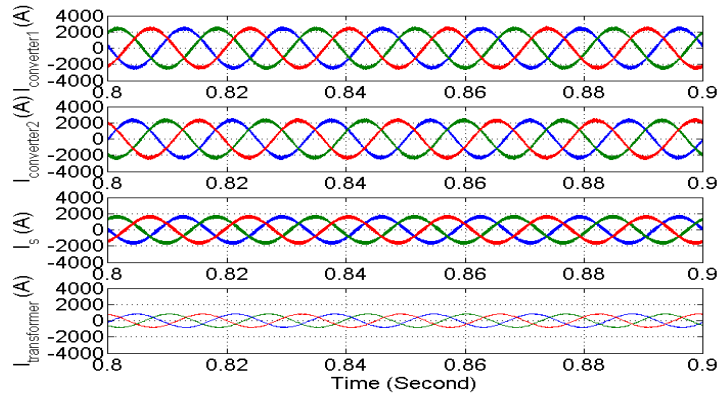
Figure 2-40. A zoomed portion of three phase ac current in shunt-shunt mode of operation.

Figure 2-41 shows dynamics of transformer and input reactive power flow when the reference value of reactive power for converter 1 has a ramp change from 0 to -9 (MVAR) at 0.4s, and it is changed from 0 to 9 (MVAR) at 1.4s. Figure 2-42 also shows dynamics of three phase ac current.

The dynamic performance of transformer and input reactive power with respect to converter 2 reactive power is shown in Figure 2-43. Figure 2-44 also shows three phase ac current for this case scenario.
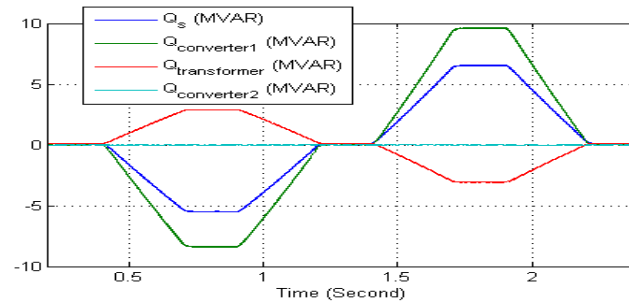
Figure 2-41. Reactive power flow dynamics of converter 1 ($Q_{ref2}=0$) in shunt-shunt mode of operation.
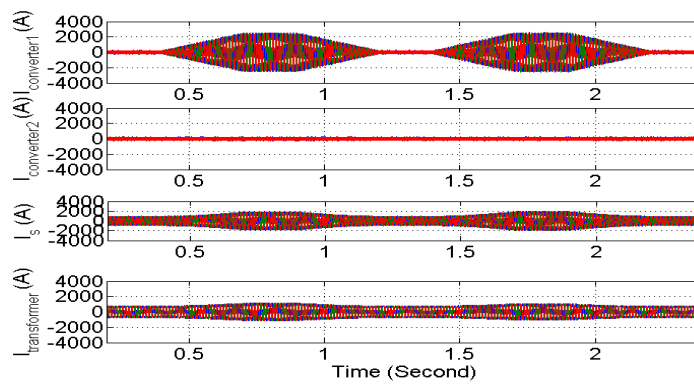
Figure 2-42. Dynamics of three phase ac current when converter 1 reactive power flow has a ramp change from 0 to rated power in shunt-shunt mode of operation.
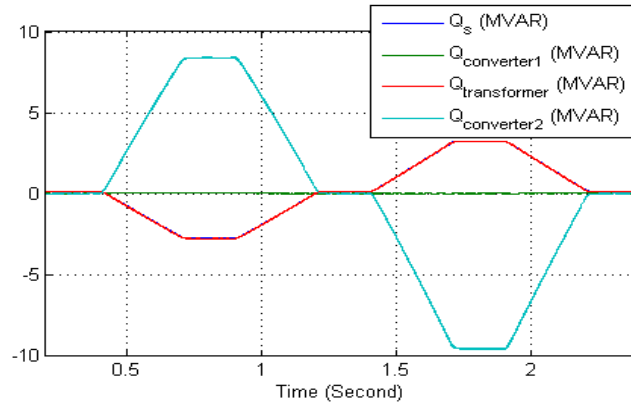
Figure 2-43. Reactive power flow dynamics of converter 2 ($Q_{ref1}=0$) in shunt-shunt mode of operation.
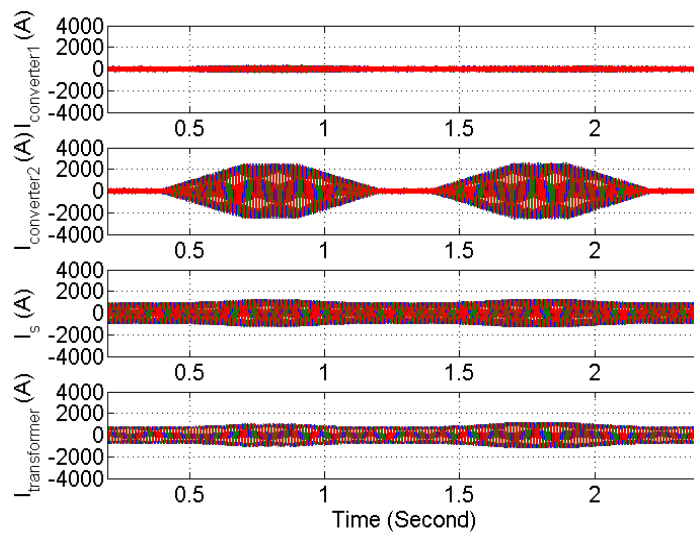
Figure 2-44. Dynamics of three phase ac current when converter 2 reactive power flow has a ramp change from 0 to rated power in shunt-shunt mode of operation.

2.7.2 Series-Shunt Connecting Configuration

In this section, the EMTDC simulation results of the MTC based CSTC system as the substation power flow controller in series-shunt mode of operation are presented. DC bus

voltage is shown in Figure 2-45. As can be seen, all controllers are enabled after 0.1s to regulate dc bus voltage at 9 kV.

The dynamic performance of transformer active power flow is also displayed in Figure 2-46. The reference value of active power flow is increased from zero to -9 (MW) at 0.4s, and it is varied from 0 to the rated power at 1.4s to show bidirectional active power flow through CSTC converter. Dynamics of input active power flow is also shown in Figure 2-47. Transformer active power flow is equal to input power flow, and it is regulated by converter 2 of CSTC converters which injects three-phase voltages in series. Three phase ac current is shown in Figure 2-48. A zoomed portion of three phase ac current is also depicted in Figure 2-49.

Figure 2-50 shows dynamics of transformer and input reactive power flow when the reference value of reactive power for converter 1 has a ramp change from 0 to -9 (MVAR) at 0.4s, and it is changed from 0 to 9 (MVAR) at 1.4s. As can be seen, transformer reactive power is zero since the reference value of reactive power for converter 2 is equal to zero $(Q_{ref2}=0)$. Figure 2-51 also shows dynamics of three phase ac current.

Dynamics of transformer and input reactive power with respect to converter 2 reactive power is shown in Figure 2-52, and Figure 2-53 shows three phase ac current for this case scenario. In this case, the reference value of converter 2 reactive power is varied from 0 to the rated power. As it can be observed from Figure 2-52, transformer and input reactive power are equal to each other because $Q_{ref1}=0$.
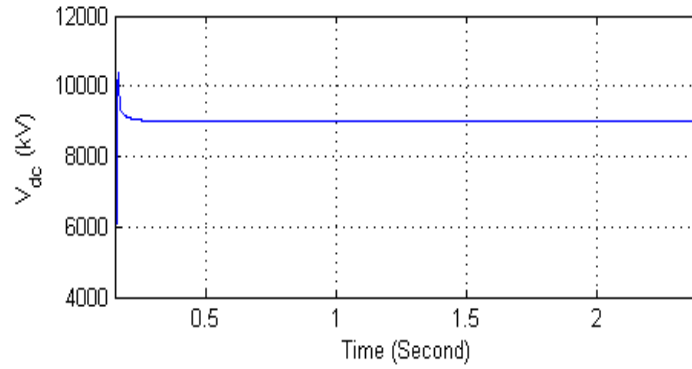
Figure 2-45. DC bus voltage in series-shunt mode of operation.
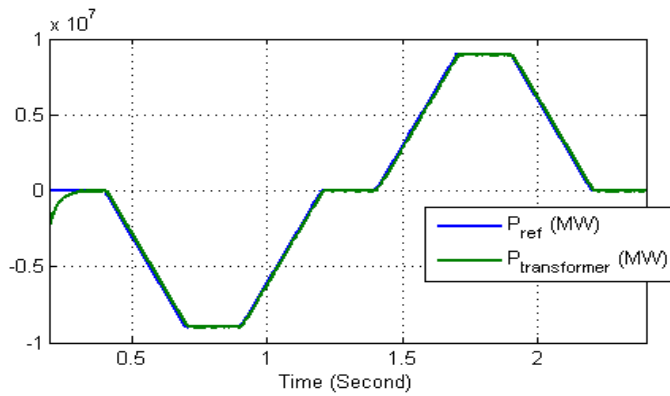
Figure 2-46. Dynamics of transformer active power flow in series-shunt mode of operation.
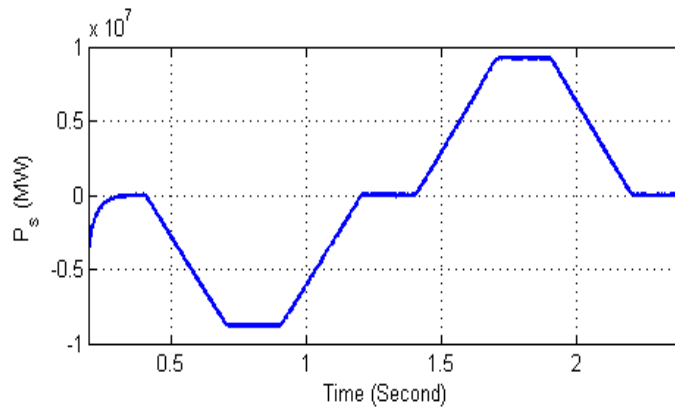
Figure 2-47. Dynamics of input active power flow in series-shunt mode of operation.
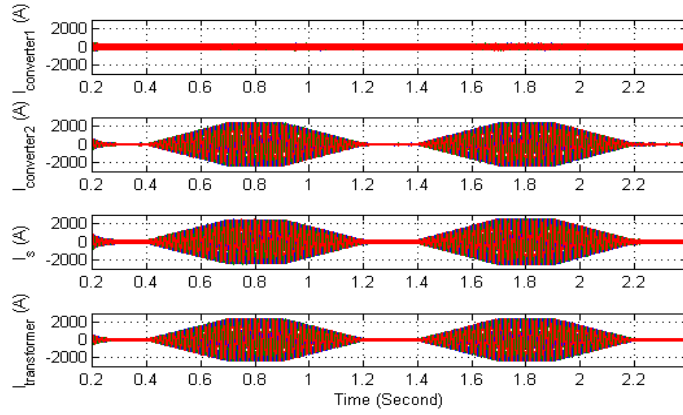
Figure 2-48. Three phase ac current in series-shunt mode of operation.
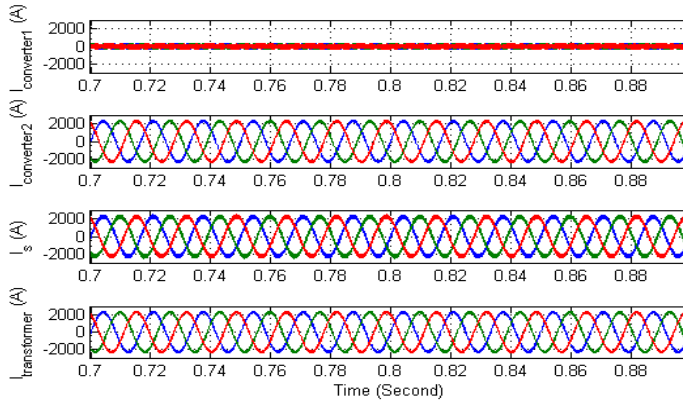
Figure 2-49. A zoomed portion of three phase ac current in series-shunt mode of operation.
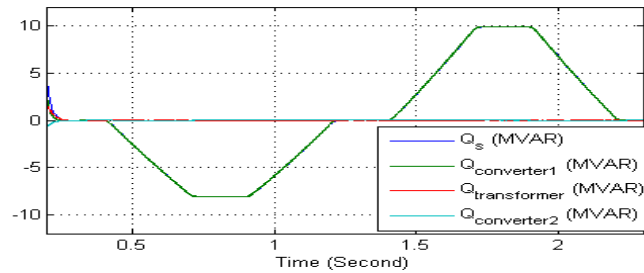
Figure 2-50. Reactive power flow dynamics of converter 1 when converter 1 reactive power flow has a ramp change from 0 to rated power ($Q_{ref2}=0$) in series-shunt mode of operation.
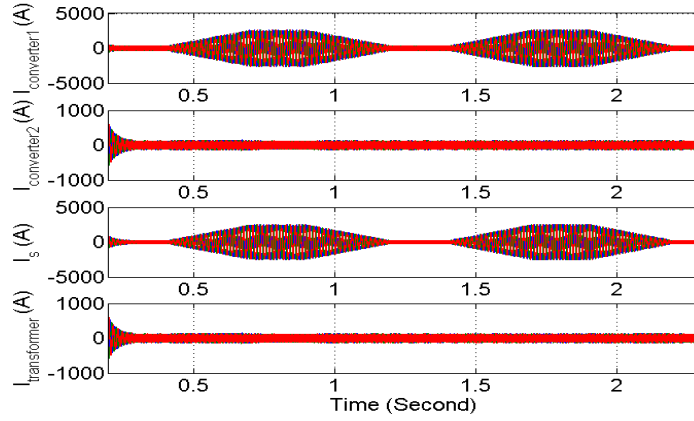
Figure 2-51. Dynamics of three phase ac current when converter 1 reactive power flow has a ramp change from 0 to rated power in series-shunt mode of operation.
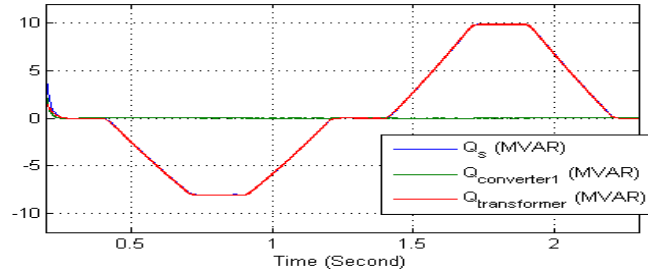
Figure 2-52. Reactive power flow dynamics when converter2 reactive power flow has a ramp change from 0 to rated power ($Q_{ref1}=0$) in series-shunt mode of operation.
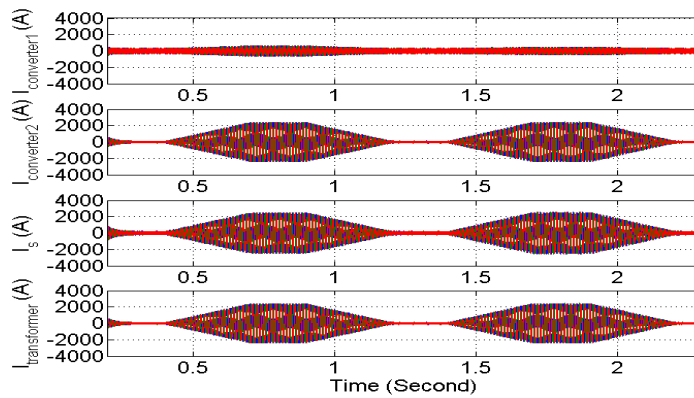
Figure 2-53. Dynamics of three phase ac current when converter 2 reactive power flow has a ramp change from 0 to rated power in series-shunt mode of operation.

2.7.3 **Series-Series Connecting Configuration**

In this section, PSCAD/EMTDC based simulation has been carried out to verify the control structure performance for CSTC in series-series mode of operation. DC bus voltage is shown in Figure 2-54. As can be observed, dc bus voltage is regulated at 9 kV.

The dynamic performance of transformer active power flow is also displayed in Figure 2-55. The reference active power of CSTC converters is increased from zero to 5 (MW) at 0.4s, and it is varied from 0 to -5 (MW) at 1.4s to show bidirectional active power flow through CSTC converter. As can be seen, input active power flow is constant, and transformer active power flow is varied according to the reference value of CSTC active power flow. Three phase ac current is also shown in Figure 2-56. Three-phase series injected voltage is shown in Figure 2-57, and a zoomed portion of that is also depicted in Figure 2-58.
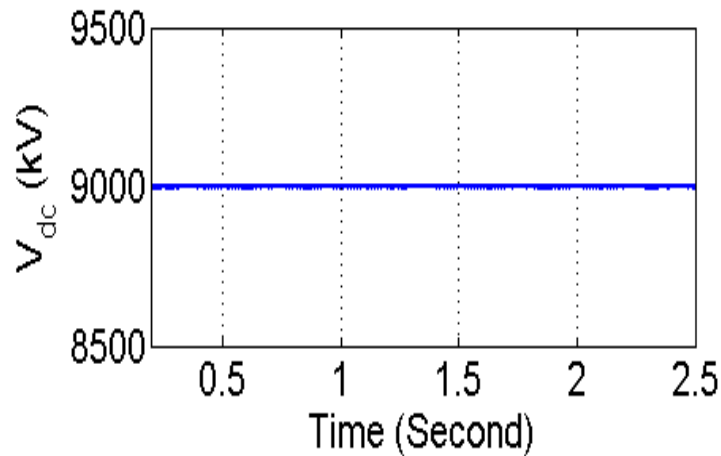
Figure 2-54. DC bus voltage in series-series mode of operation.
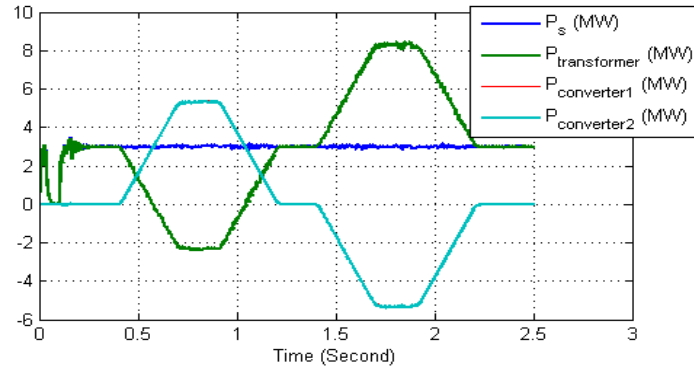
Figure 2-55. Dynamics of transformer active power flow in series-series mode of operation.
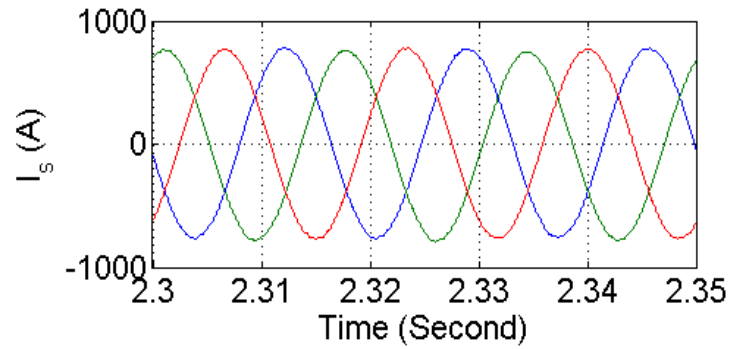
Figure 2-56. Three phase ac current in series-series mode of operation.
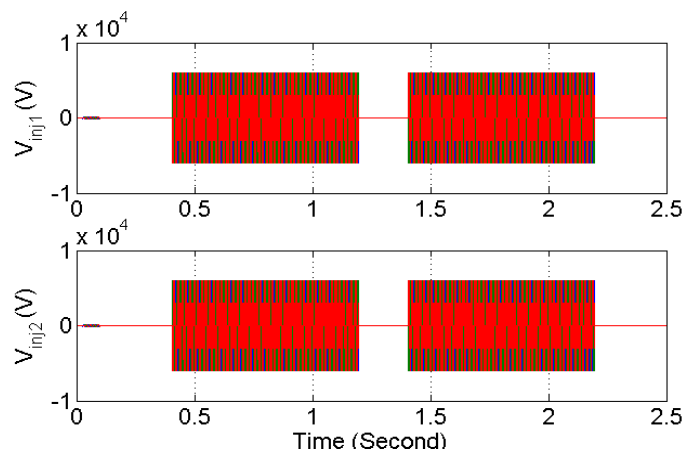
Figure 2-57. Three-phase series injected voltage in series-series mode of operation.
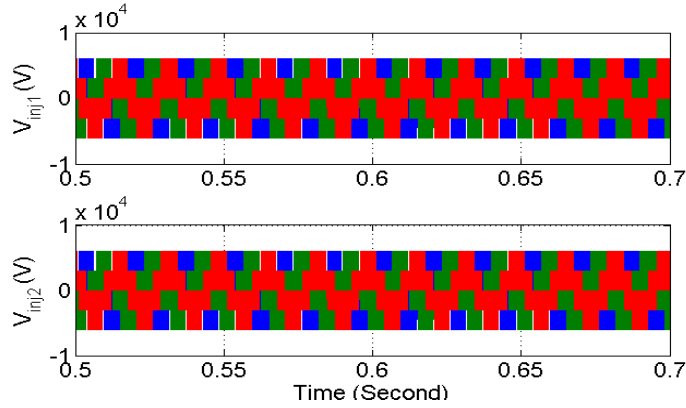
Figure 2-58. A zoomed portion of three-phase series injected voltage in series-series mode of operation.

2.8 Summary

The Convertible Static Transmission Controller (CSTC), as compared to existing FACTS solutions, provides the flexibility of full/partial utilization for the transmission grid assets. This flexibility effectively increases the system operating margins and could also provide back-up in case of power transformer failure scenarios. By providing real-time continuous power flow control, it could effectively increase transfer capacity of existing transmission systems. The MTC based CSTC concept provides a hardware based power flow controller and can also be used as an asset management tool for utilities and system operators.

This section presents the steady-state and dynamic performance of the proposed MTC based CSTC for different operation modes and configurations. From the supervisory control point of view, a control algorithm is required to set the reference values of active and reactive power flow of CSTC converters based on the desired operating points for transformer active and reactive power flow. To achieve this goal, the algebraic model of CSTC in three different

connecting configurations is derived. Algebraic model of CSTC is used for steady state and transient stability analysis. Algebraic model will present the behavior of transformer power flow with respect to various operating points of CSTC converters. The objective of algebraic model development is to set the reference values of active and reactive power flow of CSTC converters based on the desired operating points for transformer active and reactive power flow. The shunt-shunt mode of operation is used for transformer life extension and transformer back-up if transmission transformer fails. The series-series and series-shunt mode of operation are used to limit fault current and control transformer power flow, but the P-Q transformer operating range is different in these two modes of operation. The P-Q transformer operating range can be obtained based on the proposed algebraic model. From the obtained results, it was concluded that the transformer operating region depends on power system parameters, and the operating region of the transformer in the series-shunt mode of operation decreases as the receiving end impedance (X_r) increases whereas in the shunt-shunt mode of operation, the transformer operating range increases as X_r increases. Also, the active power operating region of the transformer in the series-series mode of operation is twice the transformer operating range in series-shunt mode of operation whereas the operating range of transformer reactive power flow is limited in series-series mode of operation. This paper also proposes a control structure for three different modes of operation. Dynamic performance of the CSTC system is also investigated in PSCAD/EMTDC environment, and simulation results are presented to verify the controller performance in three different connecting configurations.

Chapter 3.   ACTIVE MOBILE SUBSTATIONS

3.1 Background

The US transmission grid is not yet prepared to accommodate the desired renewable resources specially the wind generations. One hurdle that impedes the grid upgrade is the intermittency of these resources. Figure 3-1 is an example of intermittency of the wind capacity in the Midwest region showing that practically there is no generation capacity in the summer [56]. In fact, there is a common belief that commercially practiced renewable resources have less than 30% availability throughout the year. On the other hand, due to the economic grounds, the integrations are often seen in the distribution and sub-transmission grids with naturally lower impedance than that of the transmission networks. This fact with high penetration of renewables causes overloading conditions that necessitate either network upgrade (re-conductor) or curtailment in the generation while there is unutilized capacity in the transmission network, i.e. >138kV. Also, It has been reported that the average age of power transformers in US is now approaching 40 years; even though they are typically designed for 30 years. This result seems reasonable considering the transformer installations during the last 40 years [57]-[58]. Therefore, power flow controllers such as UPFC or BTB HVDC controllers become attractive albeit they are high cost solutions.
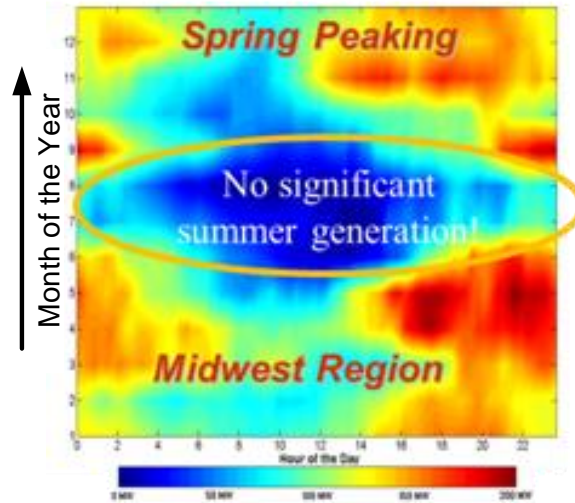
Figure 3-1.   Average wind generation capacity/year in the US Midwest region.

To address the declared situations, we propose a solution referred to as Active Mobile Substation (AMS) which functions as a

- Recovery transformer for disaster management like the recent Japan earthquake, hurricanes etc.

- Transmission transformer life extender; investment deferral.

- Seasonal transmission controller for intermittent renewable resources.

The framework to develop and utilize the AMS in the power system is depicted in Figure 3-2. In this system, the transformer sits in the core and we consider it as the control node. This control node is to be attached with peripheral sensor and communication networks. These networks are constructing the cyber domain. In the cyber domain, the control nodes are connected to the internet through communication links which further enable interoperation among transformers under supervisory control and data acquisition

(SCADA) like DNP3 and IEC 61850. As shown in the holistic diagram of Figure 3-2, there are several challenges to realize the integrated AMS including power electronic system design, weather condition prediction and monitoring, coordinated sensing and networking and grid-level impact assessment. In this section, we investigate the challenges regarding the power electronic system design and present solutions that are viable for development of the proposed AMS.
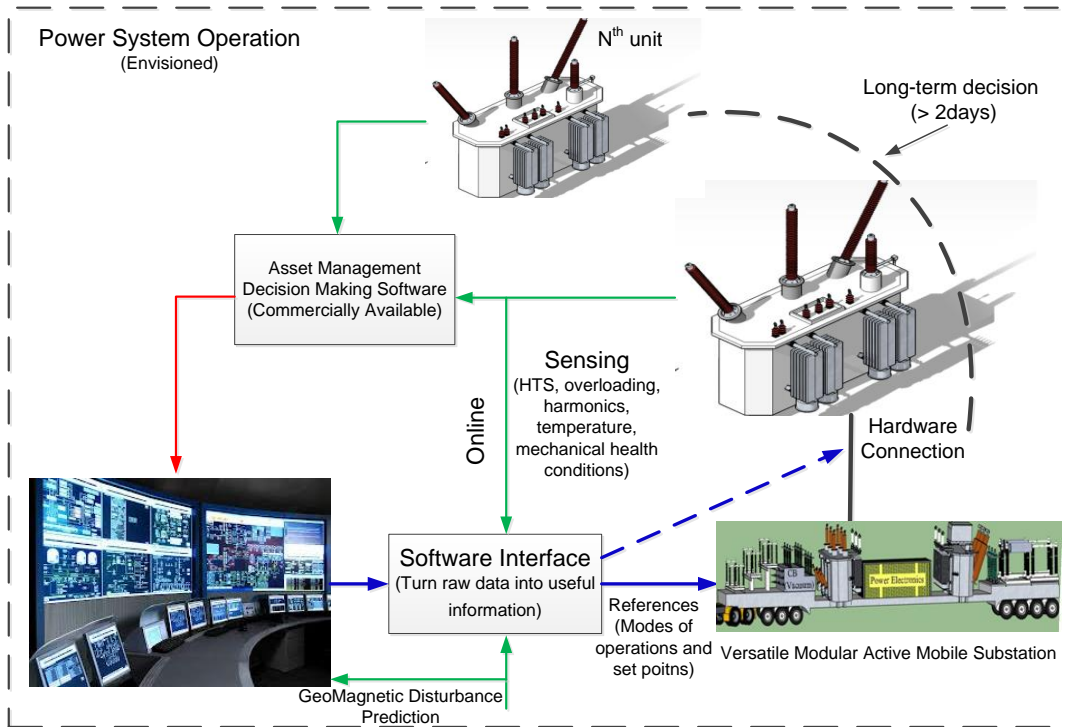
Figure 3-2.   Integrated design of the Active Mobile Substation (AMS).

3.2 Power Electronic System Design

3.2.1 Power Electronics Challenge
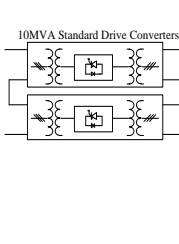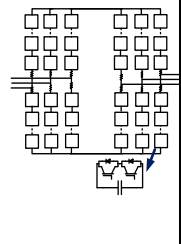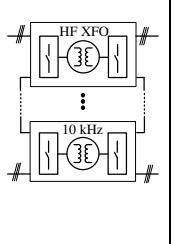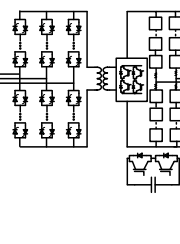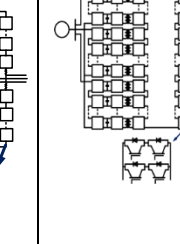
A power electronic system with "black-start" capability (grid with zero voltage) that mimics the conventional synchronous generator is the key enabling technology to realize the AMS. The technology has been studied comprehensively and more or less become mature for many applications such as motor drive. Nevertheless stringent AMS requirements raise major challenges. The AMS is a transmission-level mobile asset (>138kV); therefore, for instance, energy conversion efficiency is an absolute demand and it affects other required metrics such as weight, volume and dynamic performance. In addition, the AMS has limited value without fast response and full operation capabilities under disturbances, unlike other transmission-level applications such as High Voltage Direct Current (HVDC) solutions that their main benefit lies under normal conditions. The barrier in engineering such a system is due to the lack of sufficiently high voltage (>138KV) semiconductor switches; the current state-of-the-art technology at the R&D level is rated up to 15kV. The premise of this section is to investigate transmission-level power electronics circuits using advanced control, semiconductor switches and magnetic structures that can be used to develop the AMS.

3.2.2 System Topology Comparison

Different converter system topologies such as the Modular Transformer Converter (MTC) [59], the Modular Multilevel Converter (MMC) [60]-[63], the Solid State Transformer (SST) [64]-[66], the hybrid converter based on Cycloconverter [67], and the high frequency isolated

modular converter [68]-[69] can be considered for transmission-level active mobile substations. These topologies are compared with regard to several factors that are shown in Table 3-1. The results shown are based on an AMS which is designed to be 20 MVA and can be connected to 138-230kV/69KV transformers. Based on the comparison and with specific attention to isolation and grounding requirements, MTC and high frequency isolated modular converter approach have been selected as the preferred choices to develop the proposed AMS. It is clear that the proposed AMS requires two to four trailers to carry different components of the system.

Table 3-1.   Comparison of power electronics solutions for a 20MVA 138kV-245kV/69kV Active Mobile Substation; Target: 2-4 x Two-Axel Trailers, for Each: Volume: 2.6m*4.1m*18m and Weight: 25ton

Index	Modular Transformer Converter (MTC)	Modular M-Level Converter (MMC)	Solid-State Transformer (SST)	Hybrid Converter based on Cycloconverter	High Frequency isolated modular Converter
Weight (ton)	90	77	64	45	50
Volume (m^3)	120	55	195	70	40
Efficiency	~98%	~97%	~96%	~97%	~97%
Isolation	✓	X	✓	✓	✓
Var Support	✓	✓	✓	✓	✓
Technology & Availability	IGCT Available	LV-IGBT Available	HV 15kV SiC IGBT/MOSFET Not Commercial	LV-IGBT and HV-Thyristor Available	LV-IGBT Available
Fail-to-Short Capability	✓	✓	X	✓	✓

3.2.3 Modular Transformer Converter (MTC) as the Power Electronics Building Block for the Proposed AMS

The building block for power electronic system of the proposed active mobile substation, based MTC is a group of standard three phase drive converters shown in Table II. While AC sides of the converters can be coupled two or more high voltage phase-shifted transformers, as shown in Table II, they can be also coupled through a medium voltage Harmonic Neutralizing (HN) circuit with a third of rated power to obtain low voltage and current harmonic spectrums. An example of the HN circuit is presented in Figure 3-3. This approach allows further reduction in weight and volume of the AMS.

As explained, active mobile substations can provide back-up in case of power transformer failure or forced reduced operation scenarios in addition to power flow control for seasonal renewable energy transmission. These functions altogether have been aggregated not only because of the technical merits but also to address the economic concerns regarding the cost of the power electronics for transmission applications. Therefore, series injection is also accommodated in one of the main transformer through the third winding shown in Figure 3-3.
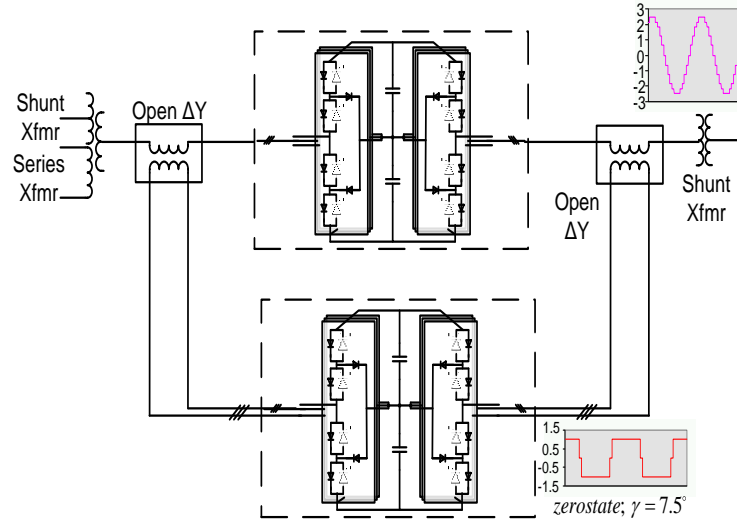
Figure 3-3. Configuration of the MTC based AMS for 20 MVA active mobile substation (230kV/69kV, 13.8kV).

3.2.4 **High Frequency Isolated Modular Converter as the Power Electronics Building Block for the AMS**

The configuration of AMS based on high frequency isolated modular converter is shown in Figure 3-4. In the high frequency isolated modular converter, every power conversion module consists of two stages: AC/DC converter and High frequency link DC/DC converter as shown in Figure 3-5. As can be seen, the AC/DC and DC/DC converter consists of H-bridge converter. The high frequency isolated modular converter has several advantages compared to the traditional Modular Multi-level Converters (MMC). In high frequency isolated modular converter, all power conversion modules in three phases are connected in series. This fact results in the lower voltage rating of each module for high power applications. In addition, lower switching power losses can be achieved by the interleaved

modulation strategies compared to MMC configuration. In fact, this converter topology modulated with a phase-shifted carriers PWM strategy, gives an effective switching frequency three times greater than the effective switching frequency obtained in MMC configuration since in the high frequency isolated modular converter, the modules in all three phases are connected in series. The isolation is also provided by the high frequency transformer in DC/DC converter.
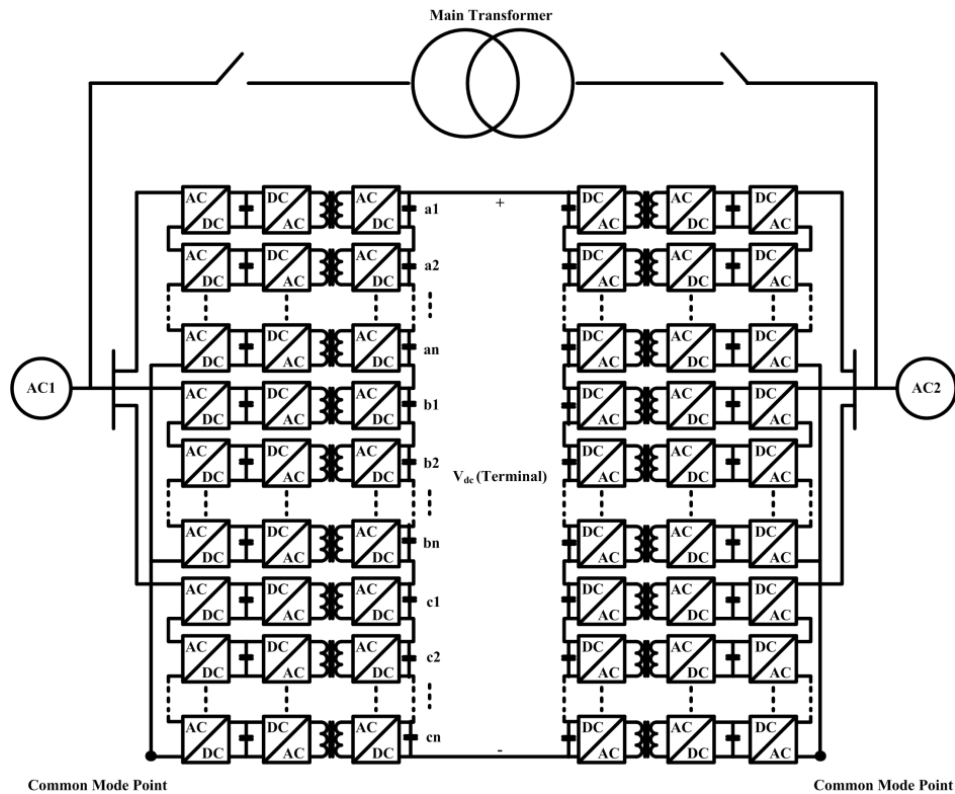
Figure 3-4. Two terminal high frequency isolated modular converter based AMS.
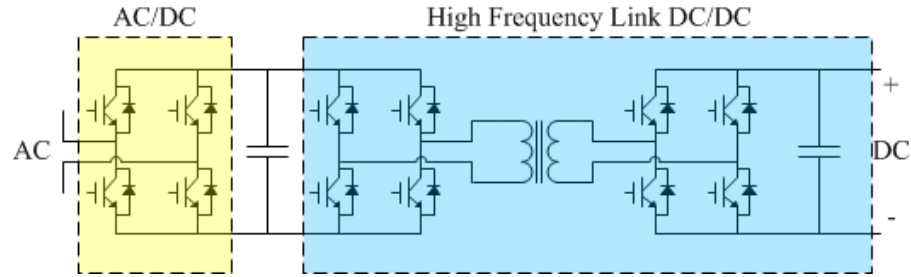
Figure 3-5.   Power conversion module with high frequency link DC/DC converter.

3.3   Control Methods on Active Mobile Substations

3.3.1   Control Structure of the MTC based AMS based on angle control method

All Voltage-Sourced Converters (VSC), the main building blocks of FACTS devices and the MTC, regardless of their topology, can be divided into the two types. One type is the vector-controlled or PWM-based inverter. The function of generating an arbitrary voltage vector is already known for this type of inverter, because the DC link voltage, which is regulated to a fixed value, can be chopped with the PWM pulses to any arbitrary voltage vector. However, this type of converter system may not be suitable or may be uneconomical for many transmission-level FACTS devices due to the output voltage quality and switching losses. Therefore, several multilevel topologies have been proposed to address these issues. The VSC can be also operated based on the output voltage angle control. So far, only reactive power compensation is demonstrated in practice, pioneered Westinghouse (currently Siemens) [70]. It has been shown that by a slight change of angle, the converter is able to

provide inductive/capacitive reactive power [71].

In addition to common benefits, high efficiency is one of the key factors that enables the transportability of the MTC system. The key component of the AMS converters is semiconductor switch and better performance can be also obtained through hybrid semiconductor configuration (like Si switch and SiC diode), circuit topology and control considerations. From control point of view, three different control structures have been considered denoted as angle, vector, and hybrid control. In the hybrid control, one side of the MTC operates with the angle control and the other side operates with the vector control structure. This mode of operation is especially beneficial for power flow control or series-shunt mode. Based on the obtained results, it has been observed that the angle-controlled MTC and the hybrid-controlled MTC provides better efficiency numbers compared to the commonly-used vector-controlled BTB VSC systems. It is important to mention that with the vector-controlled MTC system, the efficiency is expected to be lower than that of been shown considering the additional losses occurs in the harmonic filters.

A simplified advanced angle control structure is shown in Figure 3-6. The objective is to regulate the active and reactive power of the converter through the converter output voltage angle; it represents a single input two output system which has unique constraints. Clearly, one actuator cannot be used to regulate two outputs to arbitrary set-point values. Nevertheless, a one-dimensional class of set-point values is feasible as shown in [11]. The obtained results in [11] showed the possibility of enhancement in operation of angle-controlled VSC to accommodate also the active power transfer. Design limitations and tradeoffs imposed by the plant and controller for such a system have been explained through

the concept of "direction". It has been shown that although the intention might be to have the controller completely or perfectly aligned with the converter dynamics, this level of alignment can make the converter system unstable. In fact, it has been shown that if the plant and controller are perfectly aligned at all frequencies, the input open loop transfer function must necessarily possess at least one NMP (Non-Minimum-Phase) zero, which imposes some limitations on the sensitivity functions of the closed-loop system. Since a VSC with basic component design criteria has the properties of a plant whose direction does not change significantly with frequency, the perfectly aligned condition has been rejected in this research. On the other hand, any VSC system has major disturbances of DC load power. These DC load disturbances can be considered to constitute another converter forming a back-to-back system. It has been shown that if the plant is aligned with the output disturbance by considering an integral controller, that effect of the disturbance to the output can be rejected in steady state. This point is worth mentioning, since it can provide additional criteria for designing the power converter. The selected design criterion has been implemented by making the plant (VSC) aligned with the disturbance (load) at low frequency or within the bandwidth of the converter.

CSTC as a recovery transformer can operate similarly to BTB HVDC converters and an example of PSCAD simulation results for an angle-controlled 24-pulse system is presented in Figure 3-7. The CSTC in shunt-shunt mode is used for power flow control. One converter operates in PQ mode and the other one is responsible to compensate for the losses and ensures a stable operation of the DC bus voltage while it supports its reactive power demands. In vector-controlled VSC systems, reactive power is regulated independent of

65

active power and in angle-controlled CSTC system, this interaction is minimalized through proper design of the controller and physical components. The dynamic performance of the CSTC in series-shunt mode used as seasonal renewable energy transmission controller is shown in Figure 3-8. In this mode of operation, the hybrid control scheme is used. The series converter is used to control active and reactive power flow through the transformer, and the shunt converter maintains the bus voltage magnitude to the desired value by injecting or absorbing reactive power through angle control structure. As expected, the power flow control of series-shunt mode is obtained by a farcationally rated static solution; 10% rating for this study is enough to double the power flow of the node.
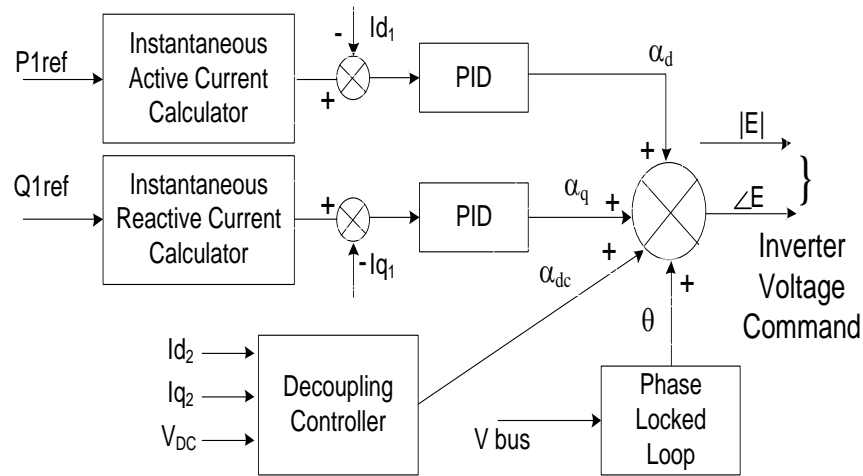
Figure 3-6.   Advanced angle control structure for the MTC based AMS system.
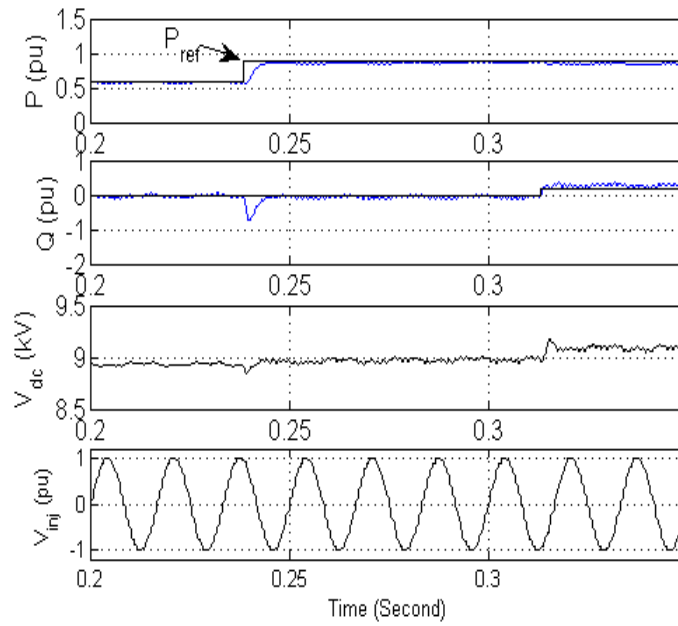
Figure 3-7.   PSCAD simulation results for 20MVA CSTC operation in shunt-shunt mode; angle-controlled.
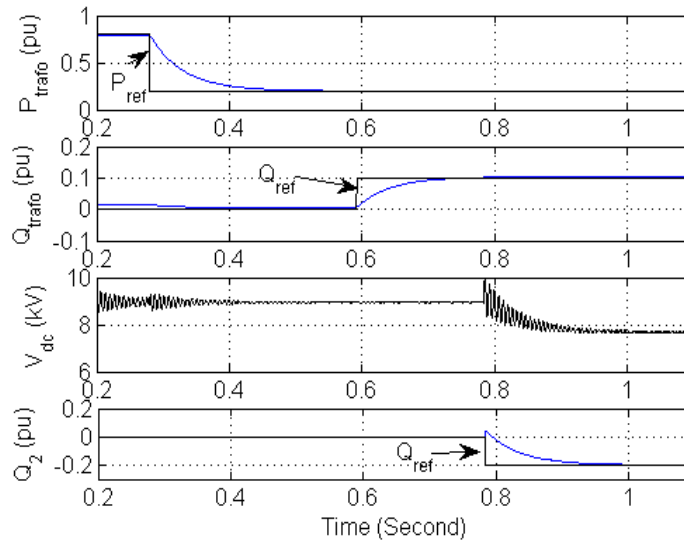
Figure 3-8.   PSCAD simulation results for 20MVA CSTC operation in series-shunt mode; hybrid-controlled.

3.3.2 Control Scheme of High Frequency Isolated Modular Converter based AMS

In this section, the control scheme of high frequency isolated modular converter is presented. In high frequency isolated modular converter, each power conversion building block consists of AC/DC converter and high frequency DC/DC converter as shown in Figure 3-5. In this configuration, several floating DC capacitors in all three phases are connected in series. So, the voltage balancing algorithm is required to match the DC capacitor voltages in all power electronic building blocks. The voltage balancing algorithm is implemented in AC/DC sub-module.

The control scheme for AC/DC sub-module has four voltage control functions. First, power flow controller determines the reference value of DC bus voltage at each terminal. Second, the control scheme has to control the terminal DC bus voltage. Third, the sum of DC capacitor voltages in each phase should be balanced with the sum of floating DC capacitor voltages in other phases. The phase voltage balancing controller is proposed to achieve this goal. Fourth, the module voltage balancing controller should be used to guarantee that the capacitor voltage of each module in each phase is similar to the capacitor voltage of other modules in that phase. The detailed control scheme of each layer is shown in Figure 3-9. With the proposed control scheme, capacitor voltage balancing control in all power conversion building blocks is achieved. In the following, each part of the proposed controller will be explained in detail.

a) Power Flow Controller

b) Terminal DC Bus Voltage Controller

c) Phase Voltage Balancing Controller

d) Module Voltage Balancing Controller

e) Control Scheme of DC/DC sub-module
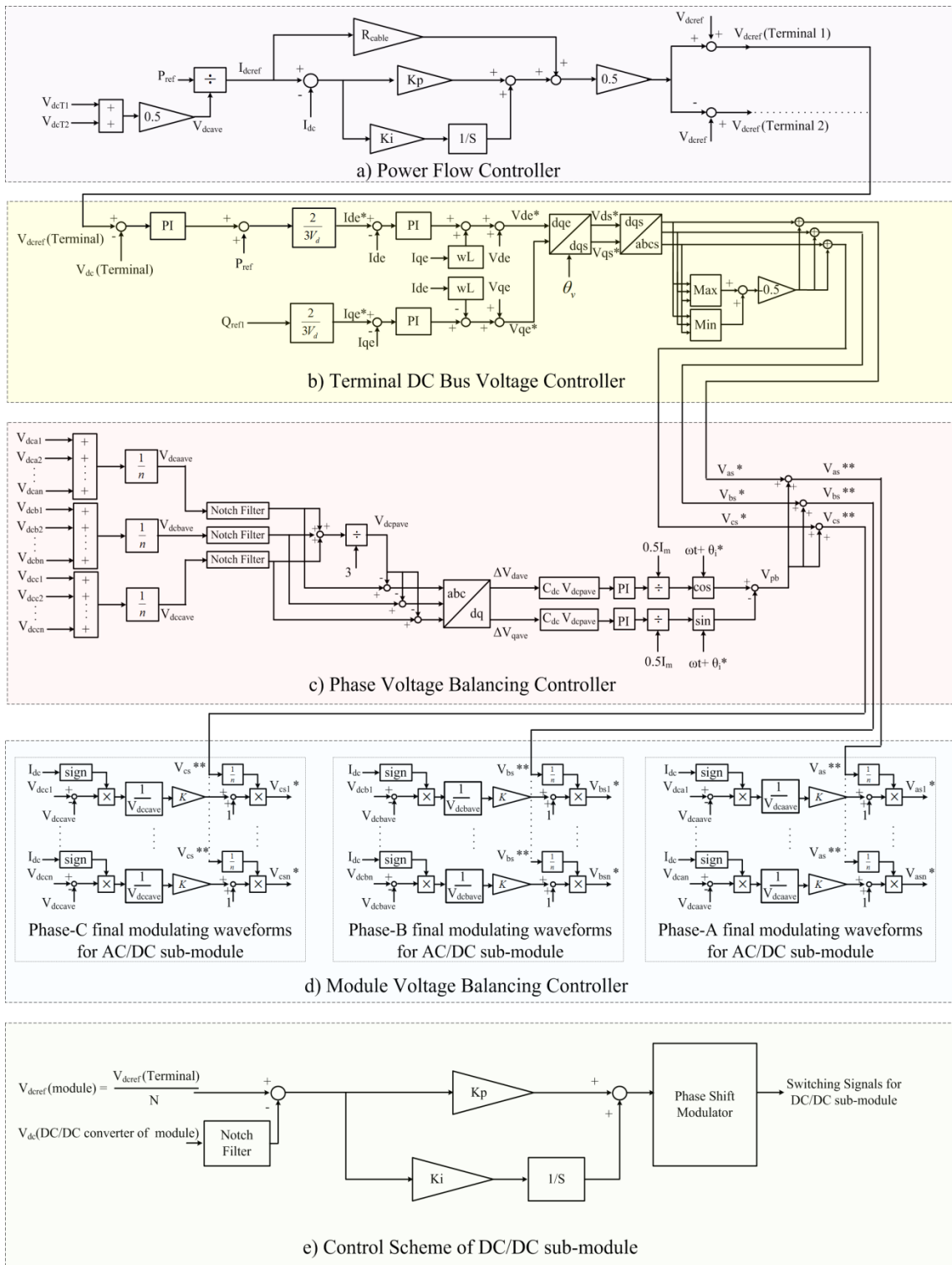
Figure 3-9.   Detailed proposed control scheme of high frequency isolated modular converter.

Power Flow Controller

Power flow controller determines the reference value of DC bus voltage of each terminal. The transferred power can be controlled by DC current, I_{dc}. To control DC current, power flow controller decides two terminal DC bus voltages. For power flow control, DC overhead line can be simply modeled with inductor and resistor as shown in Figure 3-10.
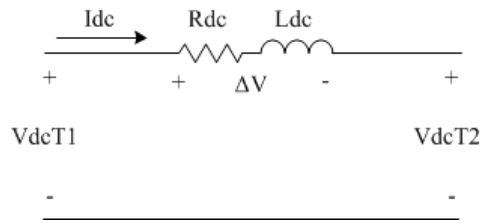
Figure 3-10. Two-terminal transmission system with DC overhead line.

The DC bus voltage at the sending-end terminal can be defined as (3.1), and the DC bus voltage at the receiving-end terminal can be written as (3.2). Therefore, the transferred power is defined as the average power of the sending-end and the receiving-end power as (3.3).

$$V_{dcT1} = V_{dcave} + 0.5\Delta V \tag{3.1}$$

$$V_{dcT2} = V_{dcave} - 0.5\Delta V \tag{3.2}$$

$$P = V_{dcave}I_{dc} = \frac{V_{dcT1} + V_{dcT2}}{2}I_{dc} \tag{3.3}$$

The DC current can be determined with the DC grid resistance and the voltage difference between two terminals as (3.4). So, the transferred power can be rewritten with the DC grid resistance and the voltage difference between two terminals as (3.5).

$$I_{dc} = \frac{\Delta V}{R_{dc}}$$

(3.4)

$$P = V_{dcave} \frac{\Delta V}{R_{dc}} = \frac{V_{dcT1} + V_{dcT2}}{2} \frac{\Delta V}{R_{dc}}$$

(3.5)

Considering the fact that the average value of terminal DC bus voltages is varying slowly, the transferred power can be determined by the DC current. As a result, power flow controller should control the DC current, I_{dc} by adjusting the voltage difference between two terminals. Power flow controller can be implemented as shown in Figure 3-9(a).

According to the reference value of active power, the reference value of DC current can be determined. To improve the dynamic performance of power flow controller, the voltage difference can be used as a feed-forward signal. This feed-forward value can be simply calculated with the overhead line resistance. The output of the controller is the voltage difference between two terminals. This voltage difference can be divided by two and added to the reference value of terminal DC bus voltage. Power flow controller generates the reference values of DC bus voltage for both terminals.

B. **Terminal DC bus voltage Controller**

In the back to back high frequency isolated modular converter, one terminal should control terminal DC bus voltage, and the other terminal will control active and reactive power flow. DC bus voltage controller generates the dq-axis current references in the synchronous

reference frame. The q-axis current reference can be calculated based on the reference value of reactive power. Figure 3-9(b) shows terminal DC bus voltage controller with the AC current controller in detail to generate the initial modulating waveforms.

C. **Phase voltage balancing controller**

If each phase has n power conversion modules, the sum of n capacitor voltages of A-phase should be balanced with the sum of n capacitor voltages of phase-B and phase-C. The phase voltage balancing can be achieved by controlling the common-mode voltage. Each phase power can be calculated by multiplication of phase voltage and phase current as (3.6). Based on (3.6), the phase power can be written as (3.7)-(3.9).

$$
\begin{aligned}
v_a &= V_m \cos(\omega t) & i_a &= I_m \cos(\omega t + \theta_i) \\
v_b &= V_m \cos(\omega t - \frac{2\pi}{3}) & i_b &= I_m \cos(\omega t + \theta_i - \frac{2\pi}{3}) \\
v_c &= V_m \cos(\omega t + \frac{2\pi}{3}) & i_c &= I_m \cos(\omega t + \theta_i + \frac{2\pi}{3})
\end{aligned}
\tag{3.6}
$$

$$
P_a = v_a i_a = \frac{1}{2} V_m I_m \cos(\theta_i) + \frac{1}{2} V_m I_m \cos(2\omega t + \theta_i)
\tag{3.7}
$$

$$
P_b = v_b i_b = \frac{1}{2} V_m I_m \cos(\theta_i) + \frac{1}{2} V_m I_m \cos(2\omega t + \theta_i + \frac{2\pi}{3})
\tag{3.8}
$$

$$
P_c = v_c i_c = \frac{1}{2} V_m I_m \cos(\theta_i) + \frac{1}{2} V_m I_m \cos(2\omega t + \theta_i - \frac{2\pi}{3})
\tag{3.9}
$$

If the common-mode voltage is added into all three voltage references, the phase power varies by the common-mode voltage. When the common-mode voltage is considered as (3.10), the phase power can be expressed as (3.11)-(3.13).

$$
V_{pb} = V_{cm} \cos(\omega t + \phi)
\tag{3.10}
$$

$$P_a^{'} = P_a + \frac{1}{2}V_{cm}I_m \cos(\phi - \theta_i) + \frac{1}{2}V_{cm}I_m \cos(2\omega t + \theta_i + \phi) \tag{3.11}$$

$$P_b^{'} = P_b + \frac{1}{2}V_{cm}I_m \cos(\phi - \theta_i + \frac{2\pi}{3}) + \frac{1}{2}V_{cm}I_m \cos(2\omega t + \theta_i + \phi - \frac{2\pi}{3}) \tag{3.12}$$

$$P_c^{'} = P_c + \frac{1}{2}V_{cm}I_m \cos(\phi - \theta_i - \frac{2\pi}{3}) + \frac{1}{2}V_{cm}I_m \cos(2\omega t + \theta_i + \phi + \frac{2\pi}{3}) \tag{3.13}$$

Each phase power has an average value as a DC term and an oscillating term as a second order harmonic component. The average value of each phase power can be written as (3.14)-(3.16).

$$P_{aavg}^{'} = \frac{1}{2}V_m I_m \cos(\theta_i) + \frac{1}{2}V_{cm}I_m \cos(\phi - \theta_i) \tag{3.14}$$

$$P_{bavg}^{'} = \frac{1}{2}V_m I_m \cos(\theta_i) + \frac{1}{2}V_{cm}I_m \cos(\phi - \theta_i + \frac{2\pi}{3}) \tag{3.15}$$

$$P_{cavg}^{'} = \frac{1}{2}V_m I_m \cos(\theta_i) + \frac{1}{2}V_{cm}I_m \cos(\phi - \theta_i - \frac{2\pi}{3}) \tag{3.16}$$

The average value of each phase power can be controlled by adjusting the magnitude of the common-mode voltage V_{cm} and the phase φ. The frequency of this common-mode voltage is the fundamental frequency. The average value of each phase power with the common-mode voltage can be written in the stationary dq reference frame as (3.17).

$$\begin{bmatrix} P_{davg}^{'} \\ P_{qavg}^{'} \end{bmatrix} = \frac{1}{2}V_{cm}I_m \begin{bmatrix} \cos(\phi - \theta_i) \\ \sin(\phi - \theta_i) \end{bmatrix} \tag{3.17}$$

Meanwhile, the phase DC voltage unbalance can be analyzed with the energy balance criteria among the capacitors of the three phases. The energy balance in the capacitors of the three phases can be written in terms of phase DC voltage variations as (3.18). This three-phase energy can be expressed in the stationary dq reference frame as (3.19). This dq-axis

energy variation can be compensated with the common-mode voltage. To balance the phase energy variation, the phase energy variation should be controlled at zero. The average phase voltage should be calculated. Figure 3-9(c) shows how to obtain the average phase voltage and how to balance these average phase voltages. The dq-axis phase voltage variation is multiplied with the effective capacitor of each phase and the average value of the three-phase voltages. These calculated values can be known as the dq-axis energy variation. These energy variations are fed to the PI-controller. The outputs of the PI-controller should be the added power reference to compensate the energy variation as (3.20). Using (3.17), the dq-axis power references are transformed to the stationary common-mode voltage as (3.21).

$$
\begin{bmatrix} \Delta E_{aavg} \\ \Delta E_{bavg} \\ \Delta E_{cavg} \end{bmatrix} = C_{dc} V_{pavg} \begin{bmatrix} \Delta V_{aavg} \\ \Delta V_{bavg} \\ \Delta V_{cavg} \end{bmatrix}
\tag{3.18}
$$

$$
\begin{bmatrix} \Delta E_{davg} \\ \Delta E_{qavg} \end{bmatrix} = \frac{2}{3} \begin{bmatrix} 1 & -\dfrac{1}{2} & -\dfrac{1}{2} \\ 0 & \dfrac{\sqrt{3}}{2} & -\dfrac{\sqrt{3}}{2} \end{bmatrix} \begin{bmatrix} \Delta E_{aavg} \\ \Delta E_{bavg} \\ \Delta E_{cavg} \end{bmatrix}
\tag{3.19}
$$

$$
\begin{bmatrix} P^*_{dpavg} \\ P^*_{qpavg} \end{bmatrix} = \frac{K_p + K_i s}{s} \begin{bmatrix} -\Delta E_{davg} \\ -\Delta E_{qavg} \end{bmatrix}
\tag{3.20}
$$

$$
V_{pb} = \frac{\cos(\omega t + \theta_i^*) P^*_{dpavg} - \sin(\omega t + \theta_i^*) P^*_{qpavg}}{0.5 I_m}
\tag{3.21}
$$

In the high frequency isolated modular converter configuration, the capacitor voltage of each AC/DC and DC/DC converter consists of a DC term and DC voltage ripple. The DC voltage ripple of each capacitor can be written as (3.22). From (3.22) it is obvious that the voltage variation of each capacitor voltage can be reduced as the capacitor value is increased.

In the phase voltage balancing controller, notch filter is also used to remove the 120 Hz DC voltage ripple in the control scheme.

$$\Delta V_{p-p} = \frac{V_{rms}I_{rms}}{4\pi fCV_{dcm0}}$$

(3.22)

D. **Module voltage balancing controller**

Figure 3-9(d) shows module voltage balancing controller. Even though the phase voltage balancing can be achieved by injecting the common-mode voltage into the phase voltage references, the module voltage balancing can be accomplished by dividing the phase voltage references into the module voltage references [72]-[73]. The phase voltage reference is divided into all module AC/DC converter voltage references. According to the voltage variation among the AC/DC converter capacitor voltages, the voltage portion in each AC/DC converter can be adjusted.

Having the modulation waveforms for all AC/DC converter modules, phase-shifted PWM modulation strategy is used to generate the final switching signals. The carrier signals are triangular and phase-shifted by $\frac{2\pi}{N}$ where N is the total number of modules in each phase. The switching signals are determined by comparing the modulating waveforms and the carrier signals. The effective switching frequency obtained in high frequency isolated modular converter with the interleaved modulation can be computed by (3.23).

$$f_{sw}(effective) = 3 \times N \times f_{sw}(actual)$$

(3.23)

E. **Control scheme of DC/DC sub-module**

The control scheme of DC/DC converter in each module is similar to the control structue used for dual active bridges [74]-[75]. Figure 3-9(e) shows the control schme of DC/DC converter sub-module. As can be seen, notch filter is used in the control scheme to remove 120 Hz oscillation of the measured value of DC/DC converter capacitor voltage.

3.4 Dynamic Performance Evaluation of the high frequency isolated modular converter through PSCAD Simulation

In this section, the dynamic performance of a 12MVA high frequency isolated modular converter for AMS application is evaluated. To verify the performance of the proposed control scheme, PSCAD/EMTDC based simulation has been carried out based on the configuration shown in Figure 3-4, and the system parameters are summarized in Table 3-2. First, the dynamic performance of active power flow, terminal DC bus voltage, and terminal AC current is shown in Figure 3-11. As can be observed from Figure 3-11, the reference value of active power is increased from zero to the rated power at t=0.5s, and it is varied from 0 to -12 (MW) at t=1.5s to show bidirectional active power flow. As can be seen, the main transformer power flow is changed from 3.6 (MW) to -3.7 (MW) at t=0.5s, and it also changes from 3.6 (MW) to 12.1 (MW) at t=1.5s. Three-phase AC current for both terminals and transformer is also shown in Figure 3-11. As can be observed, three-phase AC current changes according to the reference value of active power flow. Terminal dc bus voltage regulated at 12 kV is also presented in Figure 3-11. Figure 3-12, and Figure 3-13 show module DC capacitor voltages for terminal 1 and 2, respectively. As can be seen, all DC

capacitor voltages are regulated at 1 kV, and they are all equal to each other. It can be concluded that the phase and module voltage balancing controller can satisfactorily balance all DC capacitor voltages. From the obtained simulation results, it can be noted that the peak to peak DC voltage ripple is around 250 (V) which is closely matched with the result obtained by (3.22). Module DC capacitor voltages for terminal 1 and 2 without using the proposed phase voltage balancing controller are shown in Figure 3-14, and Figure 3-15 respectively. As can be seen, balancing control of DC capacitor voltages in both terminals is lost without using the phase voltage balancing controller.

Table 3-2.　High frequency isolated modular converter system parameters

Terminal rated power	P	12 MVA
Terminal AC input voltage (phase peak)	E	3.2 kV
Terminal voltage reference	V_{dc}	12 kV
Sending-end Leakage inductance	L_s	0.1 pu=0.374 (mH)
Transformer inductance	L_T	0.1 pu=0.374 (mH)
receiving-end Leakage inductance	L_r	0.1 pu=0.374 (mH)
Module number (per terminal)	N	12
AC/DC capacitor voltage	$V_{(AC/DC)}$	1 kV
DC/DC capacitor voltage	$V_{(DC/DC)}$	1 kV
Capacitor value	C	10 mF
AC/DC PWM switching frequency	$f_{sw}\,(AC/DC)$	540 Hz
Isolated DC/DC PWM switching frequency	$f_{sw}\,(DC/DC)$	20 kHz
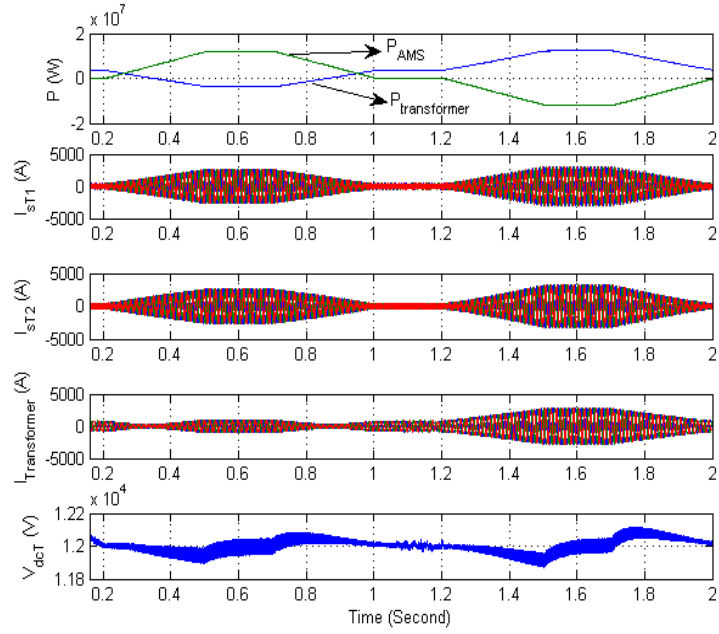
Figure 3-11. PSCAD simulation results for 12MVA high frequency isolated modular converter operation.
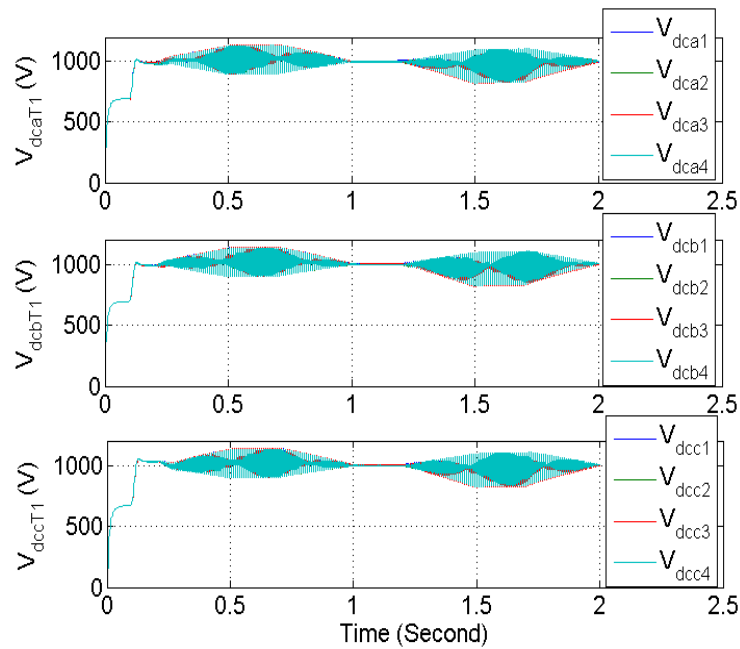
Figure 3-12. Terminal 1 capacitor voltages with phase voltage balancing controller.

78
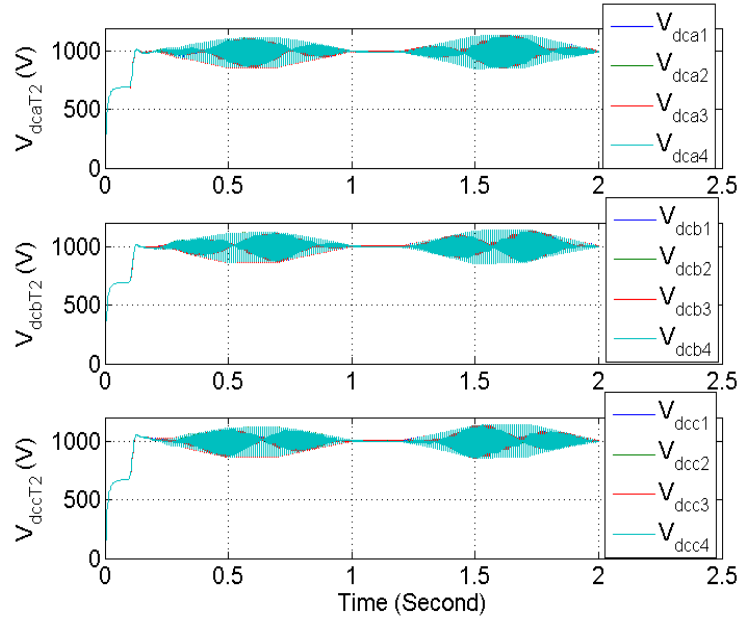
Figure 3-13. Terminal 2 capacitor voltages with phase voltage balancing controller.
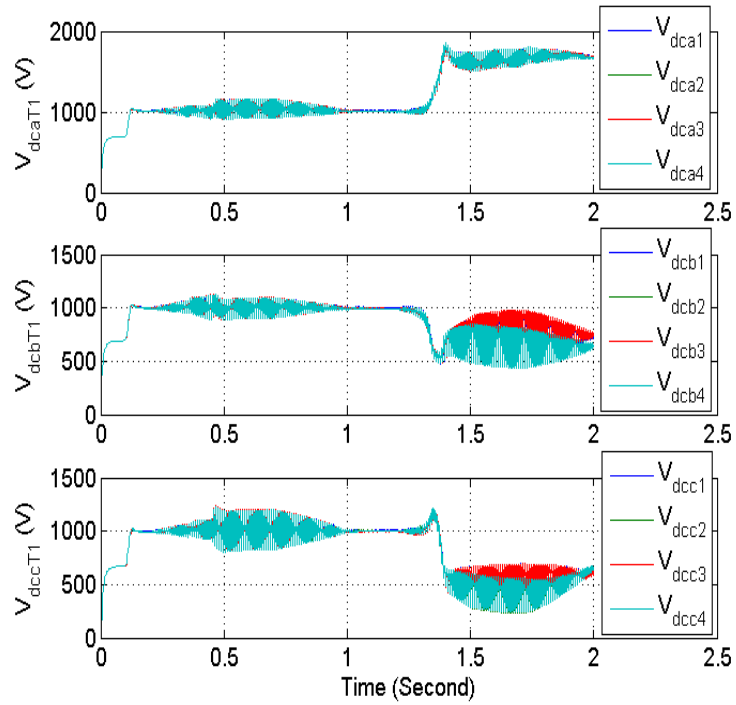
Figure 3-14. Terminal 1 capacitor voltages without phase voltage balancing controller.
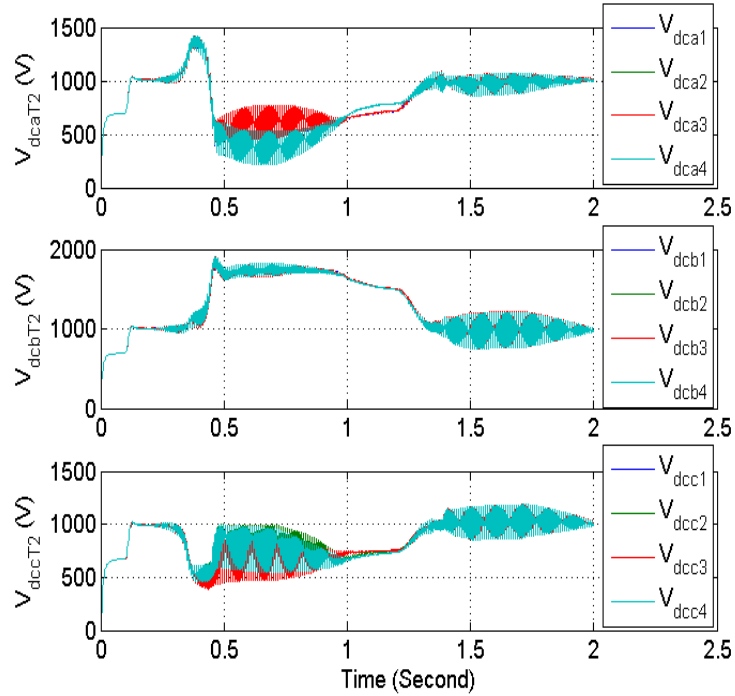
Figure 3-15. Terminal 2 capacitor voltages without phase voltage balancing controller.

3.5 Summary

With advances in power electronics circuits and control, conventional uncontrolled mobile substations can be transformed into controllable assets. This section proposed two interesting configurations that may result in advent of transmission-level active mobile substations. Active mobile substations provide back-up in case of power transformer failure or forced reduced scenarios by providing real-time continuous power flow control under normal and fault conditions. In addition to common benefits of current mobile substations, the proposed active mobile substation can be utilized as a transportable power flow controller for seasonal renewable energy sources and as a life extender for power transformer fleet. In this section,

design considerations in development of the AMS is provided in terms of power electronics building blocks, converter system control and its effects, and required supervisory control.

A high frequency isolated modular converter is also proposed as an interesting candidate for AMS. In this configuration, several bidirectional modules are connected in cascade, so the voltage balancing control of several floating dc capacitors is required. In this section, an appropriate control structure with the phase voltage balancing controller, and the module voltage balancing controller is proposed to achieve voltage balancing control of multiple floating dc capacitors. Detailed PSCAD simulation results are also presented to evaluate the performance of AMS under normal operating conditions.

Chapter 4. EMBEDDED MULTI-TERMINAL DC NETWORK IN MESHED AC POWER SYSTEM

4.1 Introduction

Currently, there is common consensus that the power grid needs to be upgraded and modernized to accommodate more renewable sources of generation. One hurdle that impedes the grid upgrade is the intermittency of these resources. In fact, there is a common belief that commercially practiced renewable resources have less than 30% availability throughout the year. This fact with high penetration of renewables causes overloading conditions that necessitate either network upgrade (re-conductor) or curtailment in the generation while there is unutilized capacity in the transmission network, i.e. >138kV. Therefore, power flow control or as recently termed power router solutions have been gaining more attractions. From the conventional Unified Power Flow Controller (UPFC) for AC systems to advanced multi-terminal High Voltage Direct Current (HVDC) systems [76]-[77], researchers have proposed several power electronic solutions in this field to improve and increase reliability, efficiency, cost-benefit factors, functions and many more. The multi-terminal DC grid is a flexible solution with right-of-way factor advantages and it can be integrated to the existing meshed AC grid system to enhance power transmission capability, and it has economic benefits especially in congested areas compared to adding AC grid system to increase power transmission capacity [78]-[79].

Development of steady state models of distributed resource units and voltage source converters is extremely important to determine the required ratings of DC components in

82

large power networks [80]-[81]. The objective of this section is to propose an appropriate model of embedded multi-terminal DC grid in meshed AC power systems to represent the behavior of AC power flow with respect to DC grid operating points. Generally, two different types of models are used to represent the performance of DC grid for power system analysis. These are algebraic models and linear differential equation models. The algebraic models are used for steady state analysis, and linear differential equation models are used for time domain simulation. In this section, the algebraic model of hybrid AC/DC grid is proposed. The proposed algebraic model is a combination of current sources and logic statements that direct iterative processes and enforce limits. The behavior of AC grid power flow with respect to multi-terminal DC grid operating points can be easily obtained by this model, and the appropriate reference values of DC grid converters based on the desired AC grid power flow can be easily computed using the proposed model. The proposed algebraic model is significantly important in defining the required ratings for DC grid.

Control strategies for the operation of multi-terminal DC grid in meshed AC power systems can be mainly categorized into two major groups, namely, master/slave control method and droop control method. In master/slave control method, DC bus voltage is controlled by one terminal, and the other terminals will control active and reactive power flow [82]-[84]. In this control algorithm, disconnection of master terminal will result in the outage of the entire DC grid. In droop control method, all terminals participate in DC bus voltage control. Droop control method is more reliable compared to master/slave control method since in this method, when fault happens in one terminal, the other terminals will try to regulate DC bus voltage, and the operation of the entire DC grid does not depend on one

terminal [85]-[88]. In this section, the control structure of DC grid converters in meshed AC power system is proposed based on the modified droop control structure. In the proposed control structure, dead-band controller is also used to improve the performance of multi-terminal DC grid. Dynamic performance of multi-terminal DC grid in a reduced order three-bus AC equivalent NYPA power system based on the proposed control method is also explored in PSCAD/EMTDC and Real time Digital Simulator (RTDS). PSCAD and RTDS simulation results are presented to verify the proposed algebraic model based on steady state results.

In the following, this paper is organized as follows. In section II, the algebraic model of embedded DC grid in meshed AC power system is presented. Section III explains the control structure based on droop control structure with dead-band controller for multi-terminal dc grid. In section IV, an embedded three-terminal DC grid in a three-bus meshed AC power system is formulated. The accuracy of the proposed algebraic model and control structure is investigated in section V based on the PSCAD and RTDS simulation, and the steady state results from algebraic model are compared with the obtained simulation results. Finally, Section VI presents the concluding remarks.

4.2 Algebraic Model of Embedded Multi-Terminal DC Network in Meshed AC Power System

In this section, the algebraic model of embedded multi-terminal DC grid in meshed AC power systems is derived. Algebraic model of multi-terminal DC grid is used for steady state and transient stability analysis. Algebraic model will present the behavior of AC transmission

line power flow with respect to various operating points of DC grid converters. The objective of algebraic model development is to set the reference values of active and reactive power flow of DC grid converters based on the desired operating points for AC grid transmission lines.

The embedded multi-terminal DC grid in meshed AC power system for n-bus system is shown in Figure 4-1. For power flow analysis, an appropriate analytical model of multi-terminal DC grid is required to formulate the network equations. To achieve this goal, independent current sources are used to model multi-terminal DC grid converters as shown in Figure 4-2. Therefore, AC and DC power flow can be combined, and the node voltage equation for *n*-bus power system can be expressed as (4.1). (4.1) can be solved to find *n* bus voltages based on (4.2). Having all *n* bus voltages, the active and reactive power flow of DC grid converter in bus *i* can be computed by (4.3).
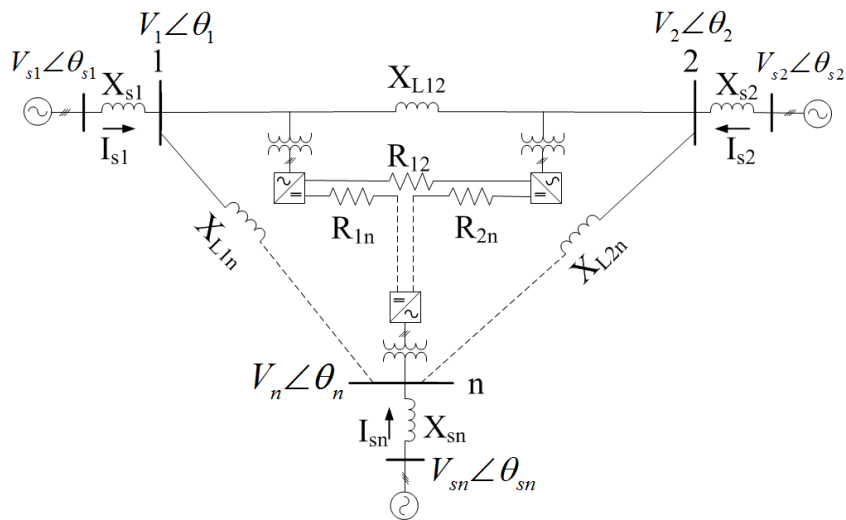
Figure 4-1.   Embedded multi-terminal DC grid in *n*-bus meshed AC power system.
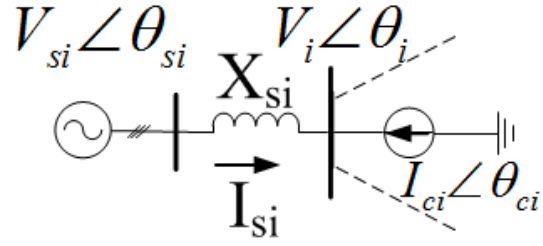
Figure 4-2.　Proposed model of a DC grid terminal in AC system.

$$
\begin{bmatrix}
Y_{11} & Y_{12} & \cdots & Y_{1n} \\
Y_{21} & Y_{22} & \cdots & Y_{2n} \\
\vdots & \vdots & \ddots & \vdots \\
Y_{n1} & Y_{n2} & \cdots & Y_{nn}
\end{bmatrix}
\begin{bmatrix}
V_1 \angle \theta_1 \\
V_2 \angle \theta_2 \\
\vdots \\
V_n \angle \theta_n
\end{bmatrix}
=
\begin{bmatrix}
\dfrac{V_{s1} \angle \theta_{s1}}{jX_{s1}} + I_{c1} \angle \theta_{c1} \\
\dfrac{V_{s2} \angle \theta_{s2}}{jX_{s2}} + I_{c2} \angle \theta_{c2} \\
\vdots \\
\dfrac{V_{sn} \angle \theta_{sn}}{jX_{sn}} + I_{cn} \angle \theta_{cn}
\end{bmatrix}
\tag{4.1}
$$

$$
\begin{bmatrix}
V_1 \angle \theta_1 \\
V_2 \angle \theta_2 \\
\vdots \\
V_n \angle \theta_n
\end{bmatrix}
= \left[Y_{bus} \right]^{-1}
\begin{bmatrix}
\dfrac{V_{s1} \angle \theta_{s1}}{jX_{s1}} + I_{c1} \angle \theta_{c1} \\
\dfrac{V_{s2} \angle \theta_{s2}}{jX_{s2}} + I_{c2} \angle \theta_{c2} \\
\vdots \\
\dfrac{V_{sn} \angle \theta_{sn}}{jX_{sn}} + I_{cn} \angle \theta_{cn}
\end{bmatrix}
\tag{4.2}
$$

$$
P_i = \mathrm{Re}\,al\left\{ \vec{V_i} \vec{I_{ci}}^* \right\} ; Q_i = \mathrm{Im}\,ag\left\{ \vec{V_i} \vec{I_{ci}}^* \right\}
\tag{4.3}
$$

Based on the operating points of DC grid terminals, the set of nonlinear equations for active and reactive power flow of each terminal (obtained by (4.3)) is solved to calculate the magnitude and the angle of each current source $(I_{ci} < \theta_{ci})$ shown in Figure 4-2. Consequently, (4.2) is used to find the magnitude and the angle of different bus voltages $(V_i < \theta_i)$. By calculating voltage vectors $(V_i < \theta_i)$ for all n nodes, active and reactive power flow of AC system nodes and transmission lines can be obtained accordingly. It should be mentioned that

(4.4) should be satisfied to maintain the power balance in multi-terminal DC grid.

$$P_{conv1} + P_{conv2} + ... + P_{convn} = \sum P_{loss}(dc) \qquad (4.4)$$

4.3   Control Structure of Multi-terminal DC Grid

A. Master/Slave Control Method

In this section, the control structure of MTDC grid based on master/slave control method is explored. In this method, one converter as a master converter is considered for DC bus voltage control, and it is used for balancing the active power in the DC grid. The control structure for master converter is shown in Figure 4-3. The master converter is controlled to regulate DC bus voltage at the desired value. The control structure for slave terminals is shown in Figure 4-4. As can be seen, the slave terminals are switched to control active and reactive power flow. Figure 4-5 shows the overview of the AC current controller. The grid angle is detected with PLL, and the feed-forward voltages are calculated based on the measured input three-phase voltages. The output of AC current controller is the produced reference voltage for each converter.
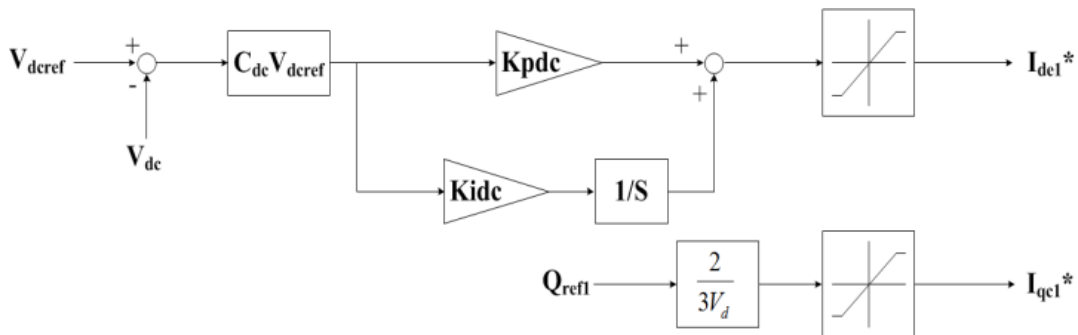
Figure 4-3.   DC bus voltage control structure (master terminal).
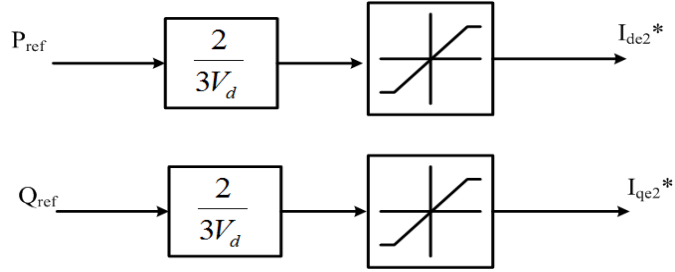
Figure 4-4.   Power flow control structure (slave terminal).
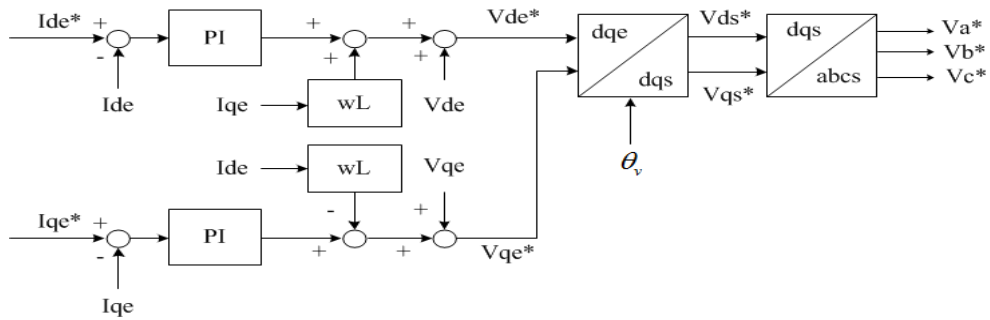
Figure 4-5.   Current Control Structure.

B.   Droop Control Method with dead-band controller

In the master/slave control structure, if master converter fails, the operation of all other DC terminals is disturbed, and most probably the operation of the entire DC grid is lost. To solve this problem, the control structure based on "droop control" method can be used. In the droop control structure, all terminals contribute to regulate DC grid voltage and power flow. In this control method, the operation of multi-terminal DC grid does not depend on a single terminal, and fault in one terminal will not result in loss of the entire DC grid. In the droop control structure, all terminals regulate power flow and DC grid voltage, but these two tasks are opposing, and DC grid voltage control results in steady state error in active power flow

control, and vice versa. In this section, as a modification to the droop-based controllers, an addition of dead-band controller is proposed in DC voltage controller loop. Accordingly, the DC voltage controller is off when DC voltage error is within dead zone. The dead-band controller is used to reduce steady state error of power flow control. The terminal active power flow is exactly regulated at the power reference without any steady state error if DC voltage controller is disabled by the dead-band controller. The control configuration based on the droop control method with dead-band controller is shown in Figure 4-6. DC voltage versus power characteristics in droop controller is shown in Figure 4-7.
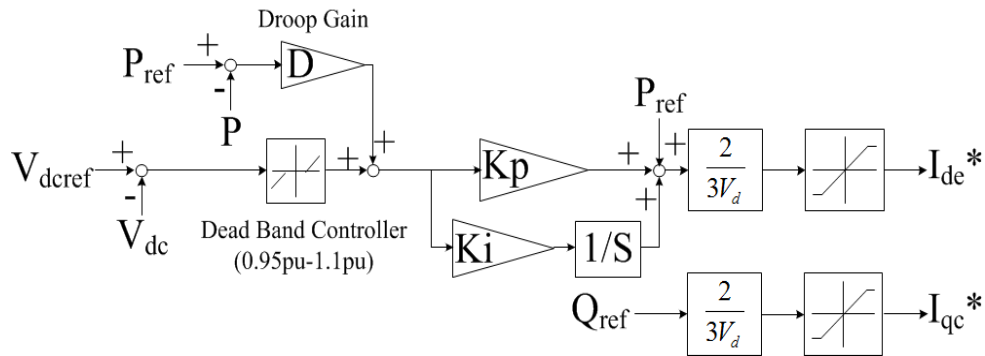
Figure 4-6.   Block diagram of control structure based on droop control method with dead-band controller.
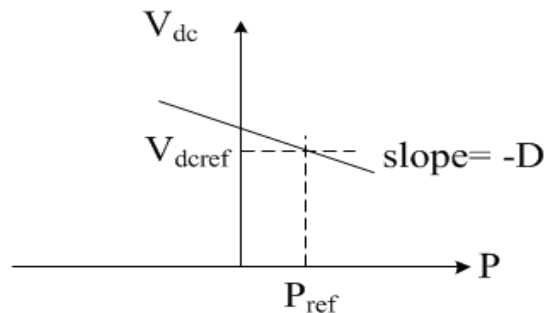
Figure 4-7.   DC voltage versus power characteristics in DC voltage droop controller.

4.4 Example of an Embedded Three-Terminal DC System in a Three-bus Meshed AC System

To show the procedure in detail, the New York Power Authority (NYPA) power system is considered as a case study to be able to solve the equations numerically. The multi-terminal DC grid configuration in a reduced order three-bus NYPA power system is shown in Figure 4-8, and the algebraic model is also illustrated in Figure 4-9. According to Figure 4-9, (4.5) is written to find the magnitude and the angle of three bus voltages.

Table 4-1.   NYPA power system parameters

Marcy Leakage inductance	X_{s1}	0.0077 pu
New Scotland Leakage inductance	X_{s2}	0.01 pu
Coopers Corner Leakage inductance	X_{s3}	0.0183 pu
Marcy- New Scotland Line inductance	X_{L12}	0.0178 pu
Marcy- Coopers Corner Line inductance	X_{L13}	0.0421 pu
New Scotland- Coopers Corner Line inductance	X_{L23}	0.0609 pu
Marcy- New Scotland Line admittance	Y_{c1}	0.788 pu
Marcy- Coopers Corner Line admittance	Y_{c3}	1.173 pu
Marcy phase angle	θ_{s1}	0°
New Scotland phase angle	θ_{s2}	-8.2°
Coopers Corner phase angle	θ_{s3}	-14.6°
Marcy- New Scotland DC cable resistance	R_{12}	0.0009 pu
Marcy- Coopers Corner DC cable resistance	R_{13}	0.0014 pu
New Scotland- Coopers Corner DC cable resistance	R_{23}	0.0014 pu
Base Voltage	E	345 kV
Base Power	P	100 MVA
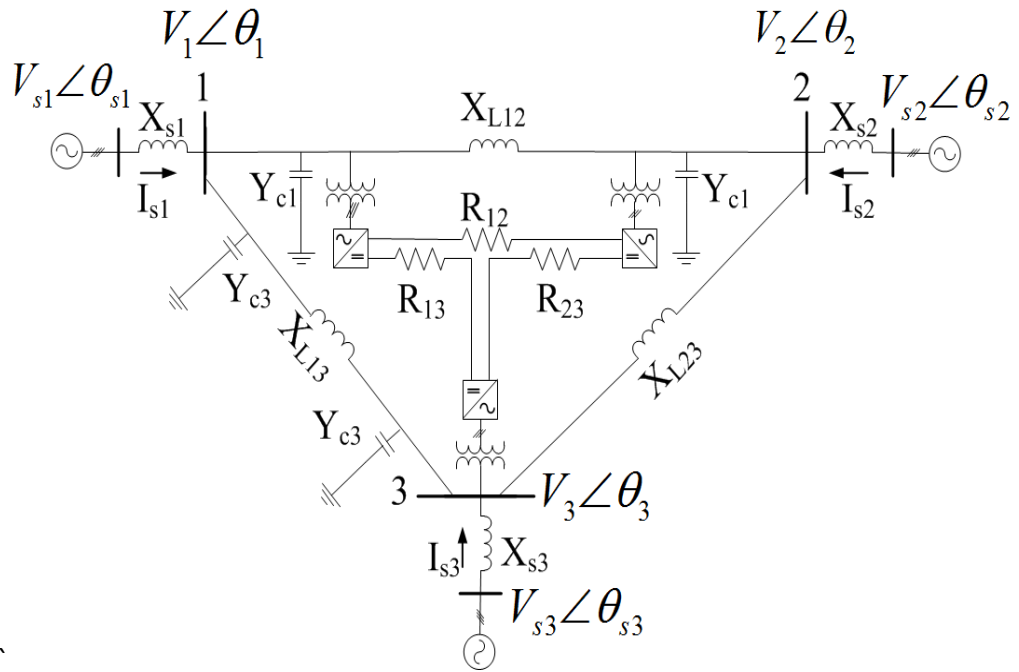
Figure 4-8.   Embedded Multi-terminal DC grid model in a three-bus meshed AC power system.
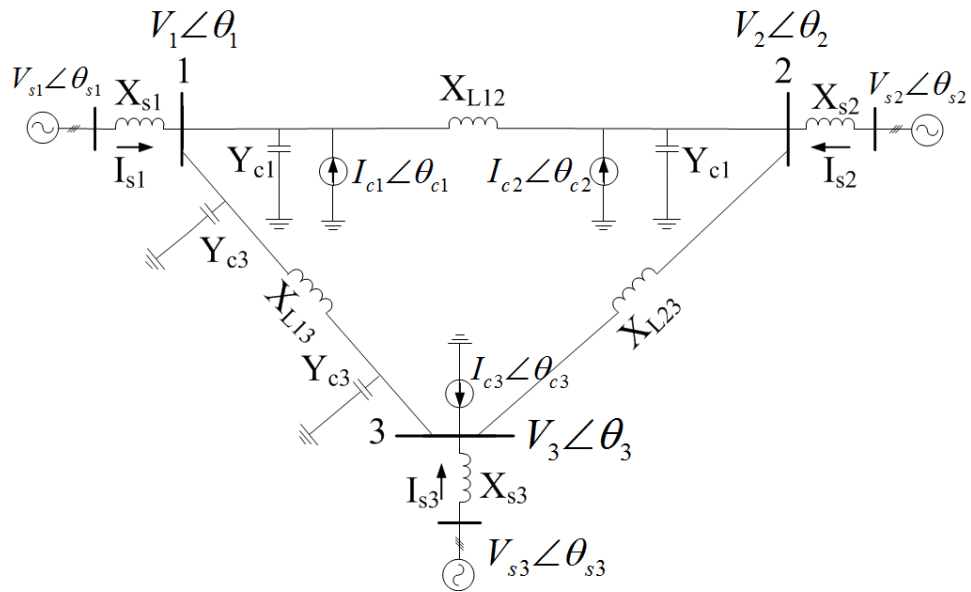
Figure 4-9.   Algebraic model of embedded multi-terminal DC grid in a three- bus meshed ac power system.

$$
\begin{bmatrix}
\dfrac{1}{jX_{s1}} + \dfrac{1}{jX_{L12}} + \\ \dfrac{1}{jX_{L13}} + j(Y_{c1}+Y_{c3}) & -\dfrac{1}{jX_{L12}} & -\dfrac{1}{jX_{L13}} \\[2em]
-\dfrac{1}{jX_{L12}} & \dfrac{1}{jX_{s2}} + \dfrac{1}{jX_{L12}} + \\ \dfrac{1}{jX_{L23}} + jY_{c1} & -\dfrac{1}{jX_{L23}} \\[2em]
-\dfrac{1}{jX_{L13}} & -\dfrac{1}{jX_{L23}} & \dfrac{1}{jX_{s3}} + \dfrac{1}{jX_{L13}} + \\ \dfrac{1}{jX_{L23}} + jY_{c3}
\end{bmatrix}
\begin{bmatrix} V_1 \measuredangle \theta_1 \\ V_2 \measuredangle \theta_2 \\ V_3 \measuredangle \theta_3 \end{bmatrix}
=
\begin{bmatrix}
\dfrac{V_{s1}\measuredangle \theta_{s1}}{jX_{s1}} + I_{c1}\measuredangle \theta_{c1} \\[1.2em]
\dfrac{V_{s2}\measuredangle \theta_{s2}}{jX_{s2}} + I_{c2}\measuredangle \theta_{c2} \\[1.2em]
\dfrac{V_{s3}\measuredangle \theta_{s3}}{jX_{s3}} + I_{c3}\measuredangle \theta_{c3}
\end{bmatrix}
\tag{4.5}
$$

The New York Power Authority (NYPA) operates much of the New York State EHV transmission system. It is divided into 5 major interfaces with low cost hydro generation located in the northern and western parts of the NY State whereas major loads and high cost generation are placed in the south, in and around New York City. The Total East and particularly Central East interface, made of seven transmission lines ranging in voltage from 115 kV to 345 kV [89]. The NYPA power system parameters are tabulated in Table 4-1. [90]-[91] is also used to find dc cable resistance value for each dc transmission line.

(4.6) can also be expressed by substituting NYPA power system parameters into (4.5).

$$
\begin{bmatrix}
-207.84j & 56.18j & 23.75j \\
56.18j & -171.81j & 16.42j \\
23.75j & 16.42j & -93.65j
\end{bmatrix}
\begin{bmatrix} V_1 \measuredangle \theta_1 \\ V_2 \measuredangle \theta_2 \\ V_3 \measuredangle \theta_3 \end{bmatrix}
=
\begin{bmatrix}
\dfrac{V_{s1}\measuredangle \theta_{s1}}{jX_{s1}} + I_{c1}\measuredangle \theta_{c1} \\[1.2em]
\dfrac{V_{s2}\measuredangle \theta_{s2}}{jX_{s2}} + I_{c2}\measuredangle \theta_{c2} \\[1.2em]
\dfrac{V_{s3}\measuredangle \theta_{s3}}{jX_{s3}} + I_{c3}\measuredangle \theta_{c3}
\end{bmatrix}
\tag{4.6}
$$

(4.6) is solved, and the solution for three AC bus voltages can be written as (4.7)~(4.9).

$$V_1 \measuredangle \theta_1 = \begin{bmatrix} 0.0055j \times (\dfrac{V_{s1}\measuredangle \theta_{s1}}{jX_{s1}} + I_{c1}\measuredangle \theta_{c1}) + \\[4mm] 0.002j \times (\dfrac{V_{s2}\measuredangle \theta_{s2}}{jX_{s2}} + I_{c2}\measuredangle \theta_{c2}) + \\[4mm] 0.0018j \times (\dfrac{V_{s3}\measuredangle \theta_{s3}}{jX_{s3}} + I_{c3}\measuredangle \theta_{c3}) \end{bmatrix} \tag{4.7}$$

$$V_2 \measuredangle \theta_2 = \begin{bmatrix} 0.002j \times (\dfrac{V_{s1}\measuredangle \theta_{s1}}{jX_{s1}} + I_{c1}\measuredangle \theta_{c1}) + \\[4mm] 0.0066j \times (\dfrac{V_{s2}\measuredangle \theta_{s2}}{jX_{s2}} + I_{c2}\measuredangle \theta_{c2}) + \\[4mm] 0.0017j \times (\dfrac{V_{s3}\measuredangle \theta_{s3}}{jX_{s3}} + I_{c3}\measuredangle \theta_{c3}) \end{bmatrix} \tag{4.8}$$

$$V_3 \measuredangle \theta_3 = \begin{bmatrix} 0.0018j \times (\dfrac{V_{s1}\measuredangle \theta_{s1}}{jX_{s1}} + I_{c1}\measuredangle \theta_{c1}) + \\[4mm] 0.0017j \times (\dfrac{V_{s2}\measuredangle \theta_{s2}}{jX_{s2}} + I_{c2}\measuredangle \theta_{c2}) + \\[4mm] 0.0114j \times (\dfrac{V_{s3}\measuredangle \theta_{s3}}{jX_{s3}} + I_{c3}\measuredangle \theta_{c3}) \end{bmatrix} \tag{4.9}$$

With the three phase AC bus voltages, active and reactive power flow of DC grid converters can be easily represented by (4.10)~(4.15).

$$P_1 = \mathrm{Re}\,al\left\{\overrightarrow{V_1}\overrightarrow{I_{c1}}^*\right\} = \begin{bmatrix} 0.0055 \times (\dfrac{V_{s1}I_{c1}}{X_{s1}}\cos(\theta_{s1}-\theta_{c1})) + \\[4mm] 0.002 \times (\dfrac{V_{s2}I_{c1}}{X_{s2}}\cos(\theta_{s2}-\theta_{c1}) - I_{c2}I_{c1}\sin(\theta_{c2}-\theta_{c1})) + \\[4mm] 0.0018 \times (\dfrac{V_{s3}I_{c1}}{X_{s3}}\cos(\theta_{s3}-\theta_{c1}) - I_{c3}I_{c1}\sin(\theta_{c3}-\theta_{c1})) \end{bmatrix} \tag{4.10}$$

93

$$Q_1 = \operatorname{Im} ag\left\{\overrightarrow{V_1}\overrightarrow{I_{c1}}^*\right\} = \begin{bmatrix} 0.0055 \times (\dfrac{V_{s1}I_{c1}}{X_{s1}}\sin(\theta_{s1}-\theta_{c1})+I_{c1}{}^2)+ \\[3mm] 0.002 \times (\dfrac{V_{s2}I_{c1}}{X_{s2}}\sin(\theta_{s2}-\theta_{c1})+I_{c2}I_{c1}\cos(\theta_{c2}-\theta_{c1}))+ \\[3mm] 0.0018 \times (\dfrac{V_{s3}I_{c1}}{X_{s3}}\sin(\theta_{s3}-\theta_{c1})+I_{c3}I_{c1}\cos(\theta_{c3}-\theta_{c1})) \end{bmatrix} \qquad (4.11)$$

$$P_2 = \operatorname{Re} al\left\{\overrightarrow{V_2}\overrightarrow{I_{c2}}^*\right\} = \begin{bmatrix} 0.002 \times (\dfrac{V_{s1}I_{c2}}{X_{s1}}\cos(\theta_{s1}-\theta_{c2})-I_{c1}I_{c2}\sin(\theta_{c1}-\theta_{c2}))+ \\[3mm] 0.0066 \times (\dfrac{V_{s2}I_{c2}}{X_{s2}}\cos(\theta_{s2}-\theta_{c2}))+ \\[3mm] 0.0017 \times (\dfrac{V_{s3}I_{c2}}{X_{s3}}\cos(\theta_{s3}-\theta_{c2})-I_{c3}I_{c2}\sin(\theta_{c3}-\theta_{c2})) \end{bmatrix} \qquad (4.12)$$

$$Q_2 = \operatorname{Im} ag\left\{\overrightarrow{V_2}\overrightarrow{I_{c2}}^*\right\} = \begin{bmatrix} 0.002 \times (\dfrac{V_{s1}I_{c2}}{X_{s1}}\sin(\theta_{s1}-\theta_{c2})+I_{c1}I_{c2}\cos(\theta_{c1}-\theta_{c2}))+ \\[3mm] 0.0066 \times (\dfrac{V_{s2}I_{c2}}{X_{s2}}\sin(\theta_{s2}-\theta_{c2})+I_{c2}{}^2)+ \\[3mm] 0.0017 \times (\dfrac{V_{s3}I_{c2}}{X_{s3}}\sin(\theta_{s3}-\theta_{c2})+I_{c3}I_{c2}\cos(\theta_{c3}-\theta_{c2})) \end{bmatrix} \qquad (4.13)$$

$$P_3 = \operatorname{Re} al\left\{\overrightarrow{V_3}\overrightarrow{I_{c3}}^*\right\} = \begin{bmatrix} 0.0018 \times (\dfrac{V_{s1}I_{c3}}{X_{s1}}\cos(\theta_{s1}-\theta_{c3})-I_{c1}I_{c3}\sin(\theta_{c1}-\theta_{c3}))+ \\[3mm] 0.0017 \times (\dfrac{V_{s2}I_{c3}}{X_{s2}}\cos(\theta_{s2}-\theta_{c3})-I_{c2}I_{c3}\sin(\theta_{c2}-\theta_{c3}))+ \\[3mm] 0.0114 \times (\dfrac{V_{s3}I_{c3}}{X_{s3}}\cos(\theta_{s3}-\theta_{c3})) \end{bmatrix} \qquad (4.14)$$

$$Q_3 = \operatorname{Im} ag\left\{\overrightarrow{V_3}\overrightarrow{I_{c3}}^*\right\} = \begin{bmatrix} 0.0018 \times (\dfrac{V_{s1}I_{c3}}{X_{s1}}\sin(\theta_{s1}-\theta_{c3})+I_{c1}I_{c3}\cos(\theta_{c1}-\theta_{c3}))+ \\[3mm] 0.0017 \times (\dfrac{V_{s2}I_{c3}}{X_{s2}}\sin(\theta_{s2}-\theta_{c3})+I_{c2}I_{c3}\cos(\theta_{c2}-\theta_{c3}))+ \\[3mm] 0.0114 \times (\dfrac{V_{s3}I_{c3}}{X_{s3}}\sin(\theta_{s3}-\theta_{c3})+I_{c3}{}^2) \end{bmatrix} \qquad (4.15)$$

Based on the operating points of DC grid converters, (4.10)~ (4.15) are solved to calculate the magnitude and the angle of current sources $(I_{c1}<\theta_{c1})$, $(I_{c2}<\theta_{c2})$, and $(I_{c3}<\theta_{c3})$ at each iteration step. As a result, active and reactive power of different transmission lines can be obtained accordingly. For instance, the reference value of active and reactive power flow for each converter of DC grid is varied between -1 pu to 1 pu in steps of 0.01 pu. At each step, six nonlinear equations ((4.10)~(4.15)) are solved to find six variables namely $(I_{c1},\theta_{c1},I_{c2},\theta_{c2},I_{c3},\theta_{c3})$, and power flow at different points of meshed AC power system can be calculated based on the computed variables. Therefore, the relationship of AC power flow with respect to operating points of multi-terminal DC grid can be easily obtained. From table IV, it can be noted that DC cable resistances for three DC transmission lines designed for NYPA power system are negligible, and total power losses in each dc transmission line is less than 0.0004%. So, total power losses in multi-terminal DC grid can be ignored, and the constraint $P_{con1}+P_{con2}+P_{con3}=0$ is accurate enough in order to maintain the power balance in the DC side.

4.5 Model Accuracy and Control Performance Investigations

4.5.1 PSCAD Simulation

The dynamic performance of multi-terminal DC grid in meshed AC power system is also investigated. PSCAD/EMTDC based simulation results are presented to verify droop control method with dead-band controller and algebraic model. Dynamics of active power flow in DC grid converters is displayed in Figure 4-10. The reference value of active power flow for

converter 1 and 2 is increased from zero to 0.5 pu at t=0.4s, and it is varied from 0 to -0.5 pu at t=1.4s. The reference value of converter 3 active power flow also changes from 0 to -1 pu at t=0.4s, and it is changed from zero to 1 pu at t=1.4s. Figure 4-11 also shows active power flow in three AC grid buses. As can be observed, AC grid power flow changes with respect to DC grid converter operating points.

Terminal DC bus voltages for all three terminals are shown in Figure 4-12. For start-up, all gating signals are initially off from t=0s to t=0.1s. The dead-band region in DC voltage controller is between 0.95 pu-1.1 pu. So, DC voltage controller is off when DC bus voltage is within the limit. Once DC bus voltage hits the lower or upper limit, DC voltage controller is enabled. Three phase AC current for three AC buses is shown in Figure 4-13. Figure 4-14 also depicts DC grid line current and DC grid terminal current. As can be observed from Figure 4-14, DC current variation in three terminals is directly proportional to the reference active power flow of DC grid converters.
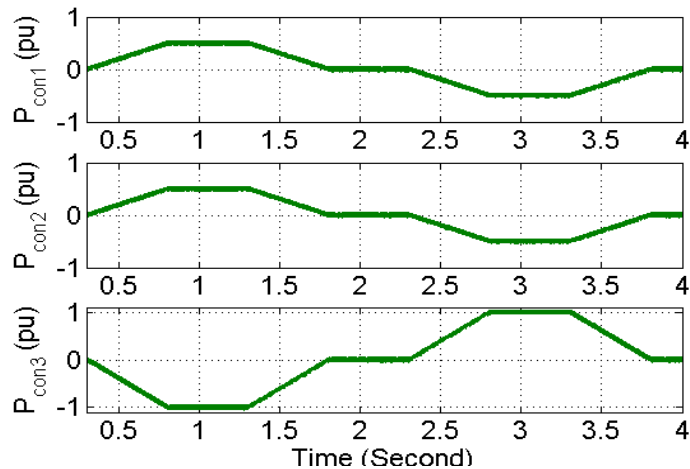
Figure 4-10. Dynamics of active power flow in three converters of DC grid- PSCAD result.
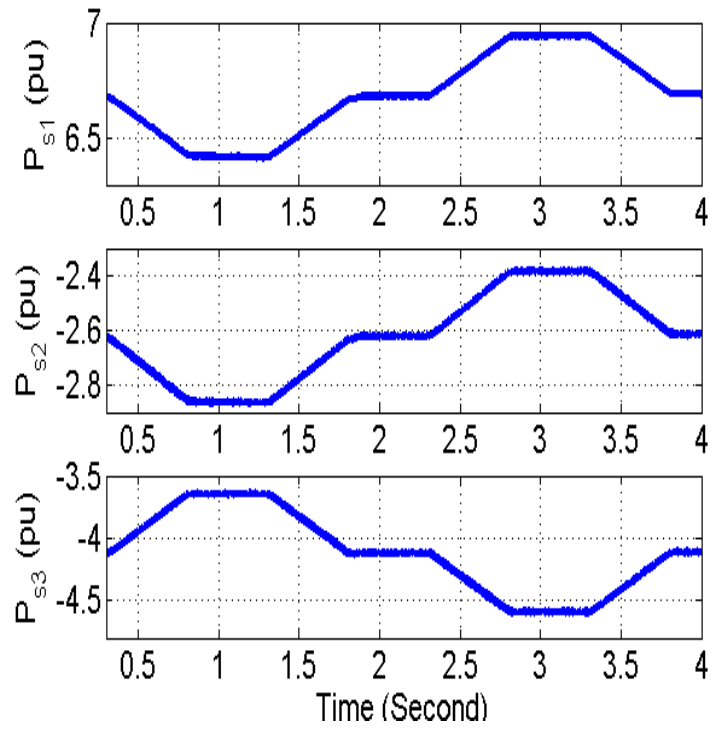
Figure 4-11. Dynamics of active power flow in three AC grid nodes- PSCAD result.
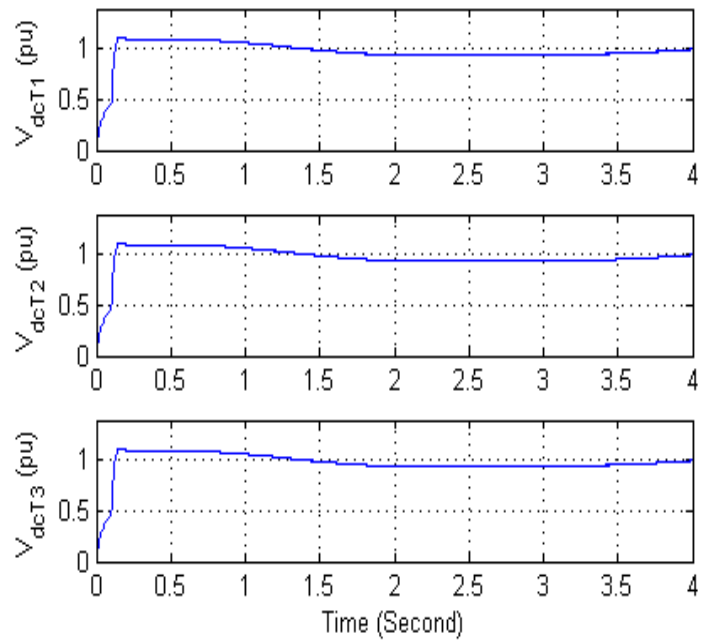
Figure 4-12. Terminal DC bus voltages- PSCAD result.
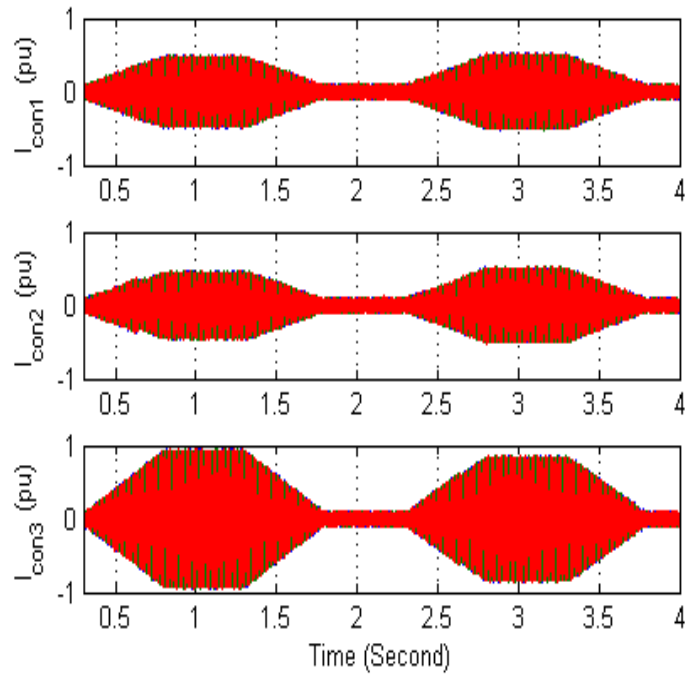
Figure 4-13. Three-phase AC current at three AC grid nodes- PSCAD result.
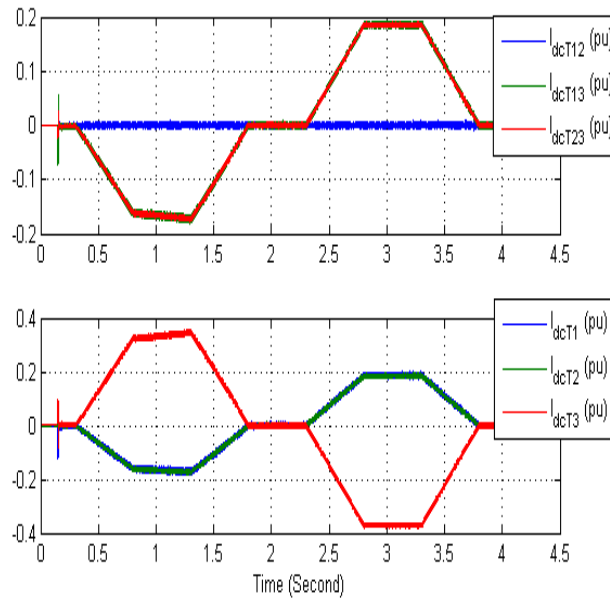
Figure 4-14. DC grid line current and terminal current- PSCAD result.

4.5.2 RTDS Simulation

This section presents and evaluates the dynamic performance of embedded multi-terminal DC grid in meshed AC power system through RTDS simulation. The proposed controller has been implemented in RTDS and compiled on GPC processor cards with controller sampling time of 50 μs and the system parameters are same as the parameters used in PSCAD simulation.

The dynamic performance of active power flow in DC grid converters is displayed in Figure 4-15. The reference value of active power flow for converter 1 and 2 is increased from zero to 0.5 pu at t=26s, and it is varied from 0 to -0.5 pu at t=36s. The reference value of converter 3 active power flow also changes from 0 to -1 pu at t=26s, and it is changed from zero to 1 pu at t=26s. Figure 4-16 also shows active power flow in three AC grid buses. As can be observed, AC grid power flow changes with respect to DC grid converter operating points.

Terminal DC bus voltages are shown in Figure 4-17. The dead-band region in DC voltage controller is between 0.95 pu-1.1 pu. So, DC voltage controller is off when DC bus voltage is within the limit. Once DC bus voltage hits the lower or upper limit, DC voltage controller is enabled. Three phase AC current for three DC grid converters is shown in Figure 4-18.
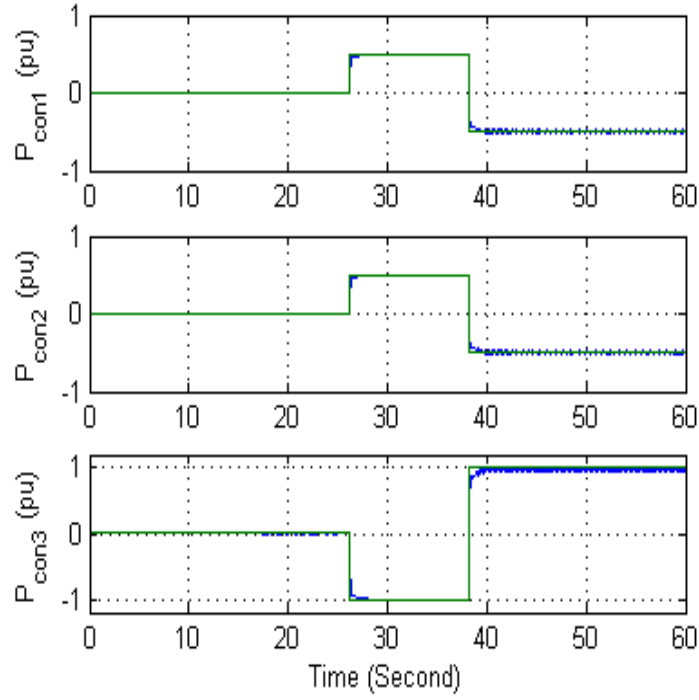
Figure 4-15. Dynamics of active power flow in three converters of DC grid- RTDS result.
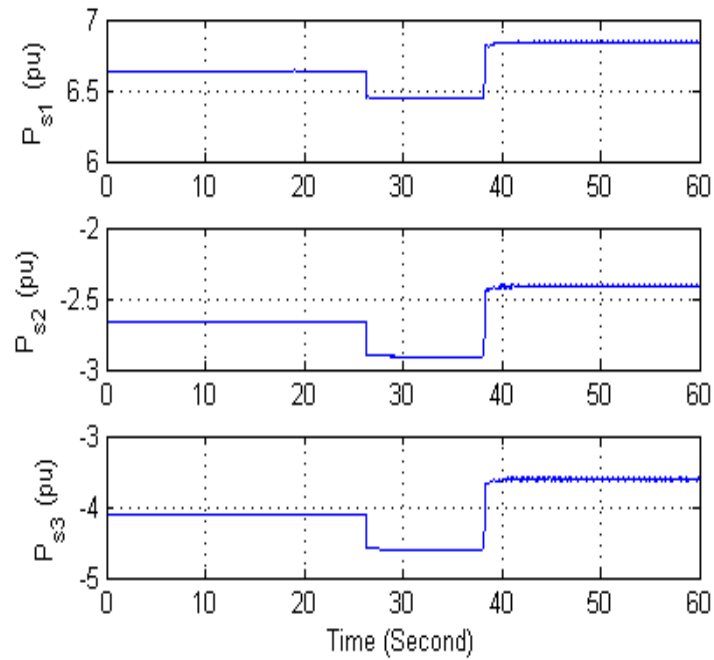
Figure 4-16. Dynamics of active power flow in three AC grid nodes- RTDS result.
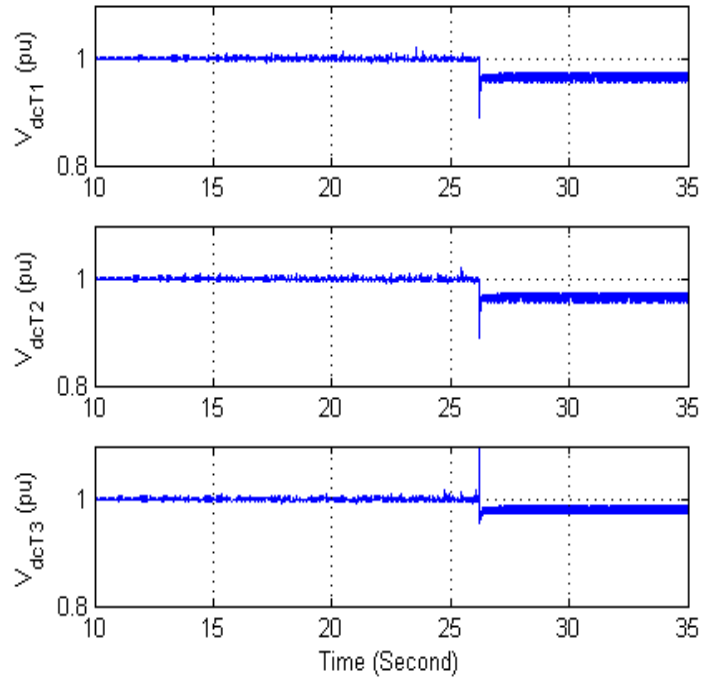
Figure 4-17. Terminal DC bus voltages- RTDS result.
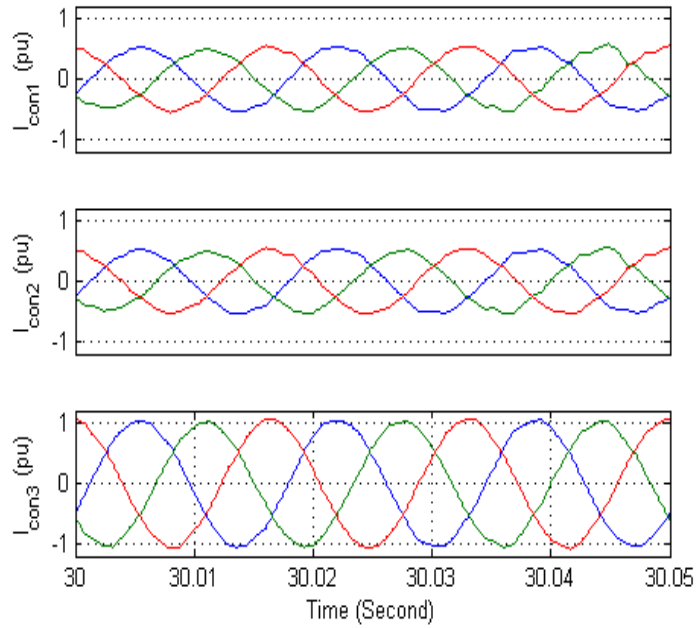
Figure 4-18. Terminal three-phase AC current - RTDS result.

4.5.3 Discussion

In order to validate the proposed algebraic model, the obtained PSCAD and RTDS simulation results are compared with the algebraic model results for different operating points of DC grid. Table 4-2 shows AC nodes active power flow with respect to three operating points of DC grid. As can be seen, $P_{s1}=6.45$ *(pu)* based on algebraic model result when *(P_{con1}, P_{con2}, P_{con3}) = (0.5, 0.5, -1)*, whereas $P_{s1}=6.42$ *(pu)* based on PSCAD simulation result, and it is equal to *6.44 (pu)* based on RTDS simulation results. Algebraic model results are also obtained for two other operating points (*(0, 0, 0), (-0.5, -0.5, 1)*). Table 4-3 also shows AC grid transmission lines active power flow with respect to DC grid operating points based on algebraic model and simulation results. As can be seen, algebraic model results are closely matched with the obtained simulation results.

Table 4-2.   AC nodes active power flow with respect to DC grid operating points

Active Power / Operating point	P_{s1} *(pu)*			P_{s2} *(pu)*			P_{s3} *(pu)*		
	Algebraic model	PSCAD	RTDS	Algebraic model	PSCAD	RTDS	Algebraic model	PSCAD	RTDS
(0.5,0.5,-1)	6.45	6.42	6.44	-2.8647	-2.87	-2.91	-3.58	-3.64	-3.6
(0,0,0)	6.71	6.66	6.64	-2.6	-2.63	-2.66	-4.11	-4.12	-4.1
(-0.5,-0.5,1)	6.98	6.94	6.84	-2.34	-2.39	-2.41	-4.64	-4.6	-4.6

Table 4-3. AC transmission lines active power flow with respect to DC grid operating points

Active Power / Operating point	P_{L12} (pu)			P_{L23} (pu)			P_{L31} (pu)		
	Algebraic model	PSCAD	RTDS	Algebraic model	PSCAD	RTDS	Algebraic model	PSCAD	RTDS
(0.5,0.5,-1)	3.61	3.63	3.6	1.25	1.29	1.27	3.34	3.34	3.37
(0,0,0)	3.65	3.68	3.66	1.05	1.07	1.05	3.07	3.06	3.05
(-0.5,-0.5,1)	3.69	3.72	3.72	0.85	0.85	0.83	2.8	2.76	2.77

Table 4-4 shows AC nodes reactive power flow with respect to DC grid operating points based on algebraic model and simulation results. As can be seen, $Q_{s1}=2.1$ *(pu)* based on algebraic model result when *(Q_{con1}, Q_{con2}, Q_{con3}) = (0.5, 0.5, -1)*, whereas $Q_{s1}=2.11$ *(pu)* based on the obtained PSCAD simulation result, and it is equal to *2.13 (pu)* based on RTDS simulation results. Table 4-5 also shows AC grid transmission lines reactive power flow with respect to DC grid operating points based on algebraic model and simulation results.

Table 4-4. AC nodes reactive power flow with respect to DC grid operating points

Reactive Power / Operating point	Q_{s1} (pu)			Q_{s2} (pu)			Q_{s3} (pu)		
	Algebraic model	PSCAD	RTDS	Algebraic model	PSCAD	RTDS	Algebraic model	PSCAD	RTDS
(0.5,0.5,-1)	2.1	2.1111	2.13	-1.3	-1.3333	-1.35	-1.35	-1.3778	-1.4
(0,0,0)	1.82	1.8333	1.85	-1.56	-1.5556	-1.58	-0.86	-0.8889	-0.9
(-0.5,-0.5,1)	1.56	1.5556	1.57	-1.78	-1.7778	-1.8	-0.4	-0.4	-0.43

Table 4-5.   AC transmission lines reactive power flow with respect to DC grid operating points

Reactive Power / Operating point	Q_{L12} (pu)			Q_{L23} (pu)			Q_{L31} (pu)		
	Algebraic model	PSCAD	RTDS	Algebraic model	PSCAD	RTDS	Algebraic model	PSCAD	RTDS
(0.5,0.5,-1)	1.4	1.4222	1.44	-0.2	-0.2333	-0.25	-0.51	-0.5222	-0.54
(0,0,0)	1.34	1.3667	1.38	0	-0.0222	-0.04	-0.8	-0.8333	-0.85
(-0.5,-0.5,1)	1.3	1.3111	1.33	0.2	0.1889	0.2	-1.15	-1.1444	-1.18

4.6 Summary

In this section, the performance of embedded multi-terminal DC grid in meshed AC power system was evaluated. An algebraic model for embedded multi-terminal DC network in meshed AC power system was proposed to analyze the steady state performance of multi-terminal DC grid converters. The proposed algebraic model can be used by transmission planners to define the required rating of multi-terminal dc grid. The control structure of embedded multi-terminal DC grid in meshed AC power system based on droop control structure with dead-band controller was proposed. The proposed algebraic model with the proposed controller was validated in a reduced order three-bus AC equivalent NYPA power system. PSCAD and RTDS simulation results were presented to verify the proposed algebraic model and the controller.

Chapter 5.   PERFORMANCE EVALUATION OF ACTIVE MOBILE SUBSTATIONS UNDER FAULT OPERATING CONDITIONS

5.1   Introduction

The AMS must be designed to operate satisfactorily under typical fault and unbalanced conditions. In this section, component design considerations in development of the AMS under unbalanced operating condition will be provided, and a new control strategy is proposed to control AMS under unbalanced operating conditions when component design is not sufficient to prevent overcurrent and trips. Dynamic performance of AMS under AC and DC fault operating conditions is explored. Component design is performed such that negative sequence current is minimized under typical AC fault conditions. A new control scheme is also proposed to control AMS under AC fault operating conditions [92]. The angle control structure is employed to control the converter under normal operating conditions, and the supervisory control will switch the control structure from angle control method to the proposed control method when component design cannot mitigate the negative sequence current component of the converter appropriately when AC fault happens.

The dynamic performance of high frequency isolated modular converter under DC fault operating condition is also explored. The control algorithm for DC fault operation and recovery after DC fault is proposed. The high frequency isolated modular converter with the

proposed control scheme can be protected against DC fault without using expensive DC circuit breakers.

The performance of multi-terminal DC grid under DC fault operating condition and loss of master terminal is also investigated.

5.2 Control Scheme of Modular Transformer Converter in d-q Reference Frame for AC Fault operating conditions

To develop the control structure for the MTC based AMS in d-q reference frame, modeling of the power electronics system is essential. The modeling used in this section is based on the principal circuit analysis writing voltage and current equations for storage elements known as state equations. The general schematic of a three phase voltage-sourced converter circuit is shown in Figure 5-1, and the state equations of each VSC in the dq synchronous reference frame under unbalanced operating conditions can be broken into two separate independent equations; one for the positive sequence and the other for the negative sequence.
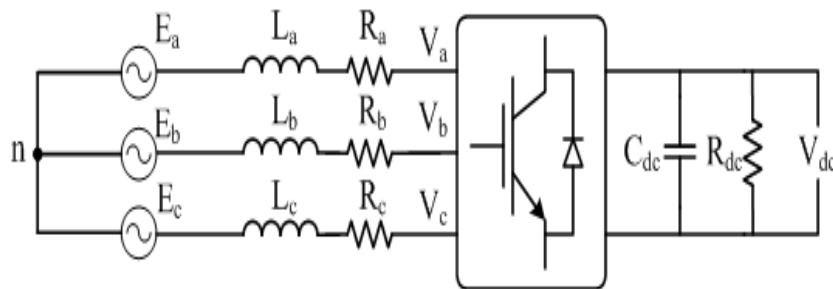
Figure 5-1. Structure of a voltage source converter.

Low-frequency network disturbances such as distortion, voltage dips, phase variation, and amplitude variation of the input voltage can be described by a sum of positive, negative and zero sequence components of the input voltage of fundamental frequency. Therefore, an unbalanced three-phase input voltage can be represented as (5.1).

$$E_{dqs} = e^{j\omega t}E_{dq}^p + e^{-j\omega t}E_{dq}^n = e^{j\omega t}(E_d^p + jE_q^p) + e^{-j\omega t}(E_d^n + jE_q^n) \tag{5.1}$$

The unbalanced three-phase input current is also expressed in the same manner as the input voltage. With the unbalanced input voltage and input current, the input complex power is obtained by (5.2).

$$S_{in} = \frac{3}{2}E_{dqs}I_{dqs}^* = \frac{3}{2}(e^{j\omega t}E_{dq}^p + e^{-j\omega t}E_{dq}^n)(e^{j\omega t}I_{dq}^p + e^{-j\omega t}I_{dq}^n)^* \tag{5.2}$$

Applying (5.1) to (5.2) and equating the terms of twice input frequency and the term of average for the real and imaginary part separately, the instantaneous active and reactive power are obtained as (5.3).

$$S_{in} = \left[P_o^{in} + P_{c2}^{in}\cos(2\omega t) + P_{s2}^{in}\sin(2\omega t) \right] + \\ \left[Q_o^{in} + Q_{c2}^{in}\cos(2\omega t) + Q_{s2}^{in}\sin(2\omega t) \right] \tag{5.3}$$

Where,

$$
\begin{aligned}
P_o^{in} &= 1.5(E_d^p I_d^p + E_q^p I_q^p + E_d^n I_d^n + E_q^n I_q^n) \\
P_{c2}^{in} &= 1.5(E_d^p I_d^n + E_q^p I_q^n + E_d^n I_d^p + E_q^n I_q^p) \\
P_{s2}^{in} &= 1.5(E_q^n I_d^p - E_d^n I_q^p - E_q^p I_d^n + E_d^p I_q^n) \\
Q_o^{in} &= 1.5(E_q^p I_d^p - E_d^p I_q^p + E_q^n I_d^n - E_d^n I_q^n) \\
Q_{c2}^{in} &= 1.5(E_q^p I_d^n - E_d^p I_q^n + E_q^n I_d^p - E_d^n I_q^p) \\
Q_{s2}^{in} &= 1.5(E_d^p I_d^n + E_q^p I_q^n - E_d^n I_d^p - E_q^n I_q^p)
\end{aligned}
\tag{5.4}
$$

Real instantaneous active power $P_{in}(t)$ is delivered to the dc link and determines the dc voltage level. Hence, if $P_{in}(t)$ varies with time for P_{c2} and P_{s2} not being equal to zero, then the dc-link voltage fluctuates. Therefore, in order to keep constant dc level, the coefficients of P_{c2} and P_{s2} have to be eliminated. The dc component Q_o of the instantaneous reactive power should also be nullified. Q_o represents the average reactive power exchanged with the network, and it should be nullified to achieve the unity power factor. Employing an additional condition on the average active power, four equations with four unknown current references are obtained, which can be expressed as (5.5).

$$\frac{2}{3}\begin{bmatrix} P_o^{in} \\ Q_o^{in} \\ P_{s2}^{in} \\ P_{c2}^{in} \end{bmatrix} = \begin{bmatrix} \frac{2}{3}P_o^{in} \\ 0 \\ 0 \\ 0 \end{bmatrix} = \begin{bmatrix} E_d^p & E_q^p & E_d^n & E_q^n \\ E_q^p & -E_d^p & E_q^n & -E_d^n \\ E_q^n & -E_d^n & -E_q^p & E_d^p \\ E_d^n & E_q^n & E_d^p & E_q^p \end{bmatrix}\begin{bmatrix} I_d^p \\ I_q^p \\ I_d^n \\ I_q^n \end{bmatrix}$$

(5.5)

The solution can be written by (5.6).

$$\begin{bmatrix} I_d^p(ref) \\ I_q^p(ref) \\ I_d^n(ref) \\ I_q^n(ref) \end{bmatrix} = \begin{bmatrix} E_d^p & E_q^p & E_d^n & E_q^n \\ E_q^p & -E_d^p & E_q^n & -E_d^n \\ E_q^n & -E_d^n & -E_q^p & E_d^p \\ E_d^n & E_q^n & E_d^p & E_q^p \end{bmatrix}^{-1}\begin{bmatrix} \frac{2}{3}P_o^{in} \\ 0 \\ 0 \\ 0 \end{bmatrix} =$$

$$\frac{2P_o^{in}}{3((E_d^p)^2 + (E_q^p)^2 - (E_d^n)^2 - (E_q^n)^2)}\begin{bmatrix} E_d^p \\ E_q^p \\ -E_d^n \\ -E_q^n \end{bmatrix}$$

(5.6)

So, the current references cannot be obtained when the determinant of *[E_dq]* is zero. The case of having a zero determinant of *[E_dq]* corresponds to the condition of extreme unbalanced input supply. Examples of this extreme unbalanced input supply include the

complete collapse of one or two input phases and the phase variations of more than 90°. Thus the control method of regulating the input currents to the references calculated from (5.6) cannot be applied to compensate for the extreme unbalanced input supply conditions [93]-[96].

In the control scheme, the positive sequence current in the positive synchronous reference frame is regulated by one controller, and the negative-sequence current is regulated in its own synchronous reference frame [97]. In the positive synchronous reference frame, positive sequence voltages are obtained by (5.7) and (5.8). Negative sequence voltages are expressed by (5.9) and (5.10) in the negative synchronous reference frame.

$$V_d^p = E_d^p - (PI)(I_d^{p*} - I_d^p) + \omega L I_q^p \tag{5.7}$$

$$V_q^p = E_q^p - (PI)(I_q^{p*} - I_q^p) - \omega L I_d^p \tag{5.8}$$

$$V_d^n = E_d^n - (PI)(I_d^{n*} - I_d^n) - \omega L I_q^n \tag{5.9}$$

$$V_q^n = E_q^n - (PI)(I_q^{n*} - I_q^n) + \omega L I_d^n \tag{5.10}$$

Finally, the output of the converter defined in the stationary reference frame as (5.11) will be controlled through proper modulation techniques.

$$V_s = e^{j\omega t}(V_d^p + jV_q^p) + e^{-j\omega t}(V_d^n + jV_q^n) \tag{5.11}$$

It can be observed that unbalanced input voltages result in the generation of even-order harmonics at dc bus voltage. A simplified control structure is shown in Figure 5-2.
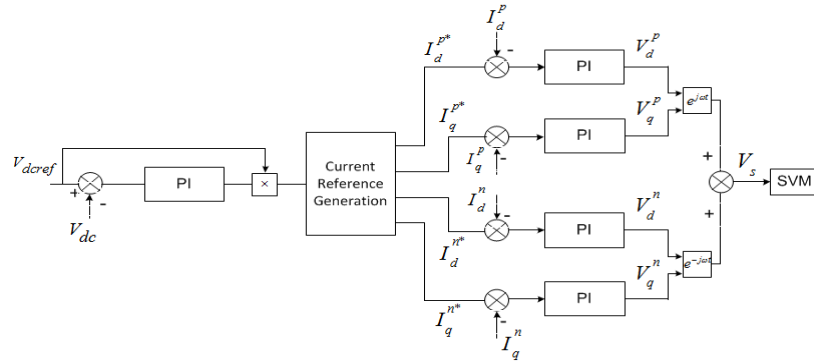
Figure 5-2. Control structure of the AMS for unbalanced operating condition (DC link voltage controller side).

The dynamic performance of the MTC based AMS system under unbalanced operating condition is presented in Figure 5-3. The unbalanced system is represented by 50% voltage drop in phase-A of the AMS (inverter and rectifier side). The reference value of active power is 9 (MW) when fault happens. As can be seen, dc bus voltage is also controlled at 9 (kV).
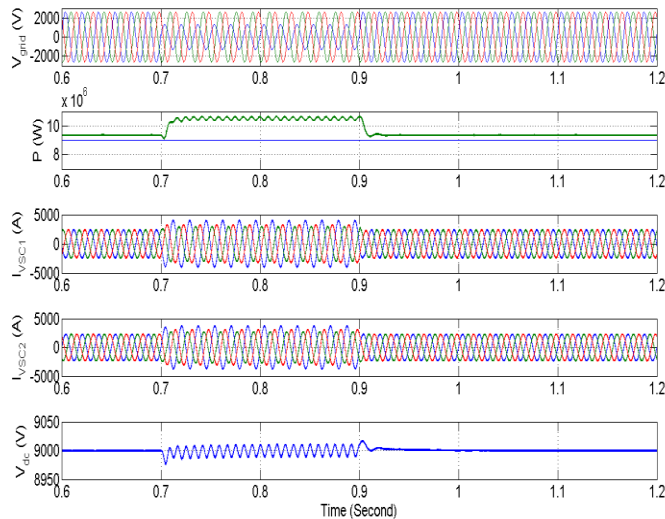
Figure 5-3. Dynamic performance of the AMS system under unbalanced operating condition (50% voltage sag in both the dc link voltage controller and power flow controller sides).

When AC fault happens, the reference power can also be reduced to very small value such as 50% of the rated power, and the negative sequence controller can be applied to reduce the active power fluctuation. The dynamic performance of the AMS system under single line to ground (SLG) fault in the rectifier side (dc voltage controller converter) is presented in Figure 5-4 when negative sequence current controller is on and the reference power is not varied during fault. Figure 5-5 presents the dynamic performance of the AMS system under SLG fault when negative sequence current controller is on and the reference power is also reduced to %50 of rated power during fault.

From the obtained results, it can be concluded that the proposed control method in [97] is effective in maintaining a robust DC link voltage under unbalanced operating condition, but the current waveform is not balanced since in this method, negative sequence current is injected to eliminate the oscillating components of the active power so that harmonics in the output dc voltage can be nullified under unbalanced operating conditions.

Figure 5-6, and Figure 5-7 show the dynamic performance of the AMS system under SLG fault when negative sequence current control is disabled. As can be observed from Figure 5-6, the reference value of active power does not change during fault. Figure 5-7 shows the dynamic performance of the AMS system under SLG fault when the reference value of active power is reduced to 50% of the full power. As can be seen from Figure 5-7, the effect of reducing active power is significantly important to mitigate the magnitude of ac current and dc voltage fluctuations during fault.
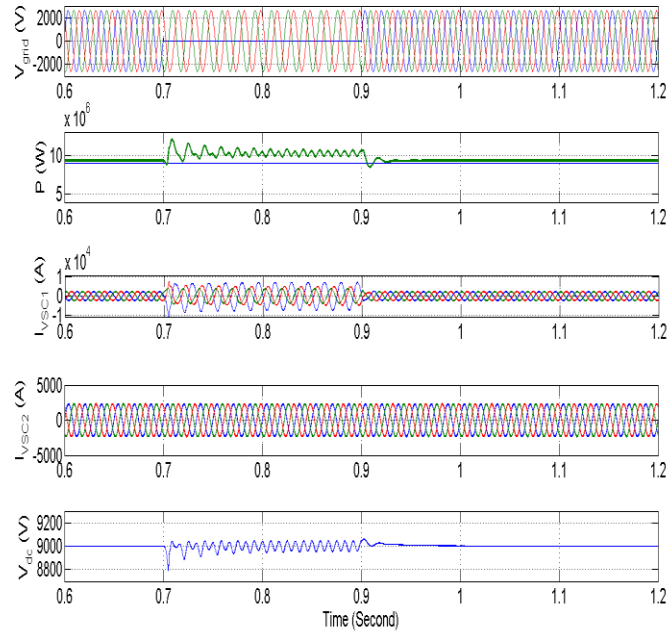
Figure 5-4. Dynamic performance of the AMS system under SLG fault in the dc link voltage controller side (Negative sequence current control is on and %100 power transfer during fault).
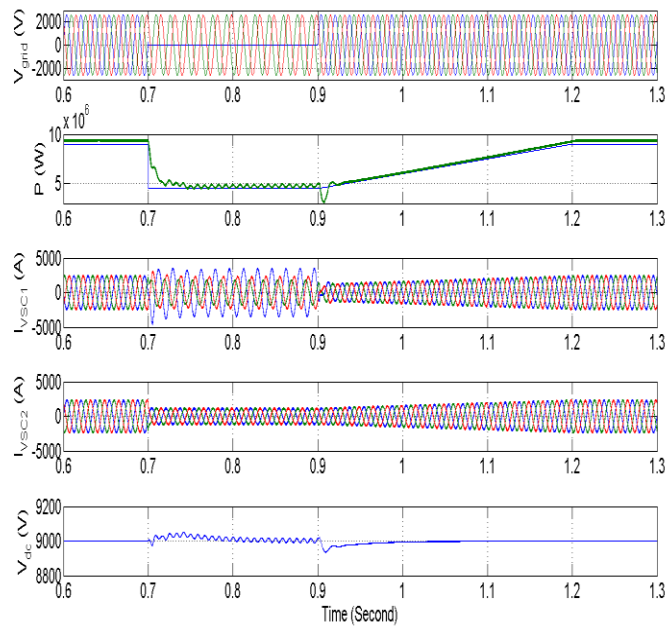
Figure 5-5. Dynamic performance of the AMS system under SLG fault in the dc link voltage controller side (Negative sequence current control is on and %50 power transfer during fault).
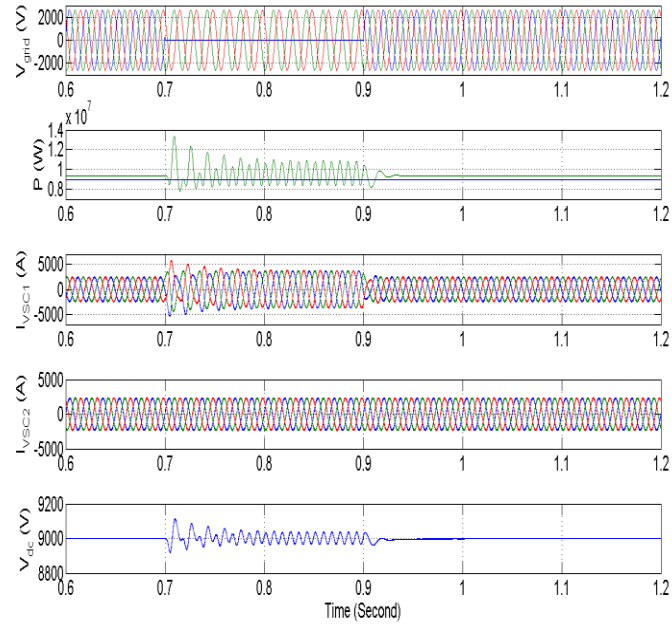
Figure 5-6. Dynamic performance of the AMS system under SLG fault in the dc link voltage controller side (Negative sequence current control is off and %100 power transfer during fault).
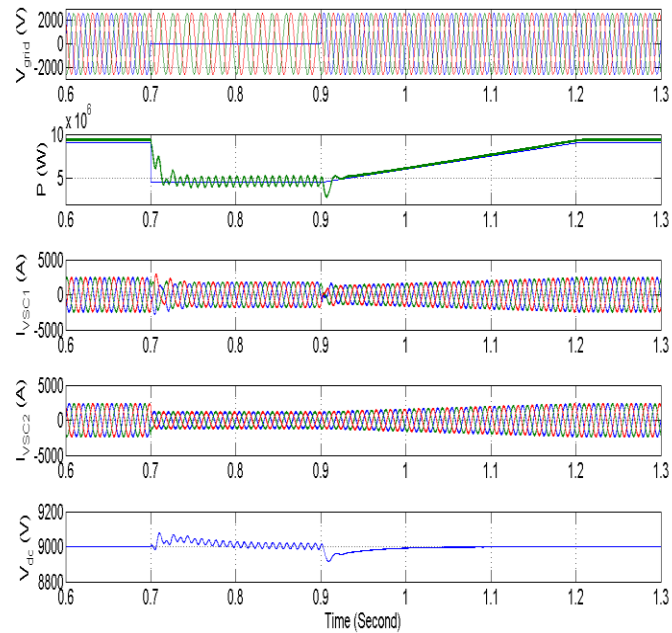
Figure 5-7. Dynamic performance of the AMS system under SLG fault in the dc link voltage controller side (Negative sequence current control is off and %50 power transfer during fault).

113

5.3 Proposed Component Design of Modular Transformer Converters for AC Fault Operating Conditions

The general schematic of a three phase AMS circuit is shown in Figure 5-8. The negative sequence harmonic currents of AMS can be obtained by inserting a harmonic voltage source in series with the input voltage source. If we ignore losses ($R=0$), the state space equations of angle-controlled AMS in the dq synchronous reference frame can be written as (5.12). α_1 and α_2 are considered as two input variables to control VSC1 and VSC2. (5.12) can be linearized around steady state equilibrium points as can be expressed by (5.13).

The linearized state space equations of angle-controlled AMS under unbalanced operating conditions and assume the steady state conditions ($\alpha_{10}=\alpha_{20}$) can be expressed as (5.14) where $V_1cos(2wt)$ and $V_1sin(2wt)$ represents the d and q components of the negative sequence voltage vector [48]. (5.14) is solved to calculate the d and q components of the input currents as can be seen in (5.15)~(5.18). (5.19) also presents an algebraic equation for dc bus voltage. The magnitude of negative sequence current is also expressed by (5.20) when $V_{1=}\ V_{2=}\ V_{-1}$, and the magnitude of second order harmonic components of dc bus voltage is also presented by (5.21).

Figure 5-9 shows negative sequence current component versus dc link capacitor value based on (5.20), and the second order harmonic component of dc bus voltage with respect to dc link capacitor is shown in Figure 5-10.
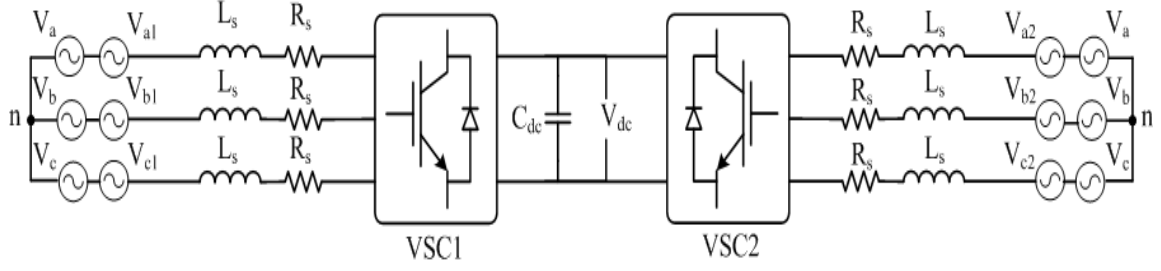
Figure 5-8. Structure of active mobile substation.

$$
p\begin{bmatrix} i_{d1} \\ i_{q1} \\ V_{dc} \\ i_{d2} \\ i_{q2} \end{bmatrix} = \begin{bmatrix} 0 & \omega & \frac{k\omega}{L}\cos(\alpha_1) & 0 & 0 \\ -\omega & 0 & \frac{k\omega}{L}\sin(\alpha_1) & 0 & 0 \\ -\frac{3}{2C}k\omega\cos(\alpha_1) & -\frac{3}{2C}k\omega\sin(\alpha_1) & 0 & -\frac{3}{2C}k\omega\cos(\alpha_2) & -\frac{3}{2C}k\omega\sin(\alpha_2) \\ 0 & 0 & \frac{k\omega}{L}\cos(\alpha_2) & 0 & \omega \\ 0 & 0 & \frac{k\omega}{L}\sin(\alpha_2) & -\omega & 0 \end{bmatrix}\begin{bmatrix} i_{d1} \\ i_{q1} \\ V_{dc} \\ i_{d2} \\ i_{q2} \end{bmatrix} - \frac{\omega}{L}\begin{bmatrix} V_{d1} \\ V_{q1} \\ 0 \\ V_{d2} \\ V_{q2} \end{bmatrix}
\tag{5.12}
$$

$$
Where: L = \frac{\omega L_s}{z_{base}}; C = \frac{C_{dc}}{\omega z_{base}}; z_{base} = \frac{V_{base}}{I_{base}}
$$

$$
p\begin{bmatrix} \Delta i_{d1} \\ \Delta i_{q1} \\ \Delta V_{dc} \\ \Delta i_{d2} \\ \Delta i_{q2} \end{bmatrix} = \begin{bmatrix} 0 & \omega & \frac{k\omega}{L}\cos(\alpha_{10}) & 0 & 0 \\ -\omega & 0 & \frac{k\omega}{L}\sin(\alpha_{10}) & 0 & 0 \\ -\frac{3}{2C}k\omega\cos(\alpha_{10}) & -\frac{3}{2C}k\omega\sin(\alpha_{10}) & 0 & -\frac{3}{2C}k\omega\cos(\alpha_{20}) & -\frac{3}{2C}k\omega\sin(\alpha_{20}) \\ 0 & 0 & \frac{k\omega}{L}\cos(\alpha_{20}) & 0 & \omega \\ 0 & 0 & \frac{k\omega}{L}\sin(\alpha_{20}) & -\omega & 0 \end{bmatrix}\begin{bmatrix} \Delta i_{d1} \\ \Delta i_{q1} \\ \Delta V_{dc} \\ \Delta i_{d2} \\ \Delta i_{q2} \end{bmatrix}
$$

$$
-\frac{\omega}{L}\begin{bmatrix} \Delta V_{d1} \\ \Delta V_{q1} \\ 0 \\ \Delta V_{d2} \\ \Delta V_{q2} \end{bmatrix} + [B_\alpha]\begin{bmatrix} \Delta\alpha_1 \\ \Delta\alpha_2 \end{bmatrix}
\tag{5.13}
$$

$$p\begin{bmatrix} i_{d1} \\ i_{q1} \\ V_{dc} \\ i_{d2} \\ i_{q2} \end{bmatrix} = \begin{bmatrix} 0 & \omega & \dfrac{k\omega}{L} & 0 & 0 \\ -\omega & 0 & 0 & 0 & 0 \\ -\dfrac{3}{2C}k\omega & 0 & 0 & -\dfrac{3}{2C}k\omega & 0 \\ 0 & 0 & \dfrac{k\omega}{L} & 0 & \omega \\ 0 & 0 & 0 & -\omega & 0 \end{bmatrix} \begin{bmatrix} i_{d1} \\ i_{q1} \\ V_{dc} \\ i_{d2} \\ i_{q2} \end{bmatrix} - \frac{\omega}{L} \begin{bmatrix} V+V_1\cos(2\omega t) \\ -V_1\sin(2\omega t) \\ 0 \\ V+V_2\cos(2\omega t) \\ -V_2\sin(2\omega t) \end{bmatrix}$$
(5.14)

$$i_{d1}(t) = \frac{(V_1-V_2)}{2L}\sin(\omega t) - \frac{(2LV_1C - V_1k^2 + V_2k^2)}{2L(LC-k^2)}\sin(2\omega t) +$$
$$\frac{\sqrt{C}(LV_1C - 2LVC + LV_2C + 2Vk^2 + V_1k^2 + V_2k^2)}{2\sqrt{L}(LC-k^2)\sqrt{(3k^2+LC)}}\sin(\frac{\sqrt{(3k^2+LC)}}{\sqrt{LC}}\omega t)$$
(5.15)

$$i_{q1}(t) = \frac{(4LVC + 3V_1k^2 + 3V_2k^2)}{4L(LC+3k^2)} + \frac{(V_1-V_2)}{2L}\cos(\omega t) - \frac{(4LV_1C - 3V_1k^2 + V_2k^2)}{4L(LC-k^2)}\cos(2\omega t) +$$
$$\frac{(LV_1C - 2LVC + LV_2C + 2Vk^2 + V_1k^2 + V_2k^2)}{2\sqrt{L}(LC-k^2)\sqrt{(3k^2+LC)}}\cos(\frac{\sqrt{(3k^2+LC)}}{\sqrt{LC}}\omega t)$$
(5.16)

$$V_{dc}(t) = \frac{(12Vk - 3V_1k - 3V_2k)}{(4LC+12k^2)} - \frac{(3V_1k + 3V_2k)}{4(LC-k^2)}\cos(2\omega t) +$$
$$\frac{3(LV_1C - 2LVC + LV_2C + 2Vk^2 + V_1k^2 + V_2k^2)}{(LC-k^2)(6k^2+2LC)}\cos(\frac{\sqrt{(3k^2+LC)}}{\sqrt{LC}}\omega t)$$
(5.17)

$$i_{d2}(t) = \frac{(V_2-V_1)}{2L}\sin(\omega t) - \frac{(2LV_2C - V_2k^2 + V_1k^2)}{2L(LC-k^2)}\sin(2\omega t) +$$
$$\frac{\sqrt{C}(LV_1C - 2LVC + LV_2C + 2Vk^2 + V_1k^2 + V_2k^2)}{2\sqrt{L}(LC-k^2)\sqrt{(3k^2+L\sqrt{L})}}\sin(\frac{\sqrt{(3k^2+LC)}}{\sqrt{LC}}\omega t)$$
(5.18)

$$i_{q2}(t) = \frac{(4LVC + 3V_1k^2 + 3V_2k^2)}{4L(LC+3k^2)} + \frac{(V_2-V_1)}{2L}\cos(\omega t) - \frac{(4LV_2C - 3V_2k^2 + V_1k^2)}{4L(LC-k^2)}\cos(2\omega t) +$$
$$\frac{(LV_1C - 2LVC + LV_2C + 2Vk^2 + V_1k^2 + V_2k^2)}{2\sqrt{L}(LC-k^2)\sqrt{(3k^2+LC)}}\cos(\frac{\sqrt{(3k^2+LC)}}{\sqrt{LC}}\omega t)$$
(5.19)

$$|i_{-1}| = \sqrt{(\frac{V_{-1}C}{LC-k^2})^2 + (\frac{V_{-1}C}{LC-k^2})^2(1-\frac{k^2}{2CL})^2} = (\frac{V_{-1}C}{LC-k^2})\sqrt{1+(1-\frac{k^2}{2CL})^2} \quad \text{(5.20)}$$

$$|V_{dch2}| = \frac{3V_{-1}k}{2(LC-k^2)} \quad \text{(5.21)}$$
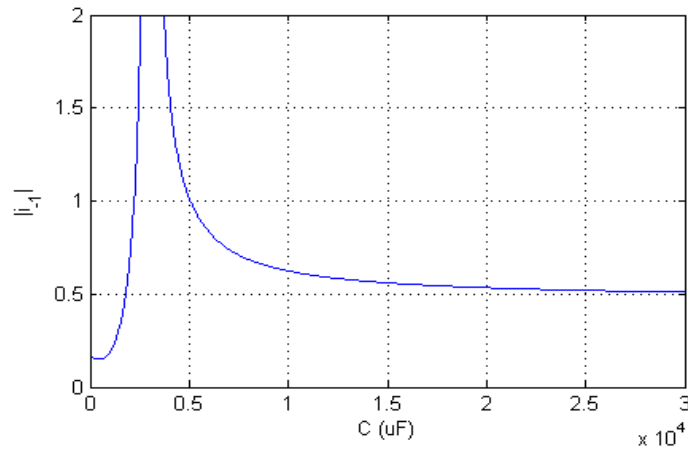
Figure 5-9. The AMS negative sequence current component versus DC link capacitor (theoretical result).
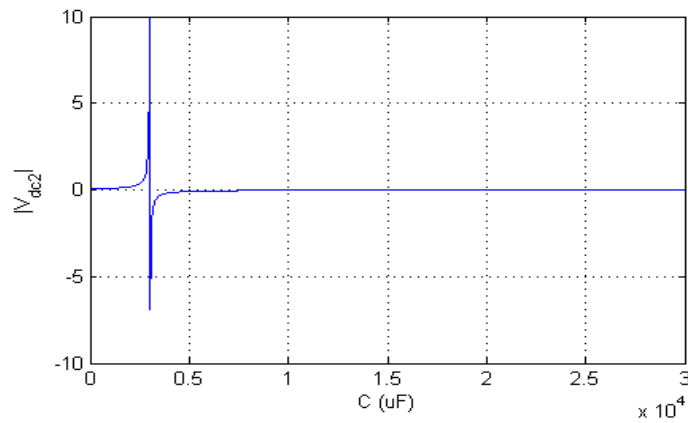
Figure 5-10. The AMS second order harmonic component of dc bus voltage versus DC link capacitor (theoretical result).

117

The AMS must be designed to operate satisfactorily under typical fault and unbalanced conditions. The control structure of the AMS is based on positive sequence synchronous reference frame. Therefore, under unbalanced conditions due to presence of negative sequence voltage, an undesired current can flow into the system. This current can be high enough to shut down the whole AMS in order to avoid saturation of the interfacing transformers and over-heating of the switches. It is worth mentioning that producing direct positive and negative sequence voltages seen in PWM or vector-controlled converters is not possible in angle-controlled converters. Therefore, we designed the system and the capacitor such that (100)120 Hz oscillations in the DC link can be tolerated under typical unbalanced conditions. The 120 Hz oscillations in the DC link can produce appropriate negative sequence voltage in control and modulation structures and consequently minimize the negative sequence current. The dynamic performance of the AMS system with 1mF and 0.1mF DC link capacitors under an unbalanced condition is simulated in PSCAD, and the results are presented in Figure 5-11 and Figure 5-12. The unbalanced system is represented by 50% voltage drop in phase-A of the inverter and rectifier side. As can be observed, the negative sequence current with higher amount of capacitance is higher. With higher active and reactive power demand, the generated negative sequence can be much higher as expected. Under the same condition, the negative sequence current flowing through the system versus the DC link capacitor value is also measured and the result is shown in Figure 5-13. As can be seen, the negative sequence current is highly dependent on the DC capacitor value. Starting from very low values of capacitance, this current can be very low. It increases as the capacitor value increases until the system can be completely unstable due to

the fact that the second harmonic of the line frequency is equal to the AMS resonant-pole frequency. Moving away from the resonant frequency brings the converter into the stable operation region. However, a huge capacitor is needed to achieve the desirable performance. Therefore, practical designs will be on the left side of the resonant frequency which is desirable.
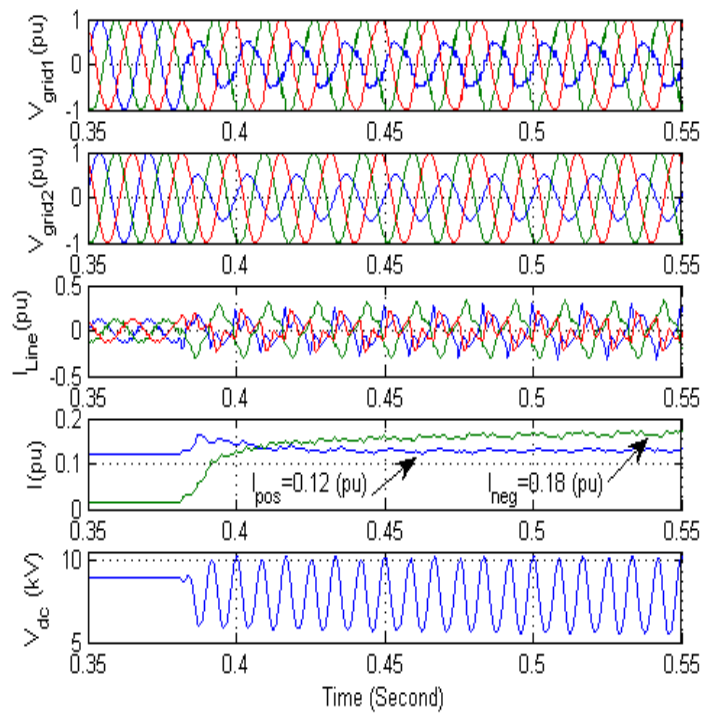
Figure 5-11. Dynamic performance of angle-controlled AMS under unbalanced condition of 50% single-line voltage sag (C=1 mF).
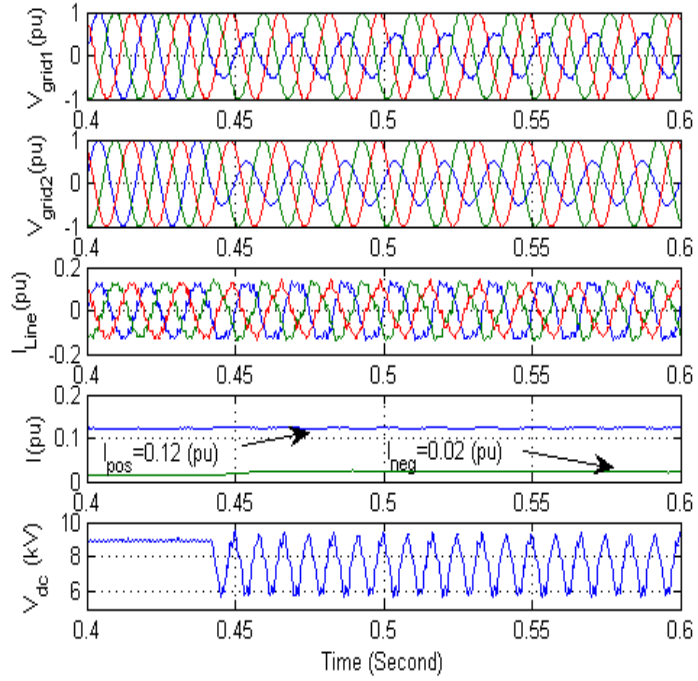
Figure 5-12. Dynamic performance of angle-controlled AMS system under unbalanced condition of 50% single-line voltage sag (C=0.1 mF).
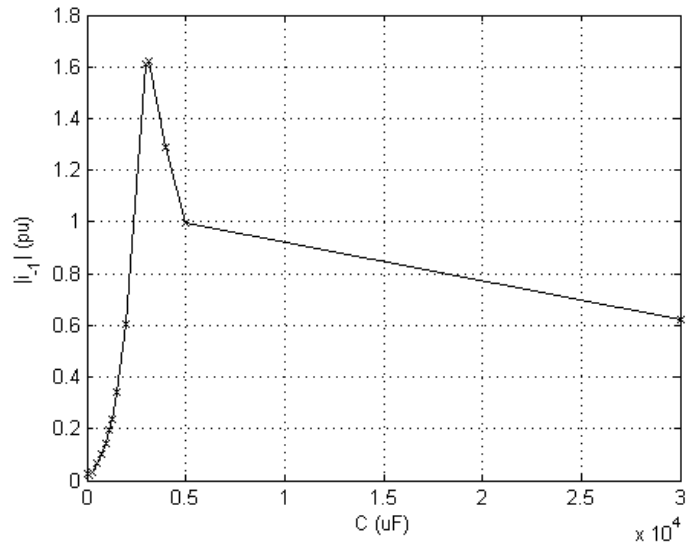
Figure 5-13. The AMS negative sequence current component versus DC link capacitor (simulation result).

5.4 Instantaneous Active Power Flow Control of Modular Transformer Converter Based AMS for AC Fault Operating Conditions

It was shown that component design criterion has some limitations on dynamic performance of the AMS under AC fault operating conditions. This section proposes a supplementary control scheme suitable for high power mobile converters that improves the dynamic performance of the system under AC fault operating conditions. The method is explained in the following.

Three-phase unbalanced input voltages and currents can be expressed as a sum of positive and negative sequence components.

$$v_a = V_{pk}^p \cos(\omega t + \theta_v^p) + V_{pk}^n \cos(\omega t + \theta_v^n) \qquad\qquad i_a = I_{pk}^p \cos(\omega t + \theta_i^p) + I_{pk}^n \cos(\omega t + \theta_i^n)$$

$$v_b = V_{pk}^p \cos(\omega t + \theta_v^p - \frac{2\pi}{3}) + V_{pk}^n \cos(\omega t + \theta_v^n + \frac{2\pi}{3}) \qquad i_b = I_{pk}^p \cos(\omega t + \theta_i^p - \frac{2\pi}{3}) + I_{pk}^n \cos(\omega t + \theta_i^n + \frac{2\pi}{3}) \qquad (5.22)$$

$$v_c = V_{pk}^p \cos(\omega t + \theta_v^p + \frac{2\pi}{3}) + V_{pk}^n \cos(\omega t + \theta_v^n - \frac{2\pi}{3}) \qquad i_c = I_{pk}^p \cos(\omega t + \theta_i^p + \frac{2\pi}{3}) + I_{pk}^n \cos(\omega t + \theta_i^n - \frac{2\pi}{3})$$

The instantaneous active power of the AMS can be written as (5.23). The average value and second order harmonic components of the instantaneous active power can be defined as (5.24) and (5.25) respectively. The instantaneous active power is delivered to the dc link and determines the dc voltage level, and if it varies with time, the dc-link voltage fluctuates. Therefore, in order to keep constant dc level, $P_{ac}(t)$ should be nullified. Eqs. (5.26), (5.27), and (5.28) are not necessary but enough to eliminate $P_{ac}(t)$. The positive sequence current component can be found as (5.29) by substituting (5.26)-(5.28) into (5.24). As noted from (5.26)-(5.29), the positive and negative sequence components of input voltages should be computed in abc frame to obtain the reference values of positive and negative sequence components of input current, and switching angles are determined based on the reference

input current. The obtained set of switching functions makes the instantaneous active power constant without any oscillating terms. The control structure of AMS based on the proposed method is shown in Figure 5-14.

When AC fault happens, the reference power can also be reduced to very small value such as 50% of the rated power, and the negative sequence controller can be applied to reduce the active power fluctuation. The dynamic performance of the AMS system under single line to ground (SLG) fault in the rectifier side (dc voltage controller converter) is presented in Figure 5-15 when the reference value of active power is not varied during fault. Figure 5-16 presents the dynamic performance of the AMS system under SLG fault when the reference value of active power is also reduced to %50 of rated power during fault.

$$P(t) = v_a i_a + v_b i_b + v_c i_c = \frac{3}{2} \begin{bmatrix} V_{pk}^p I_{pk}^p \cos(\theta_v^p - \theta_i^p) + V_{pk}^p I_{pk}^n \cos(2\omega t + \theta_v^p + \theta_i^n) + \\ V_{pk}^n I_{pk}^p \cos(2\omega t + \theta_v^n + \theta_i^p) + V_{pk}^n I_{pk}^n \cos(\theta_v^n - \theta_i^n) \end{bmatrix} \tag{5.23}$$

$$P_{dc} = \frac{3}{2} \left[V_{pk}^p I_{pk}^p \cos(\theta_v^p - \theta_i^p) + V_{pk}^n I_{pk}^n \cos(\theta_v^n - \theta_i^n) \right] \tag{5.24}$$

$$P_{ac}(t) = \frac{3}{2} \left[V_{pk}^p I_{pk}^n \cos(2\omega t + \theta_v^p + \theta_i^n) + V_{pk}^n I_{pk}^p \cos(2\omega t + \theta_v^n + \theta_i^p) \right] = 0 \tag{5.25}$$

$$V_{pk}^p I_{pk}^n = V_{pk}^n I_{pk}^p \Rightarrow \frac{I_{pk}^n}{I_{pk}^p} = \frac{V_{pk}^n}{V_{pk}^p} \Rightarrow I_{pk}^n = \frac{V_{pk}^n}{V_{pk}^p} \times I_{pk}^p \tag{5.26}$$

$$\pi + \theta_v^p + \theta_i^n = \theta_v^n + \theta_i^p \Rightarrow \theta_i^n = \theta_v^n - \pi \tag{5.27}$$

$$\theta_i^p = \theta_v^p \tag{5.28}$$

$$P_{dc} = \frac{3}{2}\left[V_{pk}^p I_{pk}^p - V_{pk}^n I_{pk}^n\right] = \frac{3}{2}\left[V_{pk}^p I_{pk}^p - (V_{pk}^n)^2 \frac{I_{pk}^p}{V_{pk}^p}\right] \Rightarrow I_{pk}^p = \frac{P_{dc}}{\frac{3}{2}\left[V_{pk}^p - \frac{(V_{pk}^n)^2}{V_{pk}^p}\right]} \qquad (5.29)$$
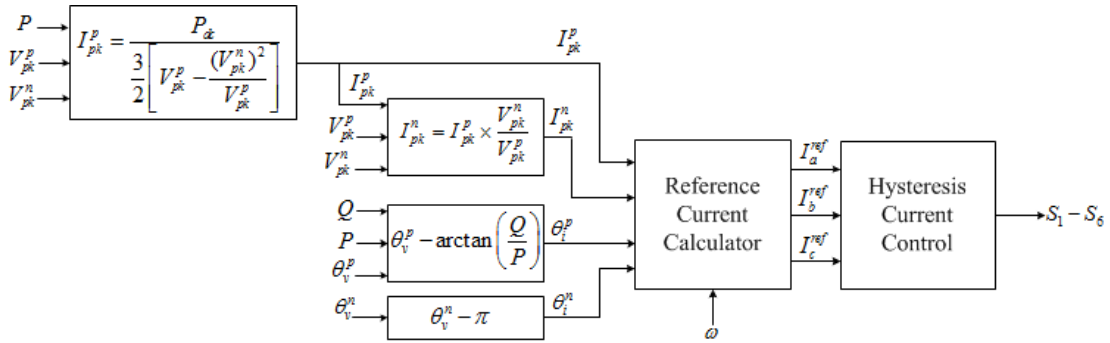
Figure 5-14. Power flow control structure of AMS based on instantaneous active power flow control.
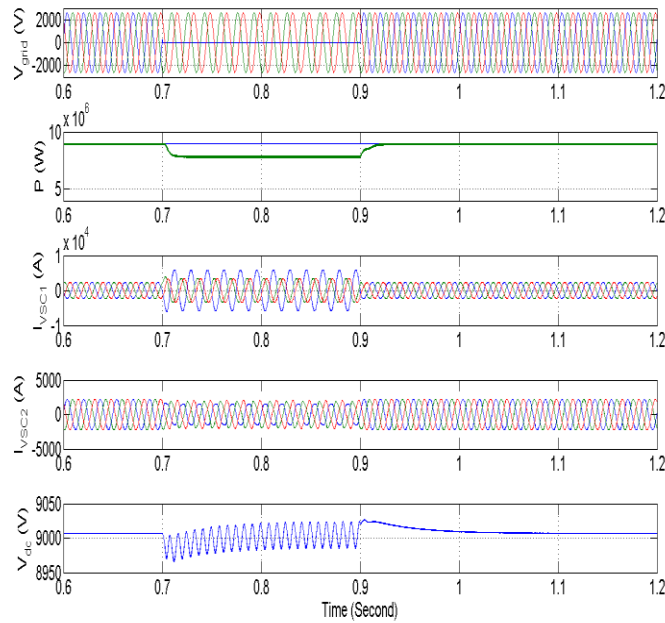
Figure 5-15. Dynamic performance of the AMS system under SLG fault in the dc link voltage controller side with instantaneous active power controller (%100 power transfer during fault).

123
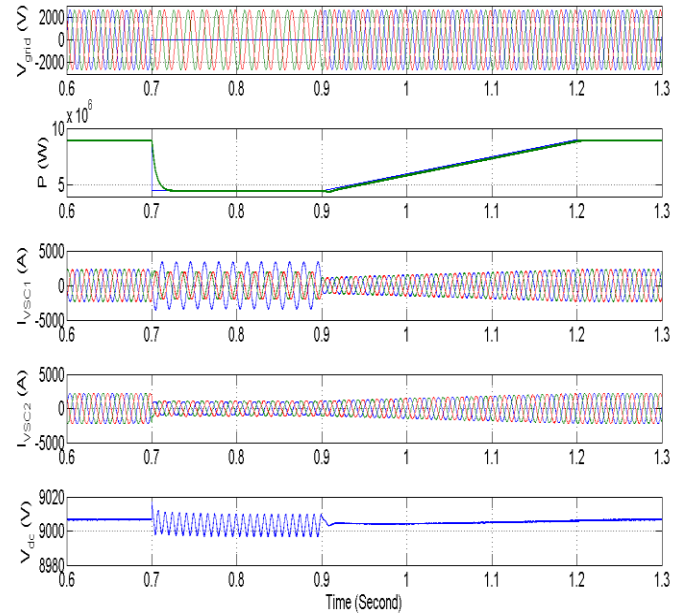
Figure 5-16. Dynamic performance of the AMS system under SLG fault in the dc link voltage controller side with instantaneous active power controller (%50 power transfer during fault).

The supervisory control scheme should be designed to determine the control strategy under fault based on the negative sequence voltage component. The overall sketch of the supervisory control is presented in Figure 5-17. The dynamic performance of the angle-controlled AMS system with 0.1mF DC link capacitors under 10% voltage drop in phase-A is shown in Figure 5-18. As can be seen, the performance of angle-controlled AMS with appropriate component design under 10% voltage sag is acceptable. However, under 50% voltage sag in phase A, the supervisory control switches the control scheme from angle control method to the proposed instantaneous active power method, and the results are presented in Figure 5-19. From Figure 5-19, it can be observed that three phase input currents are in phase with the input voltages. The stiffness of dc bus voltage is evident in Figure 5-19. Figure 5-20 illustrates the positive and negative sequence components of three

phase unbalanced voltages and currents. As can be seen, using the proposed control scheme leads a better dynamic performance compared to the case with just component design albeit with losing efficiency temporarily during significant system disturbances.
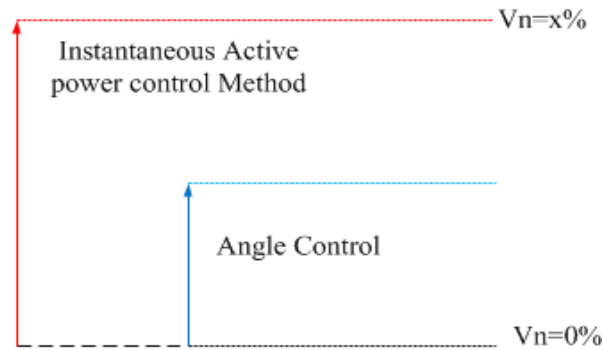
Figure 5-17. The rough sketch of supervisory control for AMS operation based on the negative sequence voltage component (Vn).
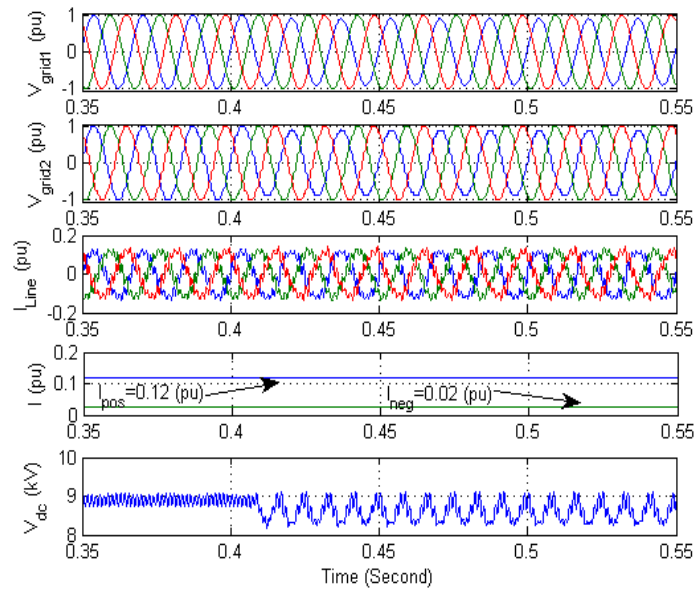
Figure 5-18. Dynamic performance of the angle-controlled AMS system under an unbalanced condition of 10% single-line voltage sag (C=0.1 mF).
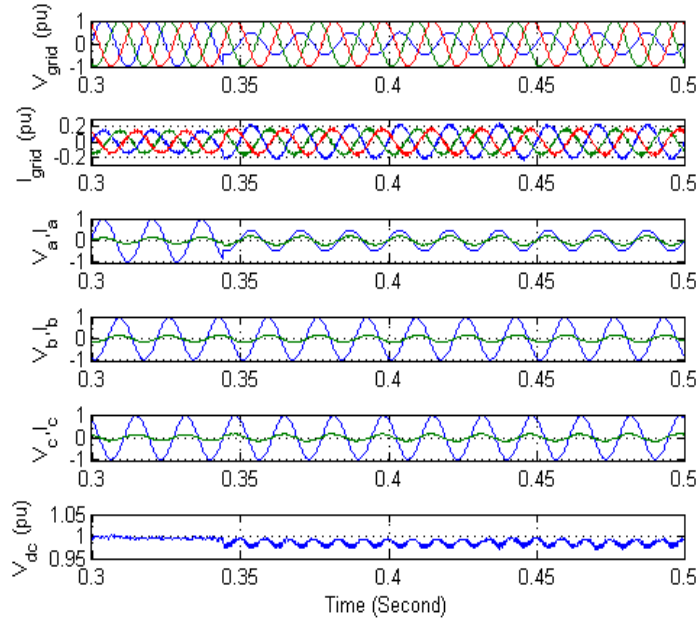
Figure 5-19. Dynamic performance of the AMS under an unbalanced condition of 50% single-line voltage sag with the proposed method (C=1 mF).
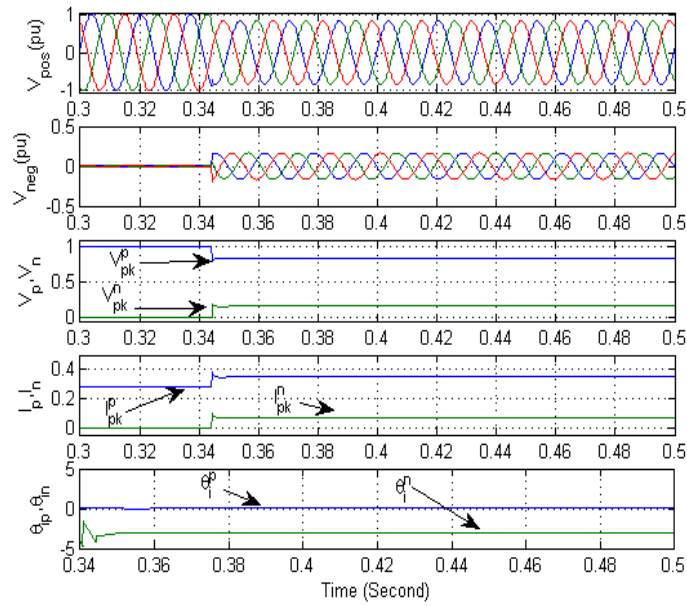
Figure 5-20. Positive and negative sequence components of voltage and currents (C=1 mF).

126

5.5 Control Scheme of High Frequency Isolated Modular Converter in d-q Reference Frame for AC Fault operating conditions

The dynamic performance of the converter under SLG fault in the rectifier side is presented in Figure 5-21. The reference value of active power is 9 (MW) when fault happens (t=0.7s). As can be seen, dc bus voltage is also controlled at 9 (kV). Terminal 1 dc capacitor voltages regulated at 1 kV are also shown in Figure 5-22. Figure 5-23 also shows the dynamics of the converter under SLG fault when the reference value of active power is reduced to 50% of the full power when fault is detected. As can be seen, the active power flow can be regulated at half of the rated power during fault, and the oscillation of terminal dc bus voltage is too low compared to the previous case. Terminal 1 dc capacitor voltages regulated at 1 kV are also shown in Figure 5-24 for this case scenario.
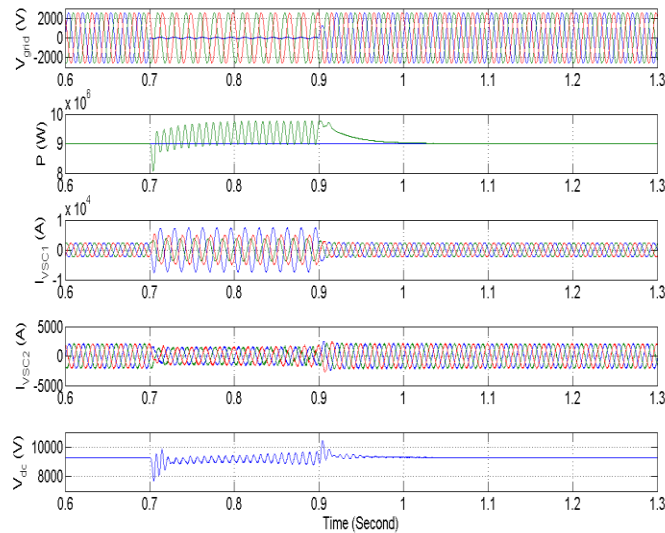
Figure 5-21. Dynamic performance of the AMS system under SLG fault in the dc link voltage controller side (Negative sequence current control is on and %100 power transfer during fault).
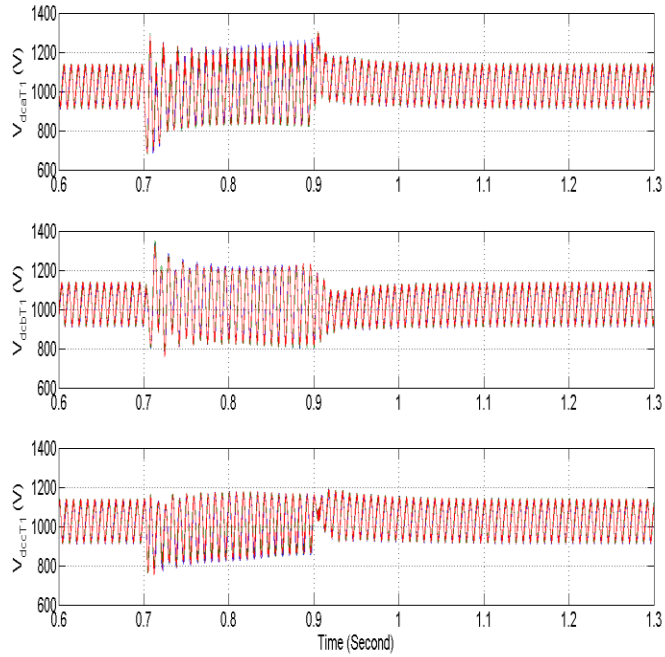
Figure 5-22. Terminal 1 dc capacitor voltages under SLG fault in the dc link voltage controller side (Negative sequence current control is on and %100 power transfer during fault).
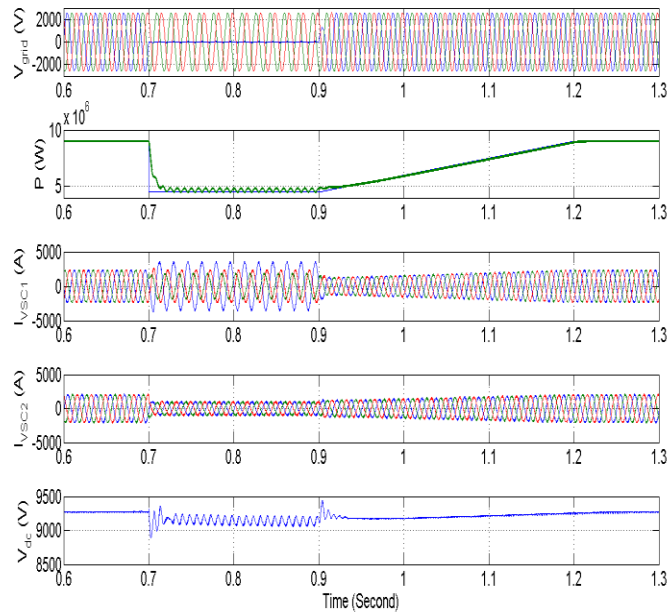
Figure 5-23. Dynamic performance of the AMS system under SLG fault in the dc link voltage controller side (Negative sequence current control is on and %50 power transfer during fault).
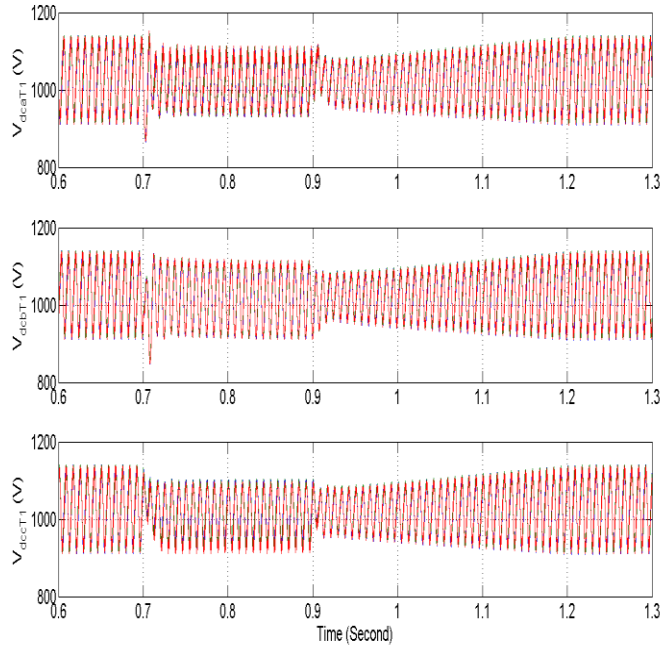
Figure 5-24. Terminal 1 dc capacitor voltages under SLG fault in the dc link voltage controller side (Negative sequence current control is on and %50 power transfer during fault).

5.6 Control of High Frequency Isolated Modular Converter under DC Fault Operating Condition

Recently, Voltage Source Converter (VSC) based Multi-Terminal DC (MTDC) transmission systems have gained more attention. Compared to current source converter technology, voltage source converters have several benefits including higher power quality, lower power transmission losses, and higher voltage capability. Flexibility in bidirectional power flow control is the main advantage of voltage source converters in large scale MTDC power transmission systems. However, VSC based MTDC transmission systems are vulnerable to DC side fault, and expensive DC circuit breakers are required to protect them

against DC fault. This section proposes a control method of the high frequency isolated modular converter which has ultra-fast electronic isolation capability following dc fault, and it can be protected against dc fault without using expensive DC circuit breakers. In fact, this advantage allows us to use AC circuit breakers instead of DC circuit breakers for DC fault protection.

The proposed control algorithm of the high frequency isolated modular converter for DC fault operation is shown in Figure 5-25. According to the control scheme for DC fault operation (Figure 5-25), DC fault is detected when the measured value of DC side current is twice the rated value of DC side current. Once DC fault is detected at time t_0, the reference value of active power flow is changed to zero. Also, once fault is detected, all switches of DC/DC converters are turned off, and DC/DC converters are disconnected from AC/DC converters. As a result, the total energy of all DC capacitor voltages is discharged in DC side inductor (L) and DC overhead line resistance (R) as can be shown in Figure 5-26. The inductor current has an initial value $i_L(t_0)=I_0$, and each capacitor voltage has an initial value $V_{cm}(t_0)=V_{c0}$. So, the total initial value of capacitor voltage for all n modules is $V_0=n\times V_{c0}$. The DC side current can be expressed as (5.30) if $R < 2\sqrt{L/C}$. The DC bus voltage is also written as (5.31).

$$i_{dc}(t) = I_0 e^{-\alpha t}\cos(\sqrt{\omega_0^2 - \alpha^2}t) + \left[\frac{\frac{V_0}{L} - I_0\alpha}{\sqrt{\omega_0^2 - \alpha^2}}\right]e^{-\alpha t}\sin(\sqrt{\omega_0^2 - \alpha^2}t) \qquad (5.30)$$

$$V_c(t) = V_0 e^{-\alpha t}\cos(\sqrt{\omega_0^2 - \alpha^2}t) + \left[\frac{V_0\alpha - \frac{I_0}{C}}{\sqrt{\omega_0^2 - \alpha^2}}\right]e^{-\alpha t}\sin(\sqrt{\omega_0^2 - \alpha^2}t) \qquad (5.31)$$

Where $\alpha = R/2L; \omega_0 = 1/\sqrt{LC}; C = C_m/n$. The time when the capacitor voltage becomes zero can be computed by (5.32).

$$t_1 = t_0 + \frac{\arctan\left[\dfrac{V_0 C \sqrt{\omega_0^2 - \alpha^2}}{I_0 - V_0 \alpha C}\right]}{\sqrt{\omega_0^2 - \alpha^2}} \tag{5.32}$$

When DC bus voltage becomes zero at time t_1, the total energy of DC side inductor is discharged in DC overhead line resistance and anti-parallel diodes as can be shown in Figure 5-27. At time t_1, the inductor current has an initial value of $i_L(t_1)=I_1$. So, the DC side current can be written as (5.33).

$$i_{dc}(t) = I_1 e^{\frac{-R}{L}t}; T = \frac{L}{R} \tag{5.33}$$

According to (5.33), the DC current is reduced, and the time when the inductor current becomes zero is obtained by (5.34).

$$t_2 = t_1 + \frac{5L}{R} \tag{5.34}$$

When the magnitude of DC current becomes zero, circuit breakers are opened to disconnect terminal 1 from terminal 2.

The control strategy for recovery after DC fault is shown in Figure 5-28. When DC fault is cleared, DC/DC converters are connected to AC/DC converter, and all switching signals of DC/DC converters are enabled to charge DC/DC capacitor voltages. Once DC bus voltage is regulated at its reference value, terminal 1 is connected to terminal 2, and the reference value of active power flow is ramped up from zero to the rated value.
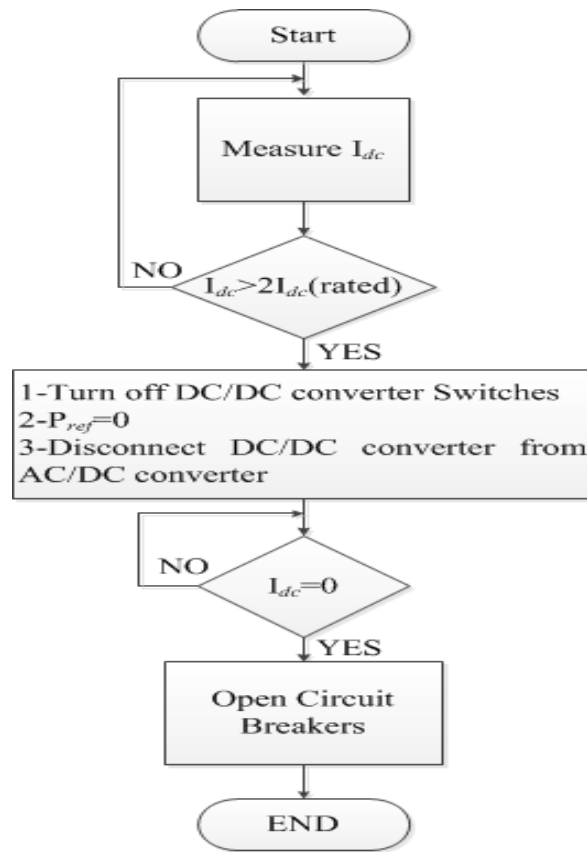
Figure 5-25. Control algorithm of high frequency isolated modular converter under DC fault operating condition.
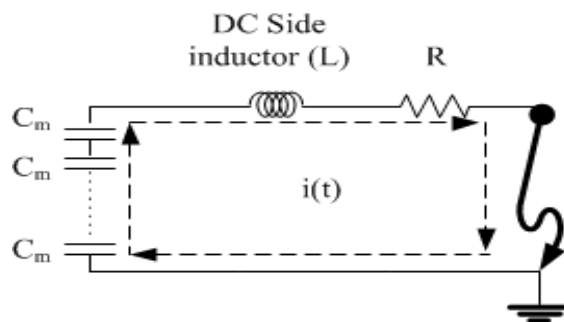
Figure 5-26. Equivalent circuit of high frequency isolated modular converter when DC fault is detected (capacitor discharging mode).
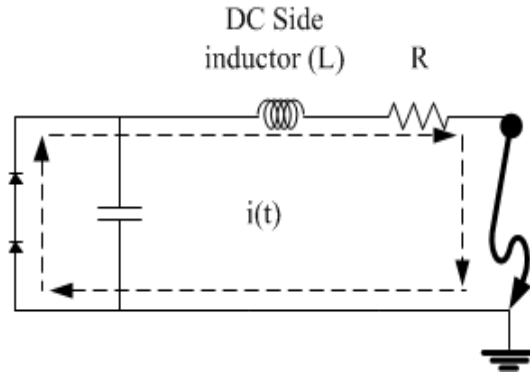
Figure 5-27. Equivalent circuit of high frequency isolated modular converter when DC bus voltage becomes zero (inductor discharging mode).
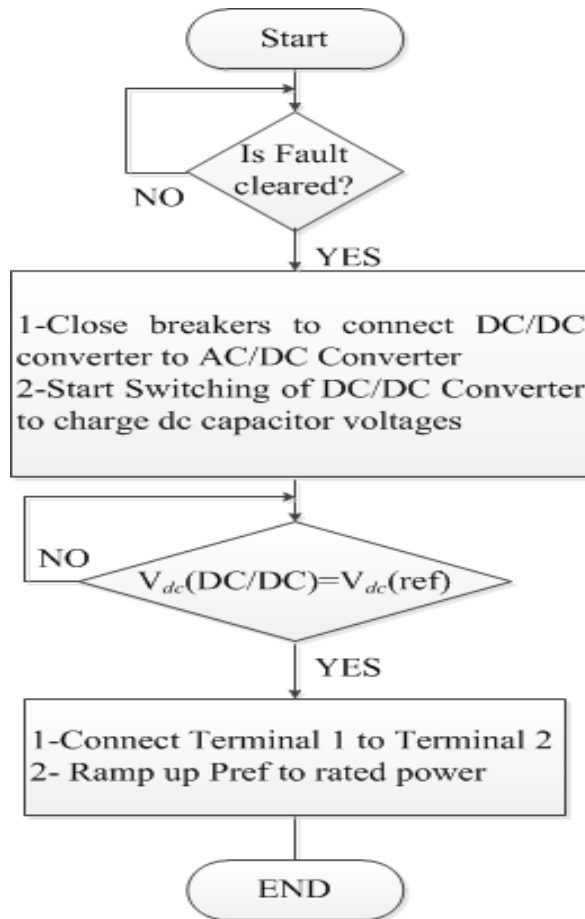
Figure 5-28. Control algorithm of high frequency isolated modular converter for recovery after DC fault.

133

In this section, the dynamic performance of the high frequency isolated modular converter under DC fault operating condition is evaluated through PSCAD simulation. For DC fault simulation, the positive DC line is connected into the ground as shown in Figure 5-29, and the system parameters are summarized in Table 5-1. DC fault happens at t=0.9s, and it is cleared at t=1s.

Both DC cables and overhead transmission lines can be used for the high frequency isolated modular converter. Although DC cables are mostly used since cable faults are so uncommon, but the application of DC cables in some rocky or mountainous areas is so limited. In these areas, DC overhead lines are used. In dc overhead lines, dc-link short circuit is so common because of insulation breakdown following lightning strikes and pollution. An overhead line with the length of 480 (km) is used in the simulation.

Table 5-1. High frequency isolated modular converter parameters for DC fault operation

Terminal rated power	P	320 MVA
Terminal voltage reference	V_{dc}	320 kV
DC gird side inductance	L_{dc}	100 mH
Overhead line resistance	R_{dc}	11.5 Ω
Module number (per terminal)	N	3
AC/DC capacitor voltage	$V_{(AC/DC)}$	106.67 kV
DC/DC capacitor voltage	$V_{(DC/DC)}$	106.67 kV
AC/DC Capacitor value	$C_{(AC/DC)}$	100 uF
DC/DC Capacitor value	$C_{(DC/DC)}$	10 uF
AC/DC PWM switching frequency	f_{sw} (AC/DC)	2 kHz
DC/DC PWM switching frequency	f_{sw} (DC/DC)	20 kHz
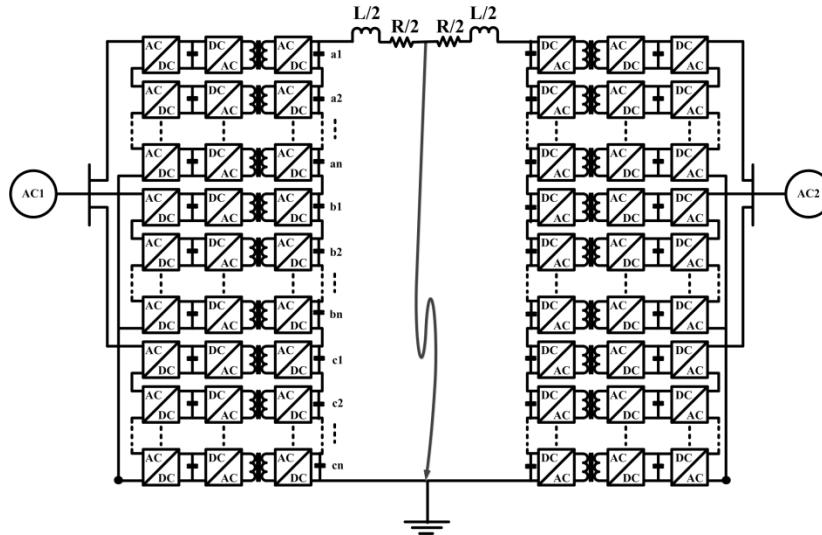
Figure 5-29. High frequency isolated modular converter system under DC fault operating condition.

Figure 5-30 shows the dynamic performance of high frequency isolated modular converter under DC fault operating condition. Initially, the switching signals of AC/DC and DC/DC converters are off, and they are enabled at t=0.1s. Therefore, terminal DC bus voltage is adjusted at 320 kV at this time. The reference value of active power is also ramped up from 0 at t=0.4s to 320 MW at t=0.7s. DC fault happens at t=0.9s when the rated power is transferred from terminal 1 to terminal 2 as shown in Figure 5-30. When DC fault is detected, the reference value of active power is reduced from 320 MW to 0 MW, and all the switching signals of DC/DC converter switches will be turned off. As a result, the total energy of all DC capacitor voltages is discharged in DC side inductor and DC overhead line resistance as explained in the previous section. When DC bus voltage becomes zero, the total energy of DC side inductor is discharged, and as a result the magnitude of DC current is reduced as can be seen in Figure 5-30. When the magnitude of DC current becomes zero, circuit breakers

will be opened to disconnect terminal 1 from terminal 2. Three-phase ac current in both terminals is also shown in Figure 5-30. DC fault is cleared at t=1s, and the control algorithm for recovery after DC fault is implemented. First, DC/DC converters are connected to AC/DC converters, and the switching signals of DC/DC converters are enabled at t=1s. At this time, DC bus voltage is regulated at 320 kV. At t=1.15s, terminal 1 is connected to terminal 2. Then, the reference value of active power is increased from zero at t=1.2s to 320MW at t=1.5s.
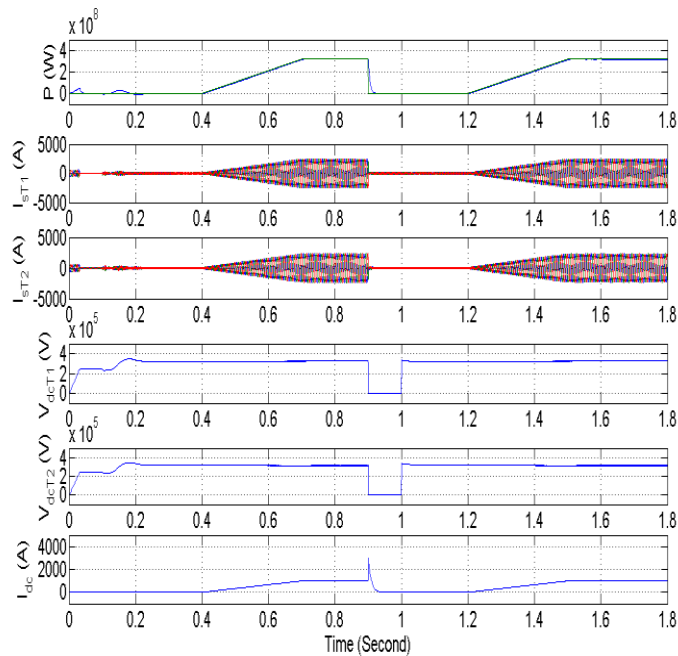
Figure 5-30. Dynamic performance of high frequency isolated modular converter under DC fault.

During fault duration, the AC/DC converters in both terminals are controlled to regulate capacitor DC voltages of each AC/DC module at 106.67 kV as shown in Figure 5-31, and

Figure 5-32. Capacitor DC bus voltages of DC/DC converters for terminal 1 and 2 are also shown in Figure 5-33, and Figure 5-34 respectively. The switching signals of DC/DC converters are enabled at t=0.1s, and the capacitor DC voltages of DC/DC converters are regulated at 106.67 kV. When DC fault is detected at t=0.9s, the switching signals of DC/DC converters are disabled. So, the capacitor voltages of DC/DC converters become zero. When DC fault is cleared at t=1s, the switching signals of DC/DC converters are enabled, and the capacitor voltages of DC/DC converters are regulated at 106.67 kV again.
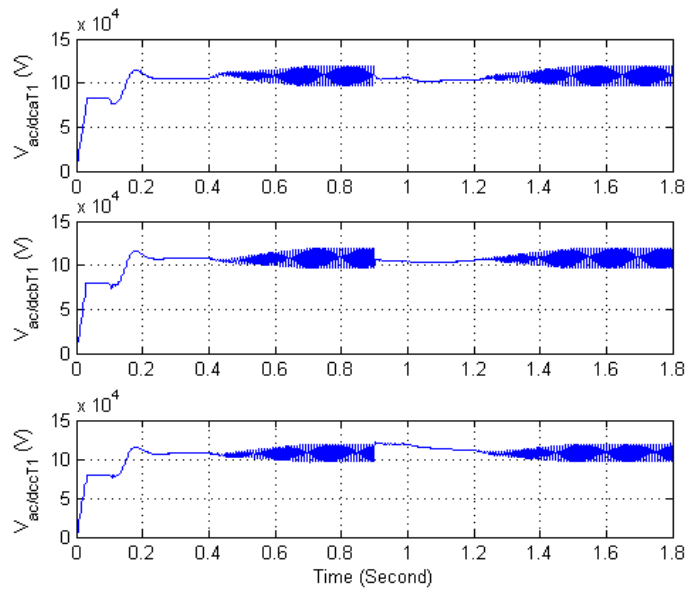
Figure 5-31. Terminal 1 AC/DC capacitor voltage variation.
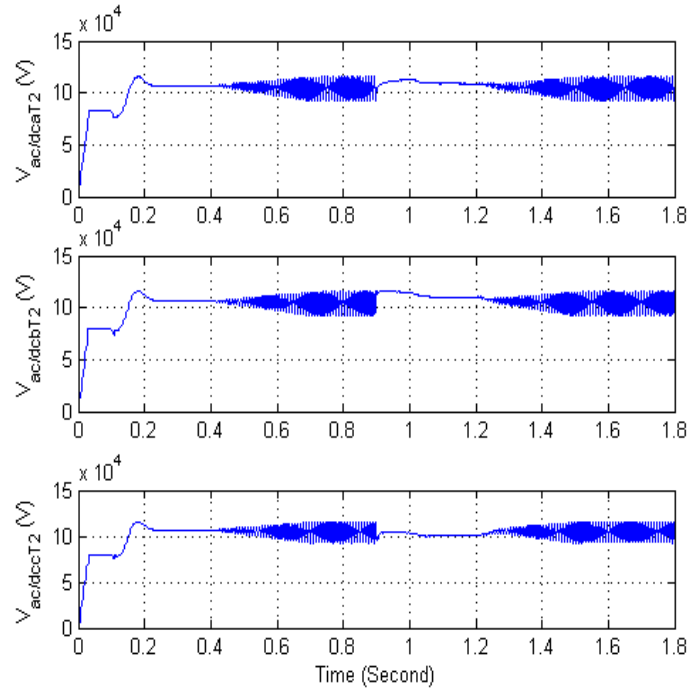
Figure 5-32. Terminal 2 AC/DC capacitor voltage variation.
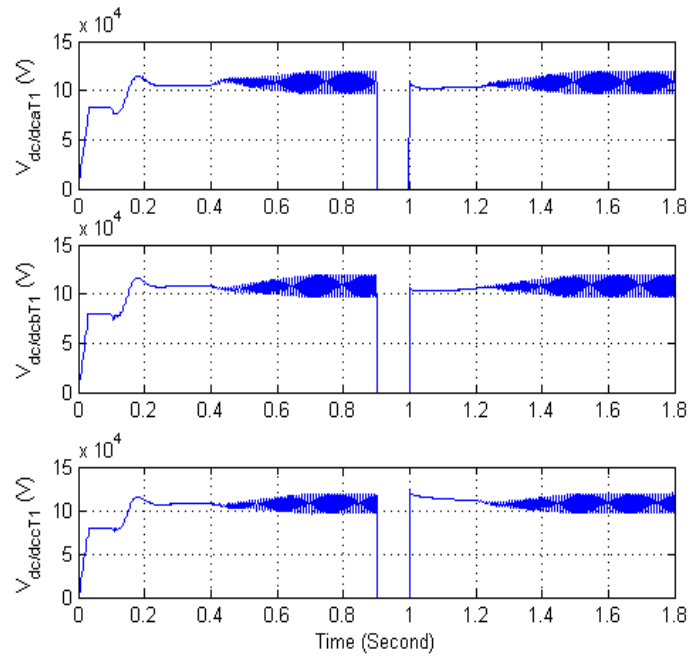
Figure 5-33. Terminal 1 DC/DC capacitor voltage variation.
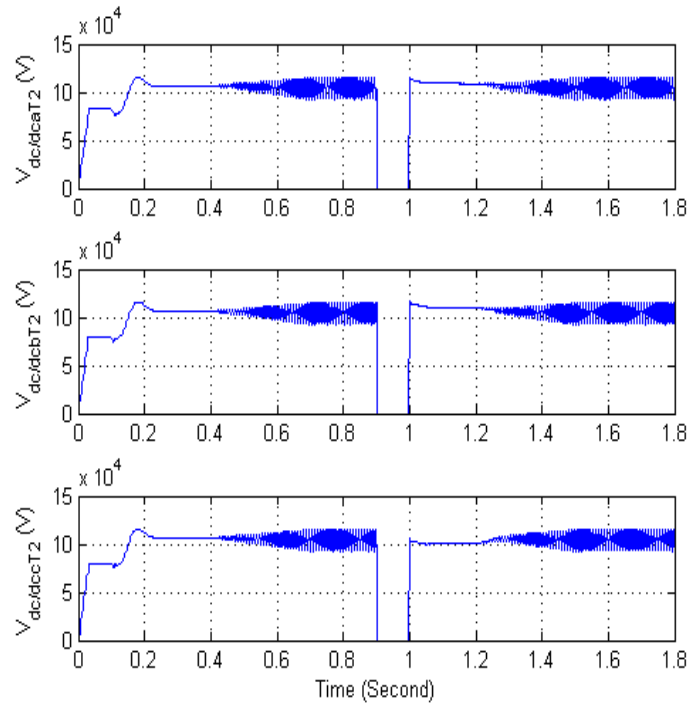
Figure 5-34. Terminal 2 DC/DC capacitor voltage variation.

Figure 5-35 shows the zero crossing time of DC current versus fault location and DC side inductor based on the theoretical results obtained by (5.34). As can be seen, DC current zero crossing time increases as DC side inductor increases. Also, as fault location increases, R value increases, and as a result zero crossing time decreases. Figure 5-36 also shows the zero crossing time of DC current versus fault location and DC side inductor based on the obtained simulation results. Comparison of simulation and theoretical results shows that Eq. (5.34) is accurate enough to find the zero crossing time of DC current.
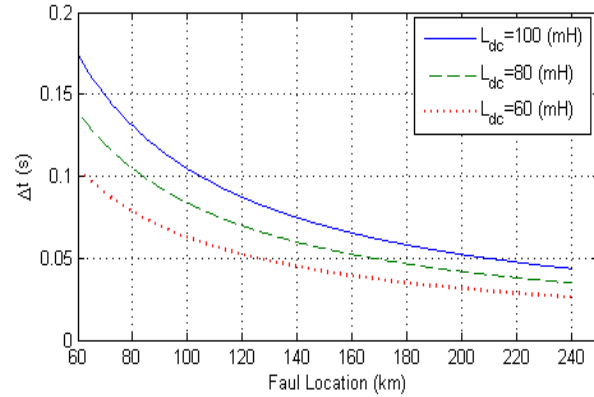
Figure 5-35. DC current zero crossing time with respect to fault location and L_{dc} - Theoretical results.
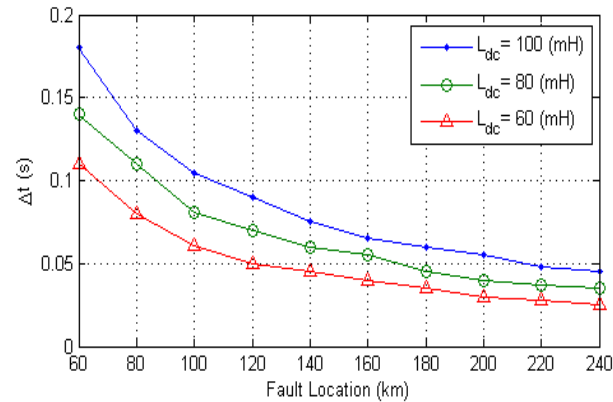
Figure 5-36. DC current zero crossing time with respect to fault location and L_{dc} - Simulation results.

5.7 Control of Multi-terminal DC Grid under DC Fault Operating Condition

Figure 5-37 shows multi-terminal DC (MTDC) grid model which consists of four voltage source converters based on the high frequency isolated modular converter shown in Figure 5-38. The proposed control algorithm of VSC based MTDC transmission system for

DC fault operation is shown in Figure 5-39. According to the control scheme for DC fault operation (Figure 5-39), DC fault is detected when the measured value of DC side current in dc transmission line is twice the rated value of DC current for that transmission line. Once DC fault is detected, the reference value of active power flow for all terminals is changed to zero, and the converter control mode in all four terminals is switched from droop control method to DC bus voltage control. In fact, dead-band controller is disabled. Also, once fault is detected, all switches of DC/DC converters are turned off, and DC/DC converters are disconnected from AC/DC converters. As a result, the total energy of all DC capacitor voltages in each terminal is discharged in DC cables connected to that terminal. When DC bus voltage becomes zero, the total energy of cable inductor is discharged. As a result, the DC currents in DC cables are reduced. When the magnitude of DC current in each terminal becomes zero, circuit breaker of that terminal is opened to disconnect that terminal from other terminals.

The control strategy for recovery after DC fault is shown in Figure 5-40. When DC fault is cleared, DC/DC converters are connected to AC/DC converters, and all switching signals of DC/DC converters are enabled to charge DC/DC capacitor voltages in all terminals. Once DC bus voltage of each terminal is regulated at its reference value, breakers are closed to connect all terminals, and the converter control mode is switched from DC voltage control to droop control method with dead-band controller, and the reference value of active power flow in all terminals is ramped up from zero to the desired values.
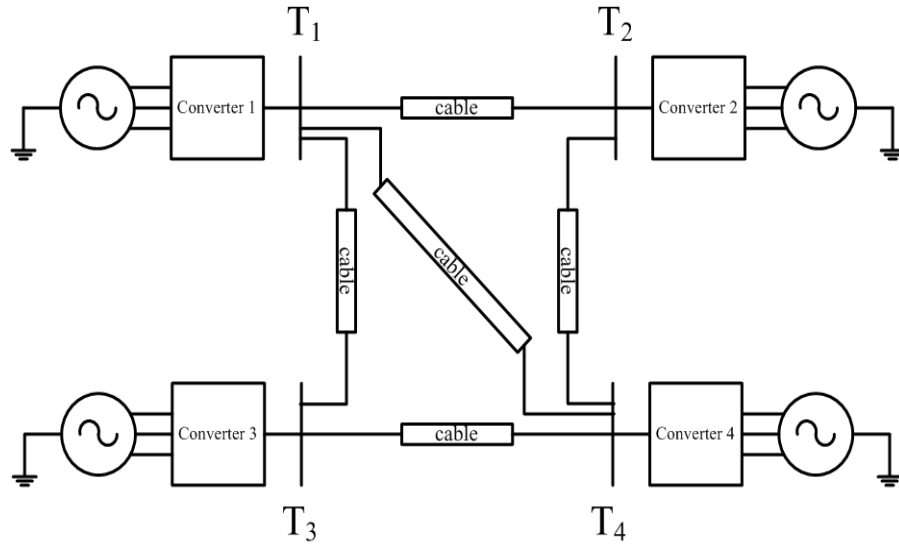
Figure 5-37. Multi-terminal DC Grid model.
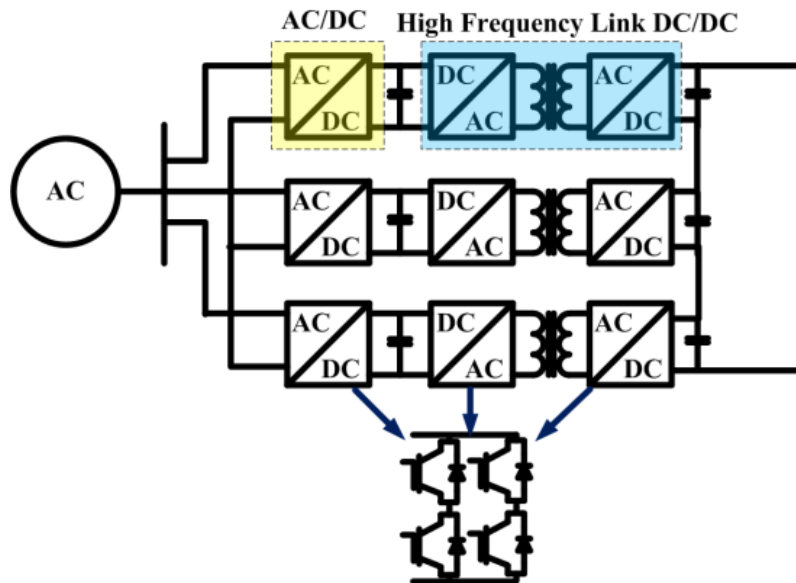
Figure 5-38. Voltage Source Converter configuration of each terminal.
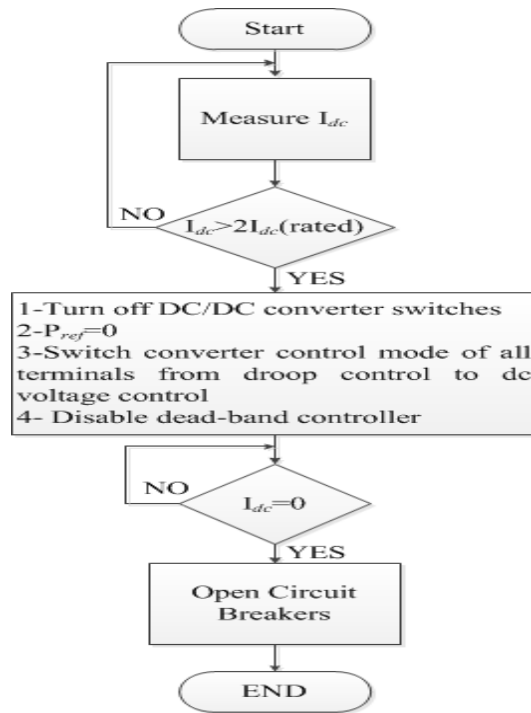
Figure 5-39. Control algorithm of MTDC grid under DC fault.
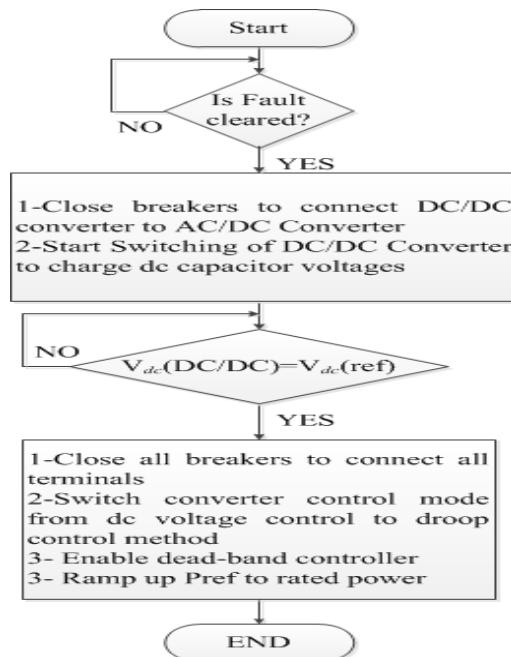
Figure 5-40. Control algorithm of MTDC grid for recovery after DC fault.

In this section, the dynamic performance of the VSC based MTDC system under DC fault operating condition is evaluated through PSCAD simulation. As shown in Figure 5-41, DC fault happens in the middle of cable connecting terminal 1 to terminal 2, and the system parameters for all four terminals are summarized in Table 5-2. DC fault happens at t=0.9s, and it is cleared at t=1s.
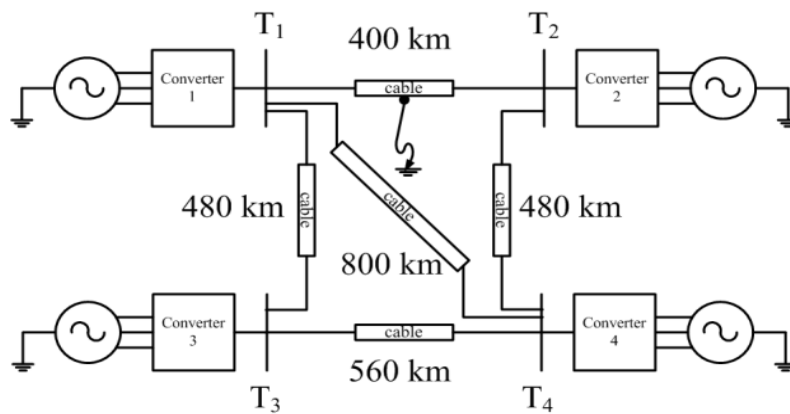
Figure 5-41. Four-terminal DC grid under DC fault operating condition.

Table 5-2.   MTDC system parameters for DC fault operation

Module number (per terminal)	N	3
Terminal rated power	P	320 MVA
Terminal voltage reference	V_{dc}	320 kV
Terminal AC input voltage (phase peak)	E	92.4 kV
AC input inductance	L_s	11.7 mH
AC/DC capacitor voltage	$V_{(AC/DC)}$	106.67 kV
DC/DC capacitor voltage	$V_{(DC/DC)}$	106.67 kV
AC/DC Capacitor value	$C_{(AC/DC)}$	100 uF
DC/DC Capacitor value	$C_{(DC/DC)}$	10 uF
AC/DC PWM switching frequency	$f_{sw}\ (AC/DC)$	2 kHz
DC/DC PWM switching frequency	$f_{sw}\ (DC/DC)$	20 kHz

[98] is used to find the cable cross-section dimensions and material properties for 320 kV DC cable. The cross sectional area of this cable is shown in Figure 5-42. The frequency dependent phase model is used to calculate the transients in PSCAD with curve fitting frequencies set at 0.01Hz for starting point and 1 MHz for ending point. The detail parameters and specifications of the 320kV cable are listed in Table 5-3.
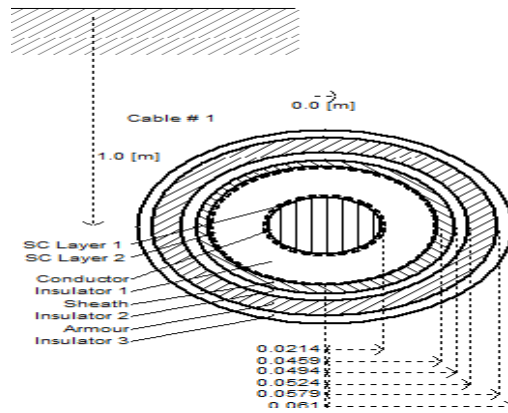
Figure 5-42. Cross-sectional area of DC cable.

Table 5-3.   320KV cable parameters

Layer	Material	Radius (mm)	Resistivity	Rel. Permittivity	Rel. Permeability
Core	Copper	21.4	1.72e-8	1	1
Insulation	XLPE	45.9	-	2.3	1
Sheath	Lead	49.4	2.2e-7	1	1
Insulation	XLPE	52.4	-	2.3	1
Armor	Steel	57.9	1.8e-7	1	10
Insulation	PP	61	-	2.1	1

Figure 5-43 shows the dynamic performance of terminal DC bus voltages in all four terminals. Initially, the switching signals of AC/DC and DC/DC converters are off, and they are enabled at t=0.1s. Therefore, terminal DC bus voltage at four terminals is adjusted at 320kV at this time. The dead-band region in DC bus voltage controller is between 0.95 pu-1.1 pu. So, DC bus voltage controller is off when DC bus voltage is within the limit. Once DC bus voltage hits the lower or upper limit, DC voltage controller is enabled. DC fault happens at t=0.9s. When DC fault is detected, all the switching signals of DC/DC converter switches will be turned off. As a result, the total energy of all DC capacitor voltages is discharged in cable impedance. So, DC bus voltages in all four terminals become zero as shown in Figure 5-43. DC fault is cleared at t=1s, and the control algorithm for recovery after DC fault is implemented. First, DC/DC converters are connected to AC/DC converters, and the switching signals of DC/DC converters are enabled at t=1s. At this time, DC bus voltage in all four terminals is regulated at 320 kV.

The dynamic performance of active power flow in all four terminals is shown in Figure 5-44. As can be seen, the reference value of active power in terminal 1 is ramped up from 0 at t=0.4s to 320 MW at t=0.7s. The reference value of active power flow in other terminals are defined as $P_{ref2}=-P_{ref1}$, $P_{ref3}=0.7P_{ref1}$, and $P_{ref4}=-0.7P_{ref1}$. When DC fault happens at t=0.9s, the reference value of all four terminals is changed to zero. When DC fault is cleared and DC bus voltage in all four terminals is regulated at 320 kV, the reference value of active power in all terminals can be ramped up to the rated value. Figure 5-45 shows three-phase AC current in all four terminals. As can be seen, three-phase AC current in each terminal changes according to the reference power flow of that terminal.

Figure 5-46 shows DC current in all four terminals and different DC transmission lines. As can be observed, DC current in each terminal is directly proportional to active power flow of that terminal. When DC fault happens at t=0.9s, first the total energy of DC capacitor voltages is discharged in cable impedance. Then, when DC bus voltage of each terminal becomes zero, the total energy of DC cable inductor is discharged, and as a result the magnitude of DC current in each terminal is reduced as can be seen in Figure 5-46. When the magnitude of DC current in each terminal becomes zero, circuit breaker of that terminal is opened to disconnect that terminal from other terminals.

The dynamic performance of AC/DC capacitor voltages is shown in Figure 5-47. During DC fault duration, the AC/DC converters in all terminals are controlled to regulate capacitor DC voltages of each AC/DC module at (320/3=106.67 kV) as shown in Figure 5-47. Capacitor DC voltages of DC/DC converters for four terminals are shown in Figure 5-48. When DC fault is detected at t=0.9s, the switching signals of DC/DC converters are disabled. So, the capacitor voltages of DC/DC converters become zero. When DC fault is cleared at t=1s, the switching signals of DC/DC converters are enabled, and the capacitor voltages of DC/DC converters are regulated at 106.67 kV.
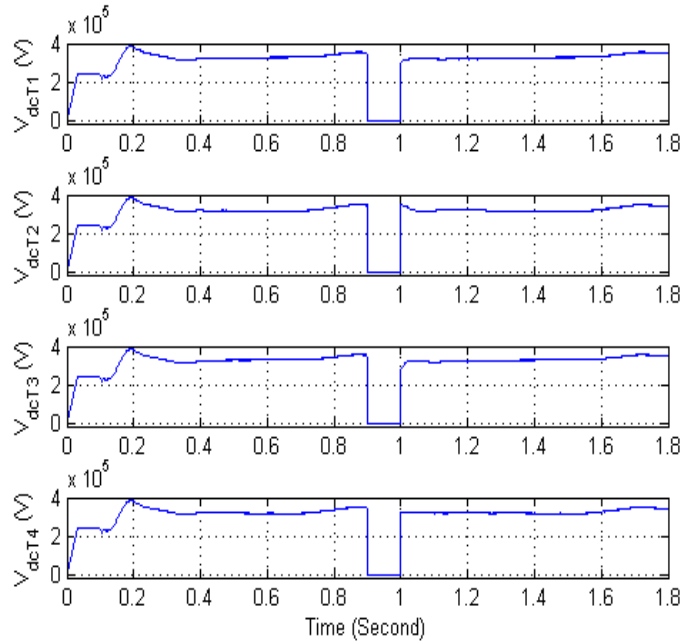
Figure 5-43. Dynamic performance of terminal DC bus voltages.
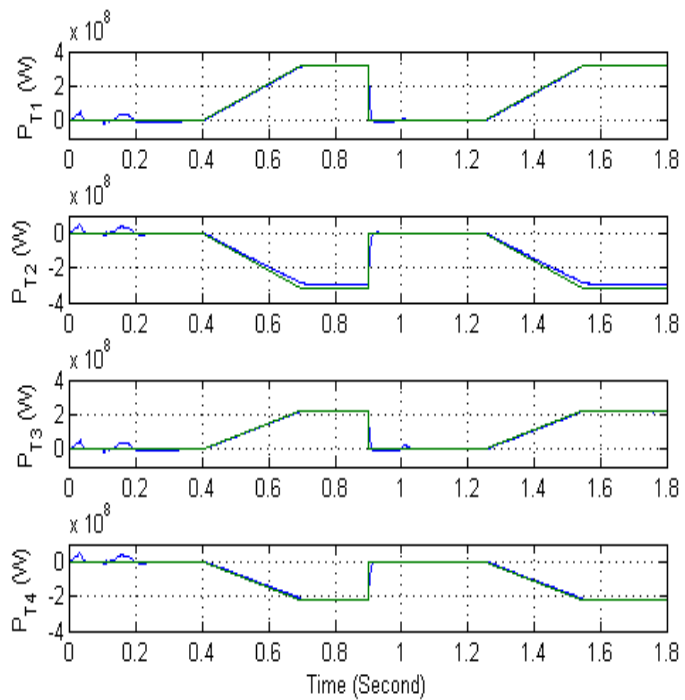
Figure 5-44. Dynamic performance of active power flow.

148
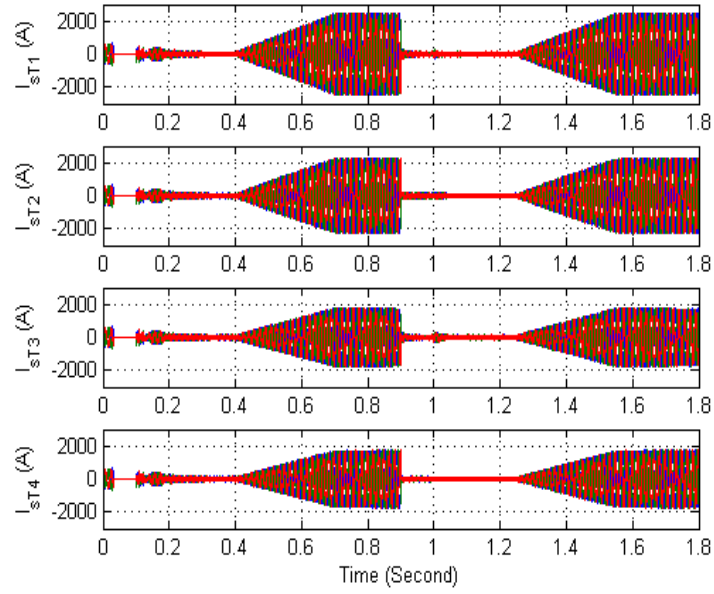
Figure 5-45. Dynamic performance of three-phase AC current.
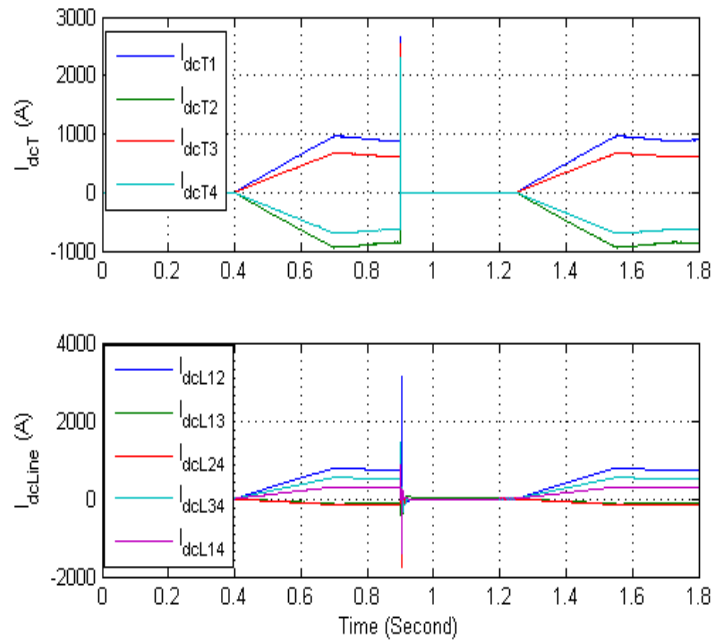
Figure 5-46. Dynamic performance of DC current.
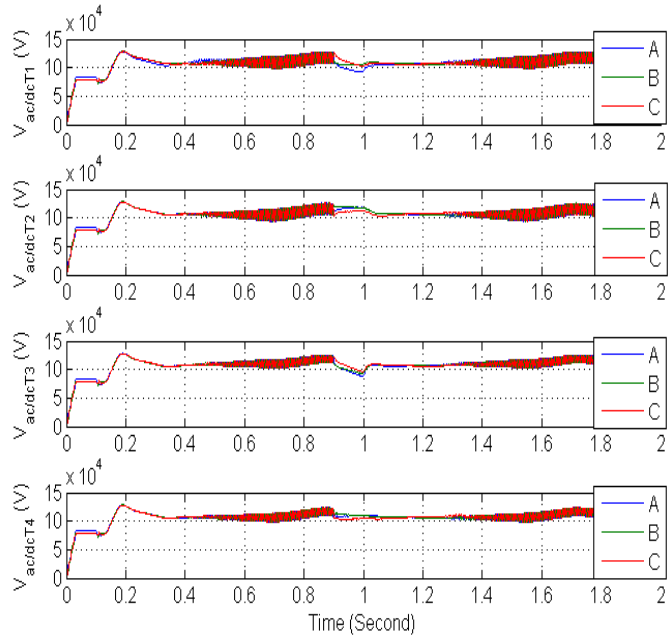
Figure 5-47. Dynamic performance of AC/DC capacitor voltages.
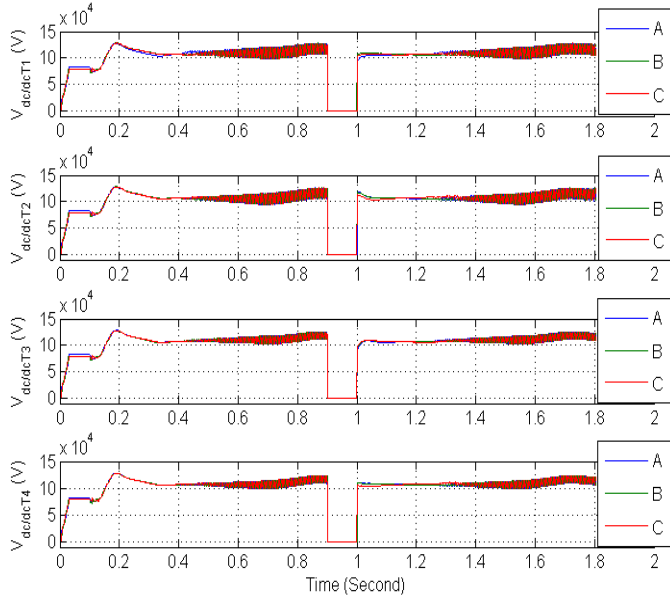
Figure 5-48. Dynamic performance of DC/DC capacitor voltages.

Figure 5-49 shows the zero crossing time of terminal 1 DC current versus fault location and DC side inductor based on the simulation results with DC cable model. As can be seen, DC current zero crossing time increases as DC side inductor increases. Also, as fault location increases, zero crossing time decreases. Figure 5-50~Figure 5-52 also show the zero crossing time of DC current versus fault location and DC side inductor for the other three terminals. As can be seen, DC current zero crossing time in terminal 2, 3, and 4 is less than 2 (ms).
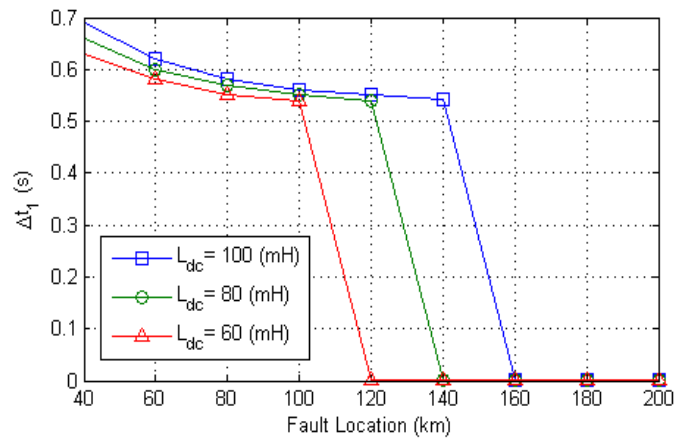
Figure 5-49. Terminal 1 DC current zero crossing time with respect to fault location from terminal 1 and L_{dc}.
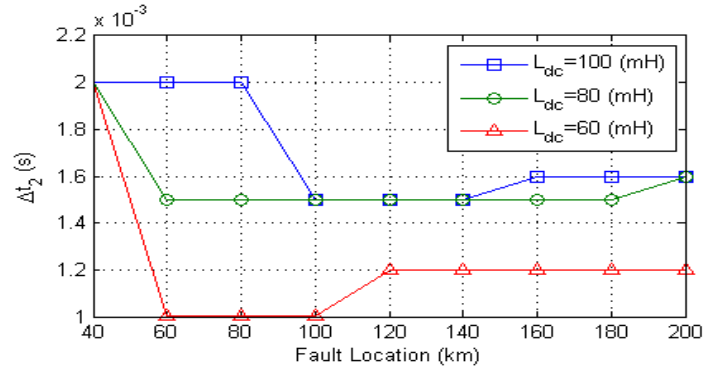
Figure 5-50. Terminal 2 DC current zero crossing time with respect to fault location from terminal 1 and L_{dc}.
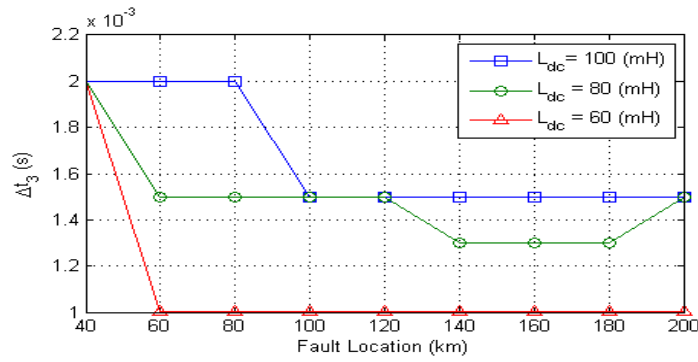
Figure 5-51. Terminal 3 DC current zero crossing time with respect to fault location from terminal 1 and L_{dc}.
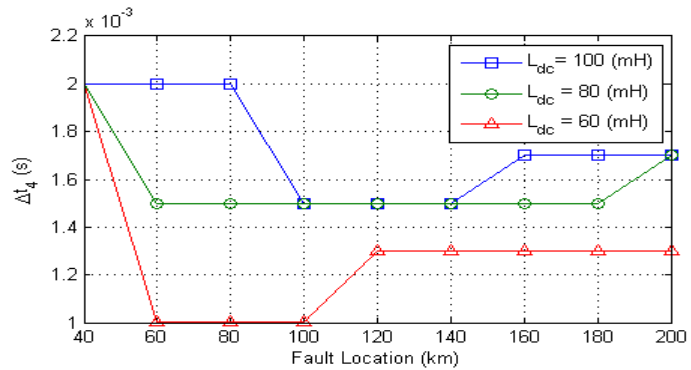
Figure 5-52. Terminal 4 DC current zero crossing time with respect to fault location from terminal 1 and L_{dc}.

152

5.8 Control of Multi-terminal DC Grid under Loss of Terminal Station

In this section, the dynamic performance of the MTDC system is presented. PSCAD/EMTDC based simulation has been carried out to verify the control structures performance. The four-terminal DC grid is shown in Figure 5-37, and the MTDC system parameters are tabulated in Table 5-4. Four case studies are considered to compare the operation of multi-terminal DC grid under normal and loss of one converter station.

Table 5-4.   MTDC system parameters for PSCAD simulation under loss of terminal station

Terminal rated power	P	12 MVA
Terminal AC input voltage (phase peak)	E	3.2 kV
AC input inductance	L_s	374 uH
AC input resistance	R_s	15 mΩ
DC gird side inductance	L_{dc}	2.4 mH
Terminal voltage reference	V_{dc}	12 kV
Terminal 1-2 DC cable resistance	R_{12}	0.3 Ω
Terminal 1-3 DC cable resistance	R_{13}	0.4 Ω
Terminal 1-4 DC cable resistance	R_{14}	0.8 Ω
Terminal 2-4 DC cable resistance	R_{24}	0.5 Ω
Terminal 3-4 DC cable resistance	R_{34}	0.6 Ω

A. *Operation of MTDC system with master/slave control method under normal operating condition*

In this section, PSCAD/EMTDC based simulation has been carried out to evaluate the performance of MTDC system with master/slave control method under normal operating condition. For this case scenario, terminal 1 will control DC bus voltage and other terminals are switched for power flow control. The dynamic performance of active power flow for all

four terminals is displayed in Figure 5-53. The reference value of active power flow for terminal 2 is decreased from zero to -12 (MW) at t=0.3s, and it is varied from 0 to 8.4 (MW) for terminal 3. In terminal 4, the reference value of active power flow is also changed from 0 to -8.4 (MW) at t=0.3s. As can be seen, power flow control is perfectly done for terminal 2, 3, and 4. Terminal 1 is also controlled to regulate DC bus voltage and balance the active power flow in the entire DC grid. Terminal 1 also supplies the total power loss of the entire DC grid. Figure 5-54 shows terminal DC bus voltages controlled at 12 (kV). Three-phase AC current for all four terminals is shown in Figure 5-55. DC currents in all four terminals and different DC transmission lines are also shown in Figure 5-56. As can be seen, DC currents in DC terminals change according to the reference value of active power.

Figure 5-53. Dynamic performance of active power flow- Master/slave control under normal operating condition.
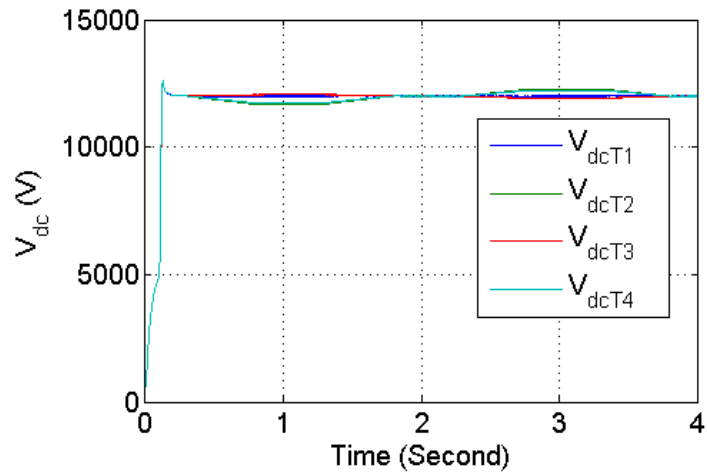
Figure 5-54. Terminal DC bus voltages- Master/slave control under normal operating condition.
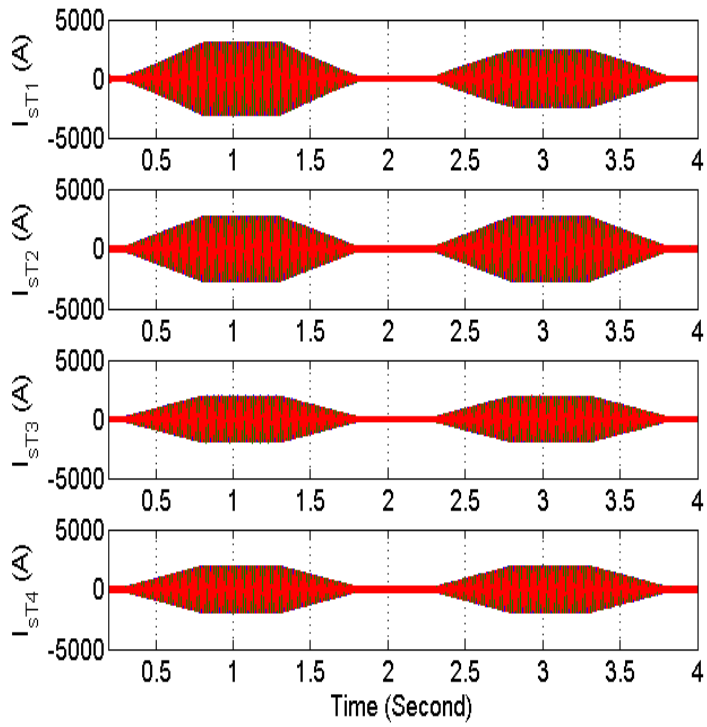
Figure 5-55. Three-phase AC current- Master/slave control under normal operating condition.

155
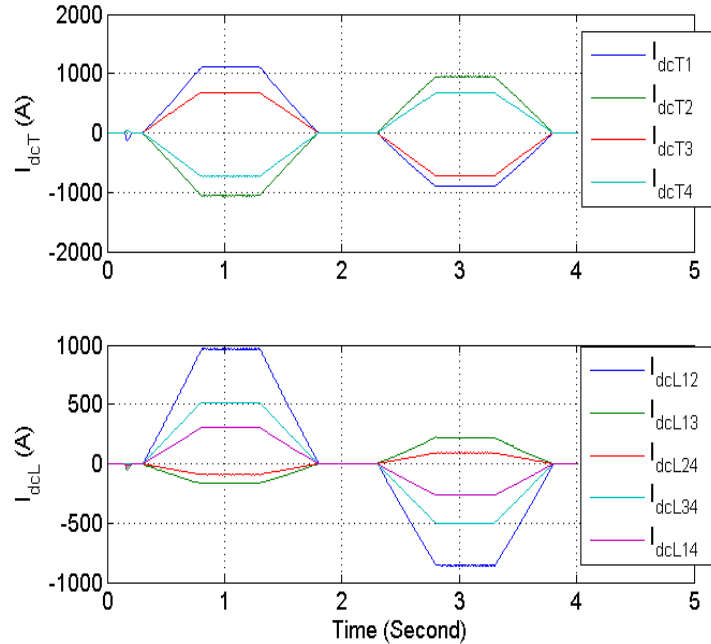
Figure 5-56. DC current- Master/slave control under normal operating condition.

B. Operation of MTDC system with droop control method and dead-band controller under normal operating condition

In this part, the dynamic performance of MTDC system based on droop control method with dead-band controller is evaluated under normal operating condition. In this case, all terminals contribute in power flow control, and dead-band controller in DC voltage controller is also used to improve the performance of MTDC system. The dynamic performance of active power flow for all four terminals is shown in Figure 5-57. The reference value of active power for terminal 1 is increased from zero to 12 (MW) at t=0.3s, and it is varied from 0 to -12 (MW) for terminal 2. In terminal 3, the reference value of active power flow is also changed from 0 to 8.4 (MW), and the reference value of terminal 4 active power flow is

156

changed from 0 to -8.4 (MW). Terminal DC bus voltage is shown in Figure 5-58. The dead-band region in DC voltage controller is between 0.95 pu-1.1 pu. So, DC voltage controller is off when DC bus voltage is within the limit. Once DC bus voltage hits the lower or upper limit, DC voltage controller is enabled. Figure 5-59 shows three-phase AC current for this case scenario. DC currents in all four terminals and different DC transmission lines are also shown in Figure 5-60.
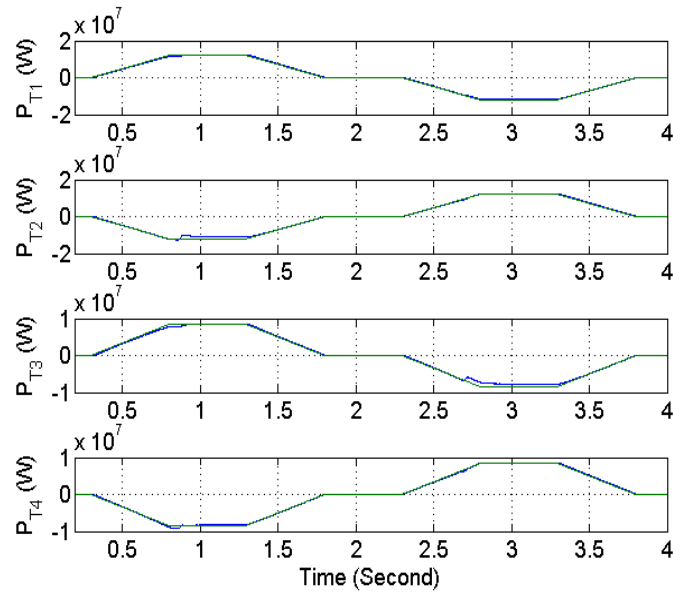
Figure 5-57. Dynamic performance of active power -Droop control with dead-band controller under normal operating condition.

Figure 5-58. Terminal DC bus voltages-Droop control with dead-band controller under normal operating condition.

Figure 5-59. Three-phase AC current- Droop control with dead-band controller under normal operating condition.

158
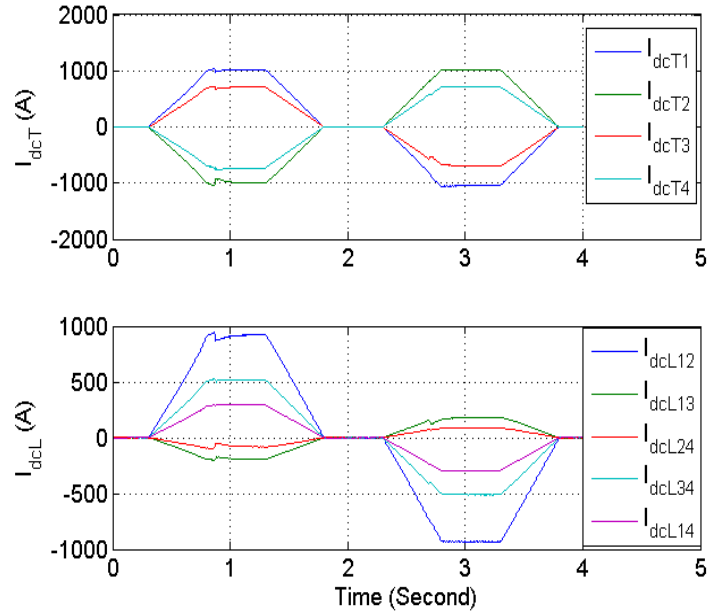
Figure 5-60. DC current- Droop control with dead-band controller under normal operating condition.

C. *Operation of MTDC system with master/slave control method under loss of master terminal*

In this case, the operation of MTDC system with master/slave control method under loss of master converter is explored. In this case, terminal 1 which controls dc bus voltage goes out at t=1.2s. Figure 5-61 shows the dynamic performance of active power flow in all four terminals. As it can be observed, when master terminal goes out, active power flow control in terminal 2, and 4 is lost. DC bus voltage is also shown in Figure 5-62. As can be seen, terminal DC bus voltage is reduced to 5 (kV) which means DC bus voltage control is lost. Three-phase AC current for all four terminals is shown in Figure 5-63. As can be seen, current limiter in the control structure limits AC current in all terminals, and three-phase AC current in terminal 2, and 4 are disturbed when terminal 1 is disconnected at t=1.2s since

159

power flow control in these two terminals is lost. DC currents in all four terminals and different DC transmission lines are also shown in Figure 5-64.
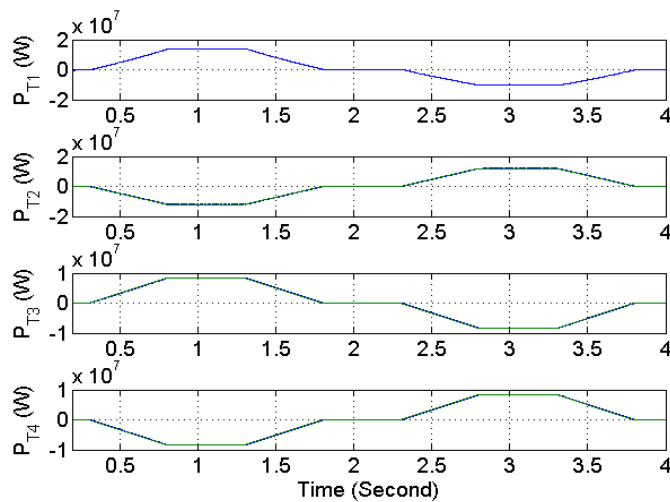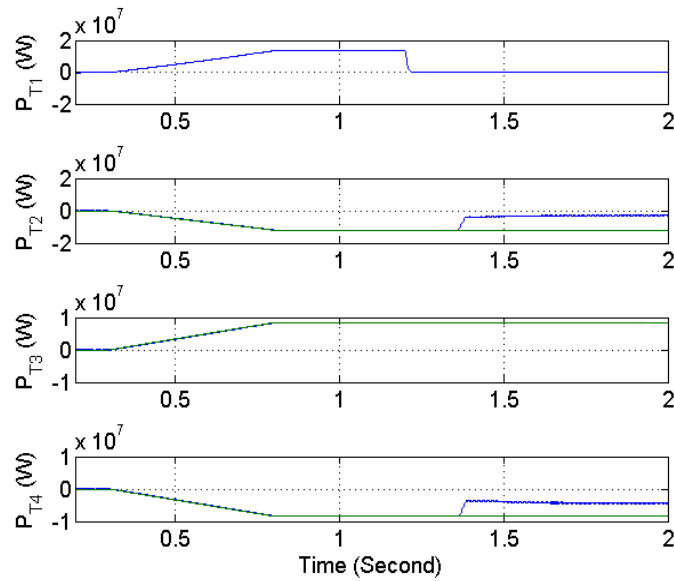

Figure 5-61. Dynamic performance of active power flow- Master/slave control under loss of master terminal.
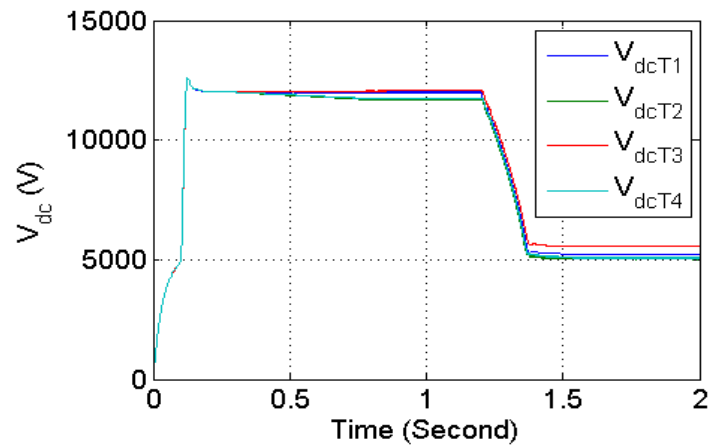
Figure 5-62. Terminal DC bus voltages - Master/slave control under loss of master terminal.
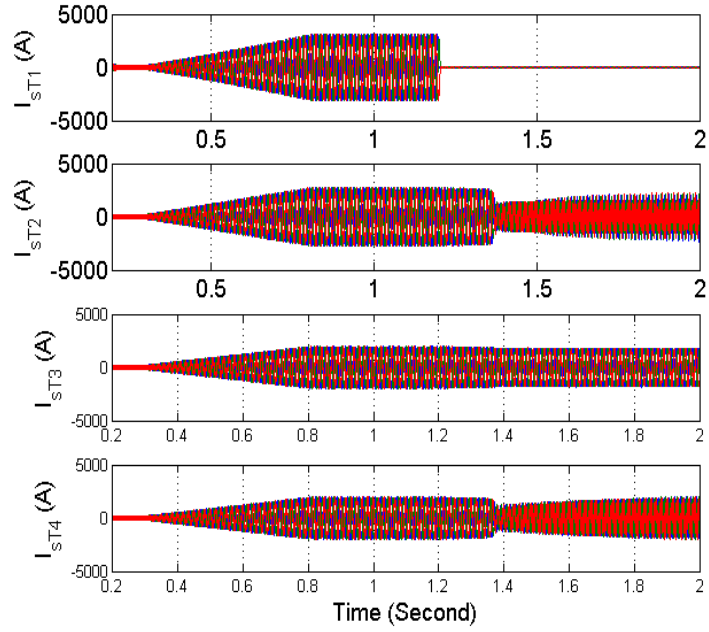
Figure 5-63. Three-phase AC current- Master/slave control under loss of master terminal.
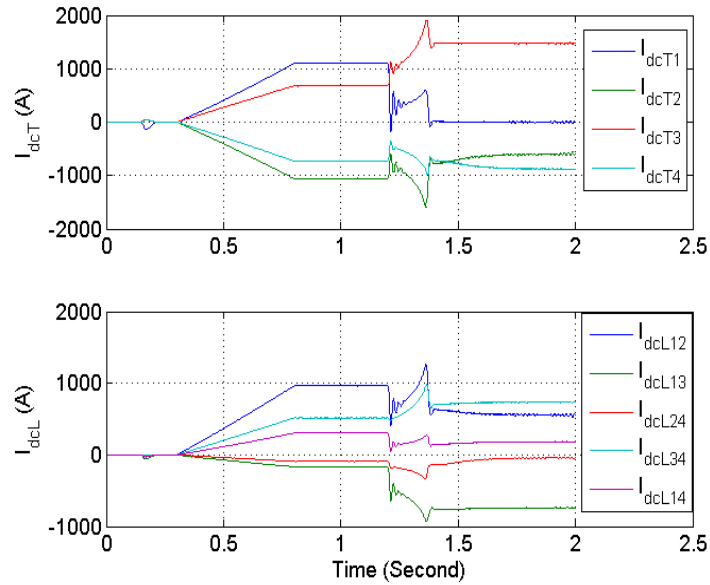
Figure 5-64. DC current- Master/slave control under loss of master terminal.

D. Operation of MTDC system with droop control method and dead-band controller under loss of terminal 1

In this section, the dynamic performance of MTDC system based on droop control method with dead-band controller is evaluated under loss of terminal 1. In this case, terminal 1 is disconnected from the entire DC grid at t=1.2s. The dynamic performance of active power flow in all four terminals is shown in Figure 5-65. As can be seen, active power flows in terminals 2, and 4 are reduced automatically at t=1.2s to balance the active power flow in the entire DC grid when terminal 1 goes out. Terminal DC bus voltage is also shown in Figure 5-66. As can be seen, DC bus voltage is still controlled since other three terminals contribute to control terminal DC bus voltage when terminal 1 is out. Figure 5-67 shows three-phase AC current in all four terminals. As can be observed, the current waveforms in all terminals are limited by current limiter when terminal 1 is out, and they are not distorted. The magnitude of current in terminal 2, and 4 is also reduced due to the fact that the active power flow in these two terminals is reduced to balance the active power flow in the entire MTDC system when terminal 1 goes out. Figure 5-68 also shows DC currents in four DC terminals and different DC transmission lines.
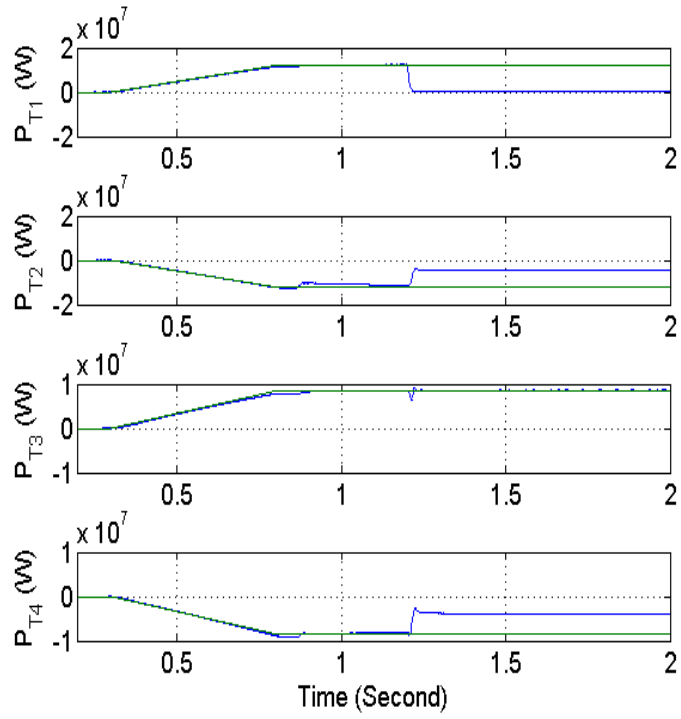
Figure 5-65. Dynamic performance of active power flow-Droop control with dead-band controller under loss of terminal 1.
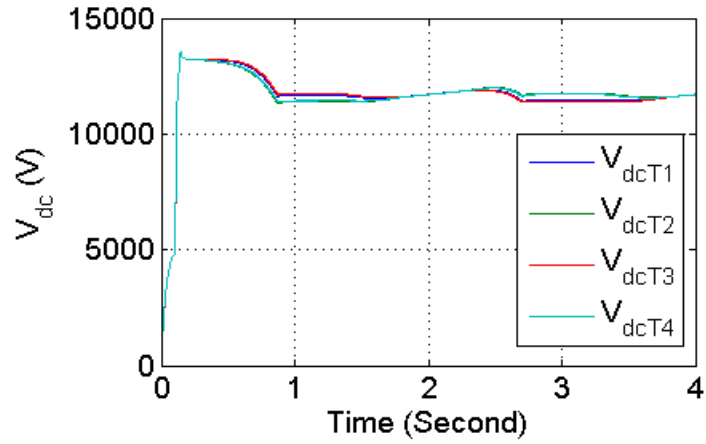

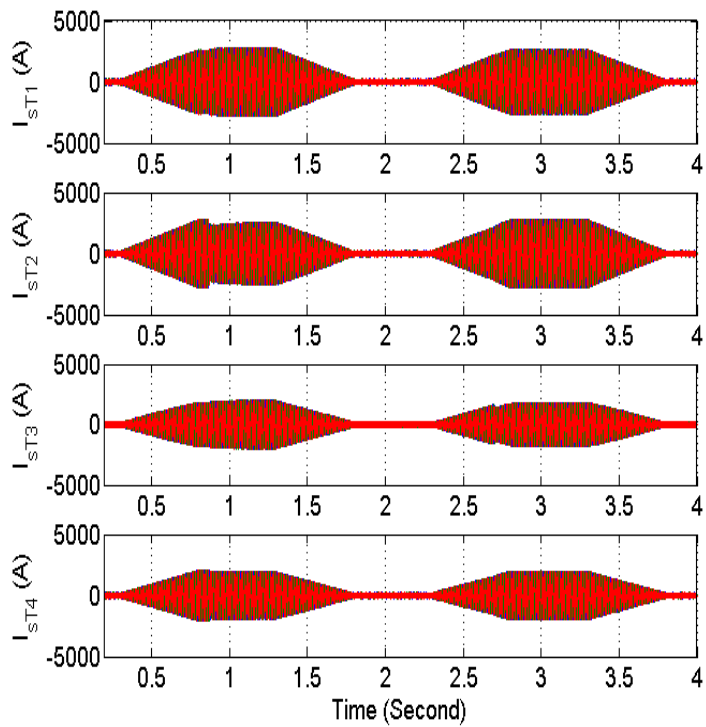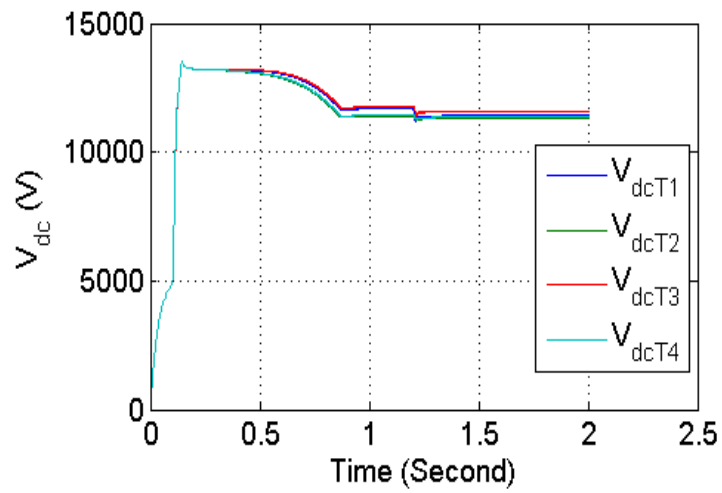Figure 5-66. Terminal DC bus voltages-Droop control with dead-band controller under loss of terminal 1.
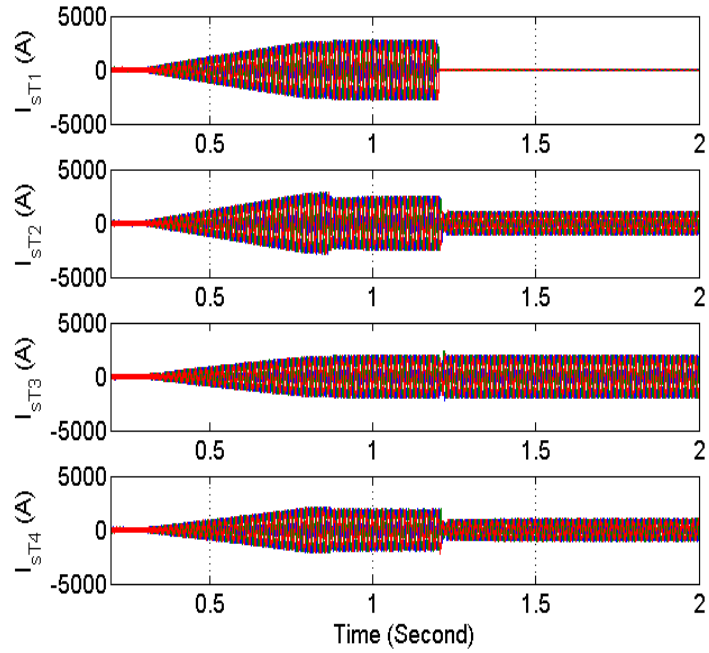
Figure 5-67. Three-phase AC current- Droop control with dead-band controller under loss of terminal 1.
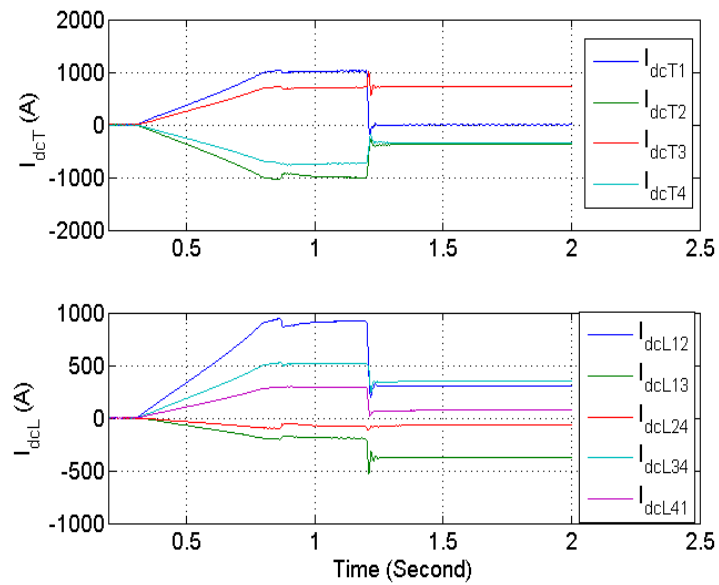
Figure 5-68. DC current- Droop control with dead-band controller under loss of terminal 1.

5.9 Summary

In this section, the dynamic performance of AMS under unbalanced operating condition is examined. Results show that the negative sequence current of MTC based AMS with angle control method is highly dependent on the DC capacitor value, and the capacitor value must be chosen appropriately such that 120 Hz oscillations in the DC link can be tolerated under AC fault operating conditions. A control scheme based on instantaneous active power flow control method is also proposed to make dc bus voltage constant. A supervisory control is also used to determine the switching strategy between angle control method and proposed control method under AC fault operating conditions.

The dynamic performance of high frequency isolated modular converter under DC fault operating condition is also explored. The control algorithm for DC fault operation and recovery after DC fault is proposed. The performance of converter is thoroughly analyzed under DC fault operating condition, and simulation results are presented to validate the control structure under DC fault operating conditions. The high frequency isolated modular converter with the proposed control scheme can be protected against DC fault without using expensive DC circuit breakers. In fact, this advantage allows us to use AC circuit breakers instead of DC circuit breakers for DC fault protection.

The performance of multi-terminal DC grid with DC cable model is also analyzed under DC fault operating condition, and simulation results are presented to validate the control algorithm for DC fault operation and recovery after DC fault.

Also, the dynamic performance of four-terminal DC grid with the master/slave control scheme and droop control method with dead-band controller is investigated under loss of

master converter. It is observed that in master/slave control method, the outage of master terminal results in the outage of the entire MTDC system since in this case, terminal DC bus voltage is only controlled by master terminal. Simulation results are presented to show the superior performance of MTDC grid with the proposed droop control method with dead-band controller under loss of a terminal station.

Chapter 6.   EXPERIMENTAL VERIFICATION

6.1 Controller Hardware-in-the-Loop Test of CSTC in Three Different Modes of Operation

The hardware in the loop implementation of the proposed CSTC is performed with Hardware-in-the-Loop real-time system platform, shown in Figure 6-1. The system platform is based on a scalable application-specific ultralow-latency (ULL) digital processor core. The CSTC converters are simulated by the ULL processor core with simulation time step of 1 µs [99]-[100]. The *TMS320F28335* processor is used in the control board. The CSTC system parameters based on the CHIL model are same as the parameters used in PSCAD simulation. Figure 6-2 shows dynamics of CSTC active power flow in the shunt-shunt mode of operation when the reference value of the CSTC active power flow is varied from 0 MW to 9 MW. As can be seen, the steady-state and transient simulation results of transformer and input active power flow are closely matched with those obtained by the PSCAD simulation results (Figure 2-38).

Dynamics of the CSTC, input and transformer current is presented in Figure 6-3 to verify PSCAD simulation results. Figure 6-4 shows dynamics of converter 1 reactive power flow when it has a step change from 0 to -9 MVAR, and dynamics of converter 2 reactive power flow is shown in Figure 6-5 when the reference value of converter 2 reactive power flow has a step change from 0 to 9 MVAR. As can be observed, the steady-state values of transformer and input reactive power flow are closely matched with the PSCAD simulation results.

In order to validate the proposed algebraic model, the CHIL simulation study has been extended for different CSTC operating points. Figure 6-6-Figure 6-8 shows transformer active and reactive power flow versus CSTC power flow based on steady state values of CHIL simulation results. Comparison of CHIL simulation results and algebraic model results (Figure 2-11, Figure 2-12, and Figure 2-13) show that the behavior of transformer power flow with respect to CSTC operating points can be appropriately represented by the algebraic model.
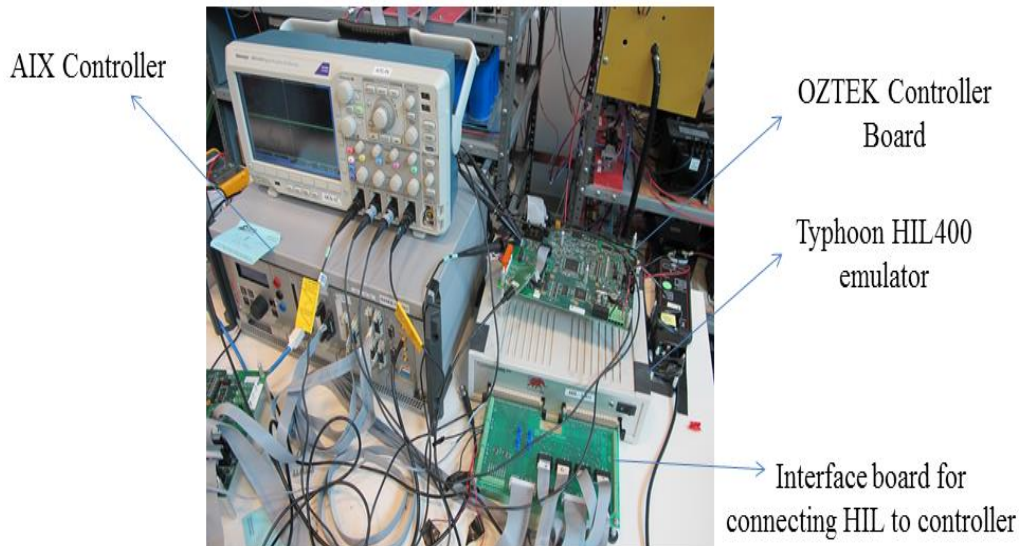
Figure 6-1. The real-time controller hardware-in-the-loop simulation setup to verify the control structure of the CSTC.
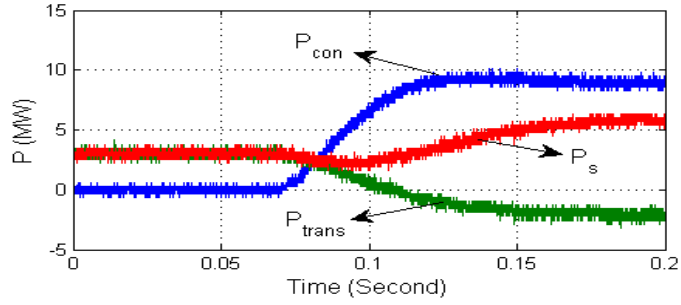
Figure 6-2. Dynamic performance of active power flow when the reference value of active power has a step change from 0 MW to 9 MW (shunt-shunt mode).
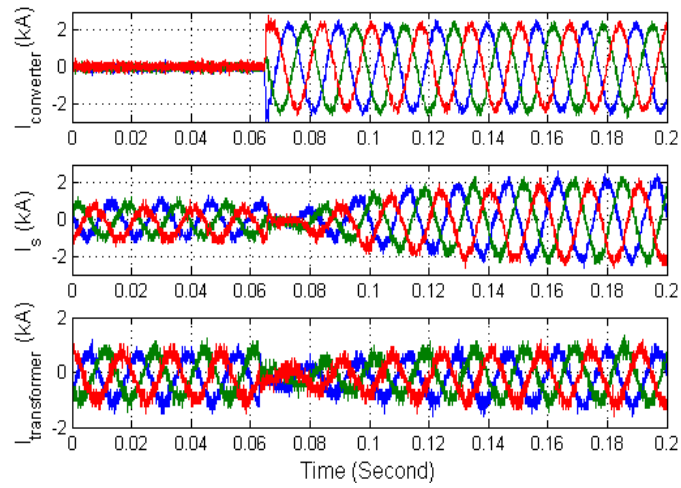
Figure 6-3. Dynamic performance of converter current when active power flow has a step change from 0 MW to 9 MW (shunt-shunt mode).
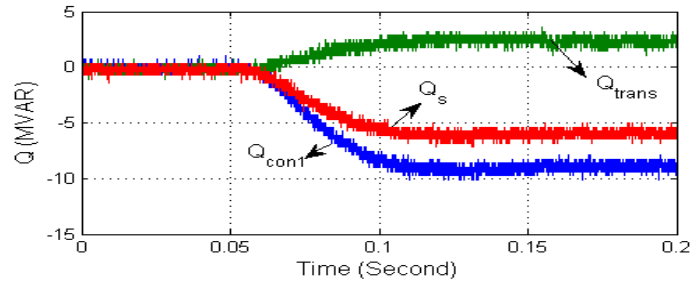
Figure 6-4. Dynamic performance of converter 1 reactive power flow when it has a step change from 0 MVAR to -9 MVAR (shunt-shunt mode).
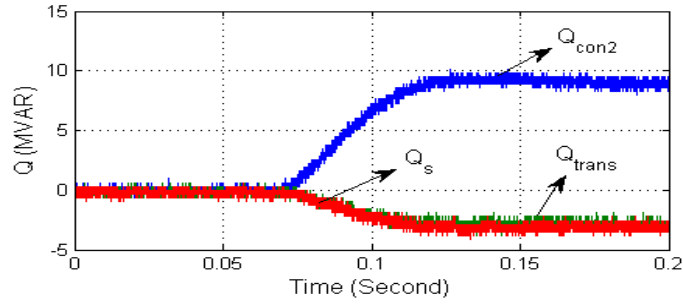
Figure 6-5. Dynamic performance of converter 2 reactive power flow when it has a step change from 0 MVAR to 9 MVAR (shunt-shunt mode).
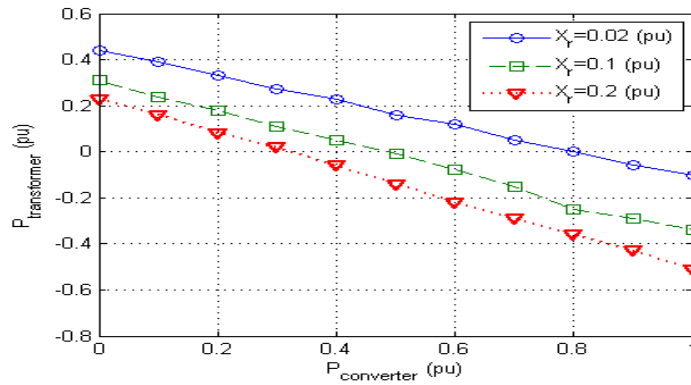
Figure 6-6. Transformer active power flow with respect to converter active power $(Q_1 =0(pu), Q_2 =0 (pu))$.
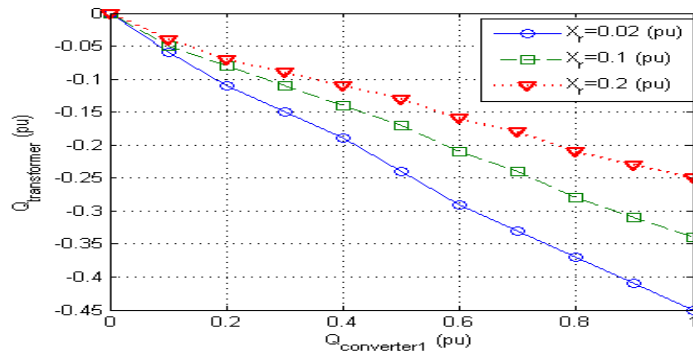
Figure 6-7. Transformer reactive power flow with respect to converter 1 reactive power $(P_{ref} =0(pu), Q_2 =0 (pu))$.
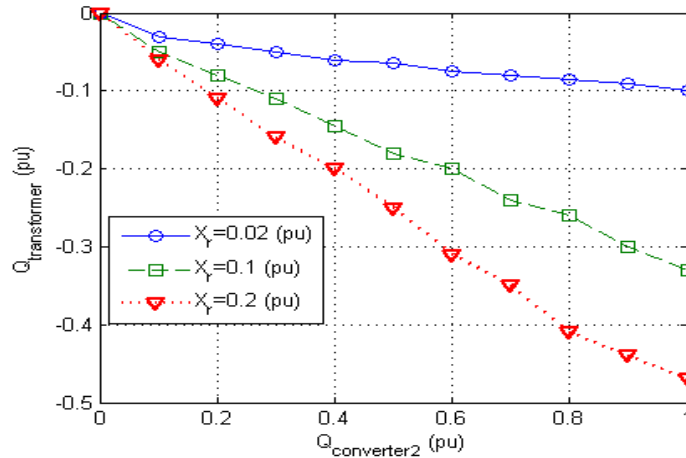
Figure 6-8.   Transformer reactive power flow with respect to converter 2 reactive power
$(P_{ref} = 0(pu), Q_1 = 0 (pu))$.

The dynamic performance of transformer active power flow in series-shunt mode of operation is presented in Figure 6-9 when the reference value of converter 2 active power flow has a step change from 0 to 9 MW. Three phase transformer current is also shown in Figure 6-10 for this case scenario. As can be seen, dynamics of transformer ac current is similar to the result obtained by PSCAD. Dynamics of transformer reactive power flow in series-shunt mode of operation is shown in Figure 6-11 when the reference value of converter 1 reactive power flow is varied from 0 to 9 MVAR. Figure 6-12 also shows dynamics of input reactive power flow when the reference value of converter 1 reactive power has a step change from 0 to 9 MVAR. As can be seen, CHIL simulation results are closely matched with PSCAD simulation results.

Figure 6-9. Dynamics of transformer active power flow when the reference value of converter 2 active power has a step change from 0 MW to 9 MW (series-shunt mode).

Figure 6-10. Dynamics of transformer current when the reference value of converter 2 active power has a step change from 0 MW to 9 MW (series-shunt mode).

Figure 6-11. Dynamics of transformer reactive power flow when the reference value of converter 2 reactive power has a step change from 0 MVAR to 9 MVAR (series-shunt mode).

172
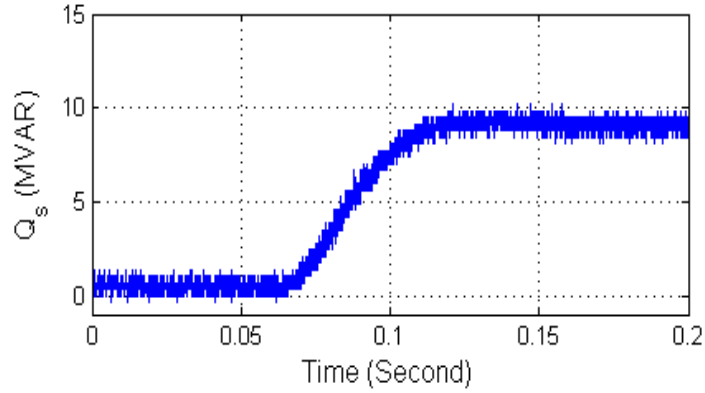
Figure 6-12. Dynamics of input reactive power flow when the reference value of converter 1 reactive power has a step change from 0 MVAR to 9 MVAR (series-shunt mode).

The dynamic performance of transformer active power flow in series-series connecting configuration is shown in Figure 6-13 when the reference value of transformer active power flow has a step change from 0 to 12MW. Three phase transformer current is also shown in Figure 6-14 for this case scenario. The transformer reactive power flow is also regulated at 0 MVAR.

Figure 6-13. Dynamics of transformer active power flow when the reference value of CSTC active power flow has a step change from 0 MW to 12 MW (series-series mode).

Figure 6-14. Dynamics of transformer current when the reference value of CSTC active power flow has a step change from 0 MW to 12 MW (series-series mode).

6.2 Controller Hardware-in-the-Loop Test of MTC Based AMS under Fault Operating Condition

The dynamic performance of the MTC system under unbalanced operating condition is presented in Figure 6-15~Figure 6-20. In this case, NPC converter is used in CSTC configuration. The unbalanced three-phase input voltages and the extracted voltage angle is shown in Figure 6-15 (V_a=20V, V_b=40V, V_c=60V). Figure 6-16 shows line to line output voltage of three-level NPC converter. Total dc bus voltage, and dc voltage of each capacitor in three-level NPC converter is shown in Figure 6-17. Figure 6-18~Figure 6-20 show three-phase input voltages and three-phase input currents when the reference value of reactive power is regulated at 0 pu. As can be seen, the CSTC converter draws sinusoidal current with unity power factor.
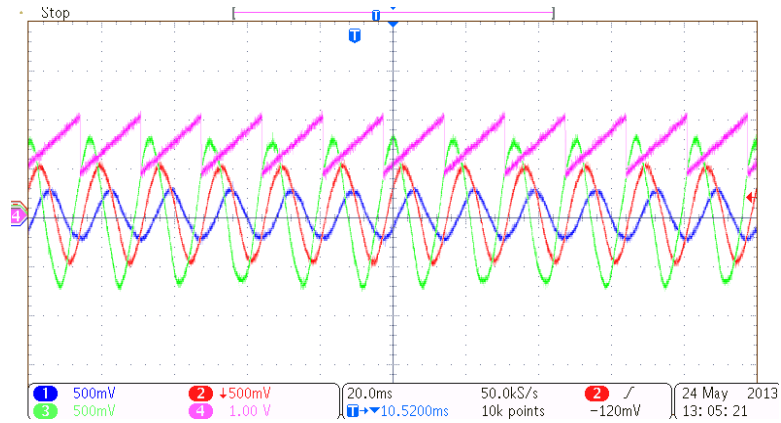
Figure 6-15. Unbalanced three-phase input voltages.
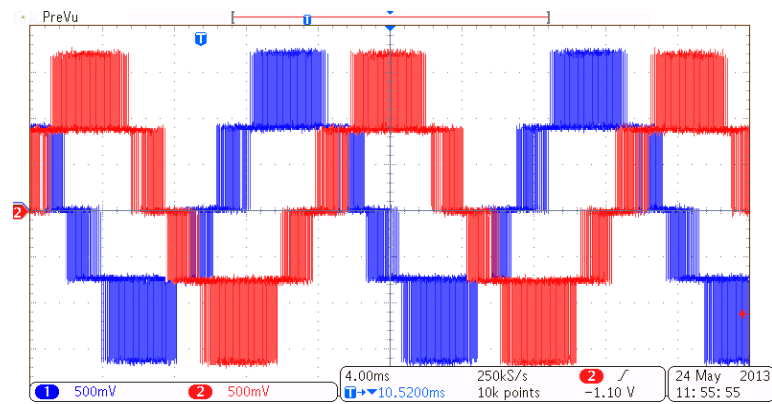
Figure 6-16. Line to line converter output voltages.
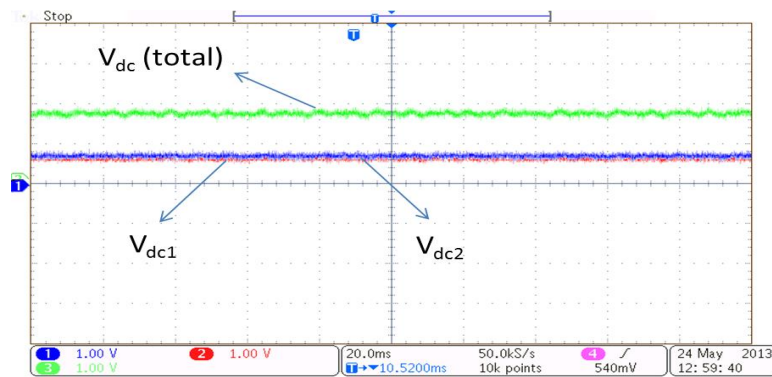
Figure 6-17. DC bus voltage (Unbalanced operating condition).
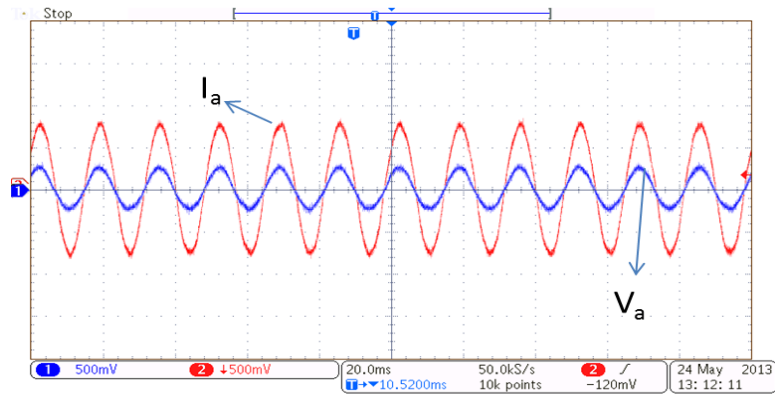
Figure 6-18. V_a and I_a for Q_{ref}=0 (Unbalanced operating condition).
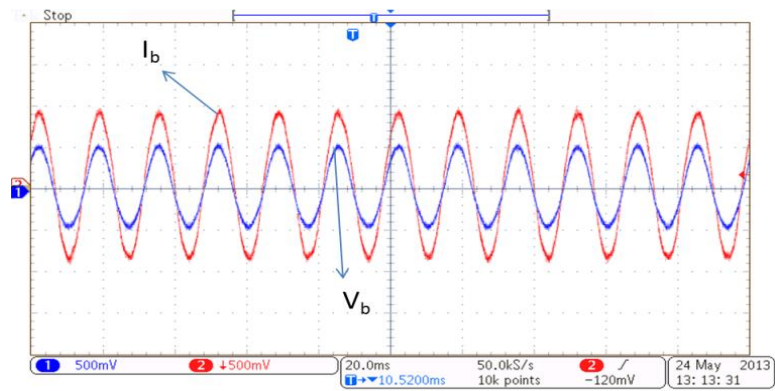
Figure 6-19. V_b and I_b for Q_{ref}=0 (Unbalanced operating condition).
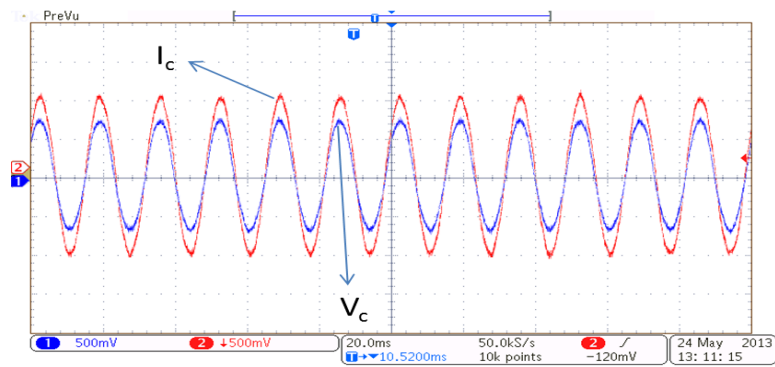
Figure 6-20. V_c and I_c for Q_{ref}=0 (Unbalanced operating condition).

6.3 Experimental Verification of CSTC in Three Different Modes of Operation

The schematic of the laboratory scale test-bed for CSTC system is shown in Figure 6-21, and the CSTC experimental test bed is also shown in Figure 6-22. The specifications of the experimental test bed have been summarized in Table 6-1. Single phase transformers are chosen for MTC since we want to study saturation effect of transformers when they are connected in series. This test bed can also serve as a Transient Network Analyzer (TNA) to benchmark MTC based CSTC with available technologies such as UPFC, SSSC, and IPFC. As can be observed from experimental test bed, a phase shifting transformer is used to produce different transmission angles. This configuration helps us to create a transmission angle between the sending-end and receiving-end without using two different voltage sources. The produced transmission angle θ depends on the windings turn ratio. The proposed transmission angle is obtained by (6.1) based on the voltage rating of phase shifting transformer.

$$\frac{n_H}{n_L} = \frac{\sqrt{3}}{2\tan(\frac{\theta}{2})} \Rightarrow \frac{230}{36} = \frac{\sqrt{3}}{2\tan(\frac{\theta}{2})} \Rightarrow \theta = 15.44^{\circ} \tag{6.1}$$

Table 6-1.   Specifications of CSTC Experimental Test Bed

Line-to-line voltage	E	208 V
Base Power	S	3 KVA
Line frequency (grid)	f	60 Hz
sending-end Leakage inductance	L_s	5 mH
Transformer Leakage inductance	L_T	5 mH
receiving-end Leakage inductance	L_r	5 mH
Switching frequency	f_{sw}	10 kHz
MTC transformer rating	S_c	15 kVA
Nominal operation of MTC transformer	S_{cn}	5 kVA
Grid main transformer	S_T	15 kVA
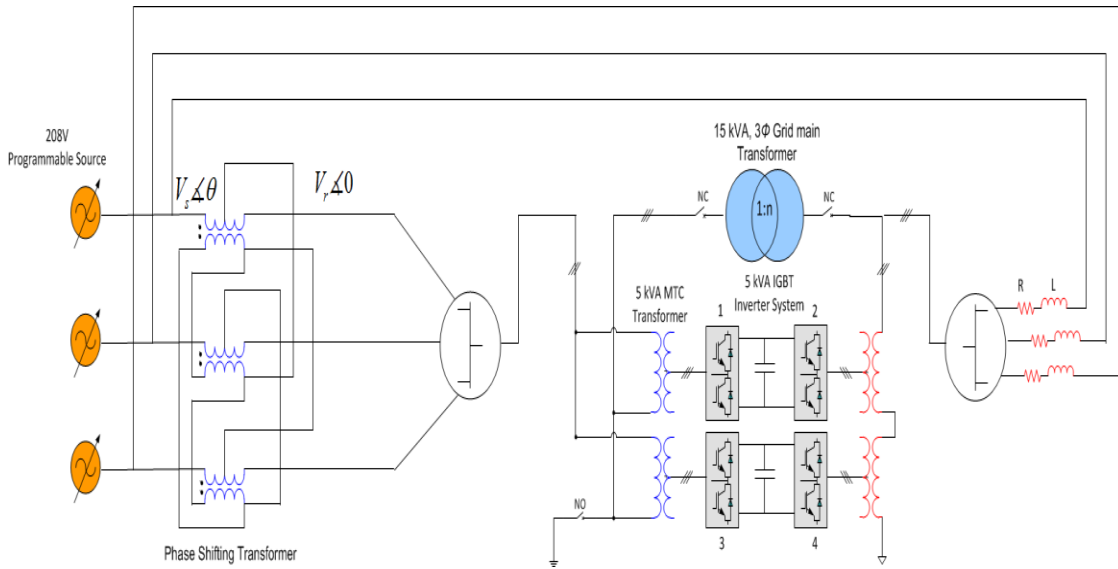
Figure 6-21. Schematic of the laboratory scale test-bed for CSTC system.
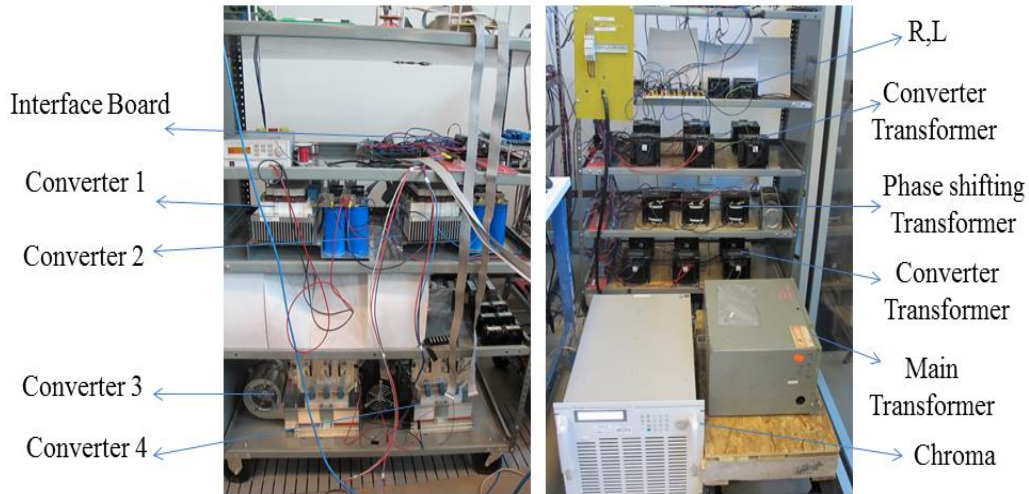
Figure 6-22. Experimental test-bed for the proposed MTC-based CSTC system.

Figure 6-23 shows dynamics of active power flow when the reference value of MTC-based CSTC active power flow is varied from 0 pu to 1 pu in shunt-shunt mode of operation. As can be seen, transformer active power flow is changed from 0.67 pu to 0 pu, and input active power flow is increased form 0.67pu to 1pu. In fact, experimental results are slightly different from the algebraic model results since power losses of the switches in the MTC-based CSTC converters are not considered in the algebraic model. However, total power losses can be added to active power flow equations to obtain the exact algebraic model. Dynamic performance of converter 2, transformer and input current are shown in Figure 6-24, Figure 6-25, and Figure 6-26 respectively for this case scenario. It can be noted that transformer current is reduced when the reference value of the MTC-based CSTC active power flow is increased from 0 pu to 1 pu.
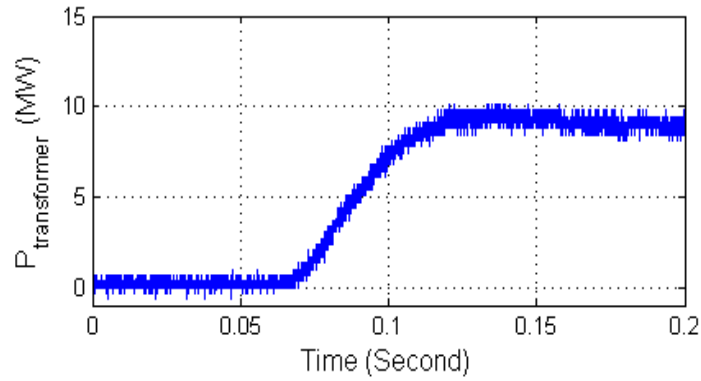
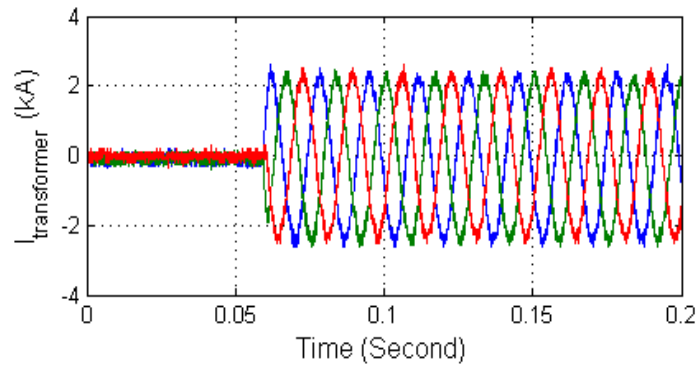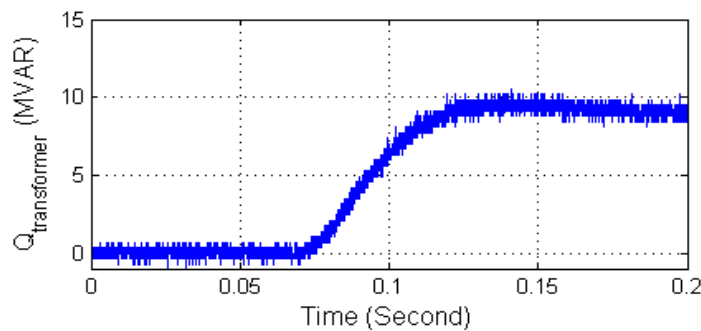Figure 6-27 shows dynamics of transformer reactive power flow when the reference value of converter 1 reactive power has a step change from 0 pu to -1 pu, and dynamics of transformer reactive power flow with respect to converter 2 reactive power flow is also shown in Figure 6-28. The steady-state values of transformer reactive power flow are closely matched with the results obtained from the proposed algebraic model.
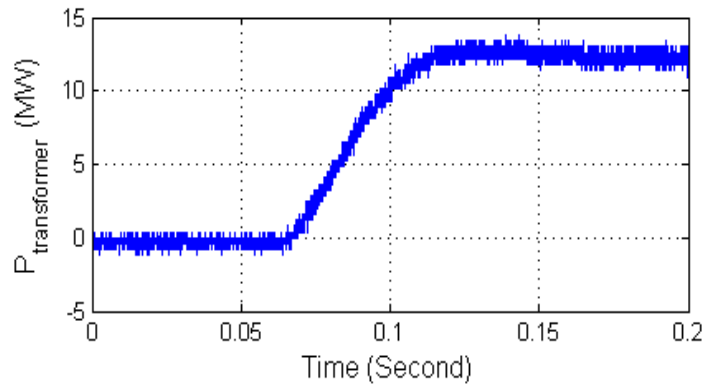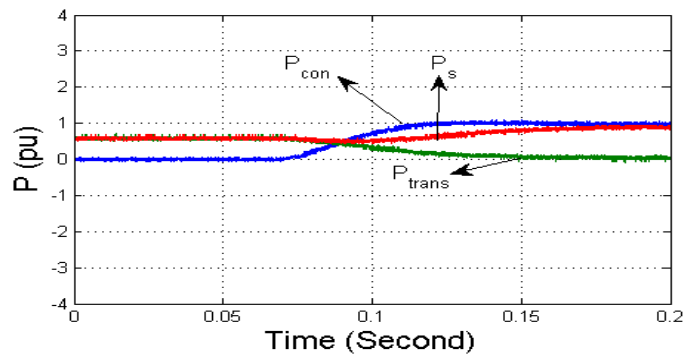

Figure 6-23. Dynamics of active power flow when the reference value of active power has a step change from 0 pu to 1.0 pu (shunt-shunt mode).
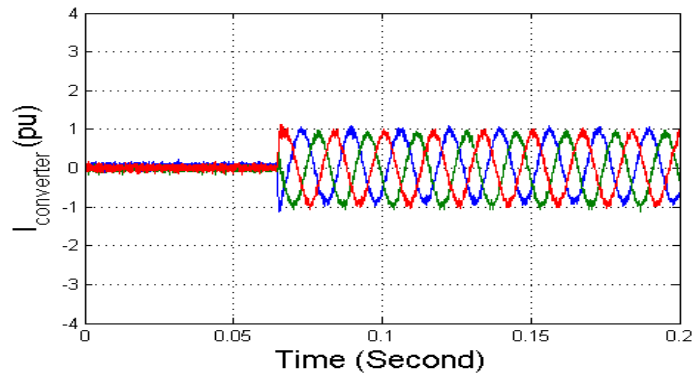
Figure 6-24. Dynamics of converter current when active power flow has a step change from 0 pu to 1.0 pu (shunt-shunt mode).

180
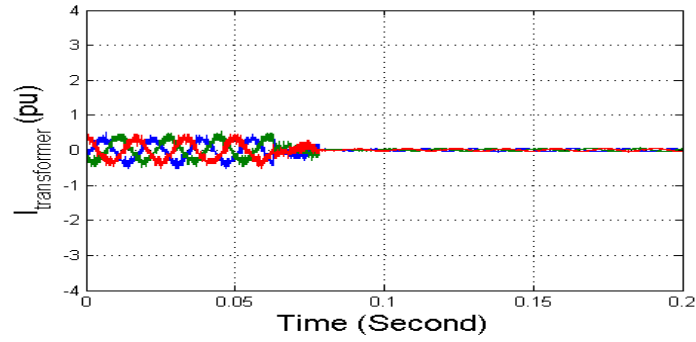
Figure 6-25. Dynamics of transformer current when active power flow has a step change from 0 pu to 1.0 pu (shunt-shunt mode).
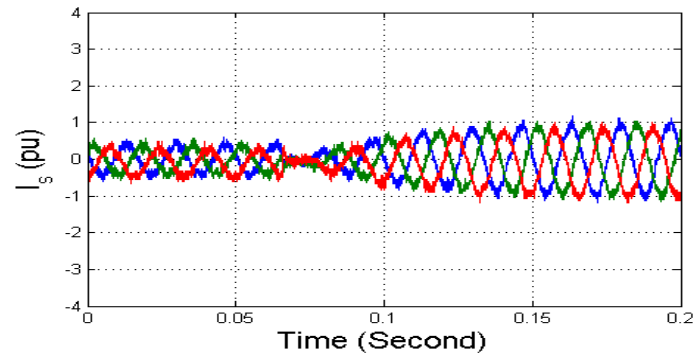
Figure 6-26. Dynamics of input current when active power flow has a step change from 0 pu to 1.0 pu (shunt-shunt mode).
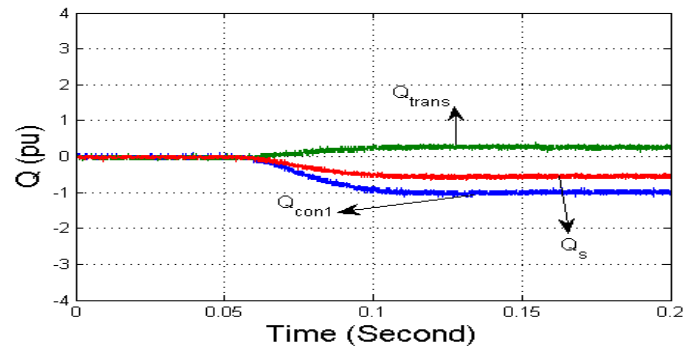
Figure 6-27. Dynamics of converter1 reactive power flow when it has a step change from 0 pu to -1.0 pu (shunt-shunt mode).
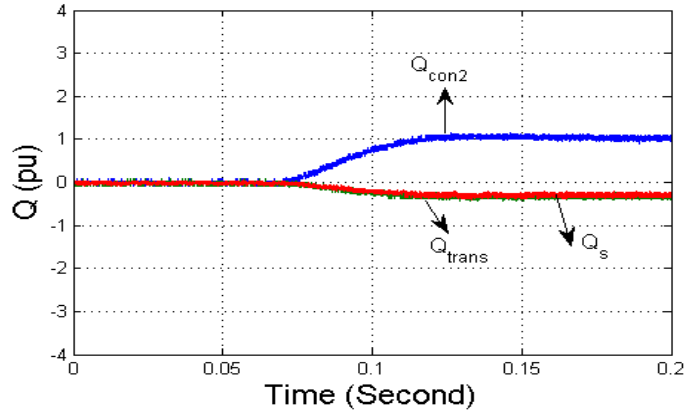
Figure 6-28. Dynamics of converter2 reactive power flow when it has a step change from 0 pu to 1.0 pu (shunt-shunt mode).

The dynamic performance of transformer active power flow in the series-shunt mode of operation is presented in Figure 6-29 when the reference value of MTC-based CSTC active power flow has a step change from 0pu to 1pu. Three-phase transformer current is shown in Figure 6-30 for this case.

Figure 6-31 shows dynamics of transformer reactive power flow when the reference value of reactive power flow for converter 2 has a step change from 0 to 1pu. Transformer current is also shown in Figure 6-32 for this case scenario. As can be seen, the reference values of converter 2 active and reactive power flow can be directly used for transformer power flow control.

182
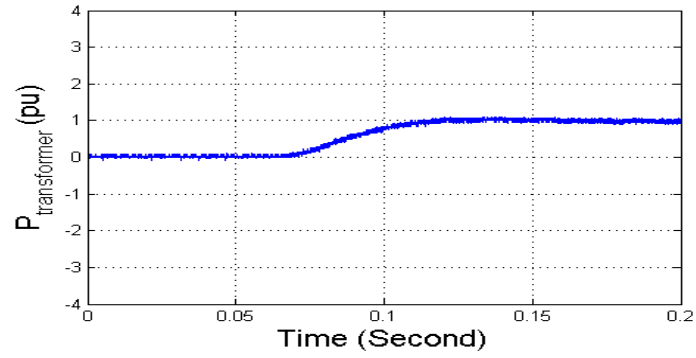
Figure 6-29. Dynamics of transformer active power flow when it has a step change from 0 pu to 1.0 pu (series-shunt mode).
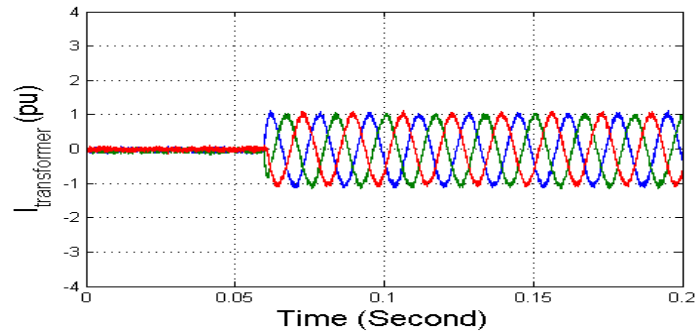
Figure 6-30. Dynamics of transformer current when active power flow has a step change from 0 pu to 1.0 pu (series-shunt mode).
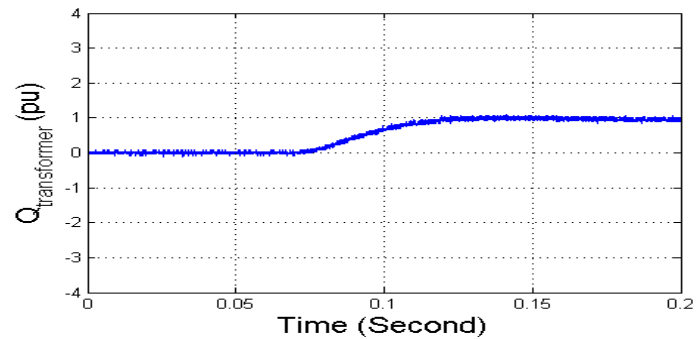
Figure 6-31. Dynamics of transformer reactive power flow when the reference value of converter 2 reactive power flow has a step change from 0 pu to 1.0 pu (series-shunt mode).
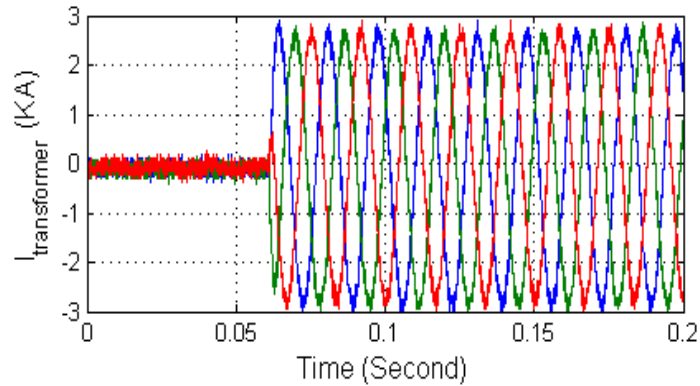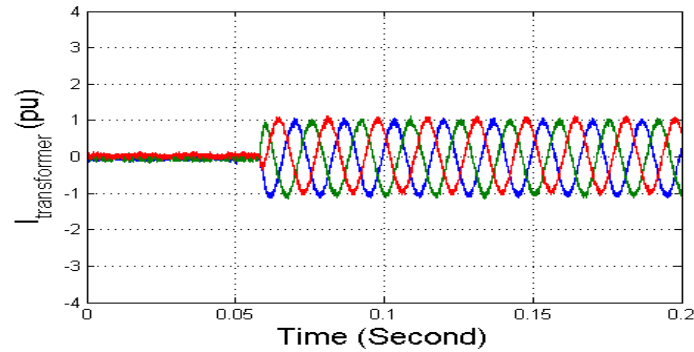
Figure 6-32. Dynamics of transformer current when converter 2 reactive power flow has a step change from 0 pu to 1.0 pu (series-shunt mode).

6.4   Experimental Verification of MTC Based AMS

The AMS experimental test bed is shown in Figure 6-33. The specifications of the experimental testbed can be summarized in Table 6-2. OZTEK controller is used to implement different control methods.

Dynamics of reactive power in the rectifier side of AMS based on angle control method is shown in Figure 6-34 under normal operating conditions. Figure 6-35 also shows dynamics of three phase ac current for this case scenario. The unbalanced three-phase input voltages and the extracted voltage angle is shown in Figure 6-36. As can be seen, there is 50% voltage sag in phase-a. The dc bus voltage and three phase ac current based on angle control method are shown in Figure 6-37, and Figure 6-38 respectively. Figure 6-39 shows dc bus voltage based on instantaneous active power method under unbalanced operating conditions. The stiffness of dc bus voltage is evident in Figure 6-39. As can be seen, the proposed control method makes the instantaneous active power constant without any oscillating terms, and it maintains a robust dc link voltage under unbalanced operating condition. Three-phase ac

current is also illustrated in Figure 6-40. Figure 6-41~Figure 6-43 also show the reference and measured value of three phase ac current based on instantaneous active power control method under unbalanced operating conditions.

Table 6-2.   Specifications of AMS Hardware prototype

Line-to-line peak voltage	E	208 V
Line frequency (grid)	f	60 Hz
sending-end Leakage inductance	L_s	5 (mH)
receiving-end Leakage inductance	L_r	5 (mH)
Switching frequency	f_{sw}	10 (kHz)
Converter Transformer	S_c	15 (kVA)
DC link capacitance	C_{DC}	2.5 (mF)

Figure 6-33. Experimental test-bed for Active Mobile Substation based on 3-level NPC converter.
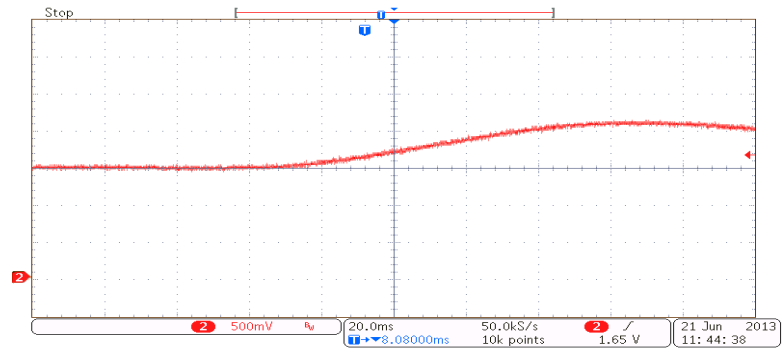
Figure 6-34. Dynamics of reactive power when reactive power has a step change from 0 pu to 1.0 pu under normal operating condition (Angle control).
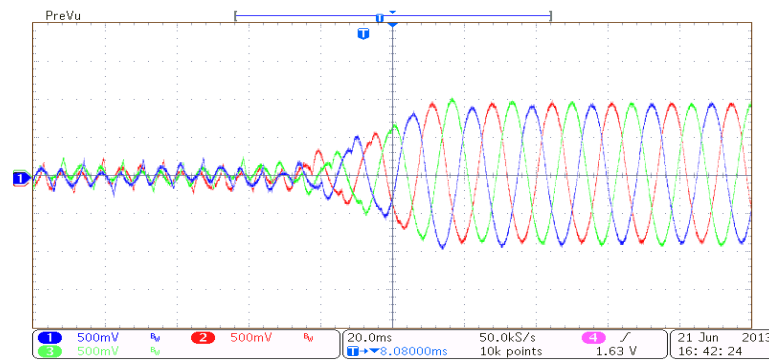
Figure 6-35. Converter current when reactive power has a step change from 0 pu to 1.0 pu under normal operating condition (Angle Control).
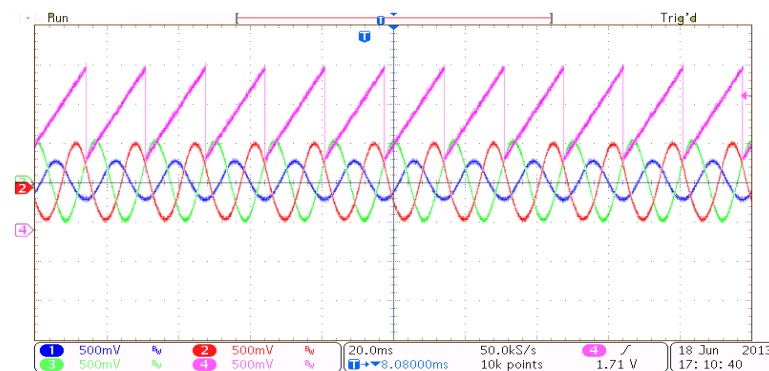
Figure 6-36. Unbalanced three-phase input voltages and extracted voltage angle.
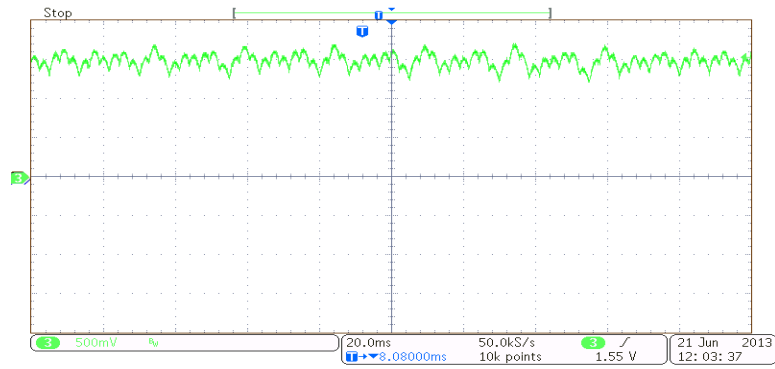
Figure 6-37. DC bus voltage under unbalanced operating conditions (Angle control method).
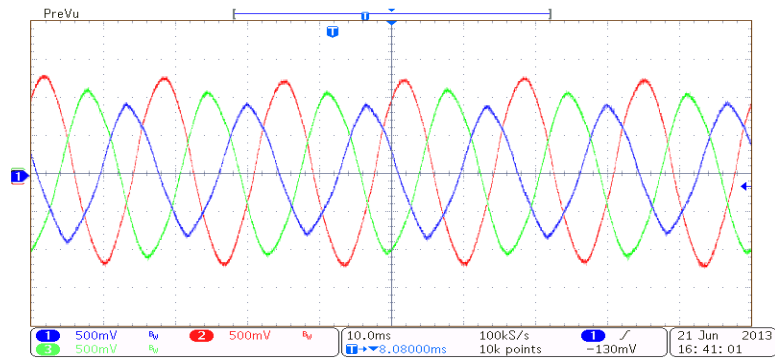
Figure 6-38. Dynamics of three phase ac current under unbalanced operating conditions (Angle control method).
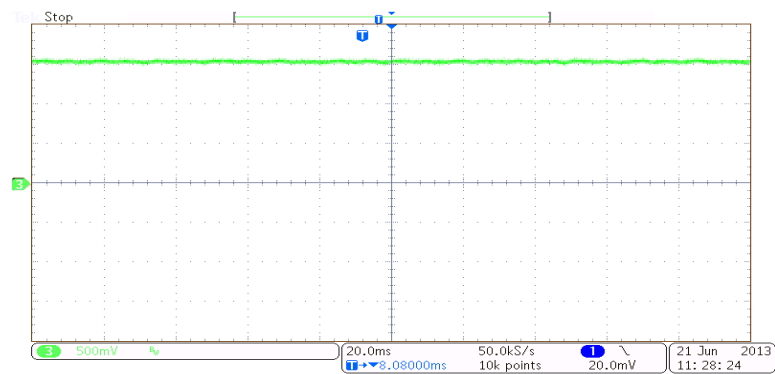
Figure 6-39. DC bus voltage under unbalanced operating conditions (instantaneous active power control method).
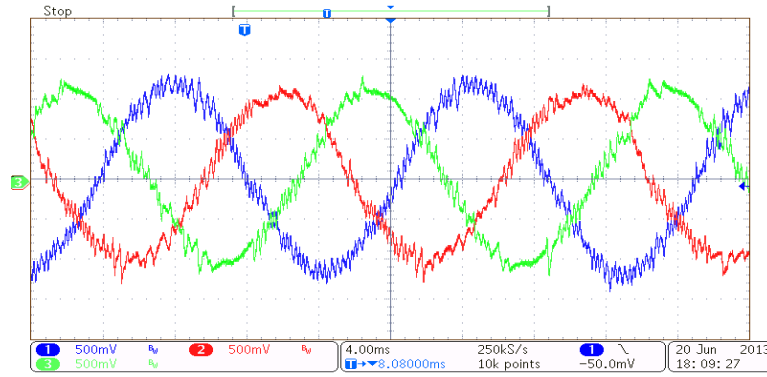
Figure 6-40. Three phase ac current under unbalanced operating conditions (instantaneous active power control).
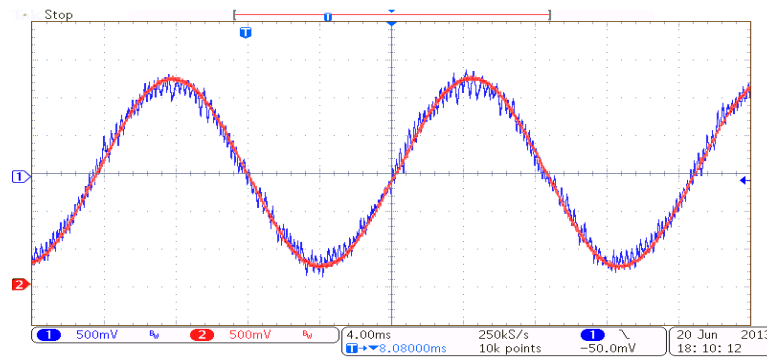
Figure 6-41. The reference and measured value of phase-a ac current.
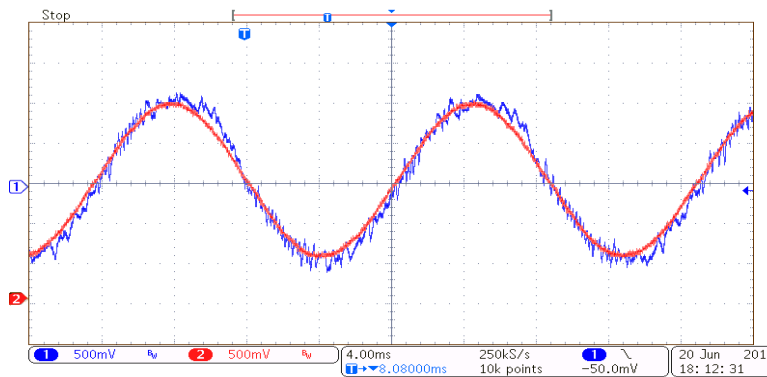
Figure 6-42. The reference and measured value of phase-b ac current.
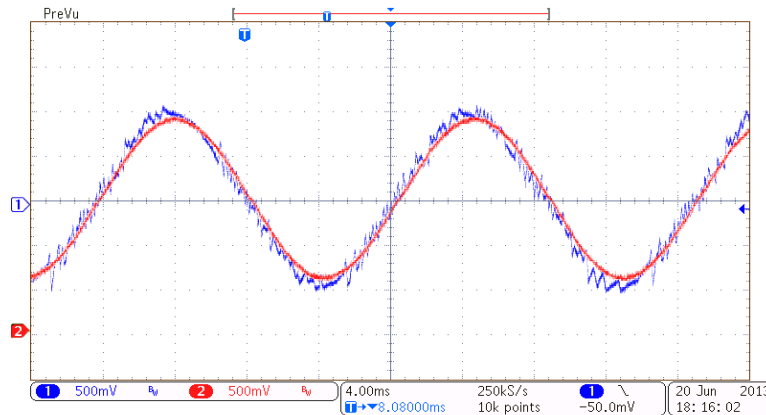
Figure 6-43. The reference and measured value of phase-c ac current.

6.5 Controller Hardware-in-the-Loop Test of High Frequency Isolated Modular Converter through Real Time Digital Simulation

The controller hardware-in-the-loop implementation of the high frequency isolated modular converter is performed with Real Time Digital Simulator (RTDS), shown in Figure 6-44. The high frequency isolated modular converter is simulated by the Real Time Digital Simulator with simulation time step of 20 μs. The *Concerto control board* is used as the main controller. The system parameters based on the RTDS model are tabulated in Table 6-3. Figure 6-45 shows three DC capacitor voltages for phase-A, B, and C regulated at 1 kV. Terminal DC bus voltage regulated at 3 kV is also shown in Figure 6-46. Figure 6-47 also shows DC current regulated at 1 kA for 3 MW active power flow. Three-phase AC current is also shown in Figure 6-48.

Table 6-3.   High frequency isolated modular converter system parameters in RTDS

Terminal rated power	P	3 MVA
Terminal voltage reference	V_{dc}	3 kV
Module number (per terminal)	N	3
AC/DC capacitor voltage	$V_{(AC/DC)}$	1 kV
DC/DC capacitor voltage	$V_{(DC/DC)}$	1 kV
Capacitor value	C	10 mF
AC/DC PWM switching frequency	f_{sw} (AC/DC)	5 kHz
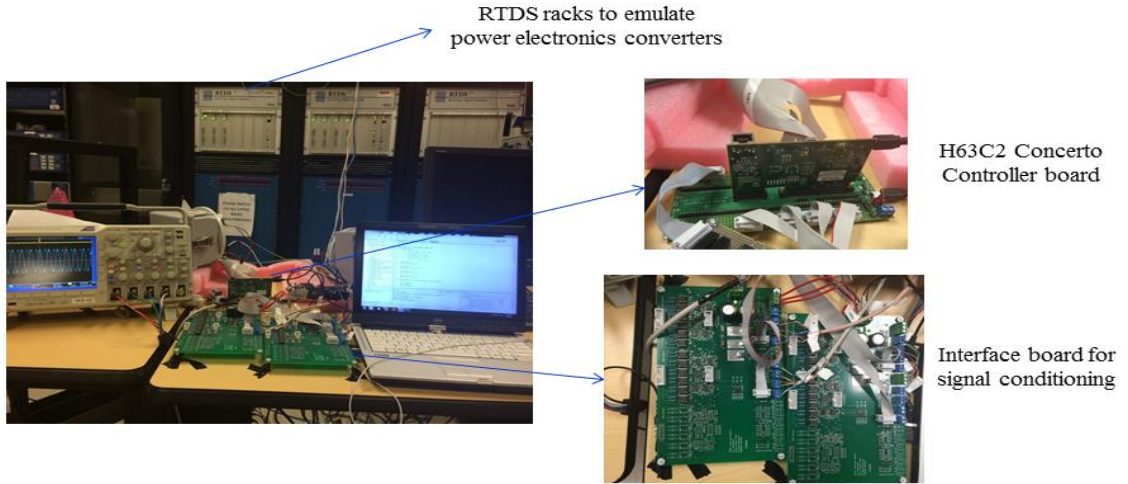
Figure 6-44. The real-time controller hardware-in-the-loop simulation setup to verify the control structure of the high frequency isolated modular converter through Real Time Digital Simulator (RTDS).
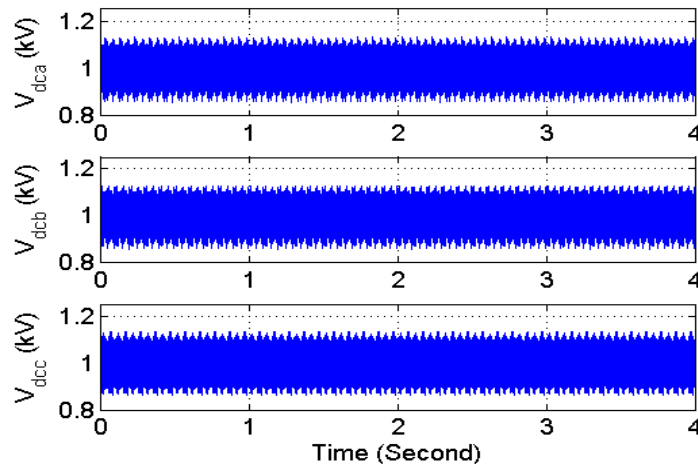
Figure 6-45. Capacitor DC voltages (V_{dc} (module)=1 (kV))- CHIL result.
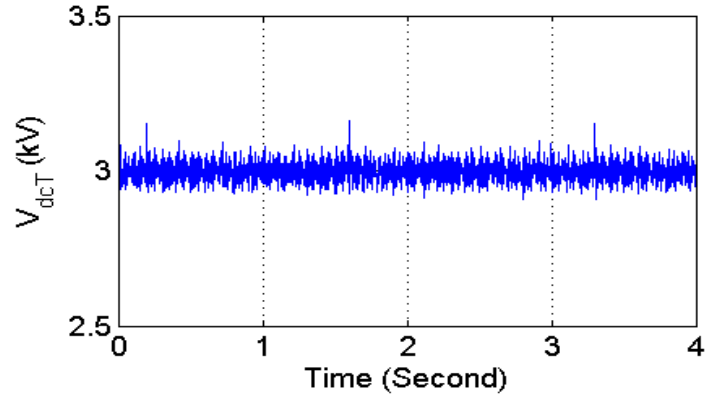
Figure 6-46. Terminal DC bus voltage (V_{dc} (terminal)=3 (kV))- CHIL result.
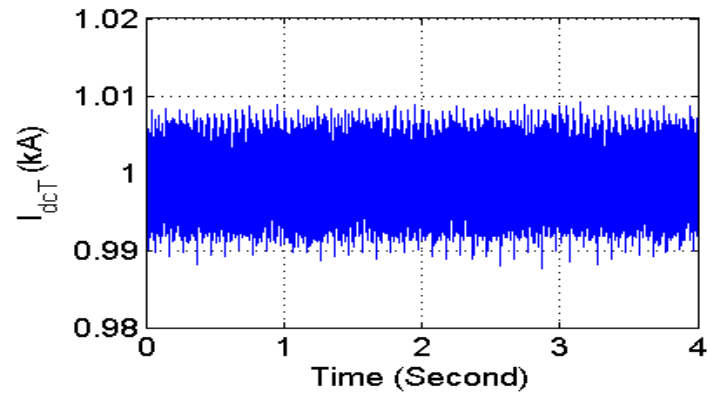
Figure 6-47. Terminal DC current- CHIL result.
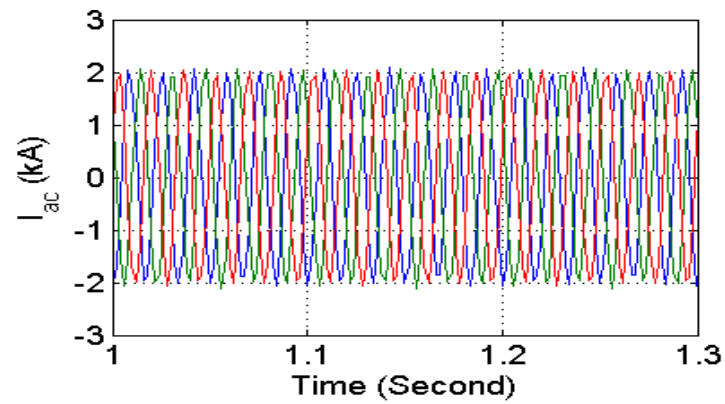
Figure 6-48. Three-phase AC current- CHIL result.

6.6 Experimental Verification of High Frequency Isolated Modular Converter

The high frequency isolated modular converter experimental test bed is shown in Figure 6-49, and the specifications of the experimental test bed have been summarized in Table 6-4. The Voltage Transformation Module (VTM) shown in Figure 6-50 is used as a chip DC/DC converter in the experimental test-bed. The H63C2 Concerto controller board is used in the control board. With the Concerto board plus the designed interface board, all the required switching signals for the 9-module converter are provided. Three DC capacitor voltages for phase-A, B, and C regulated at 35V and terminal DC bus voltage regulated at 315V are shown in Figure 6-51. Figure 6-52 shows three-phase input voltages and currents when the reference value of reactive power is regulated at 0 VAR. As can be seen, the converter draws sinusoidal current with unity power factor. Figure 6-53 also shows three DC capacitor voltages for phase-A, B, and C regulated at 50V and terminal DC bus voltage regulated at 450V. As can be seen, all DC capacitor voltages for both case scenarios (V_{dcref} *(module) =35V, and 50V*) are equal to each other showing the validity of the proposed phase and module voltage balancing controller.

Table 6-4.   High frequency isolated modular converter experimental test-bed parameters

Terminal AC input voltage (rms phase)	E	80 V
AC side inductor	L_s	5 mH
Module number (per terminal)	N	9
Capacitor value	C	4.7 mF
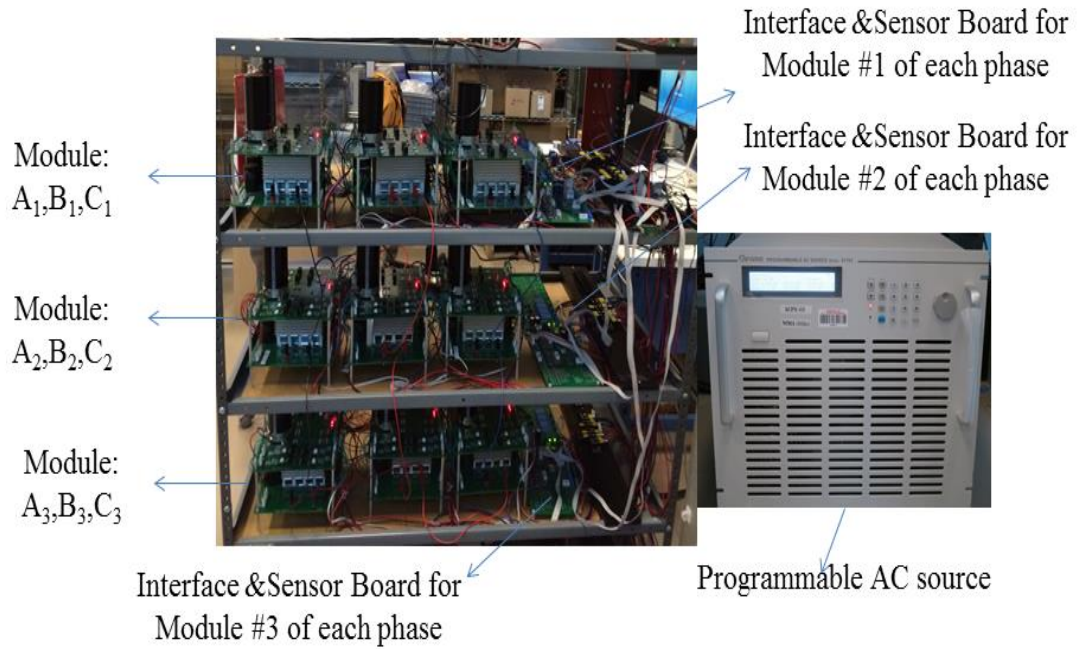
Figure 6-49. Experimental test-bed for high frequency isolated modular converter.
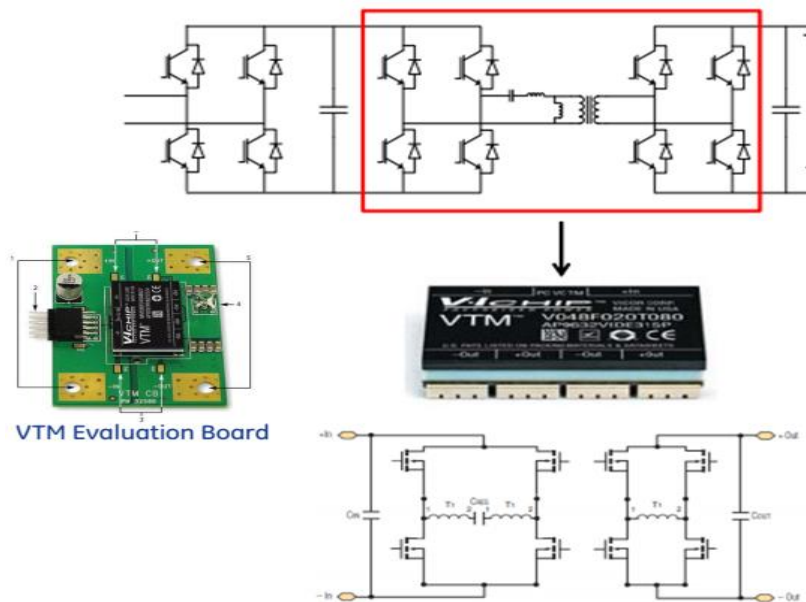
Figure 6-50. Voltage transformation module (VTM) as a chip DC/DC converter in experimental test-bed.
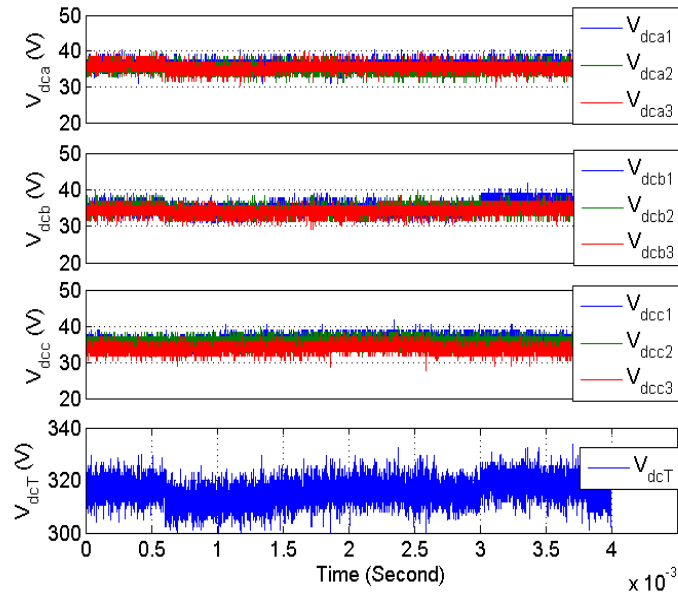
Figure 6-51. Terminal and capacitor DC voltages (V_{dc} (module)=35 (V)).
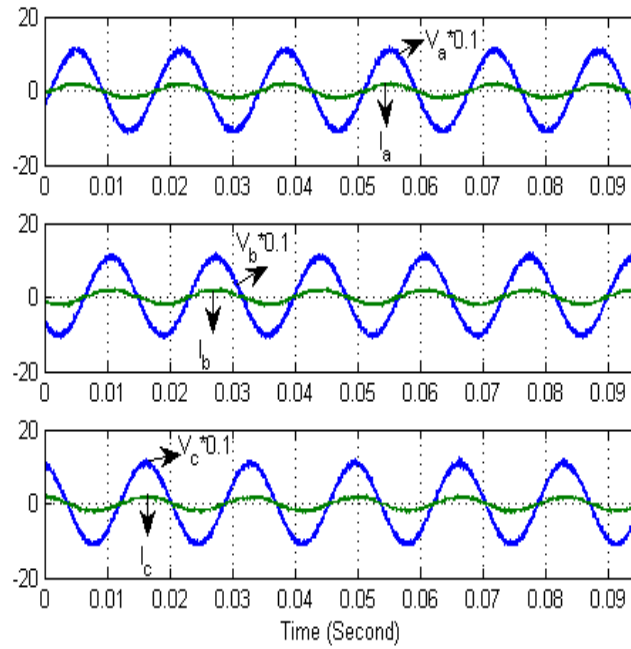
Figure 6-52. Three-phase voltages and currents (V_{dc} (module)=35 (V)).
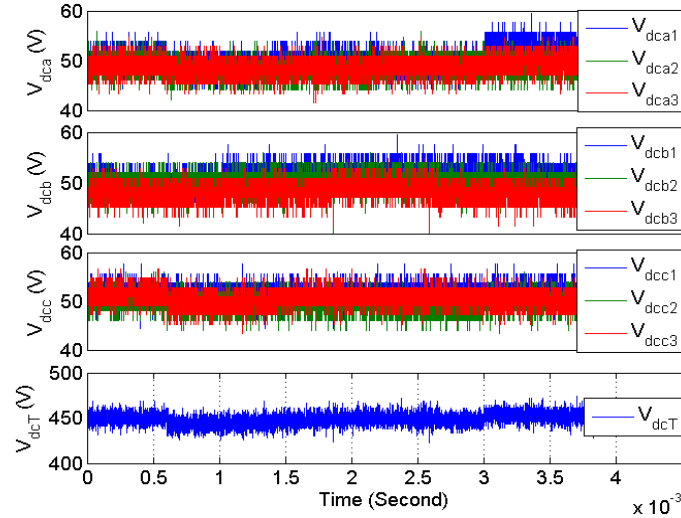
Figure 6-53. Terminal and capacitor DC voltages (V_{dc} (module)=50 (V)).

6.7   Summary

In this section, the controller hardware-in-the-loop (CHIL) simulation of CSTC in three different modes of operation is performed, and CHIL results are presented to verify the proposed control structure and algebraic model. Lab scale experimental results are also presented to evaluate the dynamic performance of CSTC in three different modes of operation.

Also, the operation of MTC based AMS under unbalanced operating condition is explored via detailed controller hardware-in-the-loop simulation. Experimental results are demonstrated to verify the proposed control structure based on instantaneous active power control method for operation of AMS under unbalanced operating conditions.

The controller hardware-in-the-loop simulation of the high frequency isolated modular converter is also performed by real time digital simulator (RTDS), and RTDS simulation

results are shown to verify the control scheme for high power applications. The hardware implementation of the high frequency isolated modular converter is also performed, and experimental results are shown to verify the proposed capacitor voltage balancing controller.

Chapter 7. CONCLUSIONS AND FUTURE WORK

7.1 Conclusion of Present Work

This thesis seeks to integrate flexible active solutions for power flow control to *existing* transmission assets, power transformer in particular while increasing the reliability of the US transmission grid. The MTC-based CSTC, by continuous real-time power flow control capability and multiple output voltages, increases the power system reliability and spare capacity, and can be connected to different voltage rating power transformers in the transmission grid. This structure has several advantages in comparison with conventional FACTS controllers. Modularity for manufacturers and utilities using standard high power electronic systems is one of the advantages of this structure. In addition, MTC-based CSTC can also be utilized in normal power system conditions to extend the life-time of aging power transformers. This thesis presented an algebraic model of the proposed MTC-based CSTC in three main operation modes (series-shunt, series-series and shunt-shunt mode of operation) to represent the behavior of transformer power flow with respect to operating points of the CSTC converters. The proposed algebraic model was used to determine the reference values for active and reactive power flow of the CSTC converters based on the desired operating points of the connecting transformer power flow. From the obtained results, it was concluded that the transformer operating region depends on power system parameters, and the operating region of the transformer in the series-shunt mode of operation decreases as the receiving end impedance (X_r) increases whereas in the shunt-shunt mode of operation, the transformer operating range increases as X_r increases. Also, the active power operating region of the

transformer in the series-series mode of operation is twice the transformer operating range in series-shunt mode of operation whereas the operating range of transformer reactive power flow is limited in series-series mode of operation. The control structure of the CSTC in three different modes of operation was proposed, and the dynamic performance of CSTC was explored based on the proposed control method. The feasibility of the CSTC operation via detailed controller hardware-in-the-loop simulation (CHIL) was demonstrated, and CHIL results verified the controller performance and algebraic model. Experimental results were also presented to further evaluate the dynamic performance and attractive features of the proposed MTC-based CSTC.

This thesis also introduced the concept of transmission-level Active Mobile Substations (AMS). The AMS is a mobile substation enabled by integrated power electronics. The AMS can be connected across different transformers of the grid by controlling its throughput power in normal conditions and as well as contingencies. AMS can provide back-up in case of power transformer failure or forced reduced operation scenarios in addition to power flow control for seasonal renewable energy sources. With state-of-the-art power electronics circuits and using even novel devices such as 15kV SiC IGBTs or 9kV Si-Thyristors, the AMS may not be practically feasible mainly due to efficiency concerns, low gravimetric and volumetric power densities of the current technologies. The design of the AMS is an example of transitioning science behind power electronics, geoscience, instrumentation, networking and control into disaster engineering practice for the US critical energy infrastructure sector. With the development of the proposed AMS, transmission owners and system operators will possess a transportable, controllable, and versatile *asset* that helps them to restore power in

case of natural disasters and emergencies. Utilities can also deploy or rent AMS to extend the life-time of their transformer fleet or to control the power flow from integration of renewable resources. Therefore, it not only improves the power system operation but also it is an effective solution that alleviates increased penetration of renewable energy sources. Furthermore, future transmission substations can be envisioned with the developed AMS technology.

A detailed comparative analysis of different power converter topologies for AMS application was performed. Based on the obtained results, it was concluded that the "high frequency isolated modular converter" is a feasible technology for the AMS. In this configuration, several H-bridge modules are connected in cascade, so the voltage balancing control of several floating dc capacitors is required. In this thesis, an appropriate control structure with the phase and module voltage balancing controller was proposed to achieve voltage balancing control of multiple floating dc capacitors. The proposed control scheme consists of four layers to control power flow and terminal DC bus voltage as well as DC capacitor voltages of each module. The phase voltage balancing controller was proposed to equalize the sum of DC capacitor voltages in phase-A with the sum of DC capacitor voltages in phases-B, and C. The common-mode voltage was used for phase voltage balancing control. The module voltage balancing controller was also used to ensure that DC capacitor voltage of each module in each phase is similar to the capacitor voltage of other modules in that phase. Simulation and lab scale experimental results were also presented to verify the proposed control structure.

In this thesis, the dynamic performance of embedded multi-terminal dc grid in meshed AC power systems was also evaluated. An algebraic model was proposed to analyze the steady state performance of embedded multi-terminal dc grid in meshed AC power systems. The proposed algebraic model was used to determine the reference values for active and reactive power flow of dc grid converters based on the desired operating points of meshed ac power system. The proposed model was validated on a reduced order ac equivalent NYPA power system. The control structure of embedded multi-terminal dc grid in meshed ac power systems based on droop control structure with dead-band controller was proposed. The dynamic performance of embedded multi-terminal dc grid in meshed ac power system based on the proposed control method was also investigated in PSCAD/EMTDC and RTDS. Steady state simulation results were used to verify the proposed algebraic model.

This thesis also examined the dynamic performance of AMS under fault operating conditions. From the obtained results, it was concluded that in MTC based AMS, the negative sequence current is highly dependent on the DC capacitor value in angle control method, and the capacitor value must be chosen appropriately such that 120 Hz oscillations in the DC link can be tolerated under unbalanced conditions. A control scheme based on instantaneous active power control method was also proposed to make dc bus voltage constant. A supervisory control was also used to determine the switching strategy between angle control method and proposed control method under AC fault operating conditions. Experimental results were also shown to verify the proposed control structure of MTC based AMS under AC fault operating conditions.

The dynamic performance of the high frequency isolated modular converter under AC fault operating conditions was also explored. This thesis proposed a control method of the high frequency isolated modular converter which can be protected against dc fault without using expensive DC circuit breakers. The control algorithm for DC fault operation and recovery after DC fault was proposed. The performance of converter was thoroughly analyzed under DC fault operating condition, and simulation results were presented to validate the control structure under DC fault operating conditions.

The dynamic performance of multi-terminal DC grid was also analyzed under DC fault operating condition, and simulation results were presented to validate the control algorithm for DC fault operation and recovery after DC fault.

The dynamic performance of multi-terminal DC grid was also evaluated under loss of master converter. The control structure of MTDC system based on master/slave control scheme and droop control structure was explained. The dynamic performance of four-terminal DC grid with the master/slave control scheme and droop control method with dead-band controller was investigated under loss of master converter. It was observed that in master/slave control method, the outage of master terminal results in the outage of entire MTDC system since in this case, terminal DC bus voltage is only controlled by master terminal. Simulation results were presented to verify the proposed droop control method with dead-band controller. Results showed that the multi-terminal DC grid operates satisfactorily under normal and loss of a terminal with the proposed droop control method with dead-band controller.

7.2   Contributions

The main contributions of this thesis can be enumerated as follows:

1. Developed control structures of Convertible Static Transmission Controller (CSTC) in three different modes of operation.

2. Proposed algebraic models of CSTC in three different modes of operation.

3. Controller hardware-in-the-loop implementation of CSTC in three different modes of operation by Typhoon HIL400.

4. Experimental verification of the proposed control schemes and algebraic models of CSTC in different modes of operation.

5. Introduction the concept of Active Mobile Substation (AMS).

6. Proposed control scheme of the high frequency isolated modular converter based AMS for capacitor voltage balancing control.

7. Controller hardware-in-the-loop implementation of the high frequency isolated modular converter by RTDS.

8. Experimental verification of the proposed control scheme of the high frequency isolated modular converter.

9. Algebraic model and control of embedded multi-terminal DC grid in a meshed AC power system.

10. Component design of Modular Transformer Converter (MTC) based AMS with angle control method to reduce the magnitude of negative sequence component of AC current and second order harmonics component of DC bus voltage under AC fault operating condition.

11. Proposed instantaneous active power flow control method for MTC based AMS under AC fault operating condition.

12. Proposed control scheme of the high frequency isolated modular converter for DC fault operation and recovery after DC fault. The high frequency isolated modular converter with the proposed control method can be protected against DC fault without using expensive DC circuit breakers.

13. Proposed control scheme of multi-terminal DC grid based on droop control method with dead-band controller.

14. Proposed control algorithm of multi-terminal DC grid for DC fault operation and recovery after DC fault.

7.3 Future Work

- Develop protocols to monitor and control the main power transformer of the CSTC concept for centralized and distributed modes of control; and develop methods (and metrics) to test the resiliency and stability of the interconnected CSTC-based transmission controllers.

- Evaluate economic impact of CSTC flexibility on integration of renewable resources, increased transmission capacity, and voltage controllability.

- Perform a survey of current commercial operations and planning models to develop a platform for CSTC integration and making recommendations on required upgrades and enhancements to operations and planning simulation models.

- Cost vs. Benefit analysis of CSTC as Transmission Controllers. Develop a simulation base case to measure the impact of CSTC device on market clearing price for Locational Marginal Pricing (LMP) and ancillary services under different load, generation, and other system conditions.

- Contingency analysis with CSTC. Select a region such as NYPA or Northeast, obtain a power flow model for the selected region, develop a set of N-1-1 contingency events under different system conditions by season and time of the day, perform steady state and N-1-1 contingency analysis for each developed N-1-1 contingency events to assess the effectiveness of installation of CSTC devices on preventing the system to become unstable and islanded following two consecutive non-simultaneous unexpected outage events.

- For AMS application, a hierarchical wireless network for implementing real time monitoring and control of AMS is required. The hierarchical wireless network should comprise of a set of wireless sensor networks or subnets that are integrated by a wireless relay network.

- Develop data processing algorithms for transformer health and condition assessment. Although the approaches for deriving many of the parameters for monitoring transformers is known, the challenge is to develop methods that can be applied to sensor nodes under its limitations of energy and computational resources.

- Reliability improvement assessment of the power grid with AMS in power system and during abnormal and/or hazardous grid level events.

- Security analysis of the grid and evaluation of the ability of AMS to bring successful improvement in hazardous failures and malfunctions.

- The ability of the AMS to effectively integrate to other grid level controllers and dispatch algorithms for increased stability and high level distributed control for a modern sustainable energy system.

Bibliography

[1]   B. Parkhideh and S. Bhattacharya, "A unified Modular Transformer Converter (MTC) system with advanced angle control structure," In Proc. ECCE'11, 2011.

[2]   D. Divan and J. Sastry, "Controllable Network Transformers," Power Electronics Specialists Conference, 2008. PESC 2008. IEEE, vol., no., pp.2340, 2345, 15-19 June 2008.

[3]   S. Bala, D. Das, E. Aeloiza, A. Maitra, and S. Rajagopalan, "Hybrid distribution transformer: Concept development and field demonstration," Energy Conversion Congress and Exposition (ECCE), 2012 IEEE , vol., no., pp.4061,4068, 15-20 Sept. 2012.

[4]   D. Divan, W. Brumsickle, R. Schneider, B. Kranz, R. Gascoigne, D. Bradshaw, M. Ingram, and I. Grant, "A distributed static series compensator system for realizing active power flow control on existing power lines," Power Systems Conference and Exposition, 2004. IEEE PES, vol., no., pp.654, 661 vol.2, 10-13 Oct. 2004.

[5]   D. Das and D. Divan, "Power flow control in networks using controllable network transformers," Energy Conversion Congress and Exposition, 2009. ECCE 2009. IEEE, vol., no., pp.2224, 2231, 20-24 Sept. 2009.

[6]   D. Divan and H. Johal, "Distributed FACTS—A New Concept for Realizing Grid Power Flow Control," Power Electronics, IEEE Transactions on, vol.22, no.6, pp.2253, 2260, Nov. 2007.

[7]   K. Hatua, S. Dutta, A. Tripathi, S. Baek, G. Karimi, and S. Bhattacharya, "Transformerless intelligent power substation design with 15kV SiC IGBT for grid interconnection," In Proc. IEEE ECCE'11, 2011.

[8]   H. Mirzaee, A. De, A. Tripathi, and S. Bhattacharya, "Design comparison of high power medium-voltage converters based on 6.5kV Si-IGBT/Si-PiN JBS diode, and 10kV SiC MOSFET/SiC-JBS diode," In Proc. at IEEE ECCE'11, 2011.

[9]   K. Fujii, P. Koellensperger, and R.W. De Doncker, "Characterization and Comparison of High Blocking Voltage IGBTs and IEGTs Under Hard- and Soft-Switching Conditions," Power Electronics, IEEE Transactions on , vol.23, no.1, pp.172,179, Jan. 2008.

[10] R. Lenke, H. van Hoek, S. Taraborrelli, R.W. De Doncker, J. San-Sebastian, and I. Etxeberria-Otadui, "Turn-off behavior of 4.5 kV asymmetric IGCTs under zero voltage switching conditions," Power Electronics and Applications (EPE 2011), Proceedings of the 2011-14th European Conference on , vol., no., pp.1,10, Aug. 30 2011-Sept. 1 2011.

[11] B. Parkhideh and S. Bhattacharya, "Active power transfer capability of shunt family of FACTS devices based on angle control," Energy Conversion Congress and Exposition, 2009. ECCE 2009. IEEE, vol., no., pp.2711, 2718, 20-24 Sept. 2009.

[12] S. Jianjiang, W.Gou H. Yuan, T. Zhao, and A.Q. Huang, "Research on Voltage and Power Balance Control for Cascaded Modular Solid-State Transformer, "Power Electronics, IEEE Transactions on , vol.26, no.4, pp.1154,1166, April 2011.

[13] X. She, R. Burgos, G. Wang, F. Wang, and A.Q. Huang, "Review of solid state transformer in the distribution system: From components to field application," Energy

Conversion Congress and Exposition (ECCE), 2012 IEEE , vol., no., pp.4077,4084, 15-20 Sept. 2012.

[14] T. Zhao, G. Wang, S. Bhattacharya, and A. Q. Huang, "Voltage and Power Balance Control for a Cascaded H-Bridge Converter-Based Solid-State Transformer," Power Electronics, IEEE Transactions on , vol.28, no.4, pp.1523,1532, April 2013.

[15] X. She, A.Q. Huang, and G. Wang, "3-D Space Modulation With Voltage Balancing Capability for a Cascaded Seven-Level Converter in a Solid-State Transformer," Power Electronics, IEEE Transactions on , vol.26, no.12, pp.3778,3789, Dec. 2011.

[16] D. Bortis, J. Biela, and J.W. Kolar, "Transient Behavior of Solid-State Modulators With Matrix Transformers," Plasma Science, IEEE Transactions on , vol.38, no.10, pp.2785,2792, Oct. 2010

[17] S. Bifaretti, P. Zanchetta, A. Watson, L. Tarisciotti, and J.C. Clare, "Advanced Power Electronic Conversion and Control System for Universal and Flexible Power Management," Smart Grid, IEEE Transactions on , vol.2, no.2, pp.231,243, June 2011.

[18] Z. Chen, J.M. Guerrero, and F. Blaabjerg, "A Review of the State of the Art of Power Electronics for Wind Turbines," Power Electronics, IEEE Transactions on , vol.24, no.8, pp.1859,1875, Aug. 2009.

[19] S. D. Sudhoff, "Solid State Transformer," US Patent No. 5,943,229, Aug. 24, 1999.

[20] A. Lesnicar and R. Marquardt, "An innovative modular multilevel converter topology suitable for a wide power range," Power Tech Conference Proceedings, 2003 IEEE Bologna , vol.3, no., pp.6 pp. Vol.3,, 23-26 June 2003.

[21] F. Iov, F. Blaabjerg, R. Bassett, J. Clare, A. Rufer, S. Savio, P. Biller, P.Taylor, and B. Sneyers, "Advanced power converter for universal and flexible power management in future electricity network," presented at the CIRED, Vienna, Austria, May 2007.

[22] M. Hagiwara and H. Akagi, "Control and experiment of pulse width modulated modular multilevel converters," IEEE Trans. on Power Electronics, vol. 24, no. 7, July 2009, pp. 1737-1746.

[23] X. Yang, T.Q. Zheng, Z. Lin, T. Xiong, and X. You, "Power quality controller based on hybrid modular multilevel converter," Industrial Electronics (ISIE), 2012 IEEE International Symposium on, vol., no., pp.1997, 2002, 28-31 May 2012.

[24] G. Mondal, R. Critchley, F. Hassan, and W. Crookes, "Design and simulation of a modular multi-level converter for MVDC application," Industrial Electronics (ISIE), 2011 IEEE International Symposium on, vol., no., pp.200, 205, 27-30 June 2011.

[25] K. Friedrich, "Modern HVDC PLUS application of VSC in Modular Multilevel Converter topology," Industrial Electronics (ISIE), 2010 IEEE International Symposium on, vol., no., pp.3807, 3810, 4-7 July 2010.

[26] A.J. Korn, M. Winkelnkemper, and P. Steimer, "Low output frequency operation of the Modular Multi-Level Converter," Energy Conversion Congress and Exposition (ECCE), 2010 IEEEs, vol., no., pp.3993, 3997, 12-16 Sept. 2010.

[27] J. Wang and F.Z. Peng, "Unified power flow controller using the cascade multilevel inverter," Power Electronics, IEEE Transactions on, vol.19, no.4, pp.1077, 1084, July 2004.

[28] B. Parkhideh and S. Bhattacharya, "Towards smart transmission substations with Modular Transformer Converter systems," Power and Energy Society General Meeting, 2011 IEEE , vol., no., pp.1,7, 24-29 July 2011.

[29] North American Electric Reliability Corporation, NERC.com.

[30] J. Robinson, "Transmission Availability Data System (TADS) draft summary," NERC TADS round meeting working group, 2011.

[31] C. L. Stiegemeier and R. Craig, "Rapidly deployable recovery transformers," In IEEE Power and Energy Magazine, 2006.

[32] Joint NERC and DOE report, "High-Impact, Low-Frequency Event Risk to the North American Bulk Power System," November 2009 Workshop.

[33] NERC Disturbance Analysis Working Group Report, "The 1989 System Disturbances: March 13," 1989 Geomagnetic Disturbance, 1990.

[34] J. Kappenman and M. Corporation, "Geomagnetic Storms and Their Impacts on the U.S. Power Grid," January 2010.

[35] J. Kappenman, "Storm Analysis Consultants, Space Weather and US Electric Power Grid Vulnerabilities: An Overview of the Risks to this Critical Infrastructure and Research Necessary to Assess Vulnerability and Mitigate Impacts," NASA Space Weather Risks and Society Workshop, Oct. 15-16, 2011, CA.

[36] S. Bhattacharya, B. Fardenesh, and B. Sherpling, "Convertible Static Compensator: Voltage Source Converter Based FACTS Application in the New York 345 kV Transmission System," Proc. of the 5th International Power Electronics Conference (IPEC), Niigata, Japan, April 2005.

[37] S. Bhattacharya, "NYPA CSC TNA Studies," EPRI Internal Report.

[38] N. G. Hingorani and L. Gyugyi, "Understanding FACTS," New Jersey: IEEE Press, 1999.

[39] J. Sun, L. Hopkins, B. Shperling, B. Fardanesh, M. Graham, M. Parisi, S. McDonald, S. Bhattacharya, S. Bekowitz, and A. Edris, "Operating Characteristics of the Convertible Static Compensator on the 345 kV Network," IEEE PES Power Systems Conference & Exposition, NY, October 2004.

[40] M. Maharsi, L. Tang, and S. Bala, "Hybrid distribution transformer," US Patent No.: US2010/0220499A1.

[41] D. Das, D. M. Divan, and R.G. Harley, "Power Flow Control in Networks Using Controllable Network Transformers," Power Electronics, IEEE Transactions on, vol.25, no.7, pp.1753, 1760, July 2010.

[42] S. Bhattacharya, T. Zhao, G. Wang, S. Dutta, S. Baek, Y. Du, B. Parkhideh, X. Zhou, and A.Q. Huang, "Design and development of Generation-I silicon based Solid State Transformer," IEEE Applied Power Electronics Conference and Exposition (APEC), 2010 , vol., no., pp.1666-1673, 21-25 Feb. 2010.

[43] www.abb.com.

[44] North American Electric Reliability Corporation, NERC.com.

[45] J. Robinson, "Transmission Availability Data System (TADS) draft summary," NERC TADS round meeting working group, 2011.

[46] B. Parkhideh, N. Yousefpoor, B. Fardanesh, and S. Bhattacharya, "Vector Analysis and Performance Evaluation of Modular Transformer Converter (MTC) Based Convertible Static Transmission Controller," IEEE PES General Meeting, 2012.

[47] B. Parkhideh, N. Yousefpoor, S. Babaei, and S. Bhattacharya, "Design considerations in development of active mobile substations," In Proc. ECCE'12, 2012.

[48] C. Schauder and H. Mehta, "Vector analysis and control of advanced static VAR compensators," IEE Proc. -C, July 1993.

[49] L. Kovalsky, C. Shauder, E. Stacy, M. Weaver, and S. MacDonald, "Convertible static compensator (CSC) for New York Power Authority," EPRI, Palo Alto, CA, Tech. Rep. 1001970, September 2001.

[50] N. Yousefpoor, S. Kim, B. Parkhideh, and S. Bhattacharya, "Supervisory Control of Convertible Static Transmission Controller in Shunt-Shunt Mode of Operation," In Proc. IECON'13, 2013.

[51] L. Gyugyi, C. D. Schauder, S. L. Williams, T. R. Rietman, D. R. Torgerson, and A. Edris, "The unified power flow controller: a new approach to power transmission control," IEEE Trans. on Power Delivery, 1995.

[52] M. Noroozian, L. Ängquist, M. Ghandhari, and G. Andersson, "Use of UPFC for optimal power flow control," IEEE Trans. Power Del., vol. 12, no. 4, pp. 1629–1634, Oct. 1997.

[53] S. Lee, J. Kang, and S. Sul, "A new phase detecting method for power conversion systems considering distorted conditions in power system," Industry Applications

Conference, 1999. Thirty-Fourth IAS Annual Meeting. Conference Record of the 1999 IEEE, vol.4, no., pp.2167, 2172 vol.4, 1999.

[54] S. Sul, "Control of Electric Machine Drive Systems," ISBN: 978-0-470-59079-9.

[55] A. Visioli, "Modified Anti-windup scheme for PID controllers," IEE Proc. Control Theory Appl., Vol. 150, January, 2003, pp. 49–54.

[56] E. Muljadi, "New challenges in high penetration wind power generation," NREL, 2010.

[57] D. Woodcock, "Transformer fleet health and risk management," IEEE PES Transformer Committee Tutorial, 2007.

[58] "Transmission availability data system automatic outage metrics and data," NERC Reports 2008 & 2009.

[59] N. Yousefpoor, B. Parkhideh, A. Azidehak, S. Bhattacharya, and B. Fardanesh, "Modular Transformer Converter Based Convertible Static Transmission Controller for Transmission Grid Management," Power Electronics, IEEE Transactions on , vol. PP, no.99, pp.1,1.

[60] A. Lesnicar and R. Marquardt, "An innovative modular multilevel converter topology suitable for a wide power range," Power Tech Conference Proceedings, 2003 IEEE Bologna , vol.3, no., pp.6 pp. Vol.3,, 23-26 June 2003.

[61] G. Mondal, R. Critchley, F. Hassan, W. Crookes, "Design and simulation of a modular multi-level converter for MVDC application," Industrial Electronics (ISIE), 2011 IEEE International Symposium on, vol., no., pp.200,205, 27-30 June 2011.

[62] K. Friedrich, "Modern HVDC PLUS application of VSC in Modular Multilevel Converter topology," Industrial Electronics (ISIE), 2010 IEEE International Symposium on, vol., no., pp.3807, 3810, 4-7 July 2010.

[63] A.J. Korn, M. Winkelnkemper, and P. Steimer, "Low output frequency operation of the Modular Multi-Level Converter," Energy Conversion Congress and Exposition (ECCE), 2010 IEEE, vol., no., pp.3993, 3997, 12-16 Sept. 2010.

[64] J. Shi, W. Gou, H. Yuan, T. Zhao, and A.Q. Huang, "Research on Voltage and Power Balance Control for Cascaded Modular Solid-State Transformer," Power Electronics, IEEE Transactions on , vol.26, no.4, pp.1154,1166, April 2011.

[65] X. She, R. Burgos, G. Wang, F. Wang, and A.Q. Huang, "Review of solid state transformer in the distribution system: From components to field application," Energy Conversion Congress and Exposition (ECCE), 2012 IEEE , vol., no., pp.4077,4084, 15-20 Sept. 2012.

[66] T. Zhao, G. Wang, S. Bhattacharya, and A. Q. Huang, "Voltage and Power Balance Control for a Cascaded H-Bridge Converter-Based Solid-State Transformer," Power Electronics, IEEE Transactions on , vol.28, no.4, pp.1523,1532, April 2013.

[67] S. Meier, "System aspects and modulation strategies of an hvdc-based converter system for wind farms," Ph.D. dissertation, Royal Institute of Technology, KTH, Stockholm, 2009.

[68] S. Bifaretti, P. Zanchetta, A. Watson, L. Tarisciotti, and J.C. Clare, "Advanced Power Electronic Conversion and Control System for Universal and Flexible Power Management," Smart Grid, IEEE Transactions on , vol.2, no.2, pp.231,243, June 2011.

[69] F. Iov, F. Blaabjerg, R. Bassett, J. Clare, A. Rufer, S. Savio, P. Biller, P.Taylor, and B. Sneyers, "Advanced power converter for universal and flexible power management in future electricity network," presented at the CIRED, Vienna, Austria, May 2007.

[70] J. Sun, L. Hopkins, B. Shperling, B. Fardanesh, M. Graham, M. Parisi, S. McDonald, S. Bhattacharya, S. Bekowitz, and A. Edris, "Operating Characteristics of the Convertible Static Compensator on the 345 kV Network," IEEE PES Power Systems Conference & Exposition, NY, October 2004.

[71] C. Schauder, M. Gernhardt, E. Stacey, T. Lemak, L. Gyugyi, T. W. Cease, and A. Edris, "Operation on +/- 100 MVAR TVA STATCON," IEEE Trans. On Power Delivery, 1997.

[72] M. Hagiwara and H. Akagi, "Control and experiment of pulse width modulated modular multilevel converters," IEEE Trans. on Power Electronics, vol. 24, no. 7, July 2009, pp. 1737-1746.

[73] M. Hagiwara and H. Akagi, "PWM control and experiment of modular multilevel converters," in Power Electronics Specialists Conference, PESC IEEE, pp. 154-161, 2008.

[74] G. D. Demetriades, "On small-signal analysis and control of the single- and the dual-active bridge topologies," Doctoral Dissertation, Royal Institute of Technology, Sweden, ISBN-91-7283-966-x, 2005.

[75] D. Costinett, D. Maksimovic, and R. Zane, "Design and Control for High Efficiency in High Step-Down Dual Active Bridge Converters Operating at High Switching

Frequency," Power Electronics, IEEE Transactions on , vol.28, no.8, pp.3931,3940, Aug. 2013.

[76] J. Beerten, S. Cole, and R. Belmans, "A sequential AC/DC power flow algorithm for networks containing multi-terminal VSC HVDC systems," in Proc. PES General Meeting, Jul. 2010, pp. 1-7.

[77] J. Pan, R. Nuqui, K. Srivastava, T. Jonsson, P. Holmberg, and Y. J. Hafner, "AC Grid with Embedded VSC-HVDC for Secure and Efficient Power Delivery," Energy 2030 Conference, 2008. ENERGY 2008. IEEE, vol., no., pp.1,6, 17-18 Nov. 2008.

[78] D. O. Dike and O. D. Momoh, "An Integrated AC/DC Super-Grid System -A Mechanism to Solving the North American Power Crisis," System Theory, 2007. SSST '07. Thirty-Ninth Southeastern Symposium on , vol., no., pp.204,209, 4-6 March 2007.

[79] H. Nikkhajoei and R. Iravani, "Steady-State Model and Power Flow Analysis of Electronically-Coupled Distributed Resource Units," Power Delivery, IEEE Transactions on, vol.22, no.1, pp.721, 728, Jan. 2007.

[80] R. L. Vasquez-Arnez and L.C. Zanetta, "A Novel Approach for Modeling the Steady-State VSC-Based Multiline FACTS Controllers and Their Operational Constraints," Power Delivery, IEEE Transactions on , vol.23, no.1, pp.457,464, Jan. 2008.

[81] R. da Silva, R. Teodorescu, and P. Rodriguez, "Power delivery in MTDC transmission system for offshore wind power applications," in Proc. IEEE PES ISGT Europe, Oct. 2010.

[82] W. Lu and B. T. Ooi, "Optimal acquisition and aggregation of offshore wind power by multi-terminal voltage-source HVDC," Power Delivery, IEEE Transactions on, vol.18, no.1, pp.201, 206, Jan 2003.

[83] W. Lu and B. T. Ooi, "Premium quality power park based on multi-terminal HVDC," Power Delivery, IEEE Transactions on, vol.20, no.2, pp.978, 983, April 2005.

[84] R. L. Hendriks, G.C. Paap, and W. L. Kling, "Control of a multi-terminal VSC transmission scheme for interconnecting offshore wind farms," in Proc. Eur. Wind Energy Conf. Exhibition, May 2007.

[85] B. Berggren, R. Majumder, C. Sao, and K. Linden, "Method and control device for controlling power flow within a DC power transmission network," WIPO International Publication Number WO 2012/000549 A1, International Filing Date: 30 June 2012; International Publication Date: 5 January 2012.

[86] J. Pan, R. Nuqui, L. Tang, and P. Holmberg, "VSC-HVDC Control and Application in Meshed AC Networks," Panel Paper, IEEE PES General Meeting, July 2008, Chicago, USA.

[87] J. Beerten, S. Cole, and R. Belmans, "Modeling of Multi-Terminal VSC HVDC Systems With Distributed DC Voltage Control," Power Systems, IEEE Transactions on , vol.PP, no.99, pp.1,9, 0 doi: 10.1109/TPWRS.2013.2279268.

[88] T. M. Haileselassie and K. Uhlen, "Impact of DC line voltage drops on power flow of MTDC using droop control," IEEE Trans. Power Syst., vol. 27, no. 3, pp. 1441-1448, Aug. 2012.

[89] L. Kovalsky, C. Shauder, E. Stacy, M. Weaver, and S. MacDonald, "Convertible static compensator (CSC) for New York Power Authority," EPRI, Palo Alto, CA, Tech. Rep. 1001970, September 2001.

[90] L. Ronström, M.L. Hoffstein, R. Pajo, and M. Lahtinen, "The Estlink HVDC light transmission system," CIGRE Regional Meeting on Security and Reliability of Electric Power Systems, Tallinn, Estonia, 2007.

[91] T. Worzyk, "Submarine Power Cables: Design, Installation, Repair, Environmental Aspects," Springer Publishing Company, 2009.

[92] N. Yousefpoor, B. Parkhideh, A. Azidehak, and S. Bhattacharya, "Control of Active Mobile Substations Under System Faults," In Proc. ECCE'13, 2013.

[93] Y. Suh, "Analysis and control of three phase AC/DC PWM converter under unbalanced operating conditions," Ph.D. thesis, University of Wisconsin-Madison, Madison, Wisconsin, U.S.A., 2003.

[94] Y. Suh and T.A. Lipo, "Modeling and analysis of instantaneous active and reactive power for PWM AC/DC converter under generalized unbalanced network," Power Delivery, IEEE Transactions on, vol.21, no.3, pp.1530-1540, July 2006.

[95] Y. Suh, V. Tijeras, and T. A. Lipo, "A control method in dq synchronous frame for PWM boost rectifier under generalized unbalanced operating conditions," in Proc. IEEE PESC, Cairns, Australia, Jun., 2002, pp. 1425–1430.

[96] Y. Suh, V. Tijeras, and T. A. Lipo, "A nonlinear control of the instantaneous power in dq synchronous frame for PWM AC/DC converter under generalized unbalanced

operating conditions," in Proc. IEEE Ind. Appl. Soc. Annu. Meeting, Chicago, IL, Oct. 2002.

[97] H. Song and K. Nam, "Dual current control scheme for pwm converter under unbalanced input voltage conditions," IEEE Trans. Ind. Electron., vol. 46, no. 5, pp. 953–959, Oct. 1999.

[98] M. K. Bucher, M. M. Walter, M. Pfeiffer, and C.M. Franck, "Options for ground fault clearance in HVDC offshore networks," Energy Conversion Congress and Exposition (ECCE), 2012 IEEE , vol., no., pp.2880,2887, 15-20 Sept. 2012.

[99] N. Yousefpoor, A. Azidehak, S. Bhattacharya, B. Parkhideh, I. Celanovic, and A. Genic, "Real-time Hardware-in-the-Loop simulation of convertible static transmission controller for transmission grid management," Control and Modeling for Power Electronics (COMPEL), 2013 IEEE 14th Workshop on , vol., no., pp.1,8, 23-26 June 2013.

[100] D. Majstorovic, I. Celanovic, N. Teslic, N. Celanovic, and V. Katic, "Ultra-Low Latency Hardware-in-the-Loop Platform for Rapid Validation of Power Electronics Designs," in IEEE Transactions on Industrial Electronics, vol. 58, pp. 4708-4716, 2011.